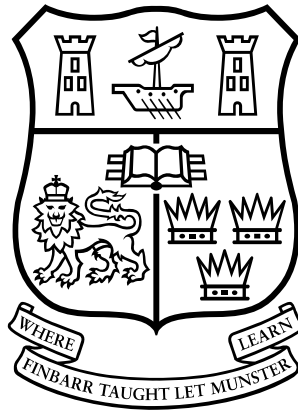


Title	Integrated magnetic components for high-power high-current dc-dc converters
Authors	Hartnett, Kevin John
Publication date	2013
Original Citation	Hartnett, K. J. 2013. Integrated magnetic components for high-power high-current dc-dc converters. PhD Thesis, University College Cork.
Type of publication	Doctoral thesis
Link to publisher's version	http://library.ucc.ie/record=b2075617
Rights	© 2013, Kevin J. Hartnett. - http://creativecommons.org/licenses/by-nc-nd/3.0/
Download date	2024-03-28 18:43:38
Item downloaded from	https://hdl.handle.net/10468/1278



Integrated Magnetic Components for High-Power High-Current DC-DC Converters

Kevin J. Hartnett

A thesis presented to the National University of Ireland for the
degree of Doctor of Philosophy

March, 2013

Supervised by Dr. John G. Hayes and Dr. Michael G. Egan

Department of Electrical and Electronic Engineering

University College Cork

Ireland

Declaration

I hereby declare that I am the sole author of this thesis and all of the work undertaken in this thesis is original in content and was carried out by the author. Work carried out by others has been duly acknowledged in the thesis.

This is a true copy of the thesis, including any required final revisions, as accepted by my examiners. The work presented has not been accepted in any previous application for a degree.

Signed: _____

Date: _____

Abstract

This thesis is focused on the design and development of an integrated magnetic (IM) structure for use in high-power high-current power converters employed in renewable energy applications. These applications require low-cost, high efficiency and high-power density magnetic components and the use of IM structures can help achieve this goal.

A novel CCTT-core split-winding integrated magnetic (CCTT IM) is presented in this thesis. This IM is optimized for use in high-power dc-dc converters. The CCTT IM design is an evolution of the traditional EE-core integrated magnetic (EE IM). The CCTT IM structure uses a split-winding configuration allowing for the reduction of external leakage inductance, which is a problem for many traditional IM designs, such as the EE IM. Magnetic poles are incorporated to help shape and contain the leakage flux within the core window. These magnetic poles have the added benefit of minimizing the winding power loss due to the airgap fringing flux as they shape the fringing flux away from the split-windings.

A CCTT IM reluctance model is developed which uses fringing equations to accurately predict the most probable regions of fringing flux around the pole and winding sections of the device. This helps in the development of a more accurate model as it predicts the dc and ac inductance of the component. A CCTT IM design algorithm is developed which relies heavily on the reluctance model of the CCTT IM. The design algorithm is implemented using the mathematical software tool Mathematica. This algorithm is modular in structure and allows for the quick and easy design and prototyping of the CCTT IM. The algorithm allows for the investigation of the CCTT IM boxed volume with the variation of input current ripple, for different power ranges, magnetic materials and frequencies.

A high-power 72 kW CCTT IM prototype is designed and developed for use in an automotive fuelcell-based drivetrain. The CCTT IM design algorithm is initially used to design the component while 3D and 2D finite element analysis (FEA) software is used to optimize the design. Low-cost and low-power loss ferrite 3C92 is used for its construction, and when combined with a low number of turns results in a very efficient design. A paper analysis is undertaken which compares the performance of the high-power CCTT IM design with that of two discrete inductors used in a two-phase (2L) interleaved converter. The 2L option consists of two discrete inductors constructed from high dc-bias material. Both

topologies are designed for the same worst-case phase current ripple conditions and this ensures a like-for-like comparison. The comparison indicates that the total magnetic component boxed volume of both converters is similar while the CCTT IM has significantly lower power loss. Experimental results for the 72 kW, (155 V dc, 465 A dc input, 420 V dc output) prototype validate the CCTT IM concept where the component is shown to be 99.7 % efficient. The high-power experimental testing was conducted at General Motors advanced technology center in Torrance, Los Angeles. Calorific testing was used to determine the power loss in the CCTT IM component. Experimental 3.8 kW results and a 3.8 kW prototype compare and contrast the ferrite CCTT IM and high dc-bias 2L concepts over the typical operating range of a fuelcell under like-for-like conditions. The CCTT IM is shown to perform better than the 2L option over the entire power range.

An 8 kW ferrite CCTT IM prototype is developed for use in photovoltaic (PV) applications. The CCTT IM is used in a boost pre-regulator as part of the PV power stage. The CCTT IM is compared with an industry standard 2L converter consisting of two discrete ferrite toroidal inductors. The magnetic components are compared for the same worst-case phase current ripple and the experimental testing is conducted over the operation of a PV panel. The prototype CCTT IM allows for a 50 % reduction in total boxed volume and mass in comparison to the baseline 2L option, while showing increased efficiency.

Acknowledgements

I wish to thank all of the individuals who have contributed to my work. This thesis would not have been possible without their support and guidance.

Firstly, I wish to thank my academic supervisors Dr. John Hayes and Dr. Michael Egan for their guidance, support, expertise and friendship. It was a pleasure to get to know John better on recent trips to Chicago, Kraków and Kassel. I wish to thank Prof. Charles Sullivan and Prof. Nabeel Riza for examining my thesis.

The financial and technical support of General Motors and dtw is greatly appreciated. I wish to thank George Woody, Terence Ward and Seok Joo Jang of General Motors and all the staff of dtw including: Jurek, Tomasz, Jakub, Marcin, Swavick and Milosz.

I wish to especially thank Dr. Marek Rylko for his help, advice and friendship. Marek's support has been incredible and very much appreciated. I will always remember our daily car trips from Bielsko to Kraków as well as getting lost in the "time-warp" that is the research department at dtw. Great memories. I also wish to sincerely thank Marek's parents, Zdzislaw i Irena, and brother, Wojciech, for their incredible hospitality.

I wish to thank all of the staff of the Department of Electrical and Electronic Engineering at University College Cork. Particular mention must go to Dr. Kevin McCarthy, Mick O' Shea, Tim Power, Geraldine Mangan and Ralph O' Flaherty. I would especially like to thank Mr. James Griffiths – so often I would call up to James to ask a quick question only still to be there an hour later deep in conversation.

I would also like to thank my fellow postgraduate students who provided great camaraderie and whom made the laboratory a wonderful place to work. Particular mention must go to Dr. Jason Hannon, Dr. David Cashman, Donal Murray, Naveen Boggarapu, Dr. Ray Foley, Brendan Barry, Jack Birmingham, Diarmaid Hogan, Judy Rae, Ann-Katrin Gerlach, Killian O' Donoghue and Neil Hanley. I also wish to thank William, Donal Og, Grace and Keara for their friendship and support.

My sincere gratitude goes to my parents, Liz and John, my brothers, Barry and Brian and sister, Amy.

And of course to Julia, for her love, support, and for sharing this with me. Thank you.

List of Publications

Journal Paper:

1. K.J. Hartnett, J.G. Hayes, M.G. Egan, M.S. Rylko, "CCTT-Core Split-Winding Integrated Magnetic for High-Power DC-DC Converters," *Power Electronics, IEEE Transactions on*, 2013.

Conference Papers:

1. K.J. Hartnett, J.G. Hayes, M.G. Egan, M.S. Rylko, J.W. Masłoń, "CCTT-core split-winding integrated magnetic interleaved boost converter for high-current renewable energy applications," *Energy Conversion Conference and Exposition 2013*, pp. --, 15-19 September, Denver, CO, 2013.
2. K.J. Hartnett, B.J. Lyons, J.G. Hayes, M.G. Egan, M.S. Rylko, J.W. Masłoń "Comparison of CCTT-Core Split-Winding Integrated Magnetic and Discrete Inductors for High-Power DC-DC Converters," *Applied Power Electronics Conference and Exposition*, pp. --, 17-22 March, Long Beach, CA, 2013.
3. K.J. Hartnett, J.G. Hayes, M.G. Egan, M.S. Rylko, "Comparison of CCTT Split-Winding and EE Integrated Magnetic for High-Power DC-DC Converters," *Vehicle Power and Propulsion Conference*, 6-9 Sept, Chicago, IL, 2011.
4. K.J. Hartnett, J.G. Hayes, M.G. Egan, M.S. Rylko, "Novel CCTT-Core Split-Winding Integrated Magnetic for High-Power DC-DC Converters," *Energy Conversion Conference and Exposition*, pp. 598-606, 17-22 Sept, Phoenix, AZ, 2011.
5. K.J. Hartnett, J.G. Hayes, M.G. Egan, M.S. Rylko, "A comparison of classical two phase (2L) and transformer coupled (XL) interleaved boost converters for fuel cell applications," *Applied Power Electronics Conference and Exposition*, pp. 787-793, 21-25 February, Palm Springs, CA, 2010.
6. M.S. Rylko, K.J. Hartnett, J.G. Hayes, M.G. Egan, "Magnetic Material Selection for High Power High Frequency Inductors in DC-DC Converters," *Applied Power Electronics Conference and Exposition*, pp. 2043-2049, 15-19 February, Washington D.C., 2009.

7. M.S. Rylko, B.J. Lyons, K.J. Hartnett, J.G. Hayes, M.G. Egan, "Magnetic material comparisons for high-current gapped and gapless foil wound inductors in high frequency dc-dc converters," *Power Electronics and Motion Control Conference*, pp. 1249-1256, 1-3 September, Washington D.C., 2009.

Table of Contents

Declaration	III
Abstract	V
Acknowledgements	VII
List of Publications	IX
Table of Contents	XI
List of Tables	XV
List of Figures	XVII
Chapter 1 Introduction	1
1.1. Overview.....	3
1.2. Thesis Objectives.....	5
1.3. Thesis Structure	6
1.4. General Background	7
1.4.1. Automotive and Photovoltaic Renewable Energy Systems.....	8
1.4.1.1. Automotive	8
1.4.1.2. Photovoltaic	10
1.4.2. DC-DC Converter Circuit Topologies.....	13
1.4.2.1. Automotive	14
1.4.2.2. Photovoltaic	15
1.4.3. Power Electronic Components	15
1.4.3.1. Semiconductors.....	15
1.4.3.2. Magnetics.....	17
1.4.3.3. Capacitors	18
1.4.4. Conclusions	18
Chapter 2 Circuit Analysis of a Two-Phase Interleaved Boost Converter using an Integrated Magnetic Structure	19

2.1. Introduction	21
2.2. IM Converter Circuit Analysis	22
2.2.1. IM Operation in Continuous Conduction Mode	23
2.2.1.1. IM Operation in Continuous Conduction Mode for D less than 0.5	24
2.2.1.2. IM Operation in Continuous Conduction Mode for D greater than 0.5	27
2.2.1.3. Current Ripple Investigation for a Variation in Magnetizing Inductance	30
2.2.2. IM Operation in Discontinuous Conduction Mode	30
2.2.2.1. IM Operation in “Soft” Discontinuous Conduction Mode for D less than 0.5	31
2.2.2.2. IM Operation in “Hard” Discontinuous Conduction Mode for D less than 0.5	36
2.2.2.3. IM Operation in “Hard” Discontinuous Conduction Mode for D less than 0.5	39
2.3. Validation of CCM and DCM Circuit Equations	45
2.4. IM Filter and Switch Currents	46
2.5. Conclusions	47
Chapter 3 CCTT-Core Split-Winding Integrated Magnetic	51
3.1. Introduction	53
3.2. IM Concepts	54
3.2.1. EE IM Approach	54
3.2.2. CCTT IM Approach	55
3.2.3. Pot Core IM Approach	56
3.2.4. Dc and Ac Inductance	58
3.3. CCTT IM Fringing Regions and Reluctance Model	59
3.3.1. CCTT IM Fringing Regions	59
3.3.2. Simple CCTT IM Reluctance Model	59
3.3.3. CCTT IM Dc Fringing Regions and Reluctance Model	61
3.3.3.1. CCTT IM Dc Fringing Regions	61
3.3.3.2. CCTT IM Dc Reluctance Model	62
3.3.4. CCTT IM Ac Fringing Regions and Reluctance Model	65
3.3.4.1. CCTT IM Ac Fringing Regions	65
3.3.4.2. CCTT IM Ac Reluctance Model	65
3.3.5. Validation of Dc and Ac Reluctance Models	66
3.4. CCTT IM Design Algorithm	67
3.4.1. Design Algorithm	69
3.4.2. Algorithm Validation	78
3.4.2.1. High-Power Conduction Cooled Design	79

3.4.2.2. Low-Power Conduction Cooled Design	83
3.4.2.3. Conduction-Cooled CCTT IM Boxed Volume Variation with an Efficiency Constraint.....	86
3.5. CCTT IM Design Trade-offs	87
3.5.1. Comparison with Traditional EE IM	87
3.5.2. Variation of CCTT IM Boxed Volume with Magnetizing Inductance.....	88
3.6. Conclusions.....	89
Chapter 4 Comparison of CCTT-Core Split-Winding Integrated Magnetic and Discrete Inductors for High-Power DC-DC Converters	91
4.1. Introduction.....	93
4.2. Baseline Three-Phase DC-DC Boost Converter	96
4.3. Inductor Design Algorithm	99
4.4. CCTT IM and 2L Magnetic Design.....	100
4.4.1. Conduction-Cooled CCTT IM and 2L Design	101
4.4.2. Conduction-Cooled CCTT IM Prototype Development and Prototype Design	104
4.4.2.1. Distributed Leakage Gap Investigation.....	111
4.4.3. Conduction-Cooled 2L Discrete Inductor Design and Validation.....	114
4.5. Semiconductor Analysis	116
4.6. Analysis of Power Loss over Variable Fuelcell Power Range	120
4.7. Capacitor Sizing and Design.....	122
4.7.1. Input Filter Capacitor Sizing	123
4.8. 2605SA1 CCTT IM Design	123
4.8.1. Conduction-Cooled 2605SA1 CCTT IM Magnetic Design	123
4.8.2. Conduction-Cooled 2605SA1 CCTT IM Optimization	125
4.8.3. Analysis of Power Loss over Variable Fuelcell Power Range	128
4.8.4. Manufacturability Issues of Metglas CCTT IM	130
4.9. Experimental Results	130
4.9.1. 97.2 kW 3L Experimental Test Results.....	130
4.9.2. 72 kW CCTT IM Experimental Test Results	131
4.9.3. 3.8 kW CCTT IM and 2L Experimental Results.....	133
4.10. Conclusions.....	135
Chapter 5 8 kW Interleaved CCTT IM Boost Converter for Photovoltaic Applications	137
5.1. Introduction.....	139
5.2. Baseline Two-Phase Interleaved DC-DC Boost Converter	142

5.2.1. Discrete Toroid Inductor.....	143
5.3. Magnetic Design of an 8 kW CCTT IM Component.....	145
5.3.1. Design of an 8 kW 3C92 CCTT IM	145
5.3.2. Optimization and Validation of 8 kW CCTT IM.....	147
5.4. Semiconductor Analysis.....	149
5.5. CCTT IM Converter Analysis.....	150
5.6. High-Flux CCTT IM Design.....	152
5.7. Experimental Results.....	154
5.7.1. Experimental Testing of 2L Discrete Inductors.....	155
5.7.1.1. Initial Toroid Development.....	155
5.7.1.2. 3C92 Discrete Toroid Testing.....	156
5.7.1.3. Conclusions on 3C92 Discrete Toroid Testing	160
5.7.2. Experimental Testing of CCTT IM	160
5.7.2.1. Initial CCTT IM Development.....	160
5.7.2.2. 3C92 CCTT IM Testing.....	162
5.7.2.3. Conclusion on Feasibility of CCTT IM for use in Photovoltaic Applications.....	166
5.8. Conclusions	168
Chapter 6 Conclusions and Future Work	169
6.1. Thesis Summary.....	169
6.2. Future Work	171
Bibliography.....	173
Appendix A Modified Steinmetz Equation	181
A.1. Application of the Modified Steinmetz Equation (MSE) to the CCTT IM Waveforms	181
Appendix B CCTT IM Schematic.....	189
B.1. High-Power 72 kW CCTT IM Schematic	189

List of Tables

Table 2.1 Input, Magnetizing and Phase Current Ripple Equations for IM Boost Converter in CCM	23
Table 2.2 Input, Magnetizing and Phase Current Ripple Equations for IM Boost Converter in “Soft” CCM	45
Table 2.3 Input, Magnetizing and Phase Current Ripple Equations for IM Boost Converter in “Hard” DCM.....	45
Table 2.4 Validation of CCM Circuit Equations for IM Boost Converter.....	49
Table 2.5 Validation of DCM Equations for IM Boost Converter	49
Table 2.6 Validation of DCM Equations for IM Boost Converter	50
Table 3.1 Results of Dc Reluctance Model Validation.....	67
Table 3.2 Comparison of Ac Reluctance Model and 3D FEA Inductance	67
Table 3.3. Magnetic Material Properties.....	79
Table 3.4 Comparison of Dc and AC Inductance for the CCTT and EE IM Options	88
Table 4.1 Phase Inductor Parameters for 16 kHz 3L Converter	98
Table 4.2 CCTT IM and 2L Inductor Parameters	103
Table 4.3 Initial 3C92 CCTT IM and Prototype 3C92 CCTT IM Parameters.....	105
Table 4.4 CCTT IM Dc Inductance Matrix	106
Table 4.5 Comparison of Dc and Ac Inductance for 72 kW Prototype CCTT IM	108
Table 4.6 Predicted and Simulated CCTT IM Prototype Thermal Results.....	110
Table 4.7 CCTT IM Ac Winding Power Loss in Watts.....	110
Table 4.8 CCTT IM Ac Winding Power Loss in Watts.....	110
Table 4.9 Dc and Ac Leakage Inductance for Multiple Airgap Designs	112
Table 4.10 Ac Power Loss for Multiple Airgap Design	112
Table 4.11 Comparison of Dc and Ac Inductance for 72 kW 2L Discrete Inductor	115
Table 4.12 Predicted and Simulated 2L Thermal Results.....	115
Table 4.13 Breakdown of System Currents in 2L and CCTT IM Topologies	119
Table 4.14 Breakdown of Conduction Loss in 2L and CCTT IM Topologies	119
Table 4.15 Breakdown of Turn-on Loss in 2L and CCTT IM Topologies.....	119

Table 4.16 Breakdown of Turn-off Loss in 2L and CCTT IM Topologies	119
Table 4.17 Breakdown of Diode Turn-on Loss in 2L and CCTT IM Topologies	119
Table 4.18 Total Loss in 2L and CCTT IM Topologies	120
Table 4.19 2L and CCTT IM Input Capacitor Sizing	123
Table 4.20 Prototype and High B_{sat} Prototype Parameters.....	126
Table 4.21 Dc Inductance Matrix for 2605SA1 CCTT IM.....	128
Table 4.22 Comparison of Dc and Ac Inductance for the 2605SA1 CCTT IM.....	128
Table 4.23 72 kW CCTT IM Power Loss	133
Table 4.24 3.8 kW Prototype Parameters.....	136
Table 5.1 2L and CCTT IM Inductor Parameters	142
Table 5.2 3C92 Discrete Toroid and CCTT IM Experimental Test Conditions and Information	155
Table 5.3 2L Toroid Inductor Parameters	155
Table 5.4 CCTT IM Inductor Parameters	161
Table A.1 Equivalent Leakage and Magnetizing Frequencies at $D = 0.63$	186
Table A.2 Steinmetz Parameters for Ferrite 3C92, Metglas 2605SA1 and JFE 10JNHF600	186

List of Figures

Figure 1.1. Various renewable energy systems that use power converters.....	7
Figure 1.2. Series/Parallel HEV powertrain.....	8
Figure 1.3. EV Powertrain	9
Figure 1.4. Lithium-ion battery state of charge curve [24]	9
Figure 1.5. FCV powertrain	10
Figure 1.6. Typical fuelcell I-V curve.....	10
Figure 1.7. Typical photovoltaic I-V curve.....	11
Figure 1.8. Typical microinverter system	11
Figure 1.9. Typical string photovoltaic system.....	12
Figure 1.10. Typical single string photovoltaic system utilizing power optimizers	12
Figure 1.11. Typical central photovoltaic system.....	13
Figure 1.12. Various methods of implementing an interleaved boost converter	14
Figure 1.13. Normalized input and phase current ripple for the 2L and IM dc-dc converters presented in Fig. 1.12	14
Figure 1.14. Typical semiconductor component regions of operation for power vs. switching frequency.....	16
Figure 1.15. Typical semiconductor regions of operation for on-resistance vs. breakdown voltage.....	16
Figure 2.1. Various methods of implementing an interleaved boost converter	21
Figure 2.2. Normalized input and phase current ripple for the 2L and IM dc-dc converters presented in Fig. 2.1	21
Figure 2.3. IM boost circuit	23
Figure 2.4. IM circuit switching waveforms for duty cycle, $D < 0.5$	24
Figure 2.5. IM equivalent circuits in CCM for duty cycle, $D < 0.5$	25
Figure 2.6. IM equivalent circuits in CCM for duty cycles, $D > 0.5$	28
Figure 2.7. IM circuit waveforms in CCM for duty cycle, $D > 0.5$	29
Figure 2.8. Normalized input and phase current ripple for various values of magnetizing inductance	30

Figure 2.9. IM circuit switching waveforms in “soft” DCM for duty cycles, $D < 0.5$	32
Figure 2.10. IM equivalent circuits in “soft” DCM for duty cycles, $D < 0.5$	33
Figure 2.11. IM circuit switching waveforms in “soft” DCM for duty cycles, $D < 0.5$	34
Figure 2.12. IM equivalent circuits in “hard” DCM for duty cycles, $D < 0.5$	36
Figure 2.13. IM circuit switching waveforms in “hard” DCM for duty cycles, $D < 0.5$	37
Figure 2.14. IM circuit switching waveforms in “hard” DCM for duty cycles, $D < 0.5$	38
Figure 2.15. IM circuit switching waveforms in “soft” DCM for duty cycles, $D > 0.5$	39
Figure 2.16. IM circuit switching waveforms in “hard” DCM for duty cycles, $D > 0.5$	40
Figure 2.17. IM equivalent circuits in “soft” and “hard” DCM for duty cycles, $D > 0.5$	41
Figure 2.18. IM circuit switching waveforms in “soft” DCM for duty cycles, $D > 0.5$	43
Figure 2.19. IM circuit switching waveforms in “hard” DCM for duty cycles, $D > 0.5$	44
Figure 2.20. Illustration of CCM/DCM boundaries in an automotive fuelcell boost converter	46
Figure 2.21. Input current, input capacitor current and phase rms currents with variation of duty cycle	47
Figure 2.22. Switch and diode rms and average currents with variation in duty cycle	47
Figure 2.23. Illustration of maximum and minimum phase currents	47
Figure 3.1. Disassembled 72 kW CCTT IM prototype	53
Figure 3.2. Assembled 72 kW prototype.....	53
Figure 3.3. EE IM realization.....	55
Figure 3.4. 3D flux plot illustrating EE IM fringing flux.....	55
Figure 3.5. CCTT IM realization	56
Figure 3.6. 3D flux plot illustrating CCTT IM fringing flux	56
Figure 3.7. Pot core IM realization	57
Figure 3.8. 3D flux plot illustrating pot core IM fringing flux.....	57
Figure 3.9. 3D flux plot illustrating the dc EE IM fringing flux	58
Figure 3.10. 3D flux plot illustrating the ac EE IM fringing flux	58
Figure 3.11. CCTT IM core dimensions	59
Figure 3.12. Simple reluctance model neglecting the fringing regions.....	60
Figure 3.13. Fringing regions around pole and winding sections of the CCTT IM	61
Figure 3.14. Pole face fringing regions of the CCTT IM.....	61
Figure 3.15. Pole corner fringing regions of the CCTT IM	62
Figure 3.16. Winding fringing regions of the CCTT IM.....	62
Figure 3.17. Complete CCTT IM reluctance model with fringing regions.....	63
Figure 3.18. CCTT IM design algorithm	68

Figure 3.19. Solid spiral winding and parallel stranded winding options.....	75
Figure 3.20. CCTT IM core 2D and 1D equivalent heat path.....	77
Figure 3.21. CCTT IM winding 2D and 1D equivalent heat path	78
Figure 3.22. Variation of CCTT IM boxed volume for ferrite 3C92.....	80
Figure 3.23. Variation of CCTT IM boxed volume for iron-based amorphous metal 2605SA1	80
Figure 3.24. Variation of CCTT IM boxed volume for silicon steel 10JNHF600.....	81
Figure 3.25. Variation in (a) CCTT IM boxed volume and (b) CCTT IM power loss for 3C92, 2605SA1 and 10JNHF600 core material at 16 kHz.....	82
Figure 3.26. Variation in (a) CCTT IM boxed volume and (b) CCTT IM power loss for 3C92, 2605SA1 and 10JNHF600 core material at 25 kHz.....	82
Figure 3.27. Variation in (a) CCTT IM boxed volume and (b) CCTT IM power loss for 3C92, 2605SA1 and 10JNHF600 core material at 50 kHz.....	82
Figure 3.28. Variation in (a) CCTT IM boxed volume and (b) CCTT IM power loss for 3C92, 2605SA1 and 10JNHF600 core material at 75 kHz.....	82
Figure 3.29. Variation in (a) CCTT IM boxed volume and (b) CCTT IM power loss for 3C92, 2605SA1 and 10JNHF600 core material at 100 kHz.....	83
Figure 3.30. Variation of CCTT IM boxed volume for ferrite 3C92.....	83
Figure 3.31. Variation of CCTT IM boxed volume for iron-based amorphous metal 2605SA1	84
Figure 3.32. Variation of CCTT IM boxed volume for silicon steel 10JNHF600.....	84
Figure 3.33. Variation in (a) CCTT IM boxed volume and (b) CCTT IM power loss for 3C92, 2605SA1 and 10JNHF600 core material at 16 kHz.....	85
Figure 3.34. Variation in (a) CCTT IM boxed volume and (b) CCTT IM power loss for 3C92, 2605SA1 and 10JNHF600 core material at 25 kHz.....	85
Figure 3.35. Variation in (a) CCTT IM boxed volume and (b) CCTT IM power loss for 3C92, 2605SA1 and 10JNHF600 core material at 50 kHz.....	85
Figure 3.36. Variation in (a) CCTT IM boxed volume and (b) CCTT IM power loss for 3C92, 2605SA1 and 10JNHF600 core material at 75 kHz.....	85
Figure 3.37. Variation in (a) CCTT IM boxed volume and (b) CCTT IM power loss for 3C92, 2605SA1 and 10JNHF600 core material at 100 kHz.....	86
Figure 3.38. Variation in (a) CCTT IM boxed volume and (b) CCTT IM power loss for 3C92, 2605SA1 and 10JNHF600 core material at 16 kHz and 99 % efficiency constraint	86
Figure 3.39. Variation in (a) CCTT IM boxed volume and (b) CCTT IM power loss for	

3C92, 2605SA1 and 10JNHF600 core material at 100 kHz and 99 % efficiency constraint.....	87
Figure 3.40. (a) Variation in CCTT IM and EE IM boxed volume with varying input current ripple and (b) highlighting the larger dc inductance of the EE IM	88
Figure 3.41. Variation in CCTT IM boxed volume for increasing values of magnetizing inductance	89
Figure 4.1. 72 kW fuelcell I-V characteristic	93
Figure 4.2. 2L and CCTT IM boost converter topologies.....	94
Figure 4.3. 2L and CCTT IM normalized current ripple assuming same input ripple	94
Figure 4.4. 2L and CCTT IM normalized current ripple assuming same phase ripple	94
Figure 4.5. CCTT IM inductance saving when compared with 2L for same worst-case phase current ripple.....	95
Figure 4.6. Variation in (a) CCTT IM boxed volume and (b) CCTT IM power loss for 3C92, 2605SA1 and 10JNHF600 core material at 25 kHz and 99 % efficiency constraint.....	96
Figure 4.7. Phase inductor of 97.2 kW three-phase boost converter.....	97
Figure 4.8. Three-phase boost converter schematic	97
Figure 4.9. Aluminium tray for 3L boost converter	98
Figure 4.10. Actual 2L and CCTT IM input and phase current ripple with varying fuelcell power.....	100
Figure 4.11. Total boxed volume vs. turns per phase.....	101
Figure 4.12. Total power loss vs. turns per phase	102
Figure 4.13. Airgap length vs. turns per phase.....	102
Figure 4.14. Isometric view of CCTT IM and 2L discrete inductors.....	104
Figure 4.15. Dc flux plot of prototype CCTT IM illustrating fringing flux from the pole section	106
Figure 4.16. Transient simulation of prototype CCTT IM at $t = 25.2 \mu s$ corresponding to the peak of the phase current ripple	107
Figure 4.17. Phase current waveforms for transient simulation.....	108
Figure 4.18. 2D thermal analysis of prototype CCTT IM core	109
Figure 4.19. 2D thermal analysis of prototype CCTT IM winding.....	109
Figure 4.20. Current density plot with no pole shielding (0 mm)	110
Figure 4.21. Current density plot with pole shielding (4 mm)	111
Figure 4.22. CCTT IM with 5 leakage airgap sections	112
Figure 4.23. CCTT IM with 8 leakage airgap sections	113

Figure 4.24. Current density plot for CCTT IM with 5 leakage airgap sections	113
Figure 4.25. Current density plot for CCTT IM with 8 leakage airgap sections	114
Figure 4.26. Dc flux density plot of 2L discrete inductor	114
Figure 4.27. Transient flux plot of 2L discrete inductor at $t = 25.2 \mu\text{s}$	115
Figure 4.28. 2D thermal analysis of 2L discrete inductor core	116
Figure 4.29. 2D thermal analysis of 2L discrete inductor winding	116
Figure 4.30. IGBT and diode characteristics	117
Figure 4.31. Turn-on and turn-off energy for Semikron IGBT module	118
Figure 4.32. Breakdown of total 2L inductor loss with varying fuelcell power	120
Figure 4.33. Breakdown of total CCTT IM power loss with varying fuelcell power	121
Figure 4.34. Breakdown of semiconductor loss in 2L topology	121
Figure 4.35. Breakdown of semiconductor loss in CCTT IM topology	122
Figure 4.36. 2L and CCTT IM converter efficiency over fuelcell power range	122
Figure 4.37. Total boxed volume vs. turns per phase	124
Figure 4.38. Total power loss vs. turns per phase	124
Figure 4.39. Airgap length vs. turns per phase	125
Figure 4.40. Isometric view of 3C92 CCTT IM, 2605SA1 2L and 2605SA1 CCTT IM	127
Figure 4.41. Dc flux plot of 2605SA1 CCTT IM	127
Figure 4.42. Transient flux plot of 2605SA1 CCTT IM at the peak of the phase current ripple at $t = 25.2 \mu\text{s}$	128
Figure 4.43. Breakdown of 2605SA1 CCTT IM power loss	129
Figure 4.44. 2605SA1 CCTT IM efficiency over fuelcell power range	129
Figure 4.45. 97.2 kW three-phase experimental test set-up	130
Figure 4.46. Experimental waveforms of 97.2 kW 3L converter	131
Figure 4.47. 72 kW experimental waveforms	131
Figure 4.48. CCTT IM converter experimental efficiency at $V_{\text{in}} = 155 \text{ V}$	132
Figure 4.49. CCTT IM converter experimental efficiency at $V_{\text{in}} = 180 \text{ V}$	132
Figure 4.50. 3.8 kW experimental set-up	133
Figure 4.51. 3.8 kW CCTT IM and 2L prototype components	134
Figure 4.52. 3.8 kW 3C92 CCTT IM experimental waveforms for $D = 0.6$	134
Figure 4.53. 3.8 kW 10JNHF600 2L experimental waveforms for $D = 0.6$	135
Figure 4.54. 3.8 kW experimental boost efficiency	135
Figure 5.1. 1L, 2L and CCTT IM topologies in a boost pre-regulator	139
Figure 5.2. Inductance saving vs. 2L when CCTT IM is designed for the same worst- case phase current ripple	140

Figure 5.3. 8 kW PV test profile	140
Figure 5.4. Input and phase current ripple variation for the 2L and CCTT IM converter.....	143
Figure 5.5. Plan view of 2L prototype inductors.....	144
Figure 5.6. Variation in CCTT IM boxed volume with turns per phase. The total 2L boxed volume is included	146
Figure 5.7. Variation in CCTT IM power loss with turns per phase.....	146
Figure 5.8. Variation in CCTT IM leakage gap length with turns per phase	147
Figure 5.9. 2D dc flux plot of $\frac{1}{2}$ model CCTT IM.....	148
Figure 5.10. Current density plot of $\frac{1}{2}$ model CCTT IM at second harmonic of phase current ripple.....	148
Figure 5.11. Close-up current density plot of $\frac{1}{2}$ model CCTT IM at second harmonic of phase current ripple.....	149
Figure 5.12. Variation in total magnetic power loss for 2L inductors	150
Figure 5.13. Variation in total magnetic power loss for CCTT IM.....	150
Figure 5.14. Variation in semiconductor power loss for 2L topology	151
Figure 5.15. Variation in semiconductor power loss for CCTT IM topology.....	151
Figure 5.16. Variation in efficiency for 2L and CCTT IM boost topologies	152
Figure 5.17. Variation in CCTT IM boxed volume with turns per phase. The total 2L boxed volume is included	153
Figure 5.18. Variation in CCTT IM power loss with turns per phase.....	153
Figure 5.19. Variation in CCTT IM leakage gap length with turns per phase	154
Figure 5.20. Two-phase interleaved test set-up.....	154
Figure 5.21. Inductance vs. dc bias for inductor #1	156
Figure 5.22. Inductance vs. dc bias for inductor #2	156
Figure 5.23. Experimental waveforms for (a) $V_{in} = 135$ V and (b) $V_{in} = 250$ V	157
Figure 5.24. Experimental waveforms for (a) $V_{in} = 135$ V and (b) $V_{in} = 250$ V	157
Figure 5.25. 2L experimental input and phase current ripple.....	157
Figure 5.26. 2L experimental boost efficiency.....	158
Figure 5.27. Temperature readings vs. time for $V_{in} = 135$ V, $V_{out} = 500$ V for (a) inductor #1 and (b) inductor #2.....	158
Figure 5.28. Temperature readings vs. time for $V_{in} = 250$ V, $V_{out} = 500$ V for (a) inductor #1 and (b) inductor #2.....	159
Figure 5.29. Temperature readings vs. time for $V_{in} = 420$ V, $V_{out} = 500$ V for (a) inductor #1 and (b) inductor #2.....	159
Figure 5.30. Thermal image for 2L inductors for $V_{in} = 135$ V.....	159

Figure 5.31. Thermal image for 2L inductors for $V_{in} = 135\text{ V}$	160
Figure 5.32. Temperature reading vs. time for (a) MOSFET and diode for $V_{in} = 135\text{ V}$ and (b) MOSFET and diode for $V_{in} = 420\text{ V}$	160
Figure 5.33. (a) Plan view and (b) isometric view of 3C92 CCTT IM.....	161
Figure 5.34. (a) Plan and (b) isometric view of 3C92 CCTT IM and 2L inductors.....	161
Figure 5.35. Leakage inductance vs. dc bias for 3C92 CCTT IM	163
Figure 5.36. Experimental waveforms for (a) $V_{in} = 135\text{ V}$ and (b) $V_{in} = 250\text{ V}$	163
Figure 5.37. Experimental waveforms for (a) $V_{in} = 350\text{ V}$ and (b) $V_{in} = 420\text{ V}$	163
Figure 5.38. CCTT IM boost experimental input and phase current ripple	164
Figure 5.39. CCTT IM and 2L experimental boost efficiency	164
Figure 5.40. Temperature readings vs. time for $V_{in} = 135\text{ V}$, $V_{out} = 500\text{ V}$ for (a) CCTT IM core, pole and winding and (b) semiconductors	165
Figure 5.41. Temperature readings vs. time for $V_{in} = 250\text{ V}$, $V_{out} = 500\text{ V}$ for (a) CCTT IM core, pole and winding and (b) semiconductors	165
Figure 5.42. Temperature readings vs. time for $V_{in} = 350\text{ V}$, $V_{out} = 500\text{ V}$ for (a) CCTT IM core, pole and winding and (b) semiconductors	165
Figure 5.43. Temperature readings vs. time for $V_{in} = 420\text{ V}$, $V_{out} = 500\text{ V}$ for (a) CCTT IM core, pole and winding and (b) semiconductors	165
Figure 5.44. Thermal image of CCTT IM for (a) $V_{in} = 135\text{ V}$, $V_{out} = 500\text{ V}$	166
Figure 5.45. Thermal image of CCTT IM for (a) $V_{in} = 250\text{ V}$, $V_{out} = 500\text{ V}$	166
Figure 5.46. Thermal image of CCTT IM for (a) $V_{in} = 350\text{ V}$, $V_{out} = 500\text{ V}$	167
Figure 5.47. Thermal image of CCTT IM for (a) $V_{in} = 420\text{ V}$, $V_{out} = 500\text{ V}$	167
Figure A.1. Normalized switching frequency for a single-phase boost converter.....	182
Figure A.2. Single-phase boost converter inductor current and flux density waveforms	182
Figure A.3. Normalized switching frequency for a CCTT IM boost converter.....	183
Figure A.4. IM circuit switching waveforms for duty cycle, $D > 0.5$	185

Chapter 1

Introduction

This chapter presents an overview of the research topic that is presented in this thesis. The thesis is focused on the design, development and optimization of IM component structures for use in high-power, high-current, power converter applications such as automotive and renewables. This chapter presents the current technology used in these applications and outlines the motivation for the development of more efficient and higher power-density magnetic components.

1.1. Overview

In 2010 renewable energy sources supplied an estimated 16.7 % of global final energy consumption. The information presented in [1] provides a complete and comprehensive overview of worldwide renewable energy markets, industry, investment, and policy developments. What is clear from this report is that modern renewables will continue to grow stronger in sectors such as power generation and transport.

In Europe, Germany is spearheading the renewable energy revolution and is a world market leader in PV technology and usage. Other major nations, such as the United States and China, are also heavily investing in renewable energy sources. Smaller nations are also making excellent use of their renewable energy resources. For example in 2011, Ireland provided 16 % of its electricity consumption by utilizing its large wind power potential and is well into its transition process to a low-carbon electricity system [2].

The generation characteristic of a renewable energy source is typically non-linear and it varies with external environmental factors, such as wind and wave profiles, the amount of available sunlight and temperature. Power converters are critical components of renewable energy systems as they help transfer and transform the energy at the source to usable energy at the load. A dc-ac inverter is used to achieve this transformation but the use of a dc-dc pre-regulator is quite common to provide a higher magnitude and stable voltage on the dc-bus.

Power converters are also critical components of microgrids [3-6] which allow for the distributed generation of energy, and dc-dc and dc-ac converters play a vital role in converting this distributed energy into a more usable form.

Various types of dc-dc converter topologies, both non-isolated and isolated, are in common use [7] but for high-power automotive and photovoltaic applications the traditional single-phase (1L) buck or boost converter is used. The quest for increased converter power density has pushed designers to explore multiphase, coupled inductor and integrated magnetic (IM) topologies. The interleaved multiphase design allows for a reduction in the input current ripple thereby reducing the stress on the input filter capacitors. The phase inductors can also be made smaller due to the lower inductance requirement and reduced dc phase current. The modularity of the multiphase design allows for phase disabling at lower power levels in order to achieve increased efficiency. The use of coupled inductor and IM topologies results in the integration of all magnetic components onto one core, resulting in an extremely power-dense solution. These topologies exhibit input current ripple reduction, similar to the multiphase option, but critically transformer coupling extends this input current ripple reduction to each phase of the converter circuit.

The dc-dc converters in question are constructed using three fundamental components: semiconductor switches, magnetic components such as inductors and transformers, and capacitors. Typically the converter design is driven by the semiconductor requirements as they are generally the biggest contributors to the converter power loss but care has to be taken when designing the magnetic components as they are typically the largest components in the converter.

1.2. Thesis Objectives

The first objective of this thesis is to investigate and understand the circuit operation of a two-phase interleaved dc-dc converter that contains an IM component structure. The converter can operate in continuous conduction (CCM) or discontinuous conduction mode (DCM) and both modes of operation are analysed in detail. It is important to analyse all of the different current and voltage waveforms in the interleaved converter in order to size the magnetic, capacitor and semiconductor components.

The second objective is the design, development and optimization of the CCTT IM. The CCTT IM is designed using a design algorithm that is implemented in the mathematical software tool Mathematica. A CCTT IM reluctance model, which incorporates fringing equations, is the backbone of the design algorithm. This reluctance model allows for the prediction of the dc and ac inductance which results in a more efficient design. A similar reluctance model is developed for the EE IM and this structure is seen to have more fringing flux, and therefore dc inductance, than the CCTT IM. 3D and 2D FEA is used to further optimize the CCTT IM structure. 3D FEA is especially useful in validating the accuracy of the reluctance model as well as running transient simulations in order to understand the flux distribution in the core at the worst-case operating conditions. 2D FEA is used to determine the ac winding power loss as well as to determine the optimal magnetic pole length in order to minimize the ac winding loss due to the significant airgap fringing flux.

The final objective is to validate the CCTT IM design concept. Firstly, a high-power 72 kW prototype is developed and experimental testing vindicates the CCTT IM concept for use in high-power fuelcell applications. In addition, 8 kW and 3.8 kW, low-power experimental testing validates the CCTT IM concept for PV and fuelcell applications, respectively.

1.3. Thesis Structure

The thesis is organized into 6 chapters. The background research and motivation for this research work is presented in Chapter 1. In this chapter, an overview of the need for efficient and high-power dense power converters for renewable energy applications is discussed. The various renewable energy systems are discussed along with the typical power converter circuits that they employ to transfer power from the renewable energy source to the load.

Chapter 2 investigates the circuit operation of a two-phase interleaved dc-dc boost converter when an IM structure is used as the magnetic component. Circuit equations are presented for both CCM and DCM operation which allow for the determination of all the critical voltage and currents in the system. The benefit of using an IM structure, in a dc-dc converter, over the other magnetic topologies is presented. This chapter develops all of the necessary equations needed in order to design an IM component.

Chapter 3 introduces the CCTT IM concept. The CCTT IM concept is compared with the EE IM option. A CCTT IM reluctance model is developed in order to accurately predict, using analytical expressions, the dc and ac inductance of the device. A design algorithm is developed which allows for quick prototyping of the CCTT IM design over various different circuit condition that may be of interest. The algorithm also allows for the comparison of the CCTT IM for various magnetic materials and winding types.

Chapter 4 presents the development of a 72 kW CCTT IM prototype. 3D and 2D FEA is extensively used to validate and optimize the CCTT IM design. A 72 kW paper design is presented that compares the CCTT IM prototype with two discrete iron-based amorphous metal inductors. The CCTT IM is shown to be of a similar boxed volume but with a significantly higher efficiency. 72 kW and 3.8 kW experimental testing validate the CCTT IM concept.

Chapter 5 presents the development of an 8 kW CCTT IM prototype for use in PV applications. The CCTT IM pre-regulator is experimentally compared with an industry standard 2L pre-regulator power converter. The CCTT IM allows for a 50 % reduction in total boxed volume and mass while maintaining, or in some cases even exceeding, the efficiency of the baseline design.

Chapter 6 presents the conclusion of the research as well as possible directions for future research.

1.4. General Background

This section presents the general background information of some typical renewable energy systems as well as outlining the main motivation as to why power converters are required in these applications. Firstly, the different renewable energy systems are discussed; secondly, the most commonly used power converter circuit topologies are presented; and finally, the individual components that make up these circuit topologies are introduced.

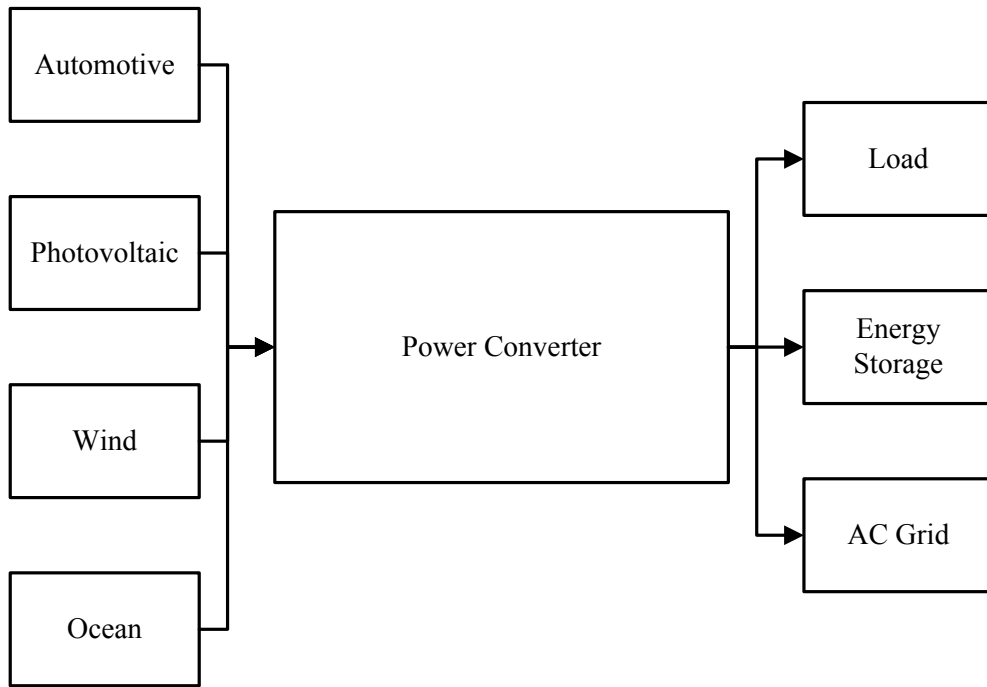


Figure 1.1. Various renewable energy systems that use power converters

Some common renewable energy systems are presented in Fig. 1.1 and all these renewable energy technologies require some degree of power conditioning, using a power converter, before they are able to deliver their energy to their specified loads. A discussion on the use of power electronics in renewable energy applications is presented in detail in [8-15]. This thesis focuses specifically on the automotive and photovoltaic sectors and these systems will be the main point of discussion for the remainder of this chapter.

1.4.1. Automotive and Photovoltaic Renewable Energy Systems

1.4.1.1. Automotive

The automotive renewable energy systems can be broadly segmented into three categories which are as follows; Hybrid Electric Vehicles (HEV), Electric Vehicles (EV) and Fuelcell Vehicles (FCV). The work presented in [16-18] investigates the development of renewable energy technologies in the automotive sector and it specifically investigates HEV and EV systems while briefly discussing FCV systems. They argue that the development of these vehicles has taken on an accelerated pace over recent years as evidenced by the fact that all major vehicle manufactures have released renewable energy versions of their best-selling vehicles [19-22].

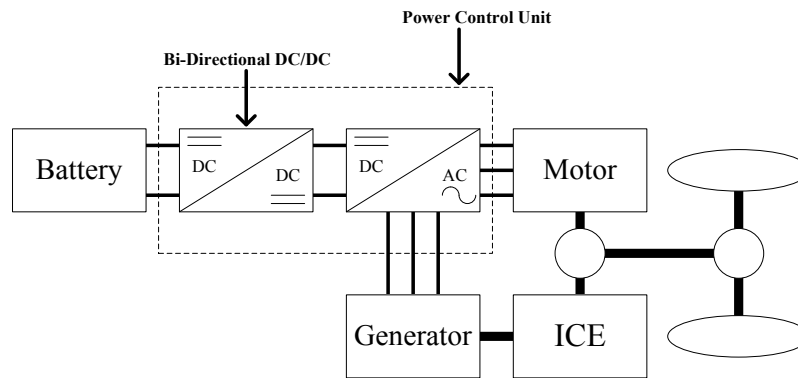


Figure 1.2. Series/Parallel HEV powertrain

The articles discussed above introduce various topologies for HEV, EV and FCV powertrains. In the case of HEV's, series and parallel powertrains are commonplace and Fig. 1.2 presents a series/parallel powertrain. This design utilizes the best of the series and parallel topologies. The world's best-selling HEV, the Toyota Prius, uses this powertrain topology.

Interestingly, the world's first commercial HEV, the Toyota Prius THS I does not include a dc-dc converter in its drivetrain and the traction motor inverter is connected directly to the battery. As a result it suffered from poor part-load efficiency. In order to increase efficiency the 2nd generation Toyota Prius included a new power control unit (PCU) [23]. The THS II incorporates more power electronics into its PCU, in the form of a bi-directional dc-dc converter, in order to increase its overall efficiency.

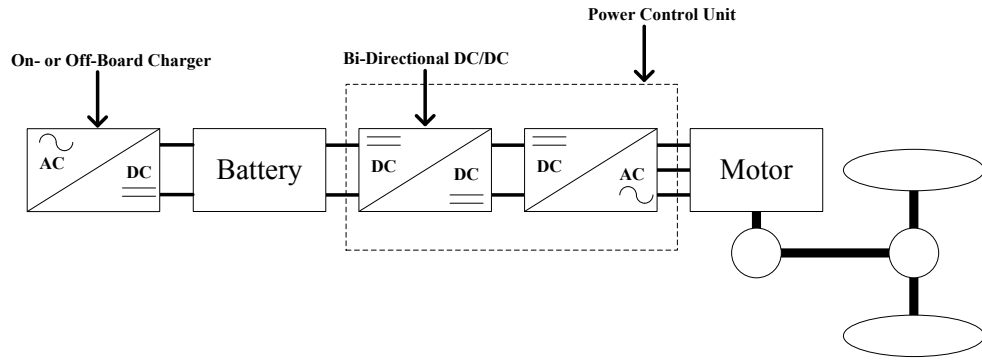


Figure 1.3. EV Powertrain

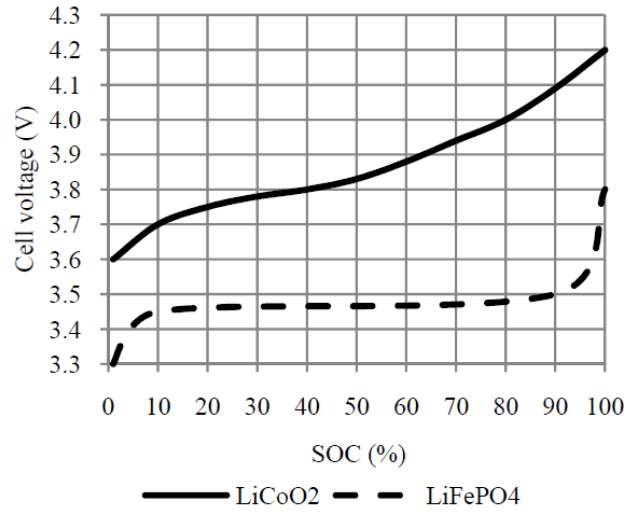


Figure 1.4. Lithium-ion battery state of charge curve [24]

A typical EV drivetrain is presented in Fig. 1.3 while a general voltage vs. state of charge curve for a lithium-ion battery is presented in Fig. 1.4. It is clear that the battery voltage varies with the state of charge and a bi-directional dc-dc converter is used in order to boost this variable voltage and produce a stable voltage on the dc-bus at the input to the inverter. Fig. 1.3 also illustrates the grid-side battery charger and this device can be employed on or off the vehicle. These devices employ active power factor correction when charging the vehicles battery.

A FCV drivetrain is presented in Fig. 1.5 and a typical source profile of a PEM fuelcell [25] is presented in Fig. 1.6. The PEM fuelcell has significant voltage reduction with load due to activation, ohmic and oxidation voltage drops from the no-load voltage. A boost converter is essential to increase the poorly-regulated output voltage of the fuelcell and efficiently distribute this voltage to the traction motor inverters. In FCV drivetrain the fuelcell provides the power for constant portions of the drive cycle while the battery provides the transient energy needed for acceleration. The battery can be replaced by other peak power units such as super-capacitors

and flywheels in order to improve the dynamic performance of the vehicle [26].

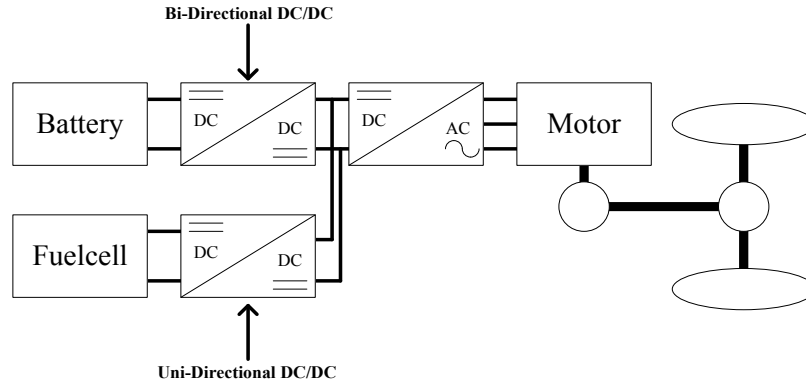


Figure 1.5. FCV powertrain

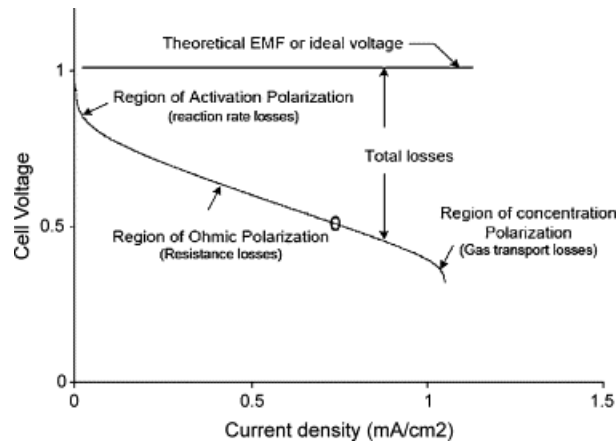


Figure 1.6. Typical fuelcell I-V curve

1.4.1.2. Photovoltaic

The typical source profile of a PV solar array is presented in Fig. 1.7. The I-V characteristics of a solar panel vary with environmental factors such as irradiation and temperature [27, 28]. A dc-dc converter is an essential requirement in a PV inverter power stage where it is used as a pre-regulator for maximum power point tracking (MPPT) as well as to stabilize the dc-link voltage for the dc-ac inverter.

The renewable energy systems for PV applications can be segmented into four separate areas which are as follows [29, 30]; 1) micro-inverter systems as presented in Fig. 1.8, 2) string systems as presented in Fig. 1.9, 3) single string systems using power optimizers as presented in Fig. 1.10 and 4) central systems as presented in Fig. 1.11.

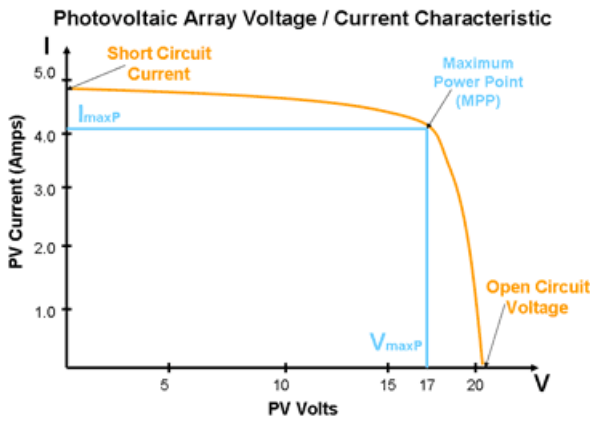


Figure 1.7. Typical photovoltaic I-V curve

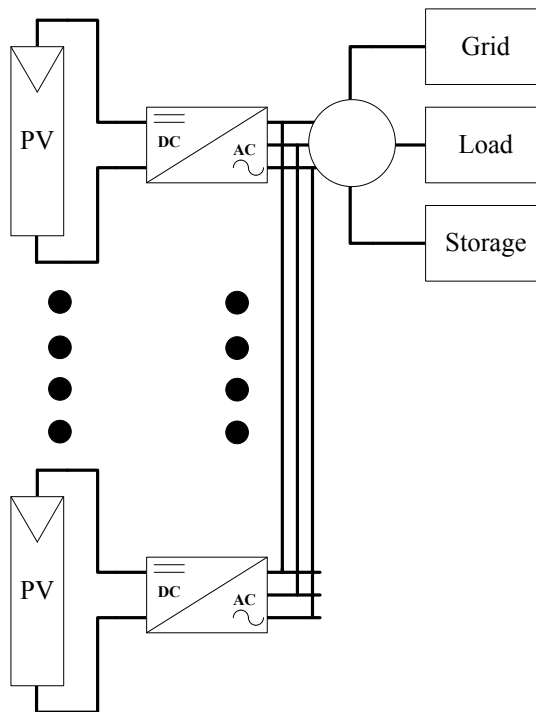


Figure 1.8. Typical microinverter system

Micro-inverter systems are used up to power levels of 2 kW. This system has the ability to combat issues such as panel shading and degradation. Micro-inverter systems allow for increased system availability and access such as; panel level MPPT and monitoring. The downside in comparison to more mature topologies is a higher cost per watt (\$0.5 - \$0.74) and more components which may reduce reliability.

The string and single string systems are employed for power levels in the range of 2 kW – 50 kW. String systems use a central inverter while the power optimizer system uses a dc-dc converter at panel or string level. The power optimizer provides similar benefits as micro-

inverter systems such as panel level MPPT, monitoring, but uses more traditional architecture in the form of a central inverter. This potentially allows for easier adaption into more mature systems. The downside of power optimiser systems is that more components are required in comparison to traditional topologies and this leads to a higher price.

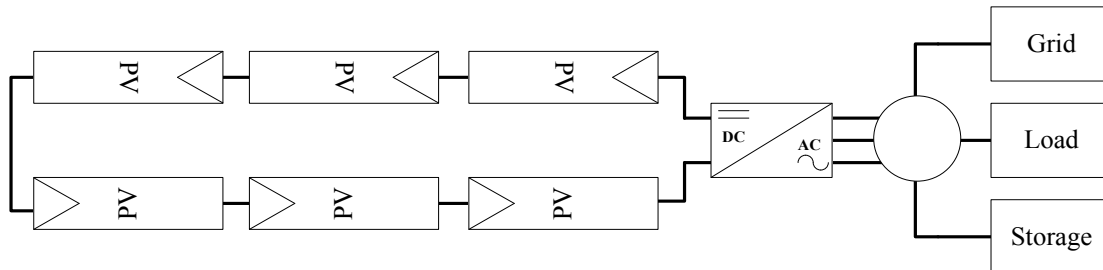


Figure 1.9. Typical string photovoltaic system

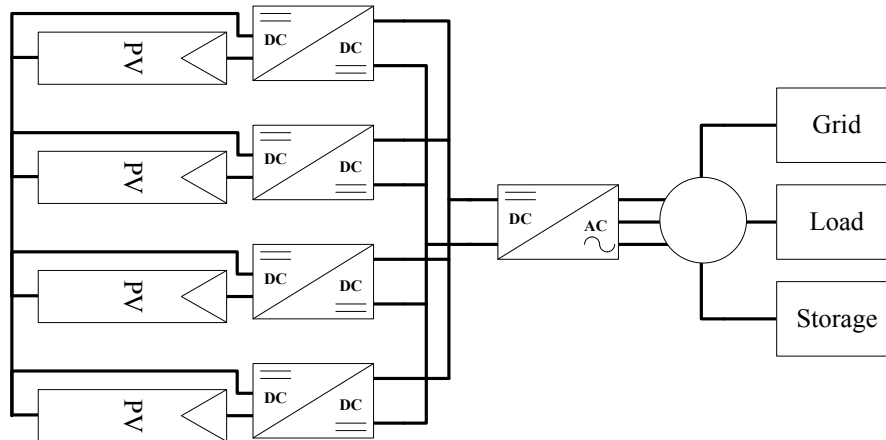


Figure 1.10. Typical single string photovoltaic system utilizing power optimizers

Central systems are used in high power applications, typically greater than 50 kW. They allow for a very low cost per watt (\$0.18 – \$0.24) and high efficiency. Some disadvantages are that the systems are very large and there is a risk of a single point of failure. Their mean time between failures (MTBF) is in the region of 10 to 15 years. In comparison the MTBF for some micro-inverter systems is greater than 380 years [31].

The next section will discuss in greater detail all of the various power electronic circuit topologies that are used in automotive and PV applications.

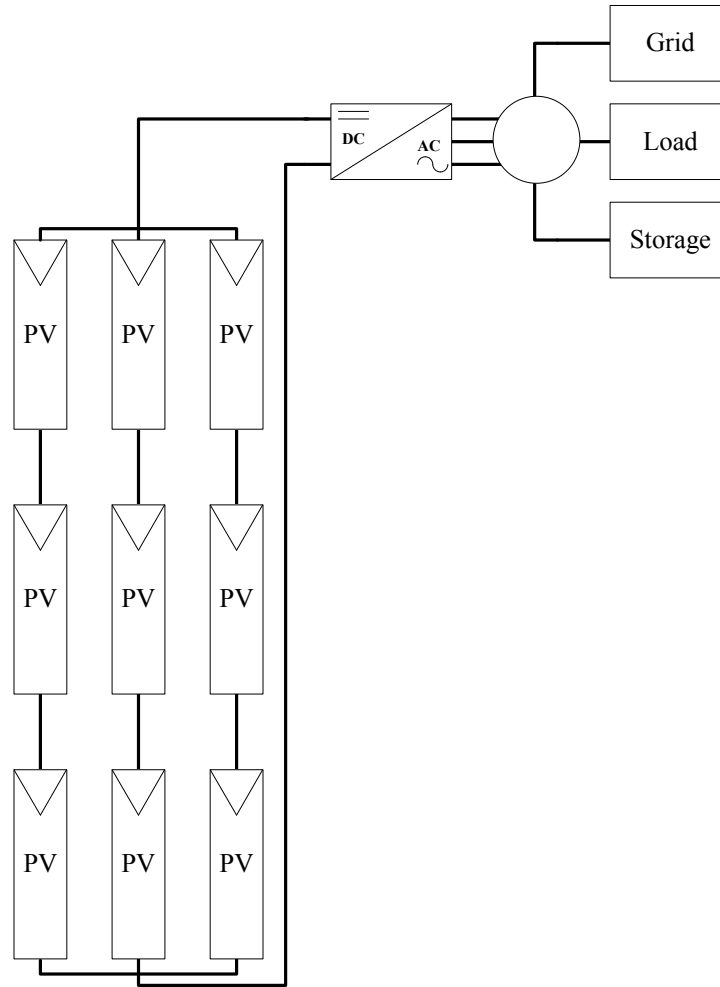


Figure 1.11. Typical central photovoltaic system

1.4.2. DC-DC Converter Circuit Topologies

The converters which are the focus of attention in this thesis are presented in Fig. 1.12. The (A) 2L topology consists of two discrete inductors, the (B) XL topology consists of a single input inductor combined with a differentially connected transformer that couples each phase and the (C) IM design is the integration of all of the converters magnetic components onto one core.

The use of a 2L design allows for the reduction of input current ripple, thereby reducing the stress on the input filter capacitors. Other benefits include; a reduction of the power loss in the discrete inductors and smaller magnetic component design. The XL and IM options also result in phase current ripple cancellation, but due to transformer coupling phase current ripple reduction is also achieved. The normalized input and phase current ripple for the IM boost converter is presented in Fig. 1.13. The current ripple is normalized to the peak value of the current ripple when the duty cycle is equal to 1. The input and phase current ripple of the 2L

solution is also included and this diagram highlights the significant phase current ripple reduction in the IM design.

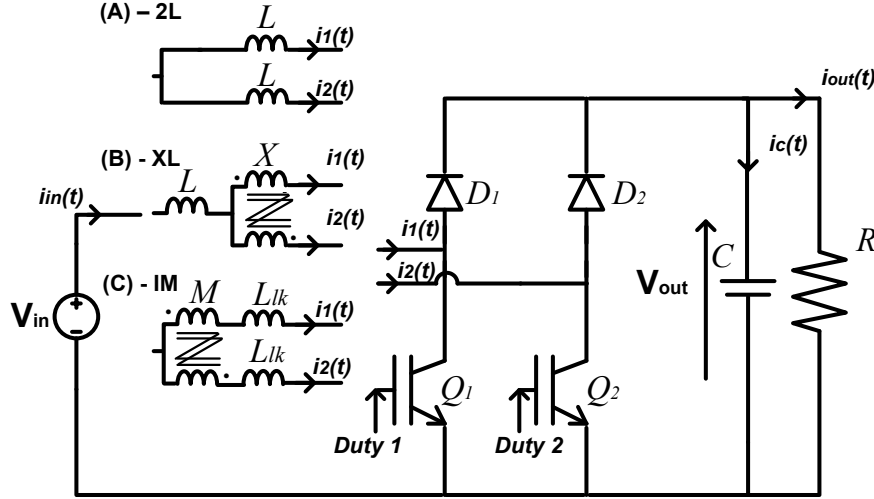


Figure 1.12. Various methods of implementing an interleaved boost converter

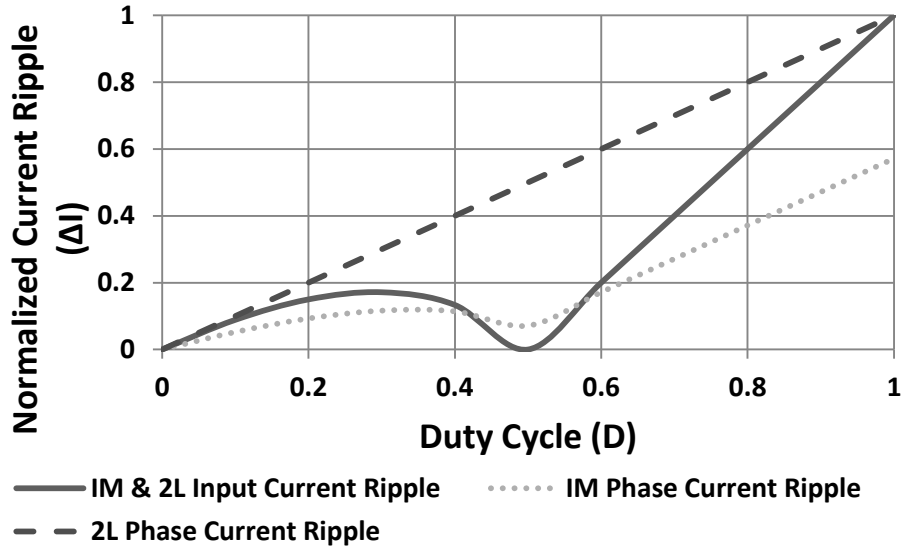


Figure 1.13. Normalized input and phase current ripple for the 2L and IM dc-dc converters presented in Fig. 1.12

1.4.2.1. Automotive

The single-phase (1L) non-isolated buck-boost converter presented in [32-36] is widely regarded as the topology of choice in automotive FCV, HEV and EV applications. It allows for bi-directional power conversion where the battery pack is recharged during regenerative braking. As previously discussed, the placement of this power converter before the traction motor inverter, such as in the THS II, allows for larger and more stable voltage on the dc-bus. This larger voltage translates into an efficiency gain as the traction motors can operate at a lower

current rating. When used in FCV applications the 1L topology operates in boost mode only. The quest for high-power density automotive converters has resulted in the design and development of multiphase, coupled-inductor and integrated magnetic dc-dc converters [37-52]. As already stated, these topologies allow for a reduction in the various filter and switch currents in the converter.

1.4.2.2. Photovoltaic

In photovoltaic applications the 1L boost converter is used in string and central inverter topologies as a pre-regulator for MPP tracking as well as to stabilize the dc-link voltage for the dc-ac inverter. The inverter then uses an isolated topology in order to provide protection from direct connection to the ac grid. The use of a 2L interleaved boost converter pre-regulator is discussed in [53], while the use of 2L [54, 55] and interleaved coupled inductor [56] topologies to achieve soft-switching are also evaluated. In terms of micro-inverter applications various topologies are presented in [57]. The single-phase full-bridge topology is deemed to be inflexible in handling a wide PV voltage range and it also requires large line frequency transformers. The next option is a two-stage inverter system using a half- or full-bridge dc-dc converter. This topology is deemed costly and complicated. The use of a interleaved flyback converter is the industry standard topology [57].

1.4.3. Power Electronic Components

1.4.3.1. Semiconductors

The selection of the semiconductor components is generally the first step in the design of a power converter as they are typically the most expensive and lossy components. The power semiconductor components control the flow of power in the power converter and have current and voltage ratings from 1 A to 1 kA and 5 V to 20 kV, respectively. The ideal power semiconductor device should have the following characteristics [58]:

- The ability to block large forward and reverse voltages when off,
- The ability to conduct large currents when on,
- The ability to switch between their on and off state instantaneously,
- They should be easy to control, rugged and reliable,

Plots of output power vs. switching frequency and on-resistance vs. breakdown voltage are presented in Fig. 1.14 [58] and Fig. 1.15 [59], respectively. These plots present the typical regions of operation of semiconductor devices.

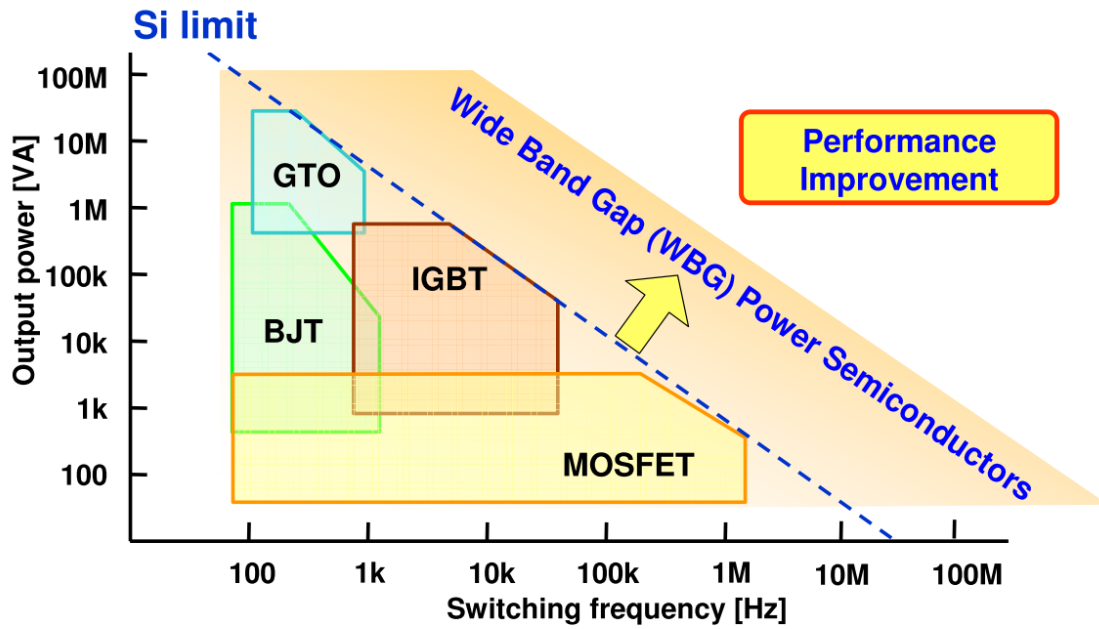


Figure 1.14. Typical semiconductor component regions of operation for power vs. switching frequency

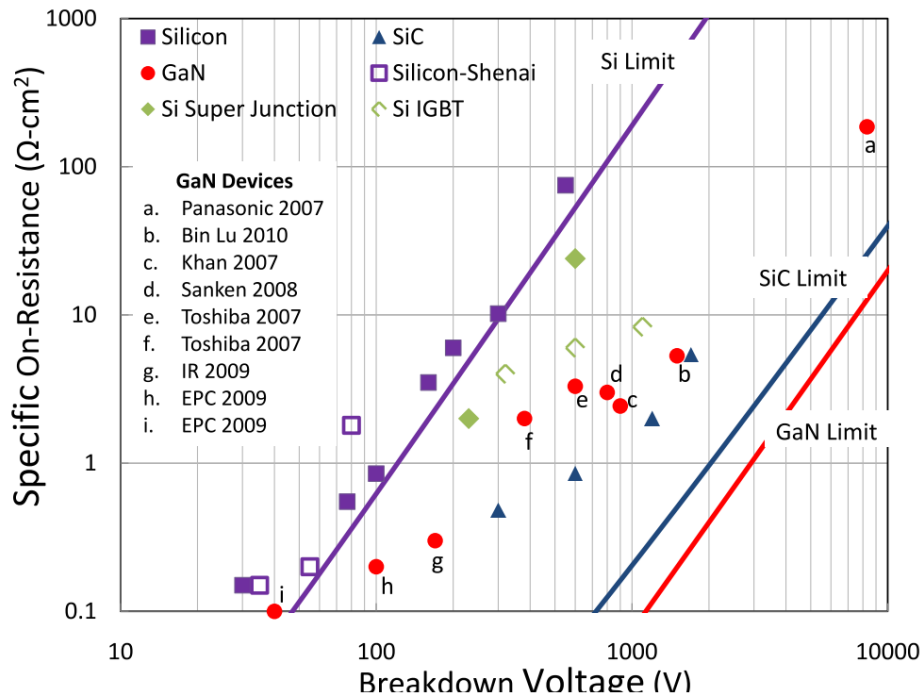


Figure 1.15. Typical semiconductor regions of operation for on-resistance vs. breakdown voltage

At present, silicon (Si) based insulated gate bipolar transistors (IGBT) and metal-oxide field effect transistors (MOSFET) are the most common components used and significant improvements have been achieved in IGBT and MOSFET technology in recent years. The use of trench and thin-wafer technology allowed for the reduction in the on-resistance of IGBT

devices while super junction technology has allowed for higher voltage and lower on-resistance MOSFET devices. The plots in Fig. 1.14 and Fig. 1.15 indicate that the limit of Si based semiconductors is close and that wide-band gap (WBG) devices using Silicon Carbide (SiC) and Gallium Nitride (GaN) are the components of the future.

The use of SiC diodes in power converters is now a common practice [60] where they allow for reduced switching losses, operation at higher switching frequencies and higher temperatures than traditional Si diodes. The information presented in [61, 62] investigates the use of SiC diodes in power-factor-correction applications. The work presented in [63] uses SiC diodes operating at 100 kHz to realize a high-power density dc-dc converter for automotive applications. The work in [64, 65] investigates the operation of dc-dc converters at high temperatures using SiC diodes. Finally, [53] looks at the use of SiC diodes in an interleaved boost converter for PV applications.

SiC power switches have made significant progress over the past 10 years [58] and high voltage, low on-resistance MOSFETs are available from all the major semiconductor manufactures. The work in [66] investigates recent advances in SiC MOSFET devices and experimental results indicate that they have significantly lower switching losses than the other devices tested. GaN devices are investigated in [67-69] and suggest that GaN has a projected 100x performance advantage over Si devices. Experimental validation and comparison of GaN devices is presented in [59]. The work investigates the use of GaN devices in a 10 W point-of-load buck converter operating at 5 MHz and in a 10 kW, 1 MHz boost converter. The GaN based converters devices exhibit superior performance over the comparable Si based designs.

The use of WBG will push designers to operate at higher frequencies in order to reduce the size of the passive components.

1.4.3.2. Magnetics

The design of any magnetic component is a complicated process and most design algorithms involve the selection of a core size in an iterative design procedure [7, 70-81]. This design process is further complicated when developing magnetic components which use non-standard core geometries, as in the case of the CCTT IM. Magnetic components are typically the largest components in power converters and they need to be designed correctly in order to ensure a compact and efficient design. The designer has many factors to consider such as the application, core material and type, winding material and type, and cooling method. The material selection process and design of inductors for high-current dc-dc converters is covered in [82, 83]. This thesis focuses on the design and development of high-power density IM structures that allow for the reduction in magnetic mass and volume.

1.4.3.3. Capacitors

The final components that are needed to realize a power converter are capacitors and there are a wide variety of capacitors available to the power converter designer [84-87]. Various different capacitors may be required in a power converter, and for example, a typical solar inverter application may require the following: dc filter capacitors, dc link capacitors, snubber capacitors and ac filter capacitors [88-90].

The important factors when selecting a capacitor for a power converter are as follows:

- Operating peak and rms voltage and current in the system
- A low equivalent series inductance (ESL) to limit switching transient over-voltages and improve dynamic response of the system
- A low equivalent series resistance (ESR) to improve the thermal stability of the capacitor and reduce heating due to the rms current. A low ESR also provides a low impedance path to high frequency ripple currents
- Capacitor lifetime and temperature rating

The type of topology used also helps in the capacitor sizing for the system. This thesis investigates interleaved topologies which can help reduce the size of the filter and dc link capacitors due to the inherent current ripple reduction.

1.4.4. Conclusions

This chapter presents an overview of the research topic that is presented in this thesis. The general background information of some typical renewable energy systems is presented. The main motivation as to why power converters are required in these applications is outlined. The various circuits and components of these power converters are presented.

The remainder of this thesis is focused on the design, development and optimization of IM component structures for use in high-power, high-current, power converter applications such as automotive and renewables.

Chapter 2

Circuit Analysis of a Two-Phase Interleaved Boost Converter using an Integrated Magnetic Structure

This thesis concerns the characterization and design of an integrated magnetic (IM) component for use in two-phase interleaved dc-dc converters. As such, it is critical to fully understand the operation of this circuit and this chapter presents the background circuit analysis. Firstly, the circuit is analysed assuming that the converter is operating in continuous conduction mode (CCM) and then for operation in discontinuous conduction mode (DCM). The characteristic currents for the high-powered 72 kW dc-dc converter examined in Chapter 4 are presented as results in this chapter, by way of example.

2.1. Introduction

In order to correctly design high-power density magnetic components it is critical to fully understand the overall circuit operation in which these structures play a crucial part. The design of single-phase non-isolated and isolated (1L) power converters are covered in detail in [7, 91] while the design of a 1L buck-boost converter for automotive applications is detailed in [32, 34]. The quest for higher efficiency and increased power density has pushed designers to explore multiphase (2L) [48, 53, 92, 93], coupled inductor (XL) [37, 38, 43, 46, 49-51] and integrated magnetic (IM) [94-103] circuit topologies.

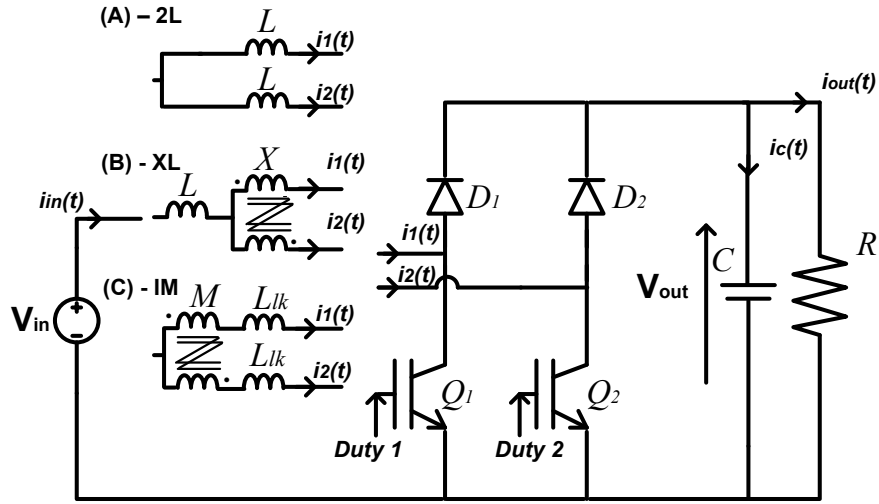


Figure 2.1. Various methods of implementing an interleaved boost converter

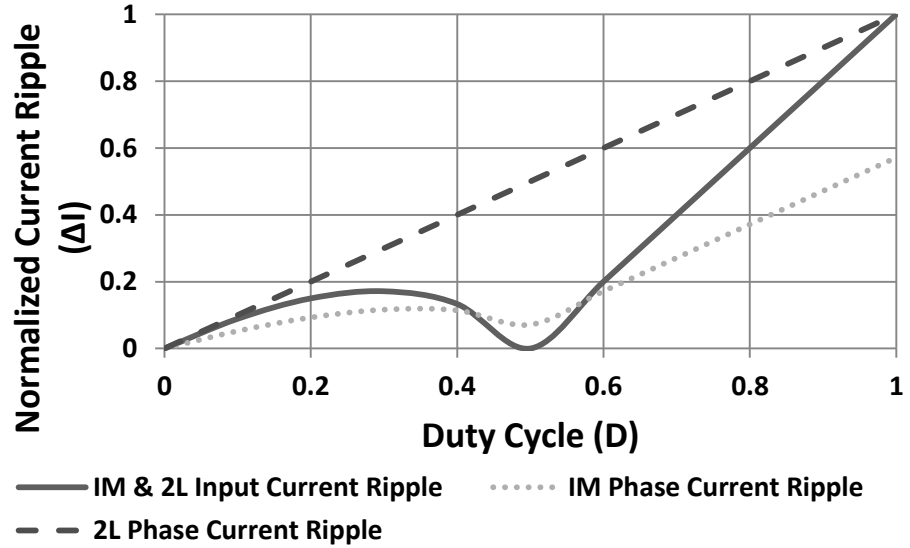


Figure 2.2. Normalized input and phase current ripple for the 2L and IM dc-dc converters presented in Fig. 2.1

These various topologies are presented in Fig. 2.1. The 2L topology consists of two discrete inductors, the XL topology consists of a single input inductor combined with a differentially-connected transformer that couples each phase and the IM design is the integration of all of the converter's magnetic components onto one core. The use of a 2L design allows for the reduction of input current ripple, thereby reducing the stress on the input filter capacitors. Other benefits include a reduction of the power loss in the discrete inductors and smaller magnetic component design. The XL and IM options also result in phase current ripple cancellation, but due to transformer coupling phase current ripple reduction is also achieved. Plots of the normalized input and phase current ripple for the IM boost converter versus duty cycle are presented in Fig. 2.2. The current ripple is normalized to the peak value of the current ripple when the duty cycle is equal to 1. The input and phase current ripple of the 2L solution are also included. This diagram highlights the significant phase current ripple reduction in the IM design.

The circuit analysis in this chapter solely focuses on non-isolated interleaved dc-dc converters using an IM component. The initial analysis assumes that the circuit is operating in CCM and the peak-to-peak input current ripple, $\Delta I_{in(p-p)}$, the peak-to-peak magnetizing ripple, $\Delta I_{m(p-p)}$, and the peak-to-peak phase current ripple, $\Delta I_{phase(p-p)}$, are determined. These equations are validated for sample design points, corresponding to the high-power automotive fuelcell design which is presented in Chapter 4, using the familiar circuit simulation software, PSpice. These current ripple values are graphed in Section 2.3 as the duty cycle is varied and they show a similar trend to the normalized curves presented in Fig. 2.2. Interestingly, as the duty cycle is decreased, the boost converter enters into DCM and the CCM circuit equations are no longer valid. Accordingly, this chapter investigates the converter operation in DCM and uses this analysis in order to predict the correct circuit operation. As in the CCM case, PSpice is used to validate the DCM circuit equations.

Additionally, the input capacitor, switch and diode currents, for both modes of operation are presented. The CCM circuit equations are used in the CCTT IM algorithm, presented in Chapter 3, in order to design an IM structure.

2.2. IM Converter Circuit Analysis

The IM is modelled using the familiar ideal transformer model. This transformer model consists of a magnetizing inductance, L_m , and a symmetrical per phase leakage inductance, L_{lk} . Due to the unity turns ratio, the mutual inductance, M , is equal to the magnetizing inductance, L_m . The IM boost converter is presented in Fig. 2.3. The converter can operate in continuous conduction mode (CCM) or in discontinuous conduction mode (DCM). The following section describes the converter operation for each mode in more detail.

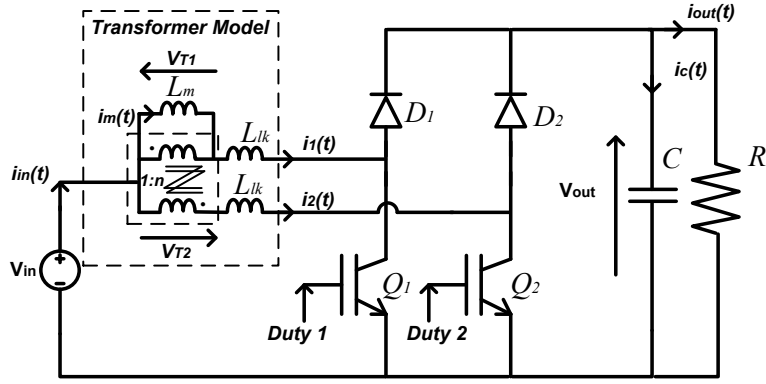


Figure 2.3. IM boost circuit

2.2.1. IM Operation in Continuous Conduction Mode

The converter operates at a constant switching frequency, f_s , with period T . The converter has a variable on-time, $t_{on} = DT$, where D is the duty cycle of switches Q_1 and Q_2 . The switches Q_1 and Q_2 are switched with a 180° phase delay and operate with the same duty cycle, D . There are four distinct modes of operation and these modes of operation differ based on whether D is less than 0.5 or greater than 0.5.

Table 2.1 Input, Magnetizing and Phase Current Ripple Equations for IM Boost Converter in CCM

Duty Ratio	$\Delta I_{in} \text{ (p-p)}$	$\Delta I_m \text{ (p-p)}$	$\Delta I_{phase} \text{ (p-p)}$
$D < 0.5$	$\frac{V_{in} \left[\left(\frac{D}{1-D} \right) (1-2D) \right] T}{L_{lk}}$	$\frac{V_{in} \left[\left(\frac{D}{1-D} \right) \right] T}{2L_m + L_{lk}}$	$\frac{\Delta I_{in(p-p)}}{2} + \frac{\Delta I_{m(p-p)}}{2}$
$D > 0.5$	$\frac{V_{in} (2D-1) T}{L_{lk}}$	$\frac{V_{in}}{2L_m + L_{lk}} T$	$\frac{\Delta I_{in(p-p)}}{2} + \frac{\Delta I_{m(p-p)}}{2}$

The peak-to-peak input current ripple, $\Delta I_{in(p-p)}$, is approximately triangular when resistance is neglected and due to converter symmetry has a frequency equal to twice the switching frequency. The input ripple is solely dependent on the leakage inductance of the IM as shown in Table 2.1. The magnetizing current flows through both primary and secondary windings and the peak-to-peak magnetizing ripple, $\Delta I_{m(p-p)}$, is given in Table 2.1. The peak-to-peak phase current ripple, $\Delta I_{phase(p-p)}$, is a combination of half the input current ripple and half of the magnetizing current ripple as shown in Table 2.1. The CCM circuit equations are validated in Section 2.3. Fig. 2.4 illustrates the switching waveforms for duty cycles of less than 0.5. As already stated, there are four distinct modes of operation for D less than 0.5 and these are presented in Fig. 2.5. Subinterval 1 is equivalent to subinterval 3 while subinterval 2 is equivalent to subinterval 4.

2.2.1.1. IM Operation in Continuous Conduction Mode for D less than 0.5

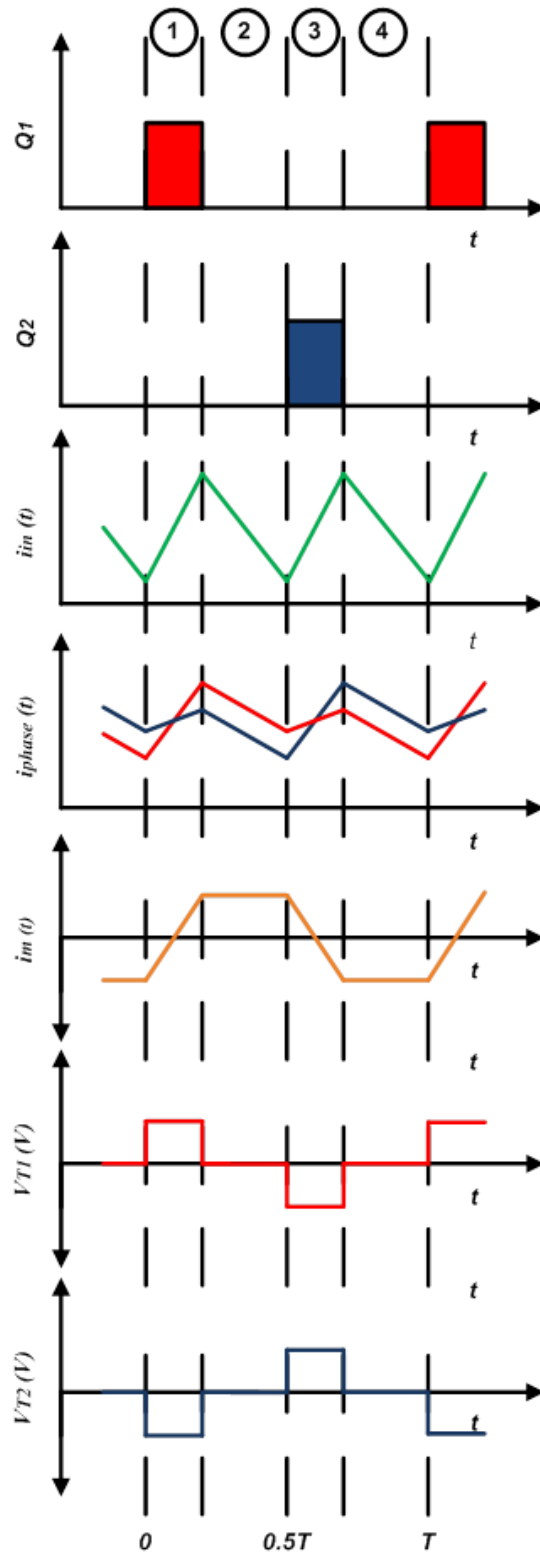


Figure 2.4. IM circuit switching waveforms for duty cycle, $D < 0.5$

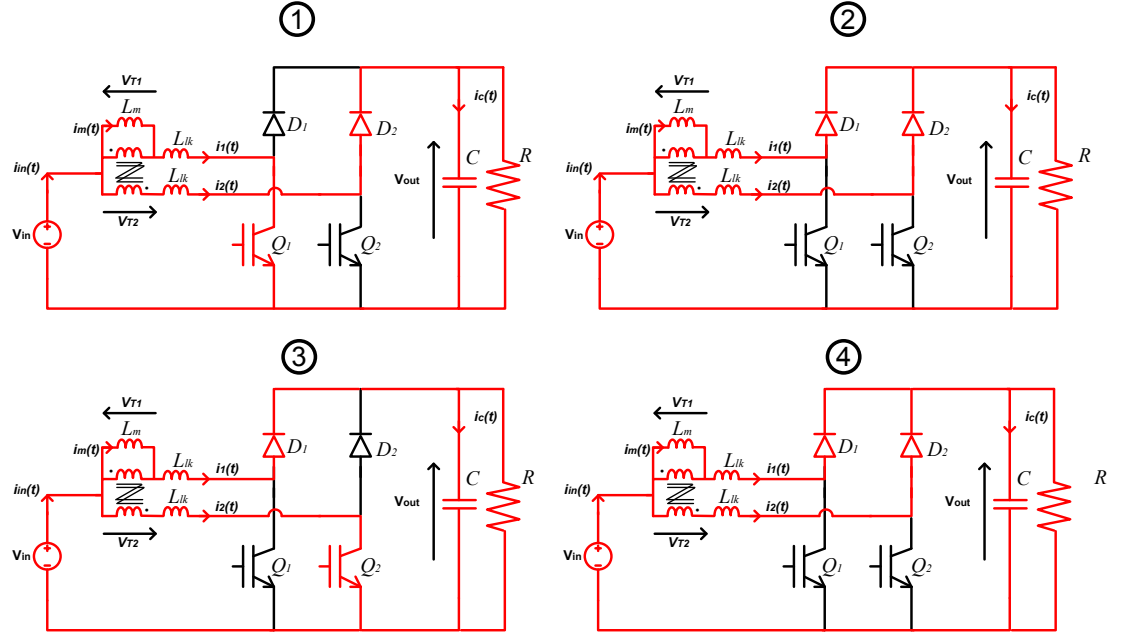


Figure 2.5. IM equivalent circuits in CCM for duty cycle, $D < 0.5$

The magnetizing current, $i_m(t)$, and its ripple, $\Delta I_{m(p-p)}$, are determined by evaluating the equivalent circuit during subinterval 1. The phase currents, $i_1(t)$ and $i_2(t)$, and their ripple due to the leakage inductance, ΔI_{lk} , are determined by analysing the equivalent circuit during subinterval 2. The peak-to-peak input current ripple, $\Delta I_{in(p-p)}$, is twice the phase current ripple due to the leakage inductance.

Firstly, it is assumed that the current in Phase 1 is the sum of the magnetizing current and current in Phase 2. Also, the back emfs across the transformer are equal:

$$i_1(t) = i_m(t) + i_2(t) \quad (2.1)$$

$$V_{T1} = V_{T2} \quad (2.2)$$

The magnetizing current, $i_m(t)$, is determined by applying Kirchhoff's voltage law (KVL) to Phase 1 and Phase 2 during the time interval DT .

For Phase 1:

$$V_{in} - V_{T1} - V_{Llk} = 0 \quad (2.3)$$

$$V_{in} - L_m \frac{di_m(t)}{dt} - L_{lk} \frac{di_1(t)}{dt} = 0 \quad (2.4)$$

For Phase 2:

$$V_{in} + V_{T2} - V_{Llk} - V_{out} = 0 \quad (2.5)$$

$$V_{in} + L_m \frac{di_m(t)}{dt} - L_{lk} \frac{di_2(t)}{dt} - V_{out} = 0 \quad (2.6)$$

Now substituting (2.1) and (2.2) into (2.4) and (2.6) results in (2.7) and (2.8):

$$V_{in} - L_m \frac{di_m(t)}{dt} - L_{lk} \left(\frac{di_m(t)}{dt} + \frac{di_2(t)}{dt} \right) = 0 \quad (2.7)$$

$$V_{in} + L_m \frac{di_m(t)}{dt} - L_{lk} \frac{di_2(t)}{dt} - V_{out} = 0 \quad (2.8)$$

By subtracting (2.8) from (2.7), simplifying and using the voltage gain equation for a boost converter in (2.9), the magnetizing currents are determined as follows:

$$V_{out} = \frac{V_{in}}{1-D} \quad (2.9)$$

$$\frac{di_m(t)}{dt} = \frac{V_{out}}{2L_m + L_{lk}} \quad (2.10)$$

$$\Delta I_{m(p-p)} = \frac{V_{in}}{2L_m + L_{lk}} \left(\frac{D}{1-D} \right) T \quad (2.11)$$

The component of the phase currents, $i_1(t)$ and $i_2(t)$, due to the leakage inductance, ΔI_{lk} , are determined using the following equations and by applying KVL to Phase 1 and Phase 2 during the time interval $(0.5-D)T$.

For Phase 1:

$$V_{in} - V_{T1} - V_{Llk} - V_{out} = 0 \quad (2.12)$$

$$V_{in} - L_m \frac{di_m(t)}{dt} - L_{lk} \frac{di_1(t)}{dt} - V_{out} = 0 \quad (2.13)$$

For Phase 2:

$$V_{in} + V_{T2} - V_{Llk} - V_{out} = 0 \quad (2.14)$$

$$V_{in} + L_m \frac{di_m(t)}{dt} - L_{lk} \frac{di_2(t)}{dt} - V_{out} = 0 \quad (2.15)$$

Again by substituting (2.1) and (2.2) by subtracting (2.15) from (2.13) and simplifying it

is possible to determine that the magnetizing current, $i_m(t)$, during the time interval $(0.5-D)T$ is equal to zero:

$$\frac{di_m(t)}{dt}(2L_m + L_{lk}) = 0 \quad (2.16)$$

$$\frac{di_m(t)}{dt} = 0 \quad (2.17)$$

By adding (2.13) to (2.15) and simplifying the phase current due to the leakage inductance, $\Delta I_{lk(p-p)}$, during the time interval $(0.5-D)T$ is as follows:

$$\frac{di_2(t)}{dt} = \frac{V_{in} - V_{out}}{L_{lk}} \quad (2.18)$$

$$\Delta I_{lk(p-p)} = \frac{V_{in} - V_{out}}{L_{lk}}(0.5 - D)T \quad (2.19)$$

Finally, the input current, $i_{in}(t)$, and its ripple, $\Delta I_{in(p-p)}$, depend entirely on the current ripple due to the leakage inductance and is as follows:

$$\frac{di_{in}(t)}{dt} = 2 \left(\frac{V_{in} - V_{out}}{L_{lk}} \right) \quad (2.20)$$

$$\Delta I_{in(p-p)} = \frac{V_{in} \left(\frac{D}{1-D} \right)}{L_{lk}}(1 - 2D)T \quad (2.21)$$

2.2.1.2. IM Operation in Continuous Conduction Mode for D greater than 0.5

Similar to duty cycles less than 0.5, there are four distinct modes of operation for D greater than 0.5 and these are presented in Fig. 2.6. Subinterval 1 is equivalent to subinterval 3 while subinterval 2 is equivalent to subinterval 4. The switching waveform for duty cycles of greater than 0.5 is presented in Fig. 2.7.

The phase current, $i_2(t)$, and its ripple due to the leakage inductance, ΔI_{lk} , is presented in (2.22) while the input current ripple is presented in (2.23):

$$\frac{di_2(t)}{dt} = \frac{V_{in}}{L_{lk}} \quad (2.22)$$

$$\Delta I_{lk(p-p)} = \frac{V_{in}}{L_{lk}}(D - 0.5)T \quad (2.23)$$

Finally, the input current, $i_{in}(t)$, and its ripple, $\Delta I_{in(p-p)}$, depend entirely on the current ripple due to the leakage inductance and is as follows:

$$\frac{di_{in}(t)}{dt} = 2 \left(\frac{V_{in}}{L_{lk}} \right) \quad (2.24)$$

$$\Delta I_{in} = \frac{V_{in}}{L_{lk}}(2D - 1)T \quad (2.25)$$

The magnetizing current, $i_m(t)$, and its ripple, $\Delta I_{m(p-p)}$, are presented in (2.26) and (2.27):

$$\frac{di_m(t)}{dt} = \frac{V_{out}}{2L_m + L_{lk}} \quad (2.26)$$

$$\Delta I_{m(p-p)} = \frac{V_{in}}{2L_m + L_{lk}} T \quad (2.27)$$

Note that the magnetizing current, $\Delta I_{m(p-p)}$, is constant for duty cycles greater than 0.5.

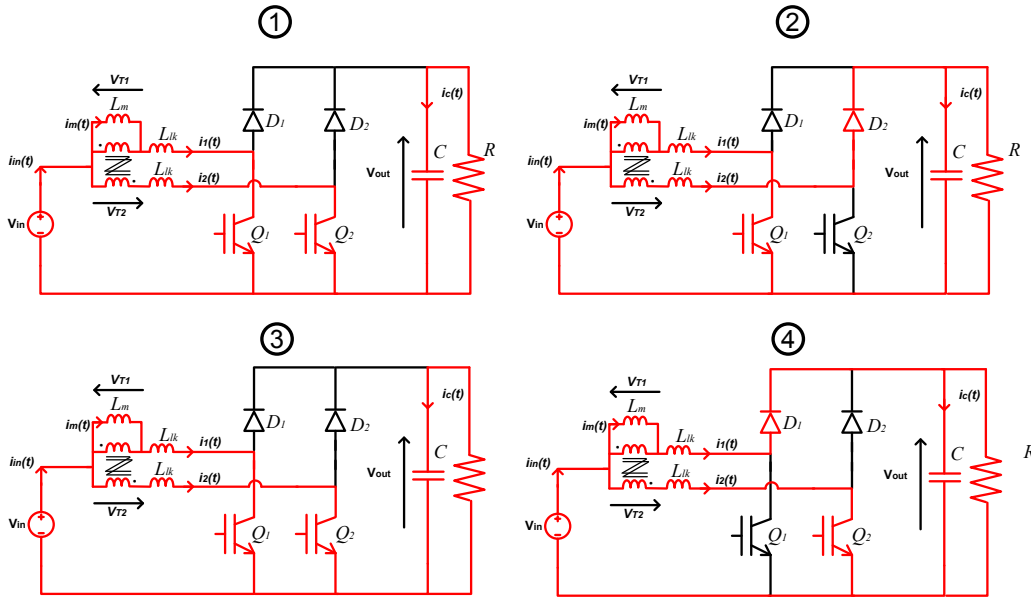


Figure 2.6. IM equivalent circuits in CCM for duty cycles, $D > 0.5$

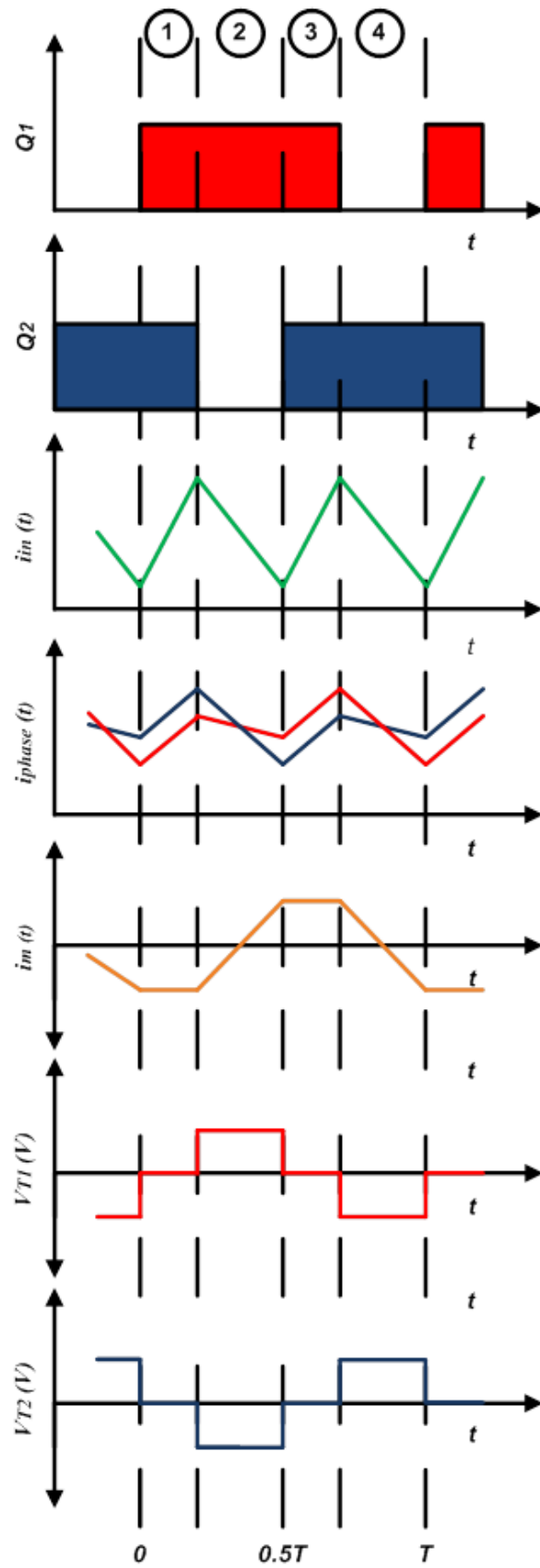


Figure 2.7. IM circuit waveforms in CCM for duty cycle, $D > 0.5$

2.2.1.3. Current Ripple Investigation for a Variation in Magnetizing Inductance

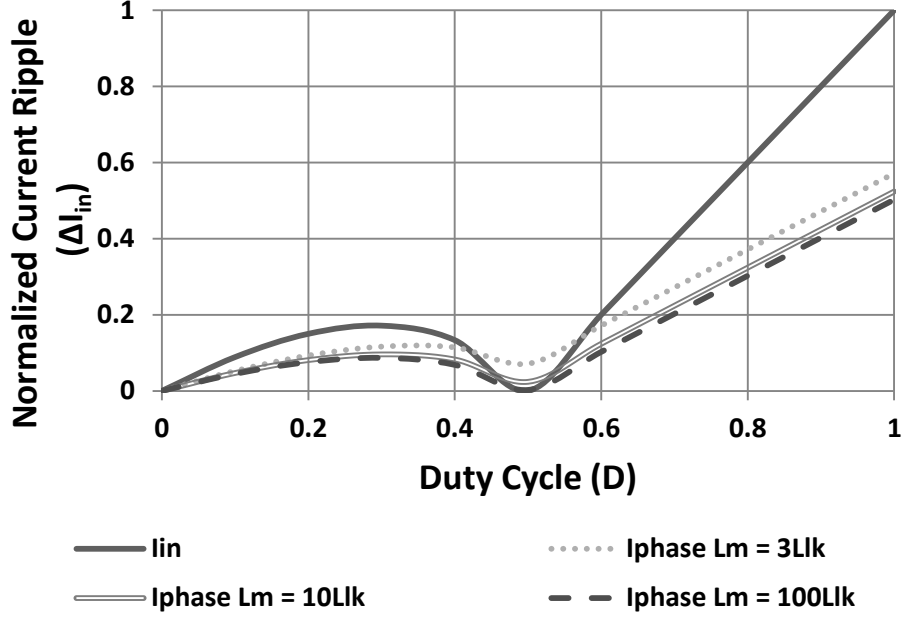


Figure 2.8. Normalized input and phase current ripple for various values of magnetizing inductance

Plots of the normalized input and phase current ripple versus duty cycle for the IM boost converter are presented in Fig. 2.8. Initially, the magnetizing inductance is set to be a value of three times the leakage inductance [104], and transformer action allows for a reduction in phase current ripple. As the magnetizing inductance is increased the phase ripple current is reduced over the duty cycle range. For all cases at $D = 0.5$ the input current ripple is zero and the phase current ripple is purely a function of magnetizing current ripple. As can be seen in Fig. 2.8, the phase current ripple reduces marginally as the magnetizing to leakage inductance ratio increases from $L_m = 3 \times L_{lk}$ to $L_m = 10 \times L_{lk}$ to $L_m = 100 \times L_{lk}$. The input current ripple is the same regardless of the magnetizing current. Section 3.7 will investigate the changes in CCTT IM boxed volume as the magnetizing inductance is increased.

2.2.2. IM Operation in Discontinuous Conduction Mode

This section investigates the operation of the CCTT IM in DCM. DCM operation is typically encountered when the CCTT IM has a large phase current ripple and is operating at part- or low-load conditions. This condition is realized in automotive fuelcell applications when the vehicle is frequently operating in a stop-start manner. The origin and explanation of DCM

operation in a single-phase boost converter is presented in [7, 91]. This methodology is easily expanded to consider DCM operation in a two-phase interleaved converter that contains two discrete inductors [48]. This methodology is not applicable for a two-phase interleaved converter that has magnetic coupling between each phase, as in the case of the CCTT IM. There are two types of DCM operation; firstly, the CCTT IM converter enters into “soft” DCM and this is when the one of the phase currents goes to zero over one switching period. In this mode of operation the input current remains in CCM; secondly, the CCTT IM enters into “hard” DCM and this when both phase currents go to zero. The input current also goes into DCM during this mode.

As in the CCM case, the converter operates at a constant switching frequency, f_s , with period T . The converter has a variable on-time, $t_{on} = D_1T$, where D_1 is the duty cycle of switches Q_1 and Q_2 . The fall-time of the phase current ripple to the point where it goes discontinuous is defined as, $t_{fall} = D_2T$, where D_2 is the duty cycle of the fall-time. Finally, the period of time that each phase current remains at zero is defined as, $t_{dcm} = D_3T$, where D_3 is the duty cycle of the discontinuous time period. There is an additional time period that corresponds to converter operation in “hard” DCM for duty cycles less than 0.5. During this time period the magnetizing current of the CCTT IM goes to zero. This is defined as, $t_{dcm,mag} = D_4T$, where D_4 is the duty cycle of the magnetizing current discontinuous time period.

There are six distinct modes of operation when the CCTT IM converter is in “soft” DCM and these modes of operation differ for D less than 0.5 and D greater than 0.5. When the converter is in “hard” DCM and for duty cycles less than 0.5 there are eight modes of operation. The following analysis investigates the operation of the CCTT IM converter in “soft” and “hard” DCM for duty cycles less than and greater than 0.5. The peak-to-peak input current ripple, $\Delta I_{in(p-p)}$, peak-to-peak magnetizing ripple, $\Delta I_{m(p-p)}$, and peak-to-peak phase current ripple, $\Delta I_{phase(p-p)}$, for “soft” and “hard” DCM operation are presented in Table 2.2 and Table 2.3, respectively. The DCM circuit equations are validated in Section 2.3 for a sample automotive fuelcell application.

2.2.2.1. IM Operation in “Soft” Discontinuous Conduction Mode for D less than 0.5

Fig. 2.9 illustrates the “soft” DCM switching waveforms for duty cycles of less than 0.5. The six distinct modes of operation are presented in Fig. 2.10. Subinterval 1 is equivalent to subinterval 3 while subinterval 2 is equivalent to subinterval 4. Subintervals A and B are when the CCTT IM current, in either phase, goes to zero. Fig. 2.11 presents a close up diagram of the phase, magnetizing and diode currents.

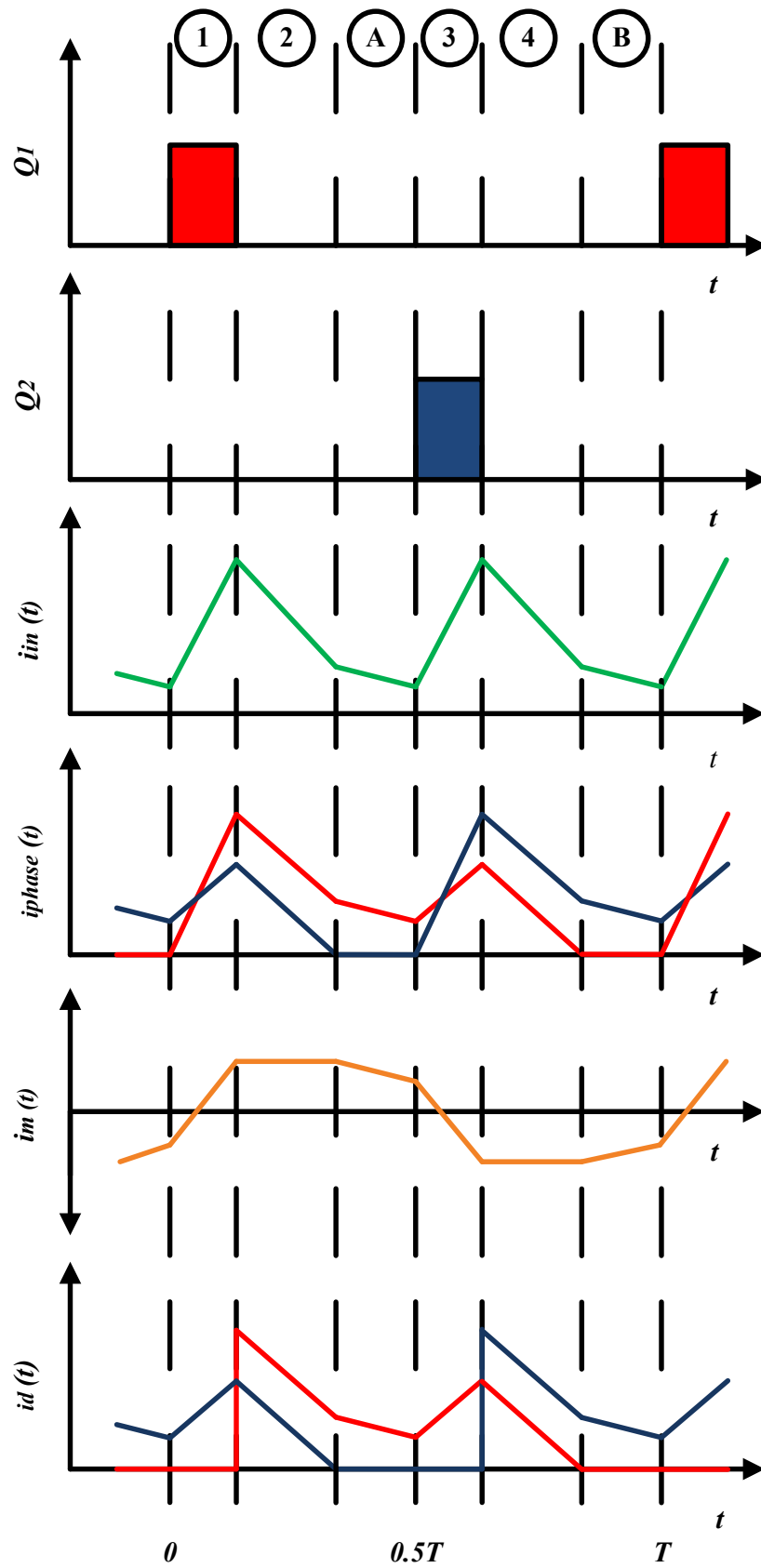


Figure 2.9. IM circuit switching waveforms in “soft” DCM for duty cycles, $D < 0.5$

Using circuit analysis techniques on the equivalent circuits presented in Fig. 2.10 the following five equations, (2.28) – (2.32), are determined corresponding to I_{max} , I_a , I_{min} and I_b :

$$I_b = -\frac{V_{in} - V_{out}}{L_{lk}} D_2 T \quad (2.28)$$

$$I_{max} = \frac{1}{2} D_1 T \left(\frac{2V_{in} - V_{out}}{L_{lk}} + \frac{V_{out}}{2L_m + L_{lk}} \right) \quad (2.29)$$

$$I_a = I_{max} + \frac{V_{in} - V_{out}}{L_{lk}} D_2 T \quad (2.30)$$

$$I_{min} = I_a + \frac{V_{in} - V_{out}}{L_m + L_{lk}} D_3 T \quad (2.31)$$

$$I_b = I_{min} + \frac{1}{2} D_1 T \left(\frac{2V_{in} - V_{out}}{L_{lk}} - \frac{V_{out}}{2L_m + L_{lk}} \right) \quad (2.32)$$

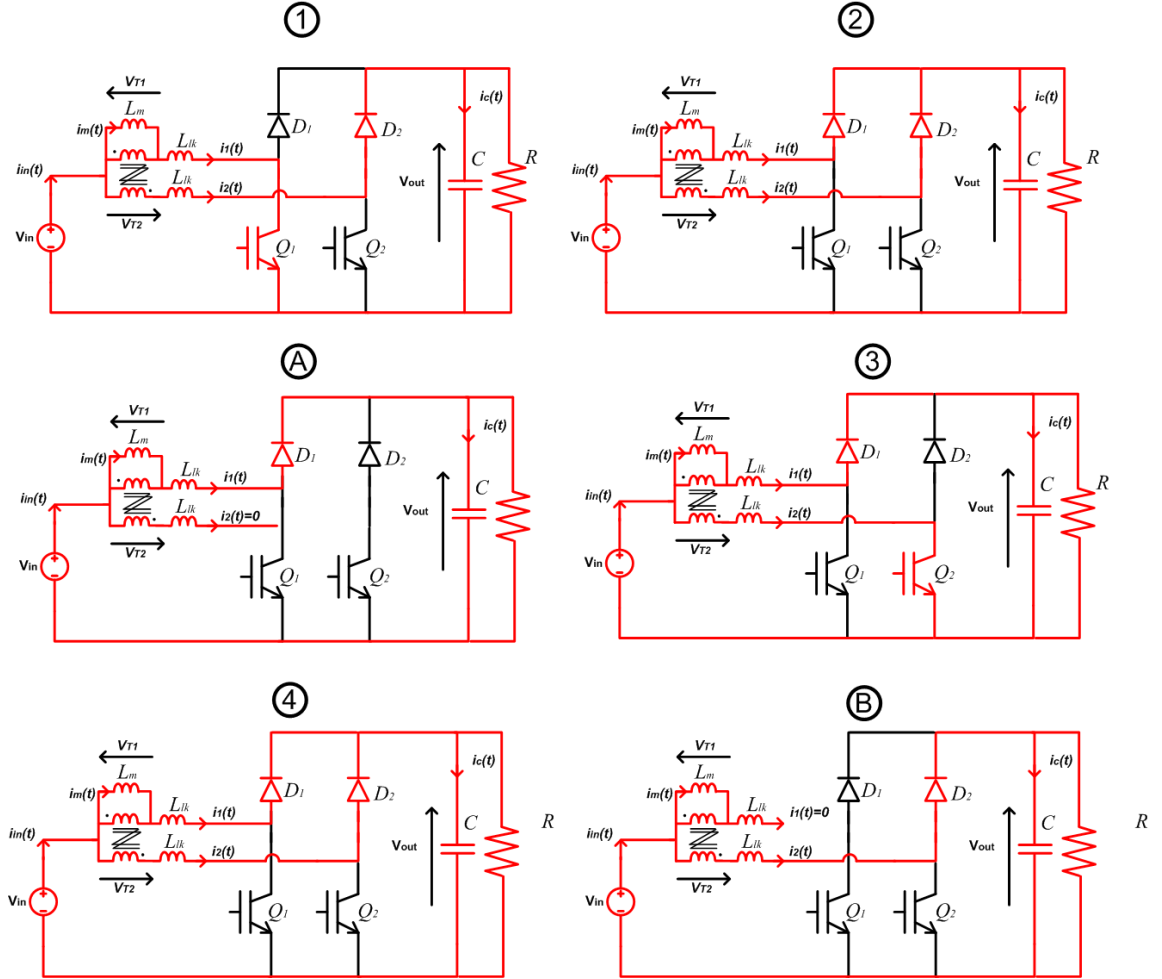


Figure 2.10. IM equivalent circuits in “soft” DCM for duty cycles, $D < 0.5$

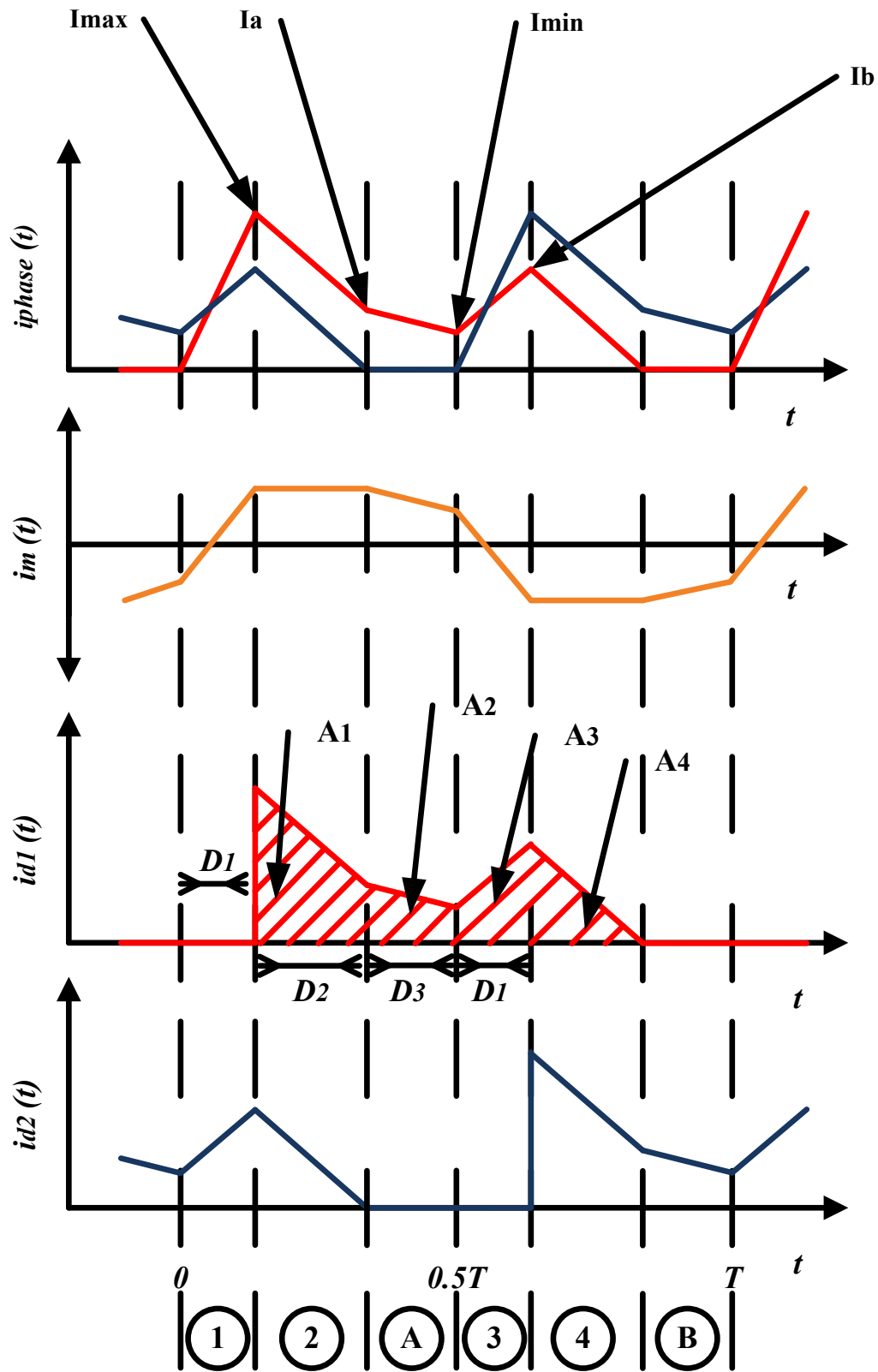


Figure 2.11. IM circuit switching waveforms in “soft” DCM for duty cycles, $D < 0.5$

Assuming that the leakage inductance, L_{lk} , magnetizing inductance, L_m , input voltage, V_{in} , output voltage, V_{out} and time period, T , are known, there are then seven unknowns in the above equation set. The seven unknown variables are as follows: I_{max} , I_a , I_{min} , I_b , D_1 , D_2 and D_3 . Therefore, two more equations are needed in order to determine a solution. The total diode current is equal to the shaded area presented in Fig. 2.11. The integral of the diode current over the switching period is equal to half of the output dc current as presented in (2.33). This integral can be represented in (2.39) which is the sum of A_1 , A_2 , A_3 and A_4 which are presented in (2.34)-(2.37).

$$\frac{1}{T} \int_0^{0.5T} I_{D1}(t) dt = \frac{V_{out}}{2R_{out}} \quad (2.33)$$

$$A_1 = \frac{1}{2}(I_{max} + I_a)D_2T \quad (2.34)$$

$$A_2 = \frac{1}{2}(I_a + I_{min})D_3T \quad (2.35)$$

$$A_3 = \frac{1}{2}(I_{min} + I_b)D_1T \quad (2.36)$$

$$A_4 = \frac{1}{2}(I_b)D_2T \quad (2.37)$$

$$\frac{1}{T}(A_1 + A_2 + A_3 + A_4) = \frac{V_{out}}{2R_{out}} \quad (2.38)$$

$$(I_{max} + I_b + I_a)D_2 + (I_a + I_{min})D_3 + (I_{min} + I_b)D_1 = \frac{V_{out}}{2R_{out}} \quad (2.39)$$

The final equation needed is presented in (2.40):

$$D_1 + D_2 + D_3 = \frac{1}{2} \quad (2.40)$$

The above equations are solved in the mathematical software tool Mathematica. As the converter enters into DCM the output voltage increases for a given duty cycle, D_1 , and the equivalent load resistance, R_{out} . The above equations are solved in order to determine the required duty cycle, D_1 , to produce the required output voltage on the dc bus.

2.2.2.2. IM Operation in “Hard” Discontinuous Conduction Mode for D less than 0.5

Fig. 2.12 the four of the eight equivalent circuits while Fig. 2.13 illustrates the “hard” DCM switching waveforms for duty cycles of less than 0.5. Subinterval D is when both phase currents go to zero. Fig. 2.14 presents a close up diagram of the phase, magnetizing and diode currents. This mode of operation introduces a further time period, D_4T , where D_4 is the duty cycle of the magnetizing current discontinuous period. In order to obtain a solution to the problem two extra equations, (2.41) and (2.42) are added to the equations presented in the previous section, (2.28) – (2.40). Equation (2.41) is added to describe that the magnetizing current ripple goes to zero while (2.40) is modified to become (2.42). This then allows for the determination of the duty cycle D_4 .

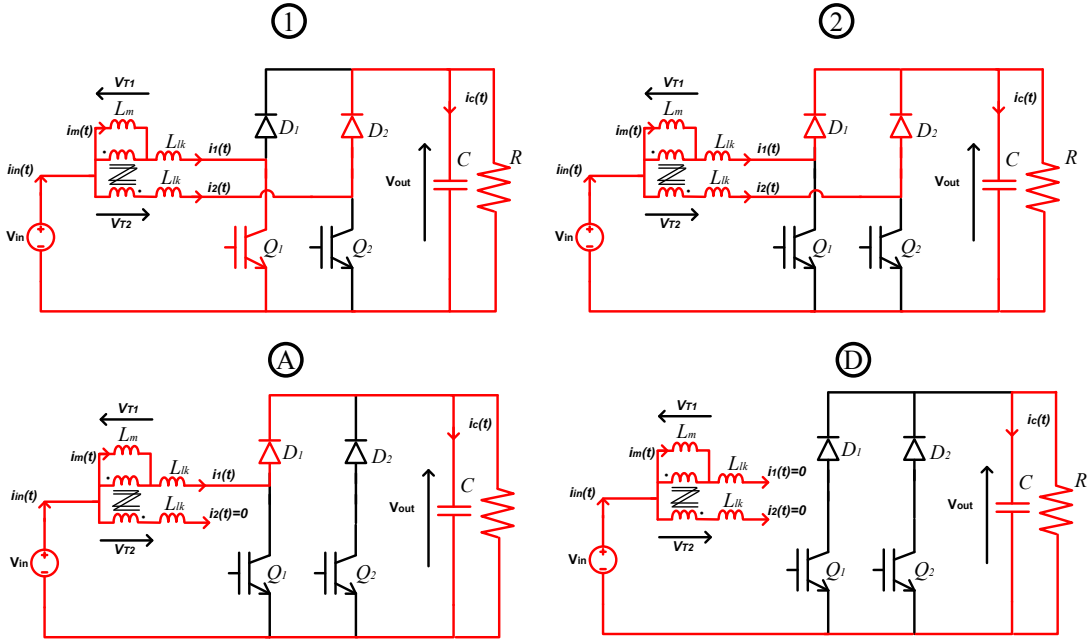


Figure 2.12. IM equivalent circuits in “hard” DCM for duty cycles, $D < 0.5$

$$I_{min} = 0 \quad (2.41)$$

$$D_1 + D_2 + D_3 + D_4 = \frac{1}{2} \quad (2.42)$$

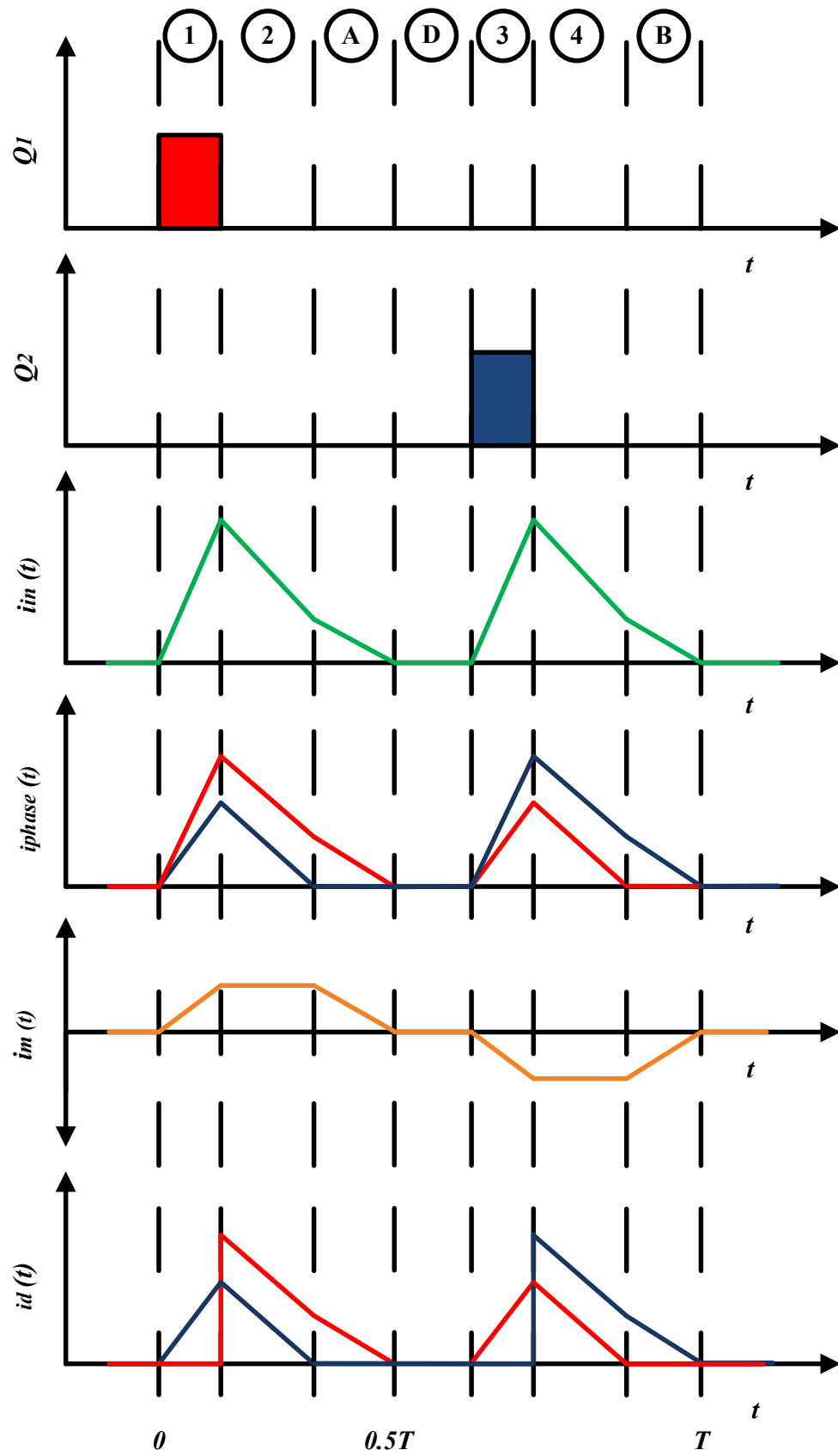


Figure 2.13. IM circuit switching waveforms in “hard” DCM for duty cycles, $D < 0.5$

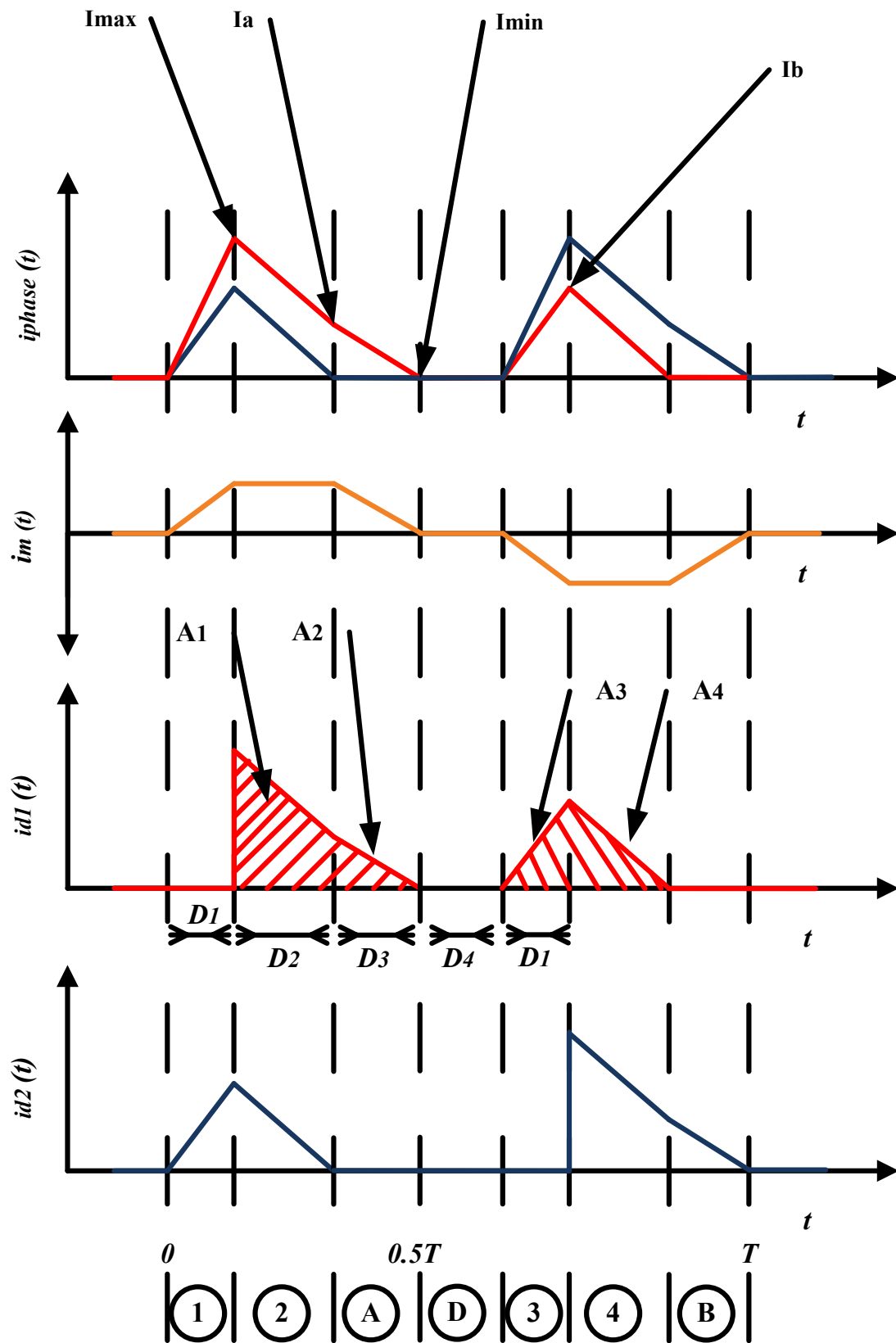


Figure 2.14. IM circuit switching waveforms in "hard" DCM for duty cycles, $D < 0.5$

2.2.2.3. IM Operation in “Soft” and “Hard” Discontinuous Conduction Mode for D greater than 0.5

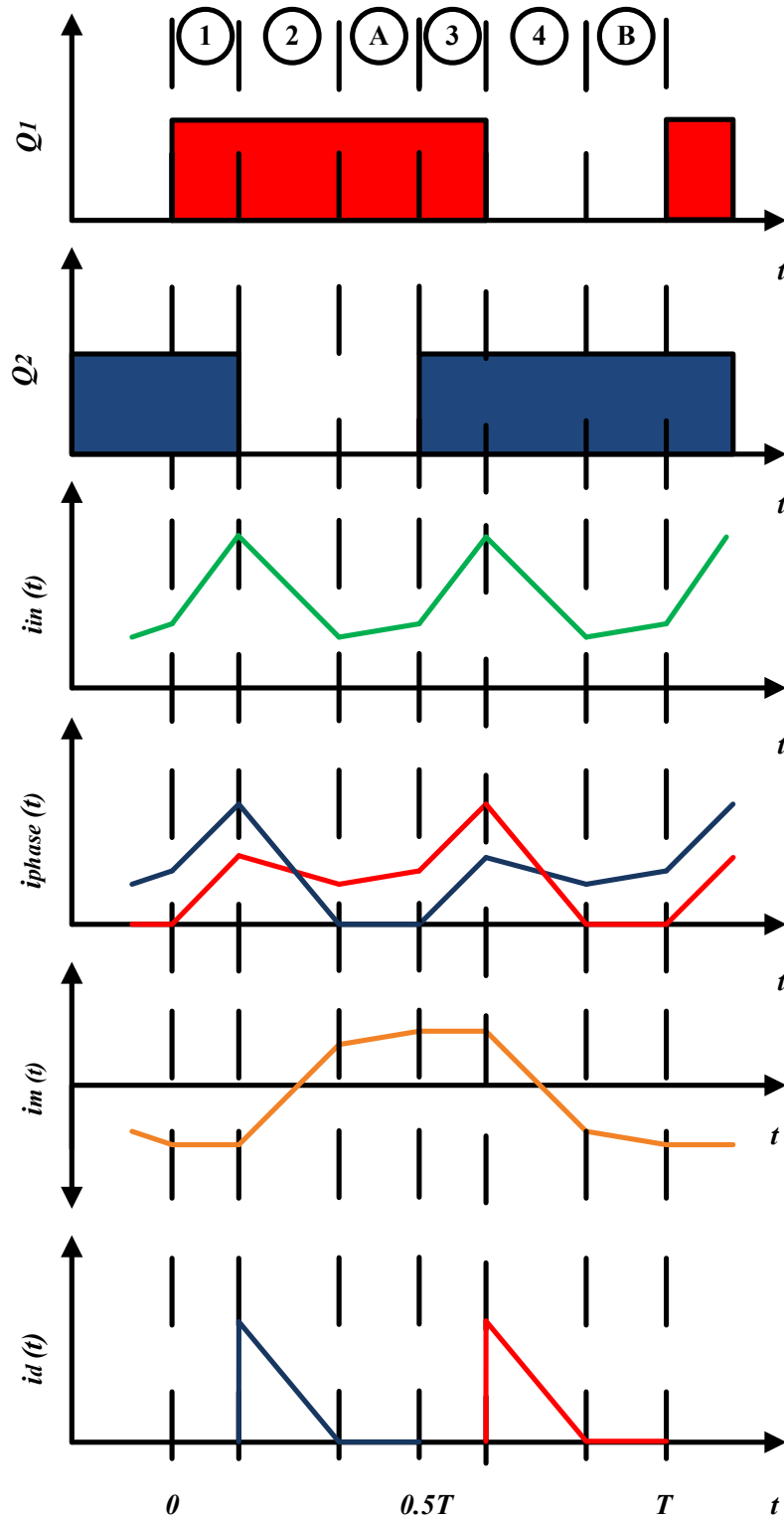


Figure 2.15. IM circuit switching waveforms in “soft” DCM for duty cycles, $D > 0.5$

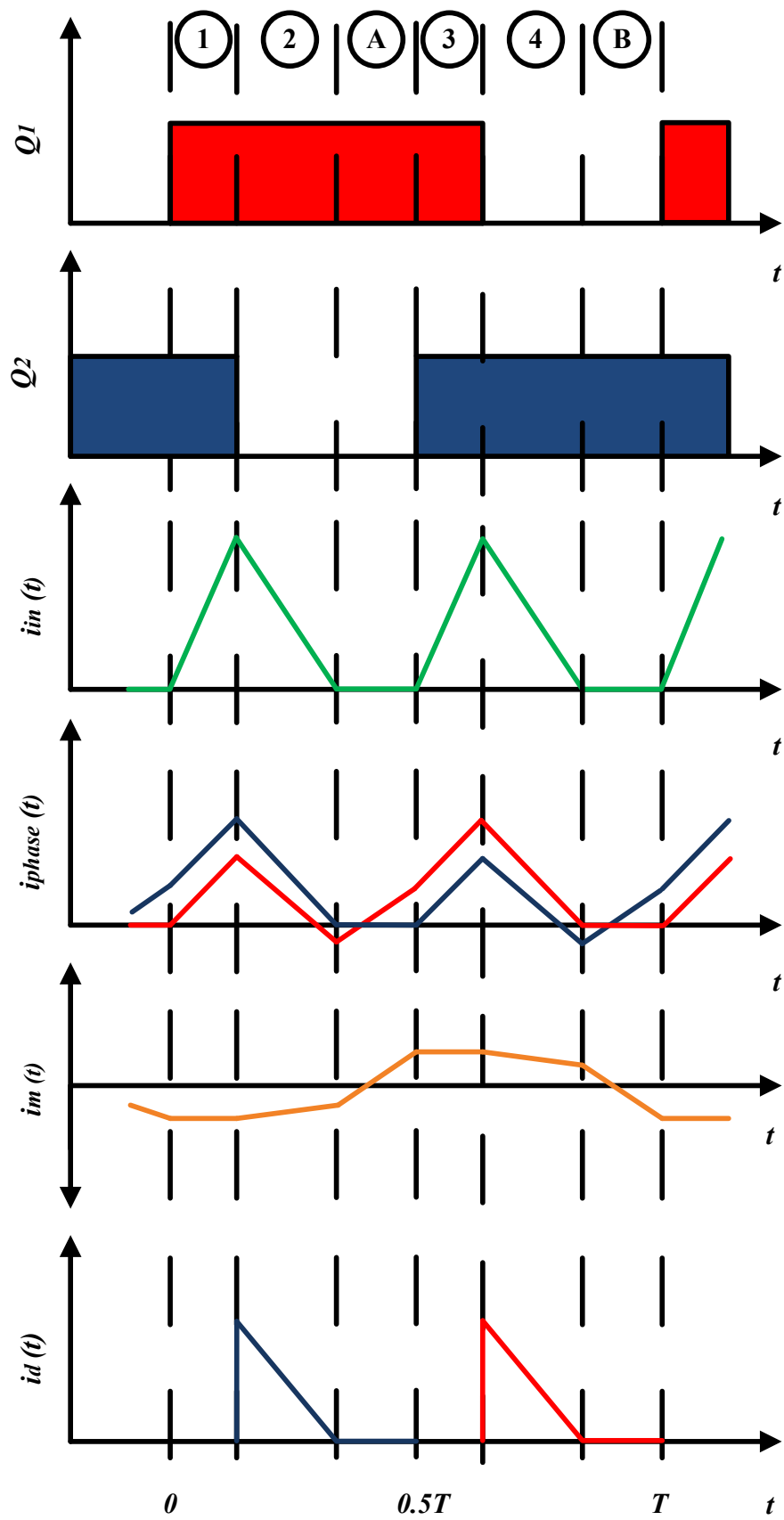


Figure 2.16. IM circuit switching waveforms in “hard” DCM for duty cycles, $D > 0.5$

Fig. 2.18 and Fig. 2.19 present a close up diagram of the phase, magnetizing and diode currents for “soft” and “hard” DCM operation, respectively. Using circuit analysis techniques on the equivalent circuits presented in Fig. 2.17 the following five equations, (2.43) – (2.47), are determined corresponding to I_{max} , I_a , I_{min} and I_b :

- 41 -

$$I_{min} = I_a - \frac{1}{2} D_2 T \left(\frac{-(2V_{in} - V_{out})}{L_{lk}} - \frac{V_{out}}{2L_m + L_{lk}} \right) \quad (2.44)$$

$$I_b = I_{min} + \frac{V_{in}}{L_m + L_{lk}} D_3 T \quad (2.45)$$

$$I_{max} = I_b + I_a \quad (2.46)$$

$$I_{max} = \frac{1}{2} D_2 T \left(\frac{-(2V_{in} - V_{out})}{L_{lk}} + \frac{V_{out}}{2L_m + L_{lk}} \right) \quad (2.47)$$

Similar to the previous analysis, assuming that the leakage inductance, L_{lk} , magnetizing inductance, L_m , input voltage, V_{in} , output voltage, V_{out} and time period, T , are known, and then there are seven unknowns in the above equation set.

The seven unknown variables are as follows: I_{max} , I_a , I_{min} , I_b , D_1 , D_2 and D_3 . Therefore, two more equations are needed in order to determine a solution. The total diode current is equal to the shaded area presented in Fig. 2.19. The integral of the diode current over the switching period is equal to half of the output dc current as presented in (2.48). This integral can be represented in (2.51) which is equal to A_1 which are presented in (2.49):

$$\frac{1}{T} \int_0^{0.5T} I_{D1}(t) dt = \frac{V_{out}}{2R_{out}} \quad (2.48)$$

$$A_1 = \frac{1}{2} (I_{max}) D_2 T \quad (2.49)$$

$$\frac{1}{T} (A_1) = \frac{V_{out}}{2R_{out}} \quad (2.50)$$

$$(I_{max}) D_2 = \frac{V_{out}}{2R_{out}} \quad (2.51)$$

The final equation needed is presented in (2.52):

$$D_1 + D_2 + D_3 = \frac{1}{2} \quad (2.52)$$

The above equations are solved in the mathematical software tool Mathematica. As the converter enters into DCM the output voltage increases for a given duty cycle, D_1 , and the equivalent load resistance, R_{out} . The above equations are solved in order to determine the required duty cycle, D_1 , to produce the required output voltage on the dc bus.

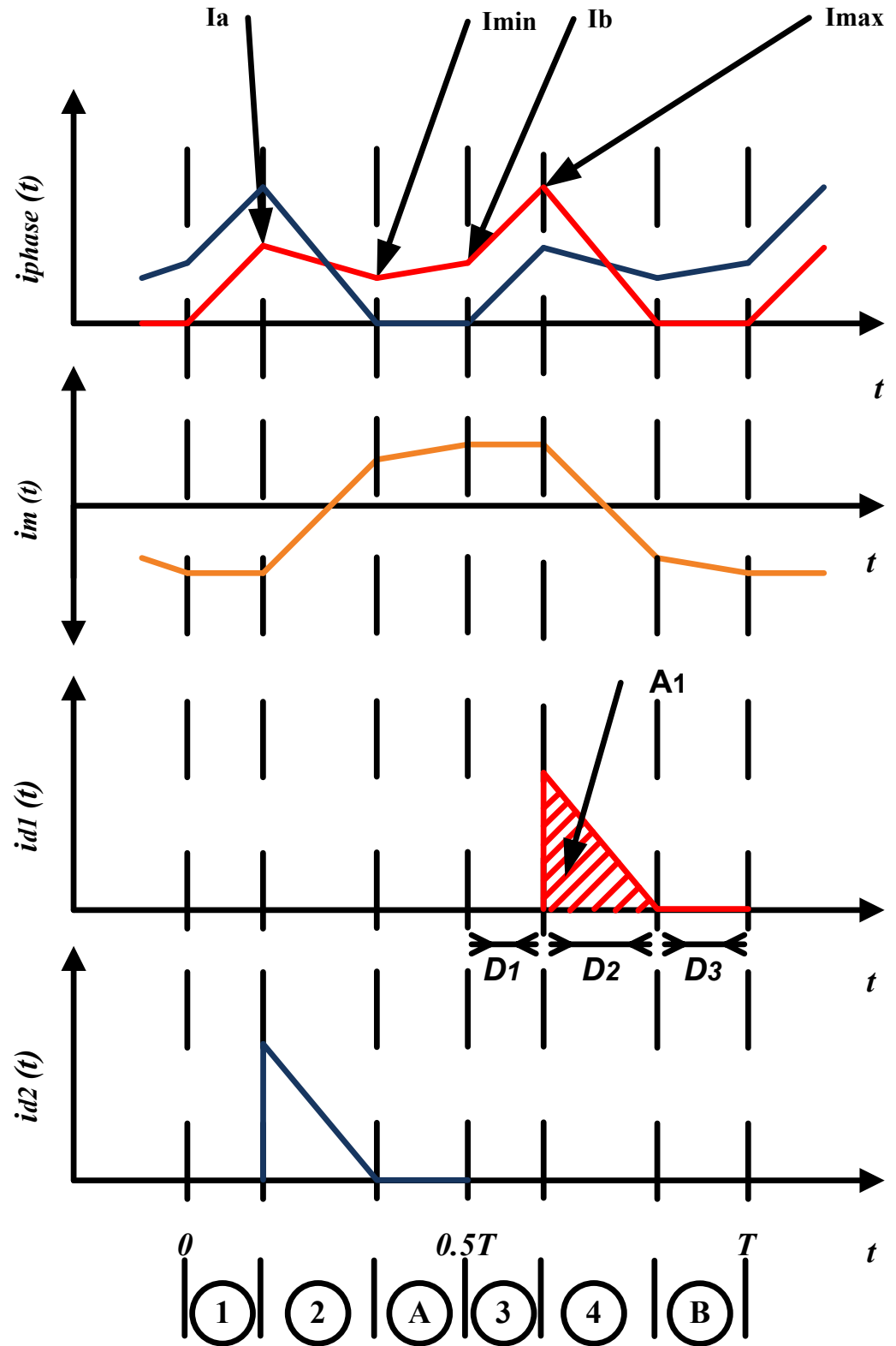


Figure 2.18. IM circuit switching waveforms in “soft” DCM for duty cycles, $D > 0.5$

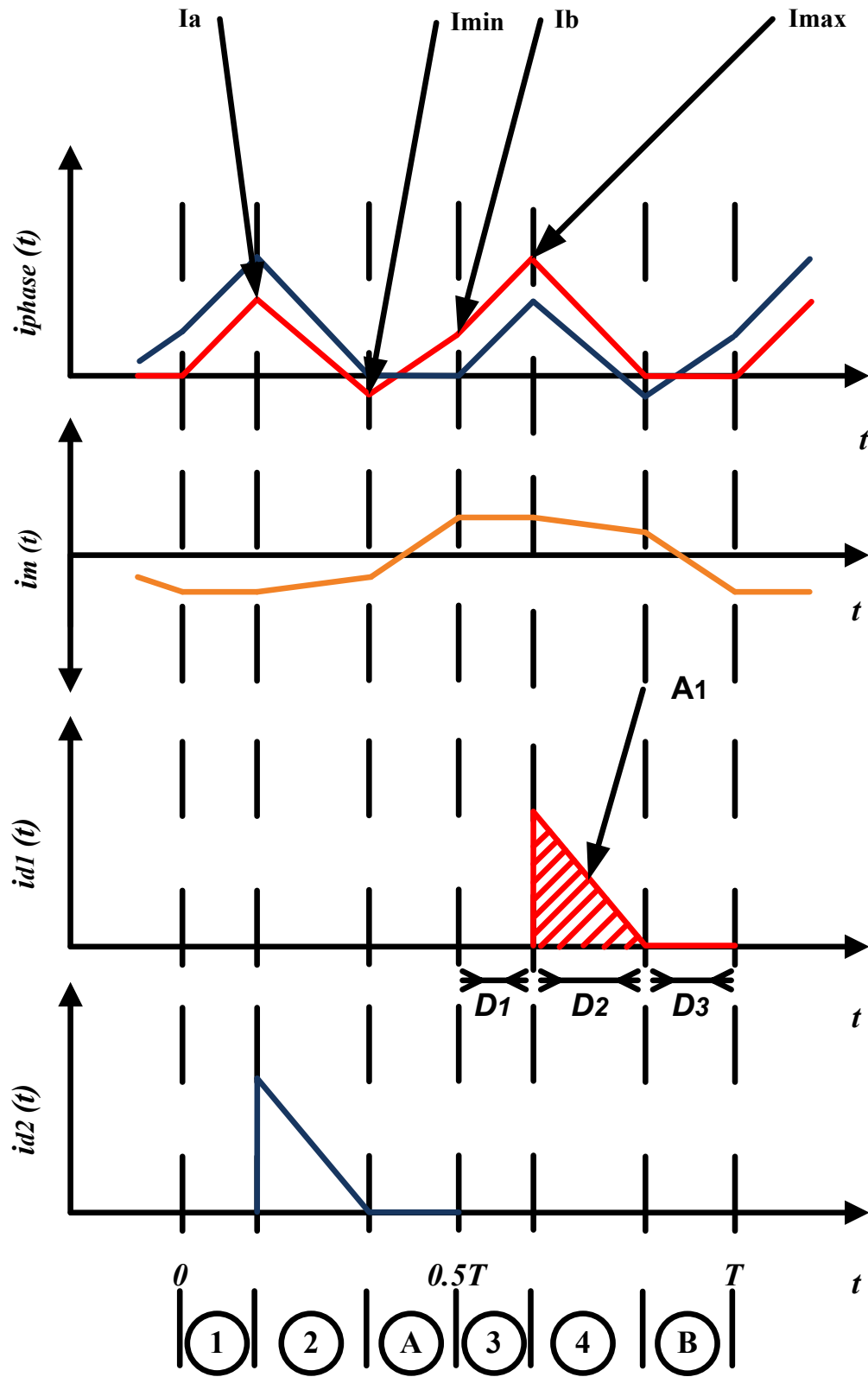


Figure 2.19. IM circuit switching waveforms in “hard” DCM for duty cycles, $D > 0.5$

Table 2.2 Input, Magnetizing and Phase Current Ripple Equations for IM Boost Converter in “Soft” CCM

Duty Ratio	$\Delta I_{in(p-p)}$	$\Delta I_{m(p-p)}$	$\Delta I_{phase(p-p)}$
$D < 0.5$	$\frac{(2V_{in} - V_{out})D_1T}{L_{lk}}$	$\frac{V_{out}D_1T}{2L_m + L_{lk}} - \frac{(V_{in} - V_{out})D_3T}{L_m + L_{lk}}$	$\frac{D_1T}{2} \left(\frac{2V_{in} - V_{out}}{L_{lk}} + \frac{V_{out}}{2L_m + L_{lk}} \right)$
$D > 0.5$	$\frac{(V_{out} - 2V_{in})D_2T}{L_{lk}}$	$\frac{V_{out}D_2T}{2L_m + L_{lk}} - \frac{V_{in}D_3T}{L_m + L_{lk}}$	$\frac{D_2T}{2} \left(\frac{V_{out} - 2V_{in}}{L_{lk}} + \frac{V_{out}}{2L_m + L_{lk}} \right)$

Table 2.3 Input, Magnetizing and Phase Current Ripple Equations for IM Boost Converter in “Hard” DCM

Duty Ratio	$\Delta I_{in(p-p)}$	$\Delta I_{m(p-p)}$	$\Delta I_{phase(p-p)}$
$D < 0.5$	$\frac{(2V_{in} - V_{out})D_1T}{L_{lk}}$	$-\frac{(V_{in} - V_{out})D_3T}{L_m + L_{lk}}$	$\frac{D_1T}{2} \left(\frac{2V_{in} - V_{out}}{L_{lk}} + \frac{V_{out}}{2L_m + L_{lk}} \right)$
$D > 0.5$	$\frac{(V_{out} - 2V_{in})D_2T}{L_{lk}}$	$\frac{V_{out}D_2T}{2L_m + L_{lk}} - \frac{V_{in}D_3T}{L_m + L_{lk}}$	$\frac{D_2T}{2} \left(\frac{V_{out} - 2V_{in}}{L_{lk}} + \frac{V_{out}}{2L_m + L_{lk}} \right)$

2.3. Validation of CCM and DCM Circuit Equations

The CCM and DCM circuit equations are validated for an automotive fuelcell application. The project is described in detail in Chapter 4 and it concerns the design and development of an IM structure for high-power automotive fuel cell applications. The IM converter structure is analysed over the typical operating range of the fuel cell in order to gain a complete picture of all of the loss components in the system. The CCTT IM topology is analysed for the following input data: $V_{in} = 155 - 260$ V, $V_{out} = 420$ V, $P_{in} = 2.6 - 72$ kW and $f_s = 25$ kHz.

The variation of input and phase current ripple as the duty cycle is varied is presented in Fig. 2.20. This diagram presents the approximate boundaries between CCM, “soft” DCM and “hard” DCM operation. The converter enters into “soft” DCM operation when the phase current ripple in one phase goes to zero over one switching period. In this design example the converter enters into “soft” DCM at a duty ratio of approximately 0.4. The converter enters into “hard” DCM when both phase currents go to zero over one switching period. This occurs in this design example at a duty cycle of approximately 0.2.

Table 2.4 presents the predicted and simulated results for CCM operation while Table 2.5 and Table 2.6 present the predicted and simulated results for DCM operation. The predicted and simulated results correlate excellently which indicates that the equations developed in the

previous sections accurately predict the operation of the circuit.

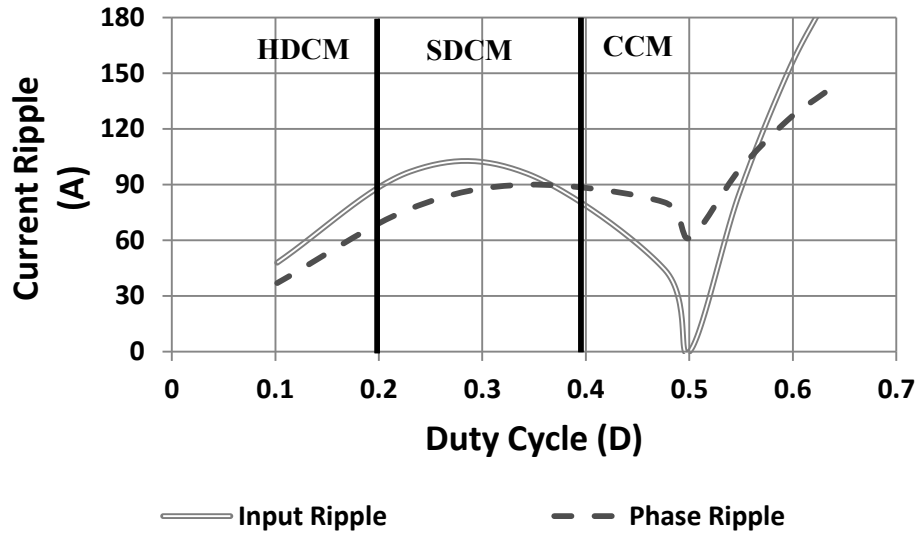


Figure 2.20. Illustration of CCM/DCM boundaries in an automotive fuelcell boost converter

2.4. IM Filter and Switch Currents

While the input, magnetizing and phase current ripple equations are required in order to design and optimize the IM circuit, various other currents are also required. The input capacitor rms current, $i_{c,in(rms)}$, phase rms current, $I_{phase(rms)}$, are used to accurately size and design the input filter capacitor and magnetic components. The switch rms, $I_{Q(rms)}$, switch average, $I_{Q(avg)}$, diode rms, $I_{D(rms)}$, and diode average, $I_{D(avg)}$, currents are used to determine the losses in the semiconductor devices. Finally, the maximum, $I_{L(max)}$, and minimum, $I_{L(min)}$, phase current values are used to characterize the semiconductor switching losses.

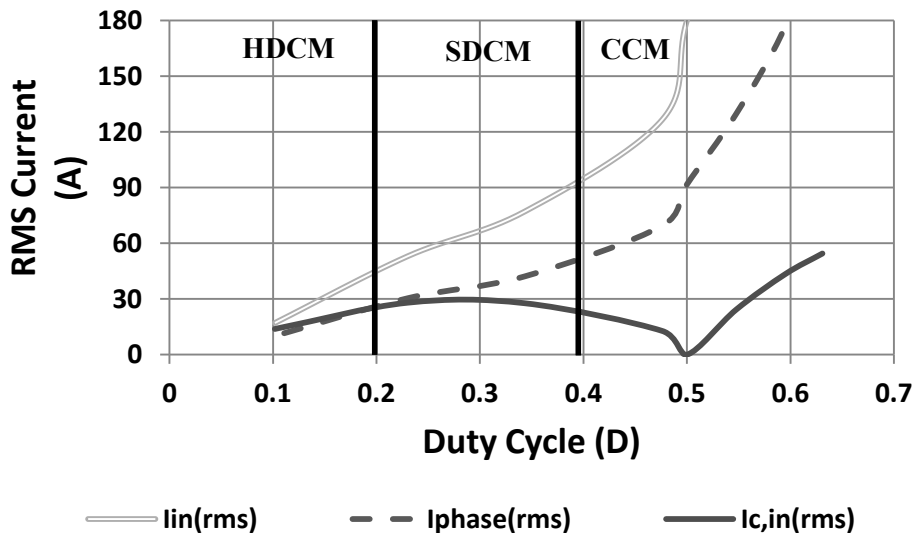


Figure 2.21. Input current, input capacitor current and phase rms currents with variation of duty cycle

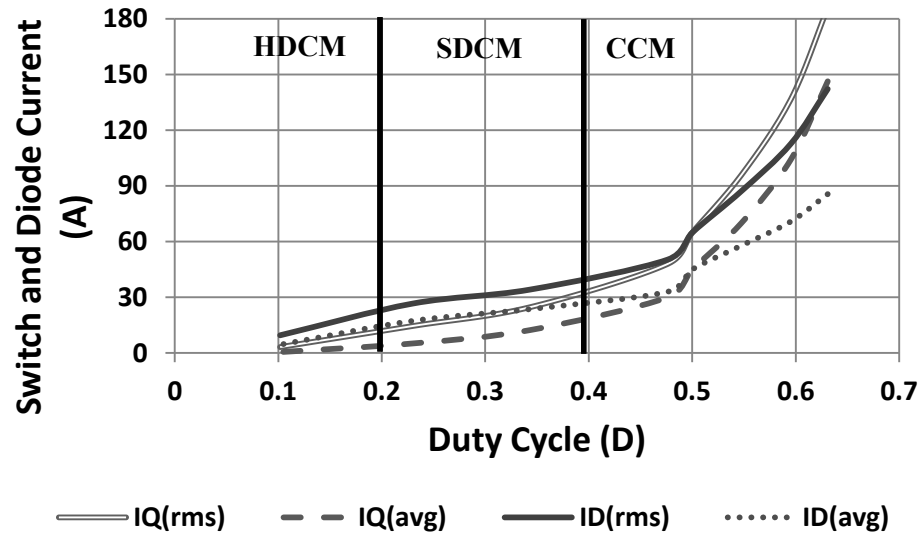


Figure 2.22. Switch and diode rms and average currents with variation in duty cycle

Fig. 2.21 presents the input rms, capacitor rms and phase rms currents. Fig. 2.22 presents the rms and average currents in the semiconductor devices. Finally, Fig. 2.23 presents the maximum and minimum phase currents in the IM converter.

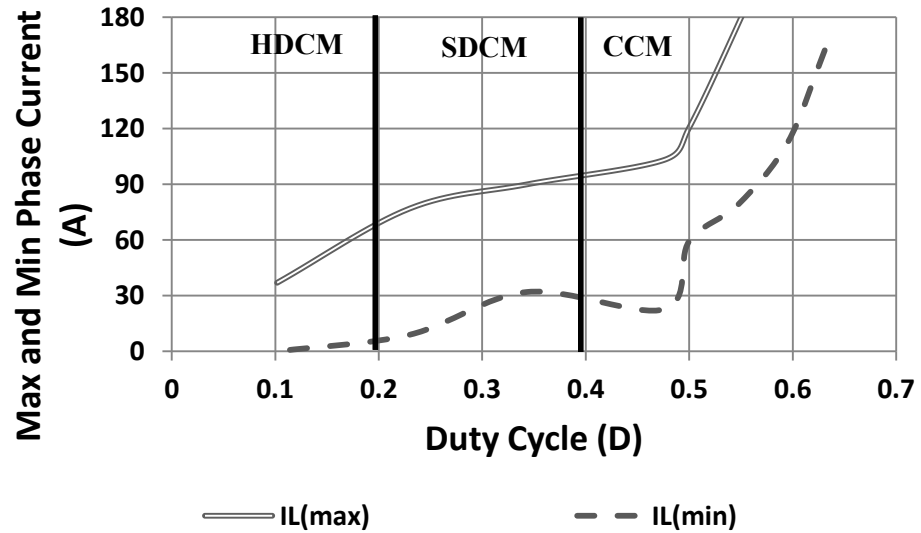


Figure 2.23. Illustration of maximum and minimum phase currents

2.5. Conclusions

This chapter presents the background circuit analysis for an integrated magnetic component operating in an interleaved dc-dc boost converter. The analysis is undertaken for both CCM and DCM areas of operation. The converter is seen to operate in two modes of DCM.

The first mode is called “soft” DCM and this is when one of the phase currents goes to zero over one switching period. The second mode is called “hard” DCM and this is when both phase currents go to zero, and consequently, the magnetizing current also does to zero.

Input, magnetizing and phase current ripple equations are presented for all modes of operation and they are validated for a sample design project. Additional, filter and switch currents are presented which allow for the accurate design of the input filter capacitor, magnetic and semiconductor devices. All of the equations presented allow for the characterization and design of the interleaved IM topology presented in this chapter.

Table 2.4 Validation of CCM Circuit Equations for IM Boost Converter

Circuit Parameters									Predicted			Simulated		
V_{in}	V_{out}	P_{in}	R_o	I_{phase}	D	L_{lk}	L_m	Mode	$\Delta I_{in(p-p)}$	$\Delta I_{m(p-p)}$	$\Delta I_{phase(p-p)}$	$\Delta I_{in(p-p)}$	$\Delta I_{m(p-p)}$	$\Delta I_{phase(p-p)}$
V	V	kW	Ω	A	-	μH	μH		A	A	A	A	A	A
155	420	72	2.5	232	0.63	8.6	30	CCM	188	90	140	185	89	137
170	420	59.5	3	175	0.59	8.6	30	CCM	150	99	124	149	98	123
190	420	48.6	3.6	128	0.54	8.6	30	CCM	84	110	97	83	110	97
210	420	37.8	4.6	90	0.5	8.6	30	CCM	0	122	61	0	122	61
220	420	27.7	6.4	62	0.47	8.6	30	CCM	44	116	80	44	116	80

Table 2.5 Validation of DCM Equations for IM Boost Converter

Circuit Parameters									Predicted				Simulated			
V_{in}	V_{out}	P_{in}	R_o	I_{phase}	D	L_{lk}	L_m	Mode	I_a	I_{min}	ΔI_b	ΔI_{max}	I_a	I_{min}	ΔI_b	ΔI_{max}
V	V	kW	Ω	A	-	μH	μH	-				A				A
240	420	17.2	10.2	36	0.34	8.6	30	SDCM	53	32	37	90	52	31	38	90
255	220	11.4	15.3	22.5	0.22	8.6	30	SDCM	48	9	29	77	47	7	30	76
260	420	2.6	67.9	5	0.1	8.6	30	HDCM	26	0	12	37	24	0	12	37

Table 2.6 Validation of DCM Equations for IM Boost Converter

Circuit Parameters									Predicted			Simulated		
V_{in}	V_{out}	P_{in}	R_o	I_{phase}	D	L_{lk}	L_m	Mode	$\Delta I_{in(p-p)}$	$\Delta I_{m(p-p)}$	$\Delta I_{phase(p-p)}$	$\Delta I_{in(p-p)}$	$\Delta I_{m(p-p)}$	$\Delta I_{phase(p-p)}$
V	V	kW	Ω	A	-	μH	μH	-	A	A	A	A	A	A
240	420	17.2	10.2	36	0.34	8.6	30	SDCM	96	105	90	96	104	90
255	420	11.4	15.3	22.5	0.22	8.6	30	SDCM	97	96	77	98	94	76
260	420	2.6	67.9	5	0.1	8.6	30	HDCM	48	25	37	49	24	37

Chapter 3

CCTT-Core Split-Winding Integrated Magnetic

In this chapter a novel CCTT-core split-winding integrated magnetic (CCTT IM) is presented. The CCTT IM concept is briefly compared with some existing IM technologies, namely the EE-core integrated magnetic (EE IM). The analysis indicates that there is significant fringing flux from the IM components that are investigated and this leads to the development of a reluctance model that attempts to quantify this relatively large fringing flux. The reluctance model uses equations presented in [105] to accurately predict the most probable fringing regions around large airgaps.

A CCTT IM design algorithm is implemented in the mathematical software tool, Mathematica. This algorithm deals with spiral- and stranded-winding integrated-magnetic coupled inductors for use in high-power applications, in the low-to-medium frequency range. The algorithm considers many factors including: winding material, core material, and thermal cooling method. The reluctance model forms the backbone of the design algorithm and allows the algorithm to estimate the dc and ac inductance of the CCTT IM. The total boxed volume of the CCTT IM is minimized in the design algorithm for high-power liquid-cooled and medium-power air-cooled applications. The design algorithm is used to develop design curves that investigate the variation of CCTT IM boxed volume with the variation of input current ripple, for different magnetic materials and frequencies. The magnetic materials in question are ferrite 3C92 from Ferroxcube [79], iron-based amorphous metal 2605SA1 from Metglas [81], and silicon steel 10JNHF600 from JFE [80].

The design algorithm is extended to the EE IM and is used to compare the CCTT IM concept with that of the EE IM. The algorithm is also used to investigate the variation of magnetic boxed volume with magnetizing inductance.

3.1. Introduction

High-power density magnetic components are required for military, industrial, aerospace and automotive applications. Compact and efficient design of magnetic devices is needed to reduce the weight and volume of dc-dc converters. The magnetic components in the conventional single-phase boost converter can be quite bulky and costly [25, 39]. Therefore, innovative methods to reduce magnetic component size, loss, and in turn, cost are major driving forces in the design of dc-dc converters. The use of interleaved dc-dc converters containing discrete, coupled or integrated magnetic components are ways in which these goals can be achieved. These types of interleaved converters are briefly discussed in Chapter 1 where their main benefits and drawbacks are discussed.

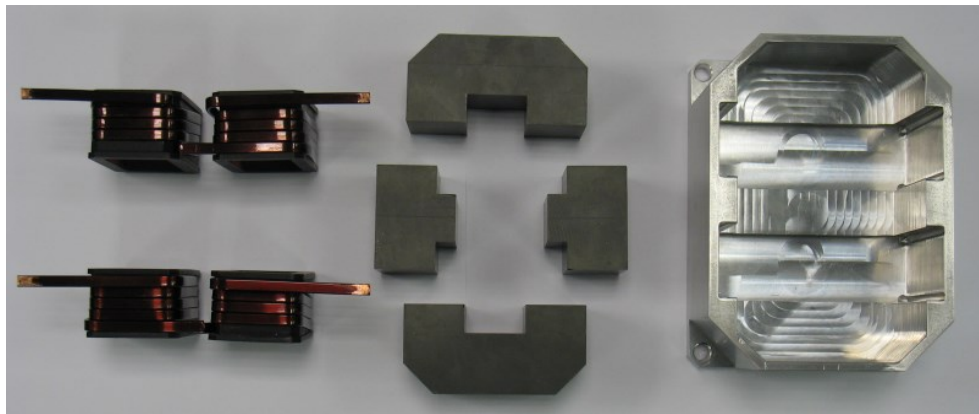


Figure 3.1. Disassembled 72 kW CCTT IM prototype

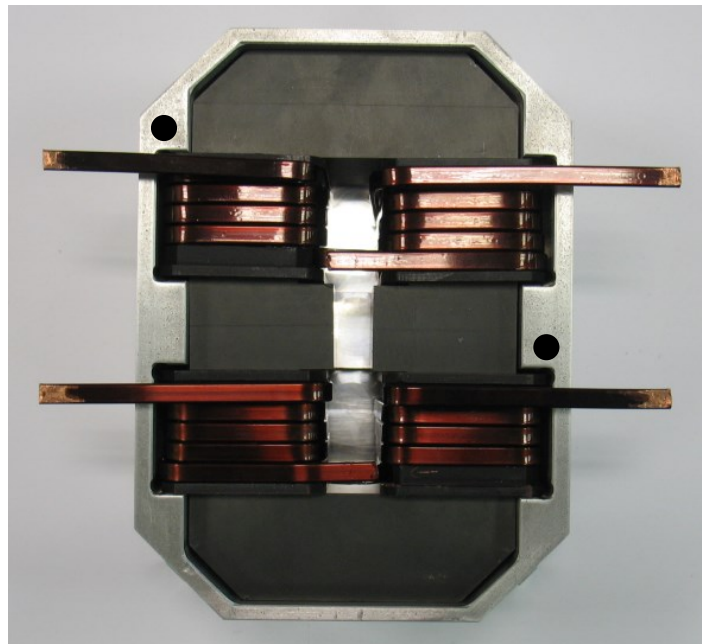


Figure 3.2. Assembled 72 kW prototype

The IM concept involves the integration of all magnetic components onto one single core. Various IM designs investigated in [43, 106] resulted in unconventional core geometries which may be difficult to manufacture and mass produce. The authors in [38, 50, 51, 107] investigated a loosely-coupled IM (EE IM) using an EE core set and compared it to the XL, but deemed it was inferior due to its large inherent dc inductance which increases the core size and volume. This thesis presents a novel IM structure [74, 108, 109] which can be seen pictured in Fig. 3.1 and Fig. 3.2. Fig. 3.1 presents the separate prototype components – the core, windings and external shield. Fig. 3.2 presents the final prototype core which is ready for potting. The dimensions of the four magnetizing airgaps are controlled using Nomex material.

The core can easily be fabricated from two C and two T sections, hence the name. The CCTT IM has minimal inter-winding capacitance due to the low number of turns. Low power loss ferrite is utilized for its construction which results in excellent efficiency when combined with low turns. The CCTT IM is optimized to allow for optimum heat extraction from the windings which are constructed from single-layer solid wire. The phase windings are split in half, distributed evenly, and placed close to the other phase in order to reduce external leakage flux.

In these structures, a shield is typically used to control the ac field. This shield significantly reduces the ac inductance while the dc inductance remains unaffected. The dc inductance is the inductance of the unshielded structure and determines the dc bias of the core. The ac inductance is the inductance of the shielded structure and is the effective inductance to be considered for ac operation, e.g. ripple current. The CCTT IM's ability to contain the ac flux within the core window allows for a more controlled ac inductance when a shield is introduced, over more traditional IM designs. The work in [110] compares the CCTT and EE IM concepts over the same input current ripple conditions and shows that the CCTT IM gives a size reduction over a wide input ripple range.

3.2. IM Concepts

3.2.1. EE IM Approach

The conventional approach, termed here as EE IM, uses an EE core set along with bank-wound differentially-connected windings and is presented in Fig. 3.3. This is a conventional IM approach with simple core and winding constructions. The main problem with this IM design is that the core size has to increase to accommodate the large external dc flux which has the effect of increasing the dc-bias in the side legs. This additional external dc flux has an equivalent external ac flux which is difficult to control and requires shielding. There is a significant reduction in the ac inductance when this shield is introduced. Fig. 3.4 presents a 3D simulation

of an EE IM design and significant flux fringing from the face of the IM can be clearly seen. As copper losses due to airgap fringing is also a problem but can be reduced by moving the windings away from the airgap by (i) extending the window or (ii) splitting the windings.

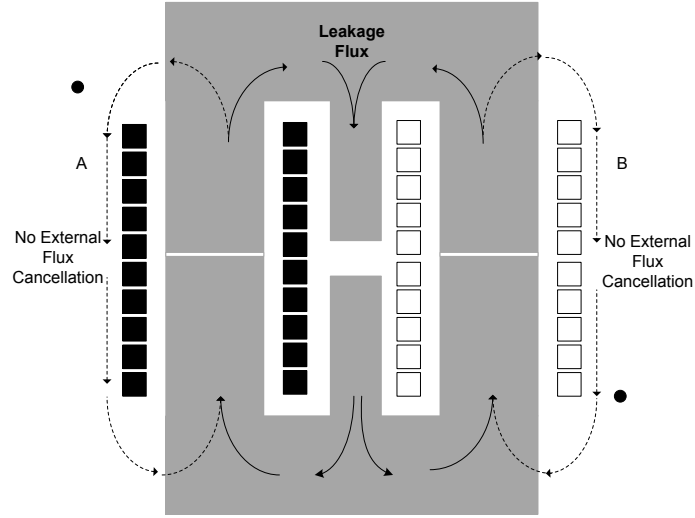


Figure 3.3. EE IM realization

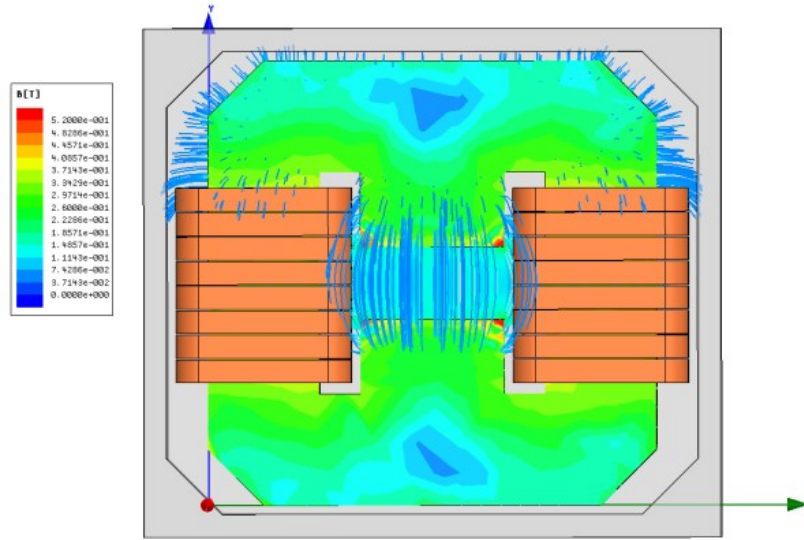


Figure 3.4. 3D flux plot illustrating EE IM fringing flux

3.2.2. CCTT IM Approach

The CCTT IM has a split-winding design which allows for external dc flux cancellation and this helps minimize the external dc inductance, as is shown in Fig. 3.5. Placing the two phase windings physically closer to each other, results in increased cancellation of the external ac fields. Similar to the EE IM it uses ferrite poles in the window to shape the leakage flux and contain it within the CCTT IM core window. An additional advantage of these poles is that they help to reduce ac winding power loss associated with the ac flux by shielding the windings. In

order to do this, the poles have to be extended beyond the winding as shown in Fig. 3.5. Fig. 3.6 presents a 3D simulation of a CCTT IM design. The fringing flux is now concentrated around the pole region of the IM and there is reduced fringing from the core face directly above and below the windings. There is also reduced fringing from the windings.

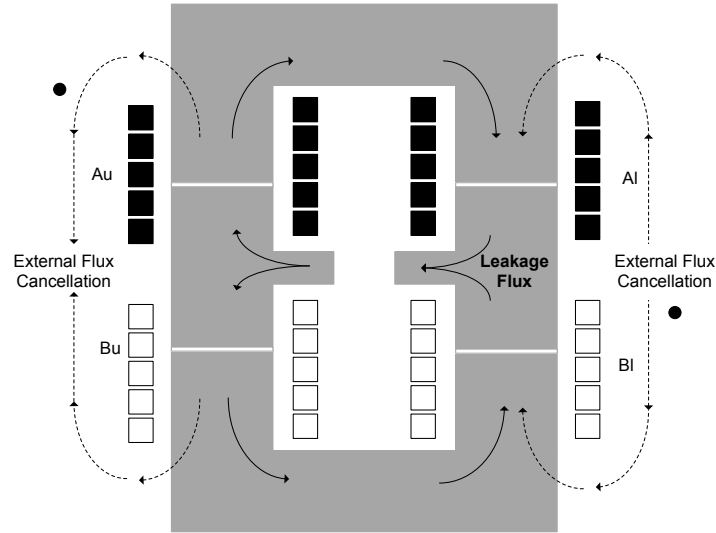


Figure 3.5. CCTT IM realization

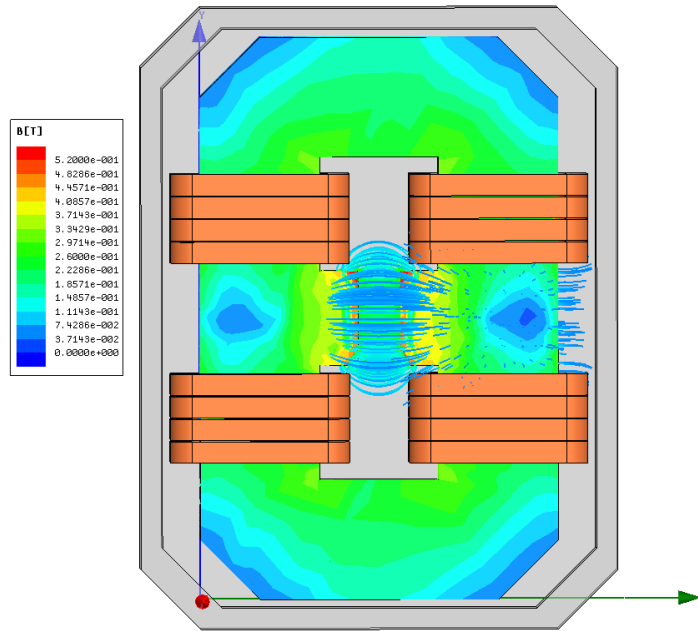


Figure 3.6. 3D flux plot illustrating CCTT IM fringing flux

3.2.3. Pot Core IM Approach

The pot core IM, presented in Fig. 3.7, has similar aspects to both of the IM designs previously discussed. It uses bank-wound differentially-connected windings on the centre leg.

The centre leg contains ferrite poles in order to shape the leakage flux. Similar to the CCTT IM, these poles are extended beyond the windings in order to shield the windings from the significant ac fringing flux. Fig. 3.8 highlights the significant fringing flux from the pole region of the pot core IM and in reality this IM option behaves in a similar manner to the EE IM described previously.

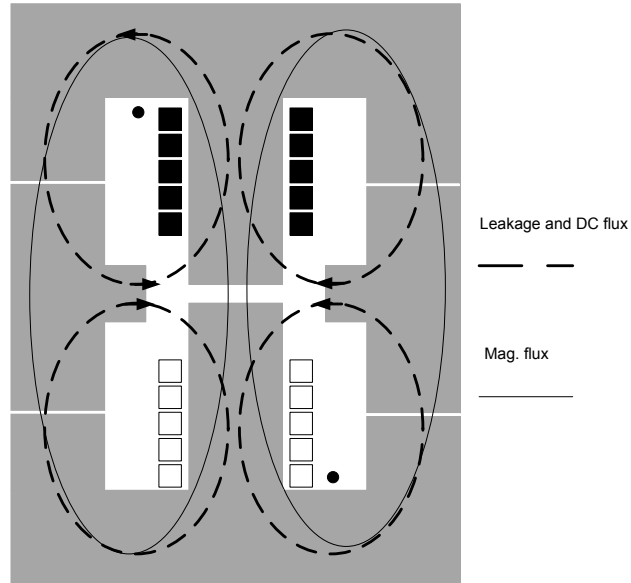


Figure 3.7. Pot core IM realization

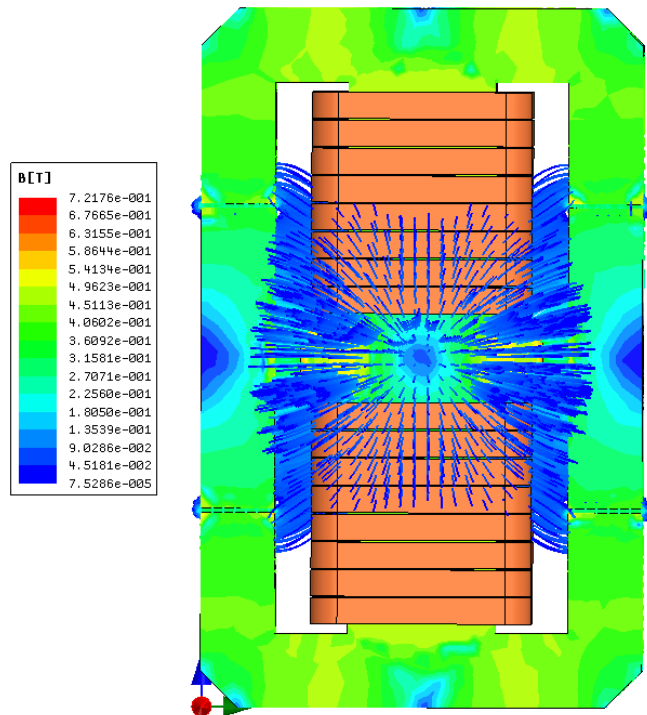


Figure 3.8. 3D flux plot illustrating pot core IM fringing flux

3.2.4. Dc and Ac Inductance

Typically, in high-power automotive applications, the magnetic component is surrounded by an aluminum case. The top section of the aluminum case is open and is filled or potted with epoxy. This helps to protect the magnetic component as well as allowing for a reduction in the audible noise. The aluminum casing has the effect of shielding the magnetic component and reducing the radiated fields. The introduction of a shield results in a reduction of the leakage inductance of both IM designs but critically, this effect is more pronounced in the EE IM option. Fig. 3.9 and Fig. 3.10 show dc and ac 3D FEA flux plots for the EE IM respectively. This is a side view of the EE IM structure. Fig. 3.9 illustrates that the shield has no effect on the dc fringing flux. Fig. 3.10 shows that the ac fringing flux at the bottom of the core, close to the aluminum shield, is reduced, while the ac flux at the open top is unaffected.

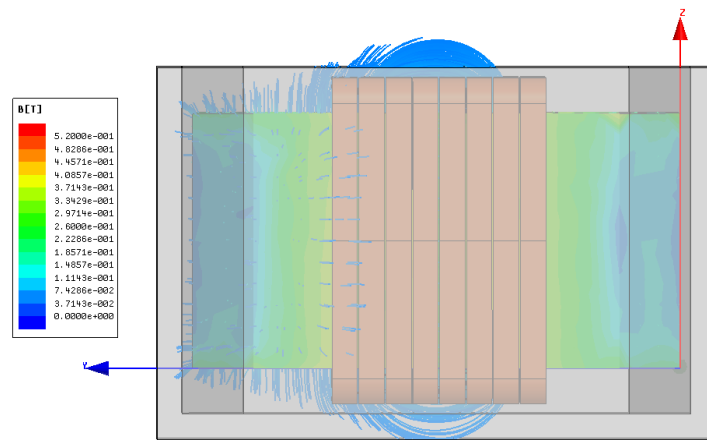


Figure 3.9. 3D flux plot illustrating the dc EE IM fringing flux

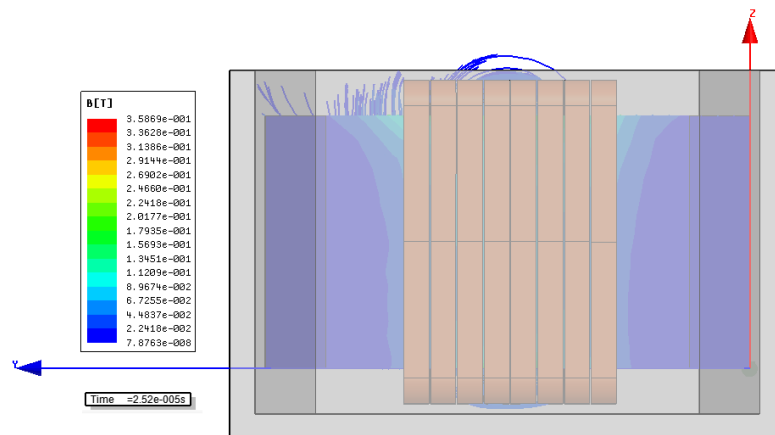


Figure 3.10. 3D flux plot illustrating the ac EE IM fringing flux

3.3. CCTT IM Fringing Regions and Reluctance Model

3.3.1. CCTT IM Fringing Regions

The calculation and estimation of fringing flux is important for the efficient design of magnetic components. Fringing estimation becomes critical when designing IM structures that contain large air gaps – especially when these magnetic devices need to be optimized to produce a controlled leakage inductance. This section uses the equations developed in [105], and additionally discussed in [111-115], to estimate the reluctance of probable flux paths around the CCTT IM pole and windings. This then allows for the development of a dc and ac reluctance model similar to that presented in [115]. Firstly, a simple reluctance model is presented that ignores the effect of fringing flux. This model is very inaccurate and sets the basis to why a more accurate model is required in order to develop an accurate CCTT IM design.

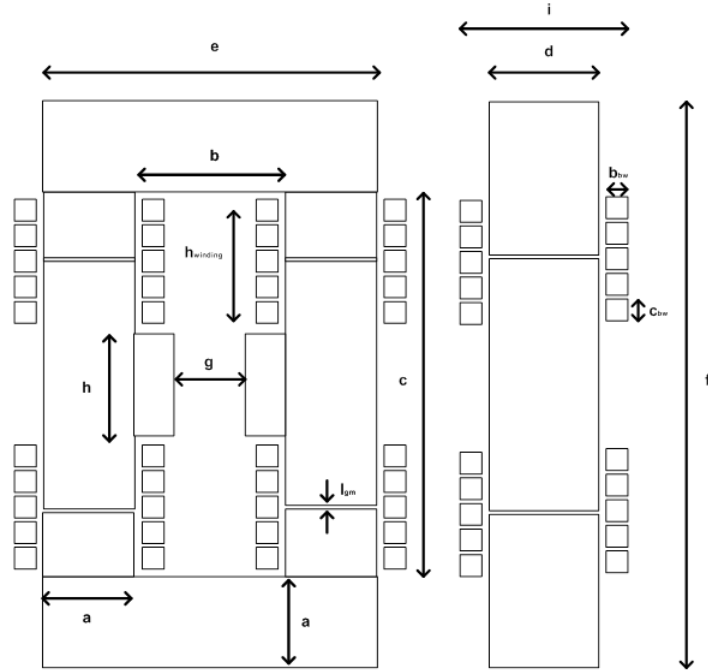


Figure 3.11. CCTT IM core dimensions

3.3.2. Simple CCTT IM Reluctance Model

A diagram illustrating the CCTT IM core geometries is presented in Fig. 3.11. A simplified reluctance model which neglects the pole and winding fringing regions is presented in Fig. 3.12. All of the reluctances in the model presented can be expressed in terms of core geometries, which are defined in Fig. 3.11. The reluctance model is used to determine the self, leakage and mutual inductance of the IM as outlined in (3.1), (3.2) and (3.3) respectively.

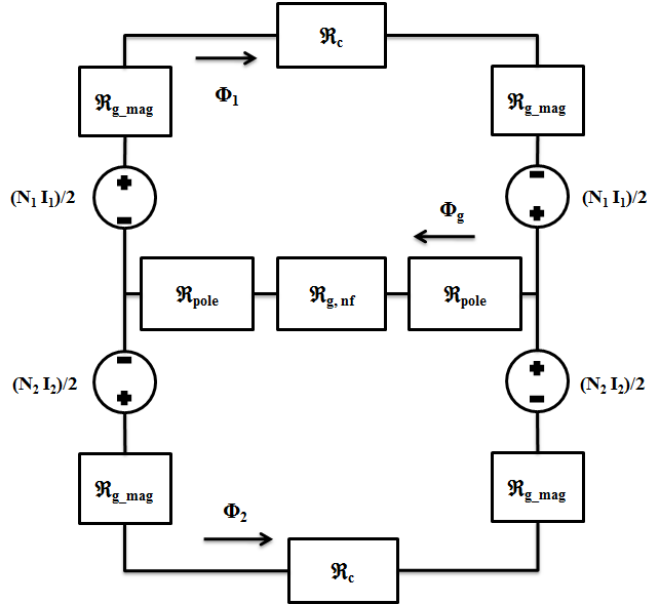


Figure 3.12. Simple reluctance model neglecting the fringing regions

$$L_{self,simple} = \frac{N^2}{(\mathfrak{R}_{core} + \mathfrak{R}_{core} \parallel \mathfrak{R}_g)} \quad (3.1)$$

$$L_{lk,simple} = \frac{N^2}{(\mathfrak{R}_{core} + 2\mathfrak{R}_g)} \quad (3.2)$$

$$L_{m,simple} = \frac{N^2 \mathfrak{R}_g}{\mathfrak{R}_{core} (\mathfrak{R}_{core} + 2\mathfrak{R}_g)} \quad (3.3)$$

where N is the number of turns per phase, \mathfrak{R}_{core} is the total reluctance of the core along the leakage path and \mathfrak{R}_g is the reluctance of the pole leakage path.

The total core and leakage gap are determined using (3.4) and (3.5) respectively.

$$\mathfrak{R}_{core} = \mathfrak{R}_c + 2\mathfrak{R}_{g,mag} \quad (3.4)$$

$$\mathfrak{R}_g = 2\mathfrak{R}_{pole} + \mathfrak{R}_{g,nf} \quad (3.5)$$

where \mathfrak{R}_c is the reluctance of the core, $\mathfrak{R}_{g,mag}$ is the magnetizing gap reluctance, \mathfrak{R}_{pole} is the reluctance of the pole sections and $\mathfrak{R}_{g,nf}$ is the total reluctance of the leakage airgap assuming zero fringing, \mathfrak{R}_g is the total reluctance of the leakage airgap and pole sections.

The results of the simple reluctance model are presented in Section 3.3.5 and they indicate that the simple model under-predicts the value of leakage inductance by approximately 50 %.

3.3.3. CCTT IM Dc Fringing Regions and Reluctance Model

3.3.3.1. CCTT IM Dc Fringing Regions

It is useful to visualize all of the various fringing regions, shown in Fig. 3.13, around the pole and winding and this section briefly discusses each of these regions. The pole-face region which corresponds to the face reluctance can be subdivided into four distinct regions, which are all in parallel, as illustrated in Fig. 3.14. The purple cylinders account for the front and back face fringing, while the green cylinders account for the top and bottom face fringing. Like the pole face regions, the corner regions, which correspond to the corner reluctance, can also be subdivided into four distinct regions, which are all in parallel with each other.

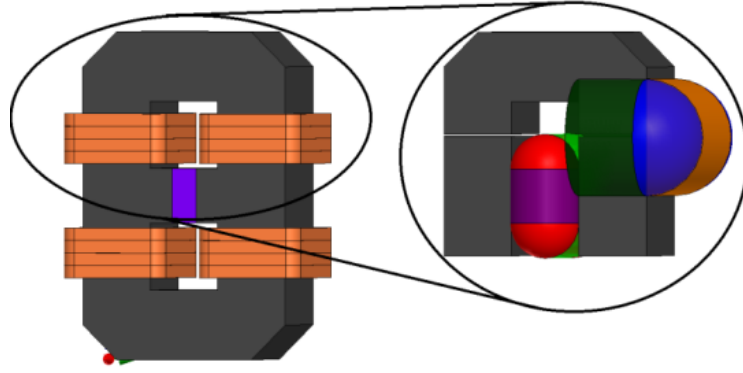


Figure 3.13. Fringing regions around pole and winding sections of the CCTT IM

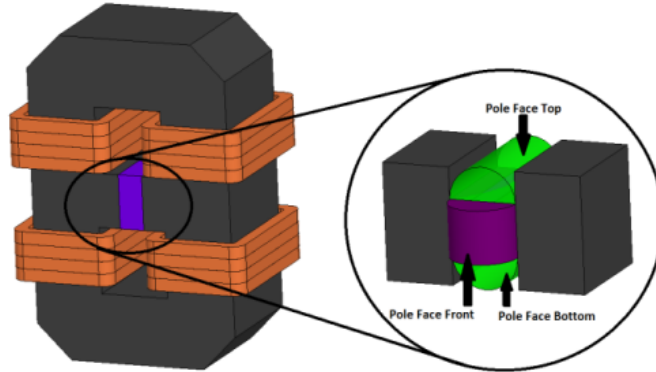


Figure 3.14. Pole face fringing regions of the CCTT IM

The corner regions are illustrated in Fig. 3.15. Finally, the winding fringing regions for one of the split-windings are presented in Fig. 3.16. The dark green and orange regions correspond to the winding fringing of the front, back and side faces, respectively, while the blue regions account for the winding corner fringing. As in previous cases, all these regions are evaluated in parallel with each other to determine an equivalent winding reluctance.

The regions presented in Fig. 3.14 - Fig. 3.16 should be considered to be the fringing regions for the unshielded CCTT IM structure and allow for the estimation of the dc leakage inductance of the CCTT IM. These regions are then modified, to account for the shield, in order to estimate the ac leakage inductance.

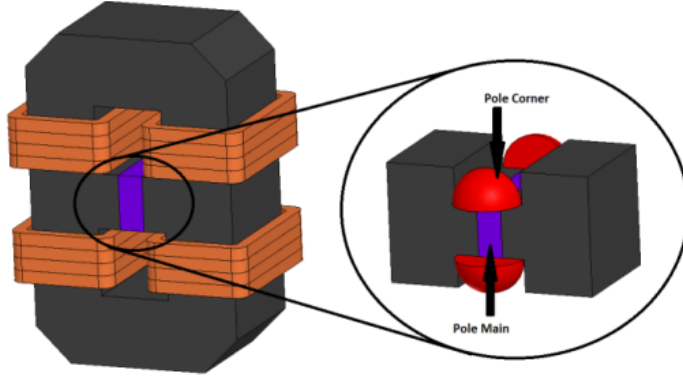


Figure 3.15. Pole corner fringing regions of the CCTT IM

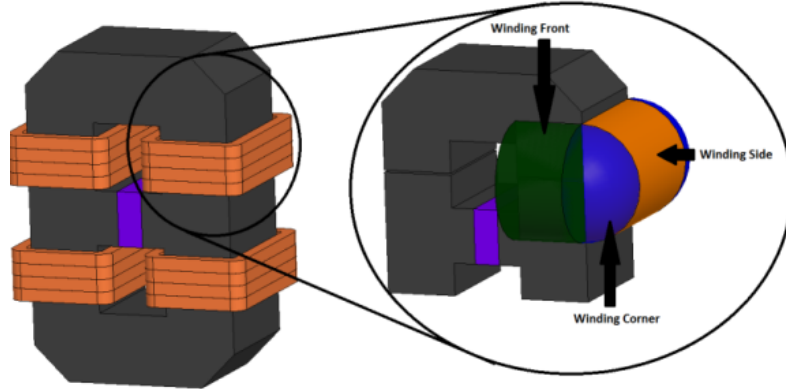


Figure 3.16. Winding fringing regions of the CCTT IM

3.3.3.2. CCTT IM Dc Reluctance Model

A complete reluctance model is presented in Fig. 3.17. This complete model includes the magnetizing path airgaps, the fringing paths from the center leg as well as the fringing paths from each of the split-windings. All of the reluctances in the models presented can be expressed in terms of core geometries, which are defined in Fig. 3.11. The reluctance model is used to determine the self, leakage and mutual inductance of the IM as outlined in (3.6), (3.7) and (3.8) respectively.

$$L_{self,dc} = \frac{N^2}{(\mathfrak{R}_{core} + \mathfrak{R}_{core} \parallel \mathfrak{R}_g)} + \frac{N^2}{\mathfrak{R}_{windingdc}} \quad (3.6)$$

$$L_{lk,dc} = \frac{N^2}{(\mathfrak{R}_{core} + 2\mathfrak{R}_g)} + \frac{N^2}{\mathfrak{R}_{windingdc}} \quad (3.7)$$

$$L_{m,dc} = \frac{N^2 \mathfrak{R}_g}{\mathfrak{R}_{core} (\mathfrak{R}_{core} + 2\mathfrak{R}_g)} \quad (3.8)$$

where N is the number of turns per phase, \mathfrak{R}_{core} is the total reluctance of the core along the leakage path, $\mathfrak{R}_{g,dc}$ is the reluctance of the pole including fringing, and $\mathfrak{R}_{winding,dc}$ is the reluctance of the split-winding sections.

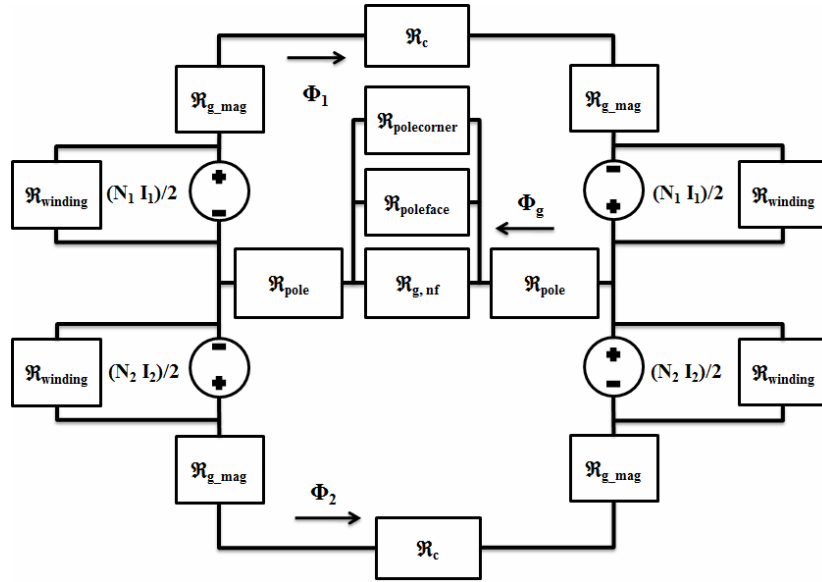


Figure 3.17. Complete CCTT IM reluctance model with fringing regions

The total core, leakage gap and winding reluctance are determined using (3.9), (3.10) and (3.11) respectively.

$$\mathfrak{R}_{core} = \mathfrak{R}_c + 2\mathfrak{R}_{g,mag} \quad (3.9)$$

$$\mathfrak{R}_{g,dc} = 2\mathfrak{R}_{pole} + \mathfrak{R}_{g,nf} \parallel \mathfrak{R}_{poleface} \parallel \mathfrak{R}_{polecorner} \quad (3.10)$$

$$\mathfrak{R}_{windingdc} = \mathfrak{R}_{windface} \parallel \mathfrak{R}_{windcorner} \quad (3.11)$$

where \mathfrak{R}_c is the reluctance of the core, $\mathfrak{R}_{g,mag}$ is the magnetizing gap reluctance which uses

a modified version of the Roter equations to account for fringing, \mathcal{R}_{pole} is the reluctance of the pole sections and $\mathcal{R}_{g,nf}$ is the total reluctance of the leakage airgap assuming zero fringing, $\mathcal{R}_{g,dc}$ is the total reluctance of the leakage airgap assuming fringing, $\mathcal{R}_{poleface,dc}$ is the reluctance of the pole face fringing path, $\mathcal{R}_{polecorner,dc}$ is the reluctance of the pole corner fringing path, $\mathcal{R}_{winding,dc}$ is the total reluctance of the winding fringing regions, $\mathcal{R}_{windface,dc}$ is reluctance of the winding face fringing path and $\mathcal{R}_{windcorner,dc}$ is the reluctance of the winding corner fringing path.

The pole face and corner reluctances, approximated using Roter equations, are presented in (3.12) and (3.13) respectively.

$$\mathcal{R}_{poleface,dc} = \frac{1}{\mu_0 2(h+d) \left(0.26 + \frac{1}{\pi} \ln \left(1 + \frac{2(x)}{g} \right) \right)} \quad (3.12)$$

$$\mathcal{R}_{polecorner,dc} = \frac{1}{\mu_0 (0.308g + x)} \quad (3.13)$$

where $\mathcal{R}_{poleface,dc}$ is the reluctance of the purple and green cylinder regions presented in Fig. 3.14 and $\mathcal{R}_{polecorner,dc}$ is the reluctance of the red quarter-cylinder regions presented in Fig. 3.15. As shown in Fig. 3.11, h is the pole height, d is the core thickness, x is the pole length, and g is the leakage gap length. These fringing regions are in parallel with the main gap reluctance and have the effect of increasing the overall inductance while reducing the total flux passing between the poles of the main airgap.

The winding face and corner reluctances are presented in (3.14) and (3.15) respectively.

$$\mathcal{R}_{windface,dc} = \frac{1}{\mu_0 (2a+d) \left(0.26 + \frac{1}{\pi} \ln \left(1 + \frac{h}{h_{winding}} \right) \right)} \quad (3.14)$$

$$\mathcal{R}_{windcorner,dc} = \frac{1}{\mu_0 (0.154h_{winding} + 0.25h)} \quad (3.15)$$

where $\mathcal{R}_{windface,dc}$ is the reluctance of the dark green and orange cylinder regions presented in Fig. 3.16 and $\mathcal{R}_{windcorner,dc}$ is the reluctance of the blue quarter cylinder regions presented in Fig. 3.16. As shown in Fig. 3.11, a is the core thickness, and $h_{winding}$ is the height of the split-winding.

3.3.4. CCTT IM Ac Fringing Regions and Reluctance Model

3.3.4.1. CCTT IM Ac Fringing Regions

The ac fringing regions of the CCTT IM assumes that a conductive external shield is placed tightly around the core. Unlike the dc inductance the ac inductance cannot penetrate the shield. When the conductive shield is subjected to a time-varying or ac magnetic field, eddy currents are induced in the conductive material. These eddy currents flow in closed circular paths perpendicular to the inducing field. In accordance with Lenz's law, the induced eddy currents flow in such a direction in order to oppose the change in the inducing field. Thus, the magnetic fields produced by the induced eddy currents attempt to cancel the larger external inducing magnetic fields close to the surface of the conductive material, thereby generating a shielding effect. The introduction of a shield results in a reduction of the leakage inductance.

The CCTT IM with an external shield is pictured in Fig. 3.6. Referring again to Fig. 3.14, Fig. 3.15 and Fig. 3.16, the number of fringing regions is reduced with respect to the dc case. Therefore in Fig. 3.14, the pole face back region, which is symmetrical to the pole face front region highlighted in purple, is neglected. Similarly in Fig. 3.16, the winding side, winding corner and winding back regions are neglected. The equations used to describe the ac fringing regions are described in the next section.

3.3.4.2. CCTT IM Ac Reluctance Model

In order to determine the ac leakage inductance or the leakage inductance of the CCTT IM when an external aluminum shield is placed around the core, equations (3.12) to (3.15) are modified to account for the reduction in fringing due to the introduction of the shield. 3D FEA is extensively used to iterate and optimize the equations in order to accurately predict the ac leakage inductance.

For example, (3.14) which is used to predict the winding face reluctance is modified to account for the shield and is presented in (3.16).

$$\mathfrak{R}_{windfaceac} = \frac{1}{\mu_0 a \left(0.26 + \frac{1}{\pi} \ln \left(1 + \frac{h}{h_{winding}} \right) \right)} \quad (3.16)$$

where $\mathfrak{R}_{windface,ac}$ is the reluctance of the dark green region in Fig. 3.16. The orange cylinder and blue quarter cylinder regions have been removed to account for the reduction in winding fringing due to the shield. As shown in Fig. 3.11, a is the core thickness, and $h_{winding}$ is

the height of the split-winding. The pole fringing regions presented in (3.12), (3.13) and (3.15) are modified in a similar manner.

The ac leakage inductance of the CCTT IM is calculated using (3.17).

$$L_{lk,ac} = \frac{N^2}{(\mathfrak{R}_{core} + 2\mathfrak{R}_{g,ac})} + \frac{N^2}{\mathfrak{R}_{windingac}} \quad (3.17)$$

The total core, leakage gap and winding reluctance are determined using (3.18), (3.19) and (3.20) respectively.

$$\mathfrak{R}_{core} = \mathfrak{R}_c + 2\mathfrak{R}_{g,mag} \quad (3.18)$$

$$\mathfrak{R}_{g,ac} = 2\mathfrak{R}_{pole} + \mathfrak{R}_{g,nf} \parallel \mathfrak{R}_{polefaceac} \parallel \mathfrak{R}_{polecornerac} \quad (3.19)$$

$$\mathfrak{R}_{windingac} = \mathfrak{R}_{windfaceac} \quad (3.20)$$

where $\mathfrak{R}_{g,ac}$ is the total ac reluctance of the leakage airgap assuming fringing, $\mathfrak{R}_{poleface,ac}$ is the reluctance of the pole face fringing path and $\mathfrak{R}_{polecorner,ac}$ is the ac reluctance of the pole corner fringing path, respectively, when an external shield is placed around the CCTT IM structure. Likewise, $\mathfrak{R}_{winding,ac}$ is the total reluctance of the winding fringing regions and $\mathfrak{R}_{windface,ac}$ is the reluctance of the winding face path, respectively, when an external shield is placed around the CCTT IM structure.

3.3.5. Validation of Dc and Ac Reluctance Models

3D FEA is used to validate the reluctance model of the prototype core. Table 3.1 presents the results of this validation. The inductance in each region is determined using the equations presented and then is compared with the simulated 3D FEA results. The results indicate that the proposed analytically based reluctance model is extremely accurate in predicting the leakage inductance of the CCTT IM.

Further results, presented in Chapter 4 and Chapter 5, indicate that the proposed reluctance model is very accurate in predicting the dc and ac leakage inductance of the CCTT IM. Interestingly, if no fringing regions were taken into consideration, then the leakage inductance would be determined by evaluating the inductance stored in the main leakage airgap. This is calculated to be $3.99 \mu H$ or roughly half of the actual ac leakage inductance of $8.5 \mu H$. When the simple reluctance model is used to determine the leakage inductance it further under

predicts the inductance value, as presented in Table 3.2.

The authors have investigated the use of other equations to help predict the correct airgap length, such as the method presented by McLyman [77], but found that the technique presented by Roters works well for structures with larger airgaps.

Table 3.1 Results of Dc Reluctance Model Validation

Region	Reluctance Model	3D FEA
	L_{lk} (μH)	L_{lk} (μH)
Main gap	3.99	3.14
Pole front	0.80	0.71
Pole top	1.41	1.43
Pole corner	0.10	0.11
Pole total	6.30	5.39
Winding front	0.30	0.24
Winding side	0.52	0.37
Winding corner	0.09	0.07
Winding total	0.91	0.68

Table 3.2 Comparison of Ac Reluctance Model and 3D FEA Inductance

Region	Complete Reluctance Model	Simple Reluctance Model	3D FEA
Total (μH)	8.5	3.96	8.4

3.4. CCTT IM Design Algorithm

The design of any magnetic component is a complicated process and most design flow charts involve the selection of a core size in an iterative design procedure [7, 70-72, 75-81, 116]. This design process is further complicated when developing magnetic components which use non-standard core geometries, as in the case of the CCTT IM. In this section, an algorithm is developed to solve for the optimum CCTT IM design. Various electrical and magnetic parameters and constraints are input into the algorithm and the minimum volume CCTT IM is determined based on the inputs. The algorithm assumes that operation is restricted to the linear portion of the material B-H curve. The algorithm is presented in Fig. 3.19.

A solution is obtained by seeking the minimum total CCTT IM boxed volume where the core basic dimensions are variables. The algorithm incorporates fringing equations, presented by Roter, in order to optimize the magnetic design to produce the required inductances.

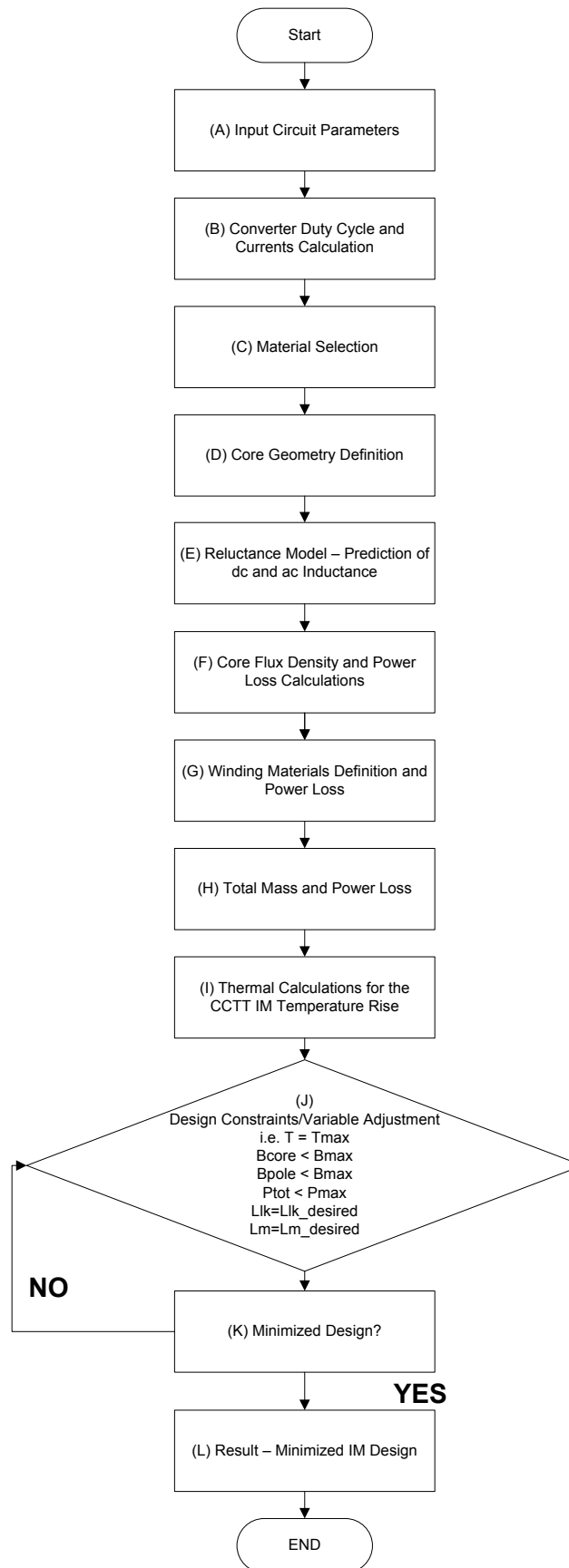


Figure 3.18. CCTT IM design algorithm

The CCTT IM reluctance model presented earlier in this chapter forms the backbone of the algorithm. The algorithm is implemented in Mathematica and relies on the FindMinimum function to obtain the minimized design. The CCTT IM design algorithm allows the design and comparison of the CCTT IM concept over a wide range of frequencies and input current ripple. The algorithm is modular in structure and this allows for efficient prototyping and quick modification of a CCTT IM design. This modular structure allows each section to be modified or replaced depending on the users design requirements. The user is presented with the option to select which core and winding material is to be used in the CCTT IM design. It is possible to select a winging configuration and the user has the choice between solid spiral and stranded windings. Typically, the solid spiral conductors are used for high-power liquid-cooled designs while stranded conductors are used for the air-cooled designs. The estimation of ac copper loss is a complex subject which is covered in detail in [71, 117-134]. Ac copper loss estimation is included for both the solid and stranded conductors. The ac loss prediction for the solid and multi-strand conductors assumes only skin effect while the proximity effects are neglected [135]. Essentially, 2D and 3D FEA is extensively used to determine the ac copper loss due to skin, proximity and airgap fringing effects in the CCTT IM.

The input circuit parameters such as V_{in} , V_{out} , P_{in} and input ripple ratio are specified in (A). The circuit currents, inductance, duty cycle and maximum power loss are calculated in (B). The core material is selected in (C). Depending on the user's choice of core material, module (C) reads the relevant material information such as core density, core permeability and Steinmetz parameters from a database. Modules (D) – (I) describe all the equations needed to develop the CCTT IM, as a function of core dimensions such as: core width, a , window width, b , window length, c , core thickness, d , pole height, h , leakage gap, g , magnetizing gap, $l_{g,mag}$, and turns per phase, N . Module (E) uses the CCTT IM reluctance model and takes all the relevant fringing regions into account in order to determine the correct gap lengths. In module (I) the CCTT IM temperature rise is determined. Module (J) uses the FindMinimum function in Mathematica to find the minimum CCTT IM boxed volume based on peak core and pole flux density, maximum allowable power loss, maximum allowable core and winding operating temperatures, core-width-to-thickness ratio, and winding height and width.

3.4.1. Design Algorithm

In (A) the typical circuit parameters are declared: input voltage, V_{in} , output voltage, V_{out} , output power, P_{out} , converter efficiency, η_{conv} , CCTT IM efficiency, η_{ccttim} , switching frequency, f_s , input current ripple ratio, r_{input} , percentage phase imbalance, P_{imb} , and number of turns per

phase, N .

In (B) the following electrical specifications are generated using the information provided in (A): switching period, T_s , duty cycle, D , input dc current, I_{in} , phase dc current, I_{phase} , phase imbalance, $I_{ph,imb}$, input current ripple, ΔI_{in} , leakage inductance, L_{lk} , magnetizing inductance, L_{mag} , magnetizing current ripple, ΔI_{mag} .

$$T_s = \frac{1}{f_s}, \quad D = 1 - \frac{V_{in}}{V_{out}}, \quad I_{in} = \frac{P_{out}}{\eta_{conv} V_{in}} \quad (3.21)$$

$$I_{phase} = \frac{I_{in}}{2}, \quad I_{ph,imb} = I_{phase}(1 + P_{imb}), \quad \Delta I_{in} = I_{in} r_{in} \quad (3.22)$$

The leakage and magnetizing inductance values depend on whether the duty ratio is less than or greater than 0.5. The algorithm selects which equation is to be used, to calculate the leakage and magnetizing inductances, once the duty cycle is determined.

For $D < 0.5$;

$$L_{lk} = \frac{V_{in}}{\Delta I_{in}} \left(\frac{D}{1-D} \right) (1-2D) T_s, \quad L_{mag} = 3L_{lk}, \quad \Delta I_m = \frac{V_{in} \left(\frac{D}{1-D} \right) T_s}{2L_{mag} + L_{lk}} \quad (3.23)$$

For $D > 0.5$;

$$L_{lk} = \frac{V_{in}}{\Delta I_{in}} (2D-1) T_s, \quad L_{mag} = 3L_{lk}, \quad \Delta I_m = \frac{V_{in} T_s}{2L_{mag} + L_{lk}} \quad (3.23)$$

Module (B) determines the following, phase current ripple due to leakage inductance, $\Delta I_{phase(lk)}$, phase current ripple, ΔI_{phase} , which is a combination of half the input current ripple and half of the magnetizing current ripple, peak phase current, $I_{phasemax}$.

$$\Delta I_{phase(lk)} = \frac{\Delta I_{in}}{2}, \quad \Delta I_{phase} = \Delta I_{phase(lk)} + 0.5 \Delta I_{mag}, \quad \Delta I_{max} = I_{phase} + 0.5 \Delta I_{phase} \quad (3.24)$$

In order to estimate the ac winding power loss, the phase current ripple harmonics [73] are evaluated from the relevant leakage and magnetizing components, $I(h)_{lk}$ and $I(h)_{mag}$. These are then used in (G) to approximate the ac copper loss due to the skin effect. They are also used as inputs to the 2D FEA solver once the final design is determined in order to obtain a more accurate value for the ac copper loss.

For $D < 0.5$;

$$I(h)_{lk} = \frac{\sqrt{2}AI_{phase(lk)}}{2(h\pi)^2} \sqrt{\frac{(1 - \cos(2h\pi(2D)))}{(2D)^2} + \frac{(1 - \cos(2h\pi(2D)))}{(1 - 2D)^2} + \frac{(2 - 2\cos(2h\pi(2D)))}{2D(1 - 2D)}} \quad (3.25)$$

$$I(h)_{mag} = 2AI_{mag} \left(\frac{\sin(h\pi(D)) \sin\left(\frac{h\pi}{2}\right)}{(h\pi)^2(D)} \right) \quad (3.26)$$

For $D > 0.5$;

$$I(h)_{lk} = \frac{\sqrt{2}AI_{phase(lk)}}{2(h\pi)^2} \sqrt{\frac{(1 - \cos(2h\pi(2D - 1)))}{(2D - 1)^2} + \frac{(1 - \cos(2h\pi(2D - 1)))}{(2 - 2D)^2} + \frac{(2 - 2\cos(2h\pi(2D - 1)))}{(2D - 1)(2 - 2D)}} \quad (3.27)$$

$$I(h)_{mag} = 2AI_{mag} \left(\frac{\sin(h\pi(1 - D)) \sin\left(\frac{h\pi}{2}\right)}{(h\pi)^2(1 - D)} \right) \quad (3.28)$$

Finally the RMS phase current, $I_{phase,rms}$, and the maximum allowable power loss, P_{loss} , are evaluated.

$$I_{rms,phase} = \sqrt{I_{phase}^2 + 0.5 \sum_{h=1}^{\infty} I(h)_{lk}^2 + I(h)_{mag}^2} \quad P_{loss} = P_{out} \left(\frac{1 - \eta_{ccttim}}{\eta_{conv}} \right) \quad (3.29)$$

The CCTT IM core loss is determined using the Modified Steinmetz Equation (MSE) [136]. The MSE uses an equivalent switching frequency for the magnetizing, $f_{eq,lk}$, and leakage, $f_{eq,mag}$, components which are determined in Block (B). The implementation of the MSE to the CCTT IM waveforms is presented in Appendix A.1.

For $D < 0.5$;

$$f_{eq, lk} = T_s \frac{4}{\pi^2} \left(\frac{0.5}{D(0.5-D)} \right) \quad f_{eq, mag} = T_s \frac{4}{\pi^2} \left(\frac{1}{D} \right) \quad (3.30)$$

For $D > 0.5$;

$$f_{eq, lk} = T_s \frac{4}{\pi^2} \left(\frac{0.5}{(1-D)(D-0.5)} \right) \quad f_{eq, mag} = T_s \frac{4}{\pi^2} \left(\frac{1}{(1-D)} \right) \quad (3.31)$$

In (C) the user can select the material of choice for the CCTT IM design. Presently, the available options are Ferrite 3C92 from Ferroxcube, Amorphous Metal 2605SA1 from Metglas and Silicon Steel 10JNHF600 from JFE. All the relevant data for each material, in the low to medium frequency range, is stored in a database that is accessible by the algorithm. Once a selection has been made the algorithm extracts the following information from the database: Steinmetz parameters, k , m and n , material density, $\rho_{material}$, material permeability, μ_r , saturation flux density, B_{sat} , maximum operating flux density, B_{max} , convection cooled coefficient, αt , core material thermal conductivity, λ_{core} and material stacking factor, k_{stack} . The Steinmetz parameters correspond with the equivalent leakage and magnetizing switching frequencies.

In module (D) various core geometry variables are initialized: magnetizing gap length, $l_{g, mag}$, conductor width, b_{bw} , conductor height, c_{bw} , distance of winding from the core, d_{core} , amount by which the pole shields the windings, d_{shield} , pole length, x , distance between each winding turn, $d_{windings}$, core area, A_{core} , pole area, A_{pole} , window width, b , window height, c , winding height, h_{wind} , ratio of core thickness to core width, r_c , and ratio of core thickness to pole height, r_p , core volume, V_{core} , pole volume, V_{pole} , core mass, M_{core} , pole mass, M_{pole} .

$$x = \frac{2b_{bw} + 2d_{shield} + 2d_{core}}{2} \quad d_{winding} = 0.3(N-2) \quad (3.32)$$

$$A_{pole} = k_{stack} ad \quad A_{core} = k_{stack} hd \quad b = g + 2b_{bw} + 2d_{shield} + 2d_{core} \quad (3.33)$$

$$c = N(c_{bw} + 4d_{core} + h + 2l_{g, mag} + d_{winding}) \quad h_{wind} = \frac{c-h}{2} - 4d_{core} \quad (3.34)$$

$$r_c = \frac{d}{a} \quad r_p = \frac{d}{h} \quad V_{core} = 2(c+b)ad + 4a^2d + hdx \quad (3.35)$$

$$V_{pole} = 2hdx \quad M_{core} = V_{core}\rho_{material} \quad M_{pole} = V_{pole}\rho_{material} \quad (3.36)$$

Module (E) develops the reluctance model for the CCTT IM. A complete reluctance model for the CCTT IM is presented earlier in this chapter which details all of the equations needed to determine the dc and ac inductance of the CCTT IM.

Module (F) presents the core and pole flux density calculations. In this module the dc and ac flux density, due to the leakage and magnetizing components, are evaluated: per phase dc leakage flux, Φ_{dclk} , differential dc flux, Φ_{dcgap} , per phase ac leakage flux, Φ_{aclk} , differential ac flux, Φ_{acgap} , pole dc flux density, B_{dcpole} , core dc flux density, B_{dcore} , dc flux density due to phase imbalance, B_{dcimb} , ac flux density due to leakage component, B_{aclk} , ac flux density due to magnetizing component, B_{acmag} , peak core flux density, B_{pkcore} , peak pole flux density, B_{pkpole} . The calculation of the flux density in the CCTT IM relies on the reluctance model, firstly the various flux components are determined and from this the relevant flux densities are determined.

$$\Phi_{dclk} = NI_{phase} \left(\frac{1}{\Re_{core} + 2\Re_{gap,dc}} \right) \quad (3.37)$$

$$\Phi_{aclk} = N\Delta I_{phase(lk)} \left(\frac{1}{\Re_{core} + 2\Re_{gap,ac}} \right) \quad (3.38)$$

$$\Phi_{dcgap} = 2\Phi_{dclk} \quad \Phi_{acgap} = 2\Phi_{aclk} \quad (3.39)$$

$$B_{dcpole} = \frac{\Phi_{dcgap}}{A_{pole}} \quad B_{dcore} = \frac{\Phi_{dclk}}{A_{core}} \quad (3.40)$$

$$B_{dcimb} = \frac{L_{mag} I_{ph_imb}}{NA_{core}} \quad B_{aclk} = \frac{\Phi_{acgap}}{2A_{pole}} \quad (3.41)$$

$$B_{acmag} = \frac{L_{mag} \Delta I_{mag}}{2NA_{core}} \quad B_{pkpole} = B_{aclk} + B_{dcpole} \quad (3.42)$$

$$B_{pkcore} = B_{acmag} + \frac{B_{aclk}}{2} + B_{dcore} + B_{dcimb} \quad (3.43)$$

Module (F) also includes the core power loss calculations, which are as follows: specific

volumetric core loss due to magnetizing component, in W/m³, P_{cspmag} , specific volumetric core loss due to leakage component, in W/m³, P_{csplk} , total specific volumetric core loss, in W/m³, P_{cspt} , specific mass core loss due to magnetizing, in W/kg, $P_{cspmagl}$, specific mass core loss due to leakage component, in W/kg, P_{csplkl} , total specific mass core loss, in W/kg, P_{csptl} , core loss due to magnetizing component, P_{mag} , core loss due to leakage component, P_{lk} , total core loss, P_t . The specific core loss is determined using the Modified Steinmetz Equation (MSE).

$$P_{cspmag} = \left(k(f_{eq,mag})^{m-1} (B_{acmag})^n \right) f_s \quad P_{csplk} = \left(k(f_{eq,lk})^{m-1} (B_{aclk})^n \right) f_s \quad (3.44)$$

$$P_{cspt} = P_{cspmag} + P_{csplk} \quad P_{cspmagl} = \frac{P_{cspmag}}{\rho_{material}} \quad (3.45)$$

$$P_{csplkl} = \frac{P_{csplk}}{\rho_{material}} \quad P_{csptl} = P_{cspmagl} + P_{csplkl} \quad (3.46)$$

$$P_{mag} = (M_{core} - M_{pole}) P_{cspmagl} \quad P_{lk} = (M_{core}) P_{csplkl} \quad (3.47)$$

$$P_t = P_{mag} + P_{lk} \quad (3.48)$$

In (G) the user has the option to choose what type of winding material and winding type is to be used in the CCTT IM design. The user can pick from copper in either a solid spiral or stranded conductor configuration both of which are presented in Fig. 3.19. Irrespective of conductor choice, (G) requires the following information: insulation thickness, t_i , winding material density, ρ_w , conductivity of material at 20 °C, σ_{20} , material temperature coefficient, k_t , operating temperature of material, T_{max} , conductivity of material at maximum temperature, σ_{max} .

If the user selects a solid spiral conductor then block (G) returns the following: winding area, $A_{w,spiral}$, conductor length, $l_{con,spiral}$, total conductor length, l_{contot} .

$$A_{w,spiral} = b_{bw} c_{bw} \quad l_{con,spiral} = 2(a+d) + 8d_{core} + 2(b_{bw} + c_{bw}) \quad (3.49)$$

$$l_{contot} = 2N l_{con,spiral} \quad (3.50)$$

If the user selects a stranded conductor then block (G) returns the following: winding area, $A_{w,strand}$, conductor length, $l_{con,strand}$, total conductor length, l_{contot} .

$$A_{w,strand} = \pi n_{strand} \left(\frac{d_{strand}}{2} \right)^2 \quad l_{con,strand} = 2(a+d) + 8d_{core} + 2(n_{strand}d_{strand}) \quad (3.51)$$

$$l_{contot} = 2Nl_{con,spiral} \quad l_{contot} = 2Nl_{con,strand} \quad (3.52)$$

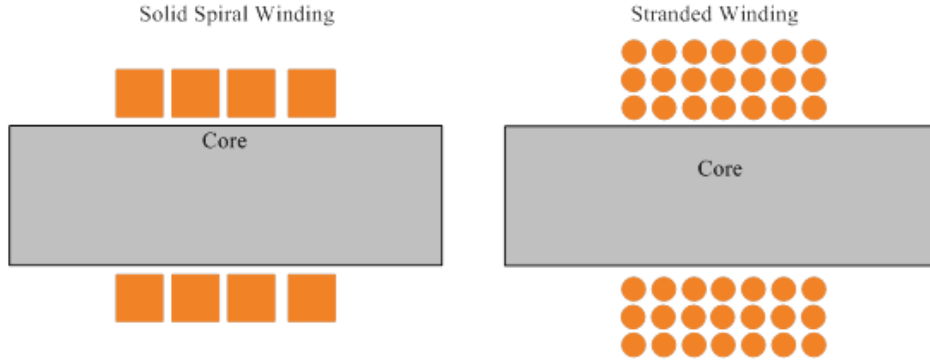


Figure 3.19. Solid spiral winding and parallel stranded winding options

Following this, the skin depth at each harmonic, $\delta(h)$, conductor volume, V_w , conductor mass, M_w , ac winding resistance at each harmonic, $R(h)_{ac}$, and ac winding loss at each harmonic, $P(h)_{wac}$ are determined. Finally, the ac power loss due to the leakage, $P(h)_{wac,lk}$, and magnetizing, $P(h)_{wac,mag}$, current ripple at each harmonic and total ac power loss, $P(h)_{wac}$, due to the skin effect is evaluated. The winding dc resistance and power loss is also evaluated.

$$\delta(h) = \frac{1}{\sqrt{\pi \sigma_{max} f_s \mu_{material} \mu_0}} \quad \sigma_{max} = \frac{\sigma_{20}}{1 + k_t (T_{max} - 20)} \quad (3.53)$$

$$V_w = l_{contot} A_w \quad M_w = \rho_{material} V_w \quad (3.54)$$

$$R(h)_{dc} = \frac{l_{contot}}{\sigma_{max} A_{w,spiral}} \quad R(h)_{dc} = \frac{l_{contot}}{\sigma_{max} A_{w,strand}} \quad (3.55)$$

$$P(h)_{wac,lk} = R(h)_{ac} I(h)_{lk}^2 \quad P(h)_{wac,mag} = R(h)_{ac} I(h)_{mag}^2 \quad (3.56)$$

$$P_{wac} = P(h)_{wac,lk} + P(h)_{wac,mag} \quad R_{dc} = \frac{l_{contot}}{\sigma_{max} A_{w,spiral}} \quad (3.57)$$

$$R_{dc} = \frac{l_{contot}}{\sigma_{max} A_{w,strand}} \quad P_{wdc} = R(h)_{dc} I_{phase}^2 \quad (3.58)$$

The selection of a stranded conductor implies the following assumptions: 1) The dc and ac current divides equally between each strand, 2) the distance in length between the inner and outer strand is negligible, and 3) proximity effects are ignored and one layer is assumed.

In block (H), the total CCTT IM mass, M_{total} , and the total winding and CCTT IM power loss, P_{wind} and P_{total} , are evaluated:

$$M_{total} = M_{core} + M_w \quad (3.59)$$

$$P_{wind} = P_{wdc} + P_{wac} \quad P_{total} = P_{core} + P_{wind} \quad (3.60)$$

In module (I) the CCTT IM temperature rise is determined. The user has the option of selecting a cooling method and can choose from convection or conduction cooling. The effective convective surface area, SA , is approximated by the surface area of a box barely enclosing the wound component [81]. In order to determine the SA , of the CCTT IM, the total width, e , total thickness, i , and total height, f , of the component is calculated. The temperature rise, T_{rise} , is then determined where αt is 0.909 for laminated materials and 0.833 from ferrite.

$$e = b + 2a + 2(b_{bw} + d_{core}) \quad i = d + 2(b_{bw} + d_{core}) \quad (3.61)$$

$$f = 2a + c \quad SA = 2ef + 2if + 2ei \quad (3.62)$$

$$T_{rise} = \left(\frac{P_{total}}{SA} \right)^{\alpha t} \quad (3.63)$$

The conduction cooling model assumes that the core and winding have separate heat paths, as shown in Fig. 3.20, and so the 2D heat transfer problem can be reduced to a 1D model. The core is assumed to be placed on a pin fin cold-plate such that both sides of the core make contact with the cold-plate, as shown in Fig. 3.20. The heat generated in the hotspot, P_{cspt1} , is removed along the core, l_c , with heat transfer surface, A_{hc} , and thermal conductivity λ_c . The core temperature rise, $T_{rise,core}$, is then calculated.

$$T_{rise,core} = \frac{P_{cspn} l_c}{2\lambda_c A_{ch}} \quad (3.64)$$

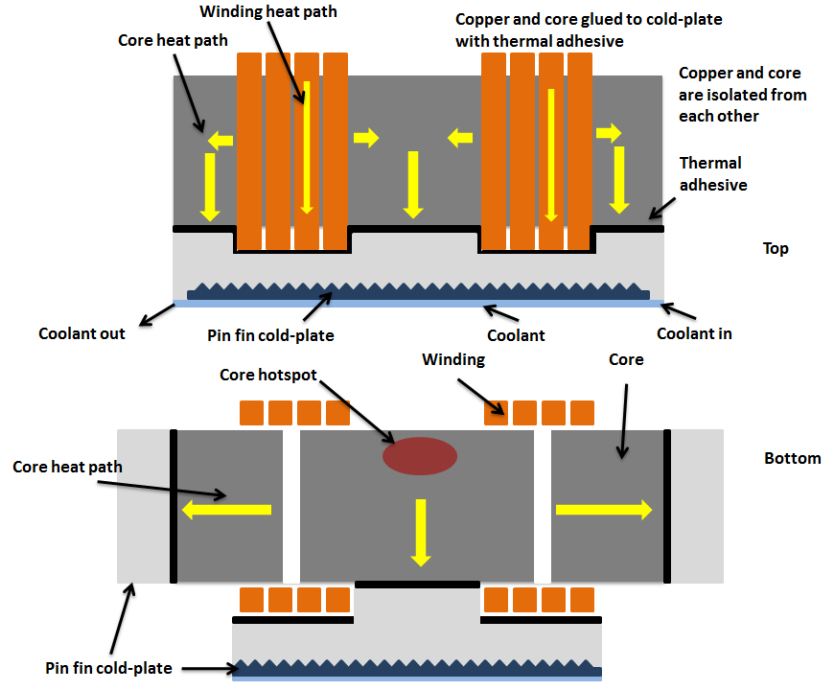


Figure 3.20. CCTT IM core 2D and 1D equivalent heat path

The winding is modeled as an equivalent straight winding with a length equal to the average heat path length, l_{eqcu} , with a thermal conductivity λ_{cu} . This is presented in Fig. 3.21. The total power loss generated in the winding, $P_{cspwind}$, is transferred through the insulation layer, with thermal conductivity, λ_i , between the winding and the cold-plate. The temperature rise, $T_{rise,cu}$, is calculated as follows:

$$T_{rise,cu} = \frac{P_{cspwind} l_{eqcu}}{2\lambda_{cu} A_{cu}} + \frac{P_{cspwind} l_{eqcu}}{\lambda_i A_{cu}} \quad (3.65)$$

In block (J) the FindMinimum function is utilized in order to find the minimum total CCTT IM mass. The CCTT IM is optimized for the temperature rise, depending on the thermal model selected; whether $L_{lk,ac}$ and $L_{mag,ac}$ are equal to L_{lk} and L_{mag} respectively; that the peak pole and core flux does not exceed B_{max} and that the main leakage airgap length, g , is greater than 0. The core and pole ratios are allowed to vary along with the desired conductor size. The core width, a , core thickness, d , pole height, h and leakage gap length, g are initialized to a start value and the solver determines the minimum CCTT IM boxed volume. Once the minimum

volume is determined, providing all the constraints have been reached, the solver ends. If the solver does not converge on a minimum design or if some of the constraints have not been achieved, the initialized values can be altered to help the solver converge to an optimum solution.

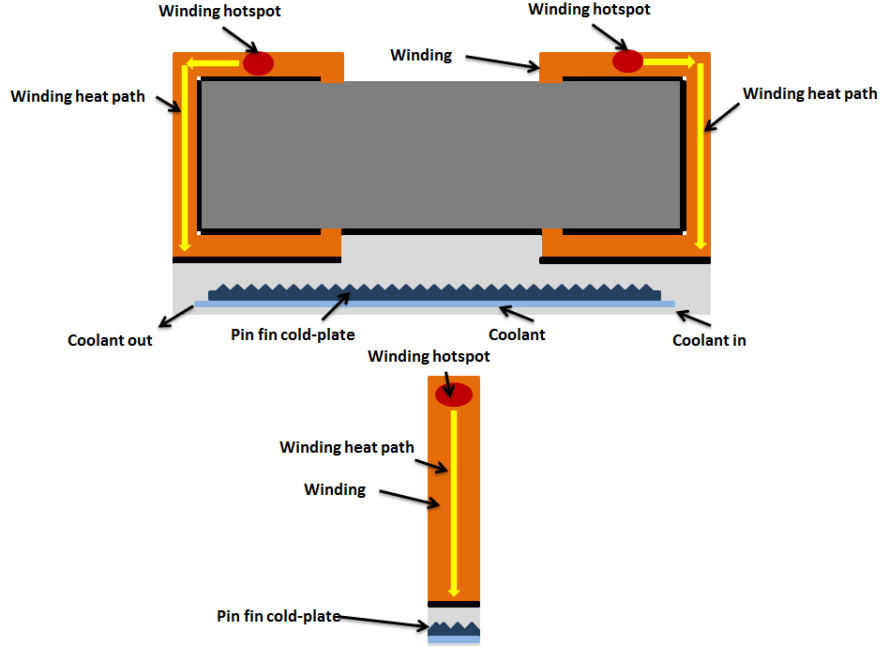


Figure 3.21. CCTT IM winding 2D and 1D equivalent heat path

3.4.2. Algorithm Validation

In this section, CCTT IM size variation is investigated as a function of magnetic material, input current ripple, frequency and cooling method. Magnetic components are designed to be saturation or power limited, where the power loss limit is due to temperature rise or efficiency [77, 114]. The most optimum design is produced when all three constraints meet their limits. The saturation flux density of the material used in the analysis is de-rated by 20 % to account for the temperature rise of the core and high dc-bias operation. To account for phase current imbalances due to control tolerances, the analysis inherently considers a 2 % phase current imbalance, which increases core size in a similar manner to the magnetizing current.

The cold-plate temperature is set at 70 °C. The maximum allowable temperature for the magnetic component is set at 140 °C. Thus, the maximum allowable temperature rise of the magnetic component is 70 °C. The core profile ratio, r_c , which is the ratio of the core thickness d and the core width a , is allowed to change within the range of 2 and 6 while the pole profile ratio, r_p , which is the ratio of the pole thickness d and the pole height h , is also allowed to

change within the range of 2 and 6. The magnetizing path air gap is divided into four separate air gaps.

The magnetic materials used in this analysis are ferrite 3C92 from Ferroxcube, iron-based amorphous metal 2605SA1 from Metglas and silicon steel 10JNHF600 from JFE. Table 3.3 [137] presents the relevant material properties of the three materials in question.

Table 3.3. Magnetic Material Properties

Magnetic Material Type	Manufacturer	Material	Composition	Saturation Flux Density @ 25 °C (T)	Rel. Permeability (100 °C @ 20 kHz)	Curie temp (°C)	Continuous Operating Temperature (°C)	Thermal Conductivity (W/m K)	Density (g/cm ³)	Core Loss @ 0.1 T, 20 kHz (kW/m ³)	Core Loss @ 0.1 T, 100 kHz (kW/m ³)
AM	Metglas	2605SA1	Fe-B-Si	1.56	600	395	150*	10**	7.18	70	1380
SS	JFE	10JNHF600	Fe-Si 6.5 %	1.88	600	700	150*	18**	7.53	150	1750
Ferrite	Ferroxcube	3C92	Mn-Zn	0.52	1800	250	150	3.5-5	4.8	5	49

*limited by lamination adhesive

** along laminations

3.4.2.1. High-Power Conduction Cooled Design

The liquid cooled designs compared in this section share the same prototype specifications: $V_{in} = 155$ V, $V_{out} = 420$ V, $P_{in} = 72$ kW and $f_s = 16, 25, 50, 75$ and 100 kHz. The number of turns per phase is allowed to vary and the conductor cross-sectional area is allowed to vary between 4 – 25 mm². The variation in CCTT IM boxed volume for increasing frequency is presented in Fig. 3.22, 3.23 and 3.24 respectively. Fig. 3.22 presents the results for ferrite 3C92. At low input ripple the boxed volume, especially at low frequencies, is large due to the large inductance requirement. As the input ripple increases the inductance requirement is reduced and the IM boxed volume reduces. As expected the overall volume of the CCTT IM decreases with increasing frequency. In the case of 3C92, due to its low saturation flux density, all of the designs are saturation flux limited.

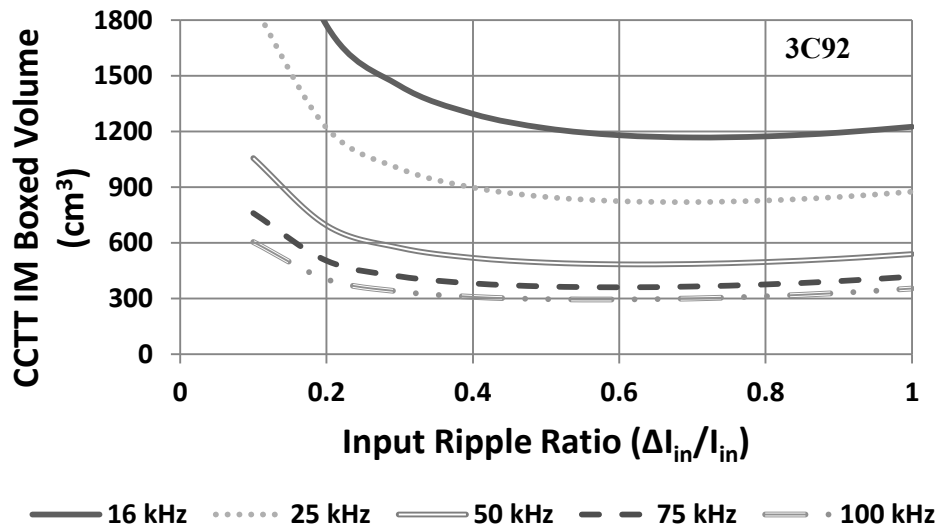


Figure 3.22. Variation of CCTT IM boxed volume for ferrite 3C92

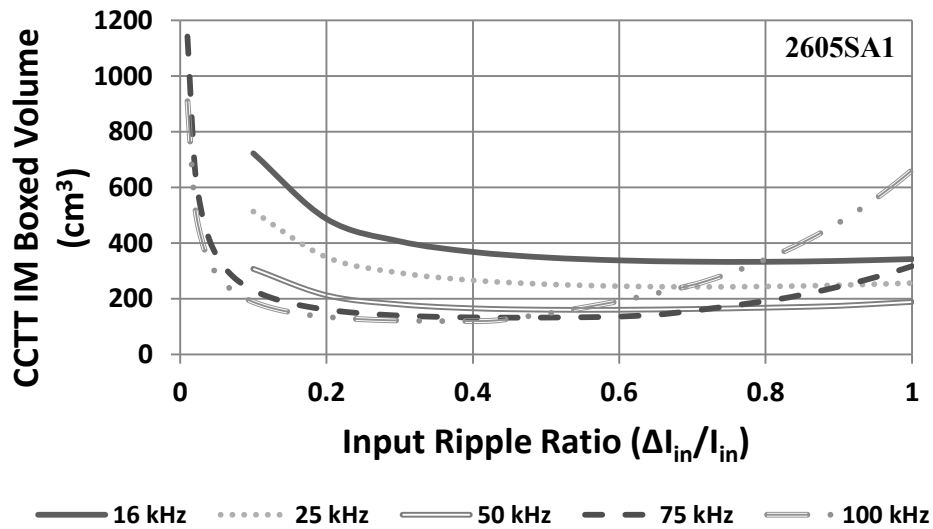


Figure 3.23. Variation of CCTT IM boxed volume for iron-based amorphous metal 2605SA1

Fig. 3.23 presents the results for Metglas 2605SA1 material. At low input ripple ratios, the boxed volume is large due to the large inductance requirement and the CCTT IM is flux limited in this region. As the input ripple increases the volume of the CCTT IM decreases until the component becomes core loss limited due to the increased flux swing, at which point its volume begins to increase again. At low frequency operation the minimum CCTT IM boxed volume is observed in the region of 60 % input ripple and as the frequency increases the optimal design point, for minimum boxed volume, converges to ripple ratios of 40 %. The results for silicon steel 10JNHF600, presented in Fig. 3.24, follow a similar pattern to that of the iron-base amorphous metal material. The minimum boxed volume is observed in the region of 40 % at

low frequencies and as the frequency increases the optimal ripple ratio is seen to be between 10 – 20 %. Interestingly as the frequency and input ripple ration increases the overall volume increases dramatically due to the large core loss in the component.

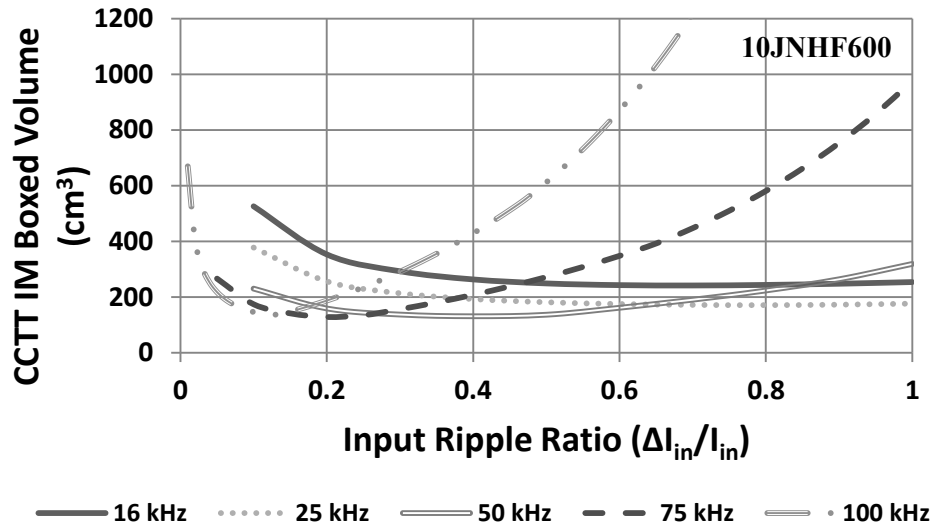


Figure 3.24. Variation of CCTT IM boxed volume for silicon steel 10JNHF600

Fig. 3.25, 3.26, 3.27, 3.28 and 3.29 illustrate the breakdown of CCTT IM volume and power loss for the three core materials in question for 16, 25, 50, 75 and 100 kHz switching frequency, respectively. The results indicate the laminated materials result in the lowest boxed volume between 16 – 50 kHz, but this comes at the expense of increased power loss with respect to the ferrite solution.

Interestingly, silicon steel performs similarly to that of the iron-based amorphous-metal in this frequency range albeit with a larger power loss. The larger thermal conductivity of the silicon material and the liquid cooled design allows for the efficient removal of heat with results in a similar boxed volume as the amorphous material. It is shown in Section 3.4.2.3 that when an efficiency constraint is introduced, the silicon solution is only competitive at low input ripple conditions.

At all frequencies, as the ripple ratio increases, the ferrite material is, in reality, the only option as the boxed volume of the high-flux designs rapidly increases due to their significantly higher power loss.

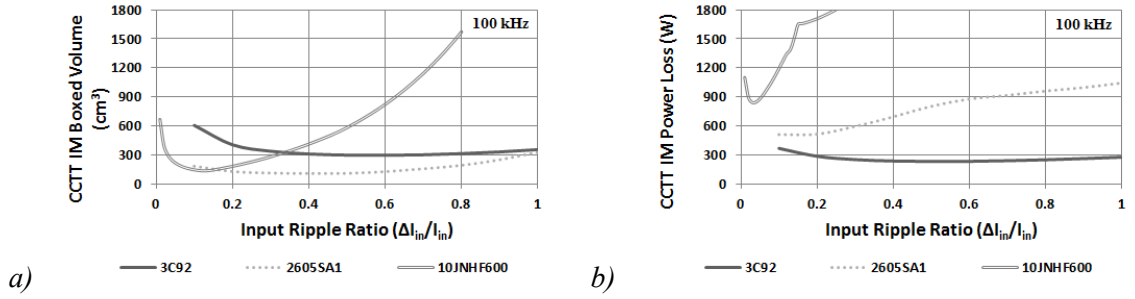


Figure 3.29. Variation in (a) CCTT IM boxed volume and (b) CCTT IM power loss for 3C92, 2605SA1 and 10JNHF600 core material at 100 kHz

3.4.2.2. Low-Power Conduction Cooled Design

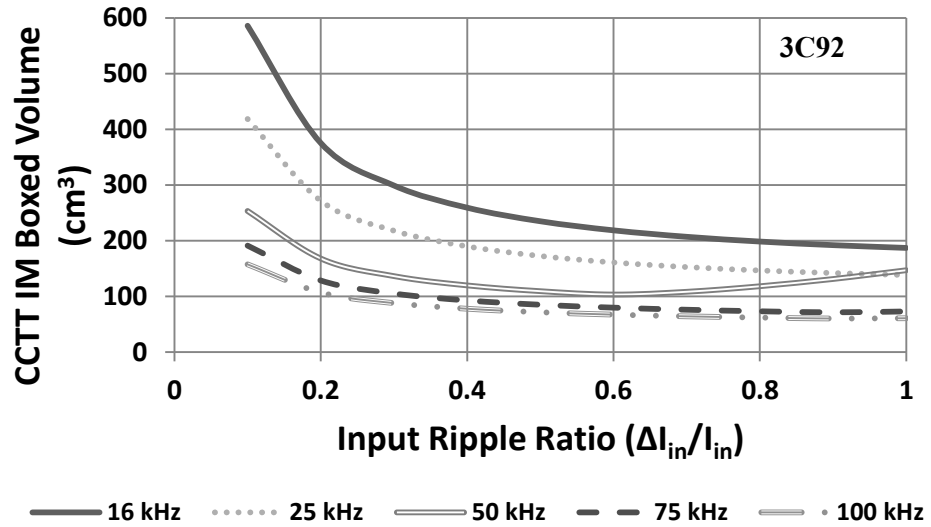


Figure 3.30. Variation of CCTT IM boxed volume for ferrite 3C92

The air cooled designs compared in this section share the same prototype specifications: $V_{in} = 135 \text{ V}$, $V_{out} = 500 \text{ V}$, $P_{in} = 3 \text{ kW}$ and $f_s = 16, 25, 50, 75$ and 100 kHz . The number of turns per phase is allowed to vary, the number of strands is fixed at 6, while the cross-sectional area of each strand is allowed to vary between $0.5 - 1.1 \text{ mm}^2$. Similar to the liquid-cooled designs, the variation in CCTT IM boxed volume for increasing frequency is presented in Fig. 3.30, 3.31 and 3.32 for ferrite 3C92, amorphous metal and silicon steel, respectively. As expected, the volume of the CCTT IM is large at low input ripple due to the large inductance requirement. The ferrite option is flux limited over the entire ripple and frequency range. The laminated materials are initially flux limited but their volume reduces with increasing input ripple to the point where they become core loss limited. This occurs in the region of 10 % input ripple for both designs. Interestingly, the boxed volume of both the laminated options is seen to increase in a much more

dramatic fashion than witnessed previously in the conduction-cooled designs.

Fig. 3.33, 3.34, 3.35, 3.36 and 3.37 illustrate the breakdown of CCTT IM volume for the three core materials in question for 16, 25, 50, 75 and 100 kHz switching frequency, respectively. The results indicate the laminated materials are competitive with the ferrite material in the medium-to-low input ripple range but critically they again have significantly more power loss. As the frequency is increased over 50 kHz the laminated materials are really only competitive at very low input ripple ratios.

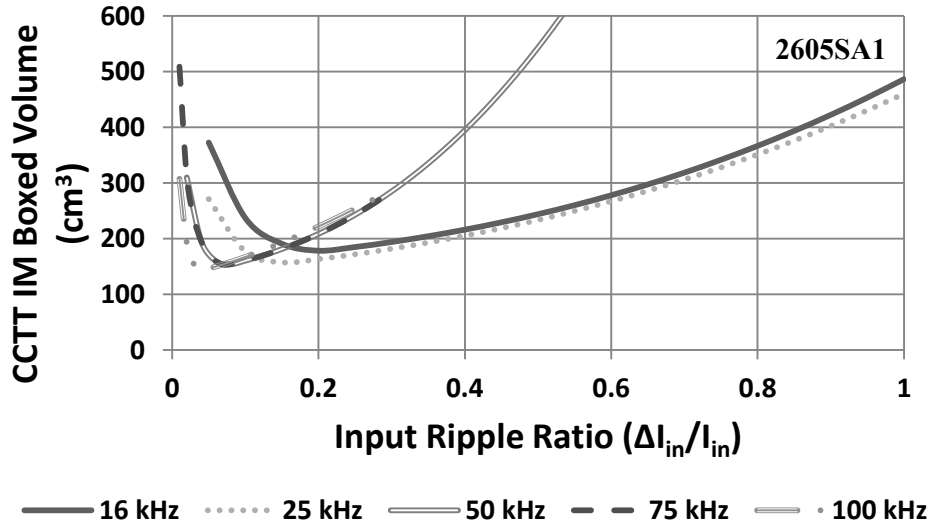


Figure 3.31. Variation of CCTT IM boxed volume for iron-based amorphous metal 2605SA1

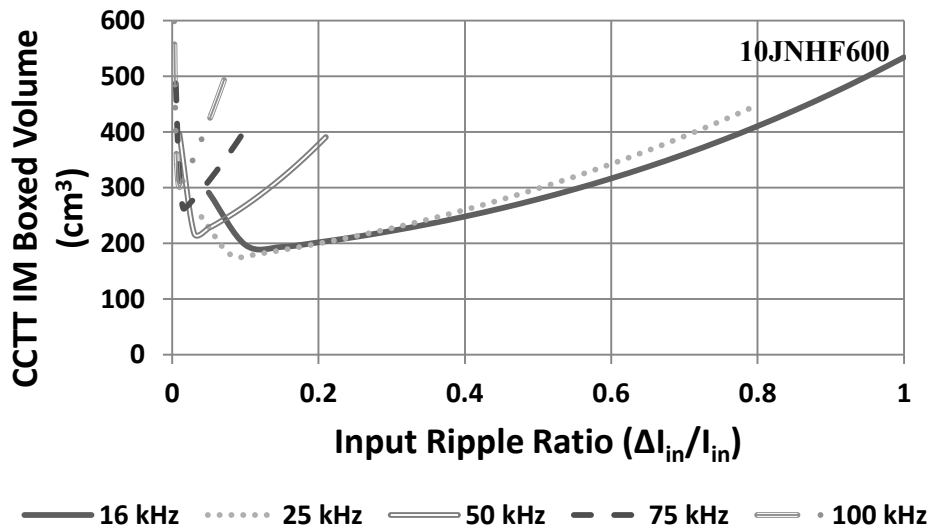


Figure 3.32. Variation of CCTT IM boxed volume for silicon steel 10JNHF600

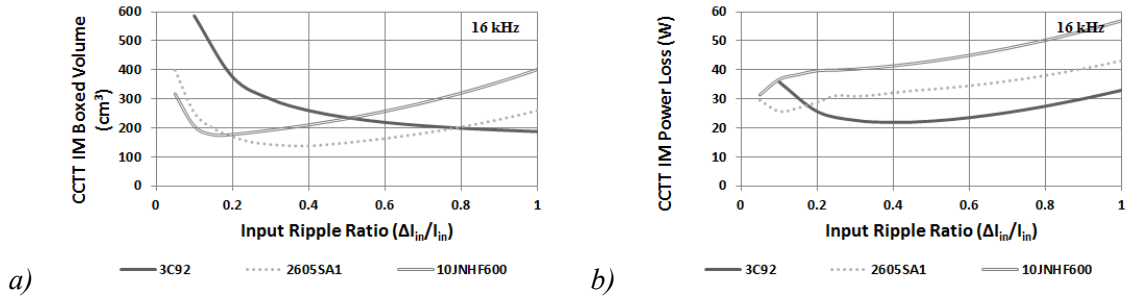


Figure 3.33. Variation in (a) CCTT IM boxed volume and (b) CCTT IM power loss for 3C92, 2605SA1 and 10JNHF600 core material at 16 kHz

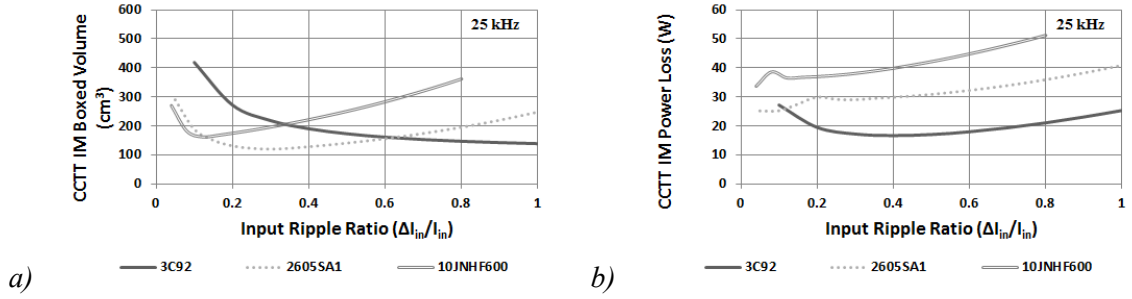


Figure 3.34. Variation in (a) CCTT IM boxed volume and (b) CCTT IM power loss for 3C92, 2605SA1 and 10JNHF600 core material at 25 kHz

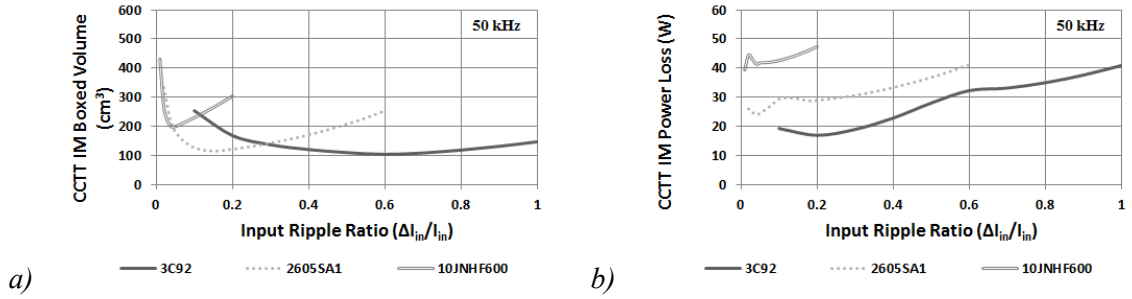


Figure 3.35. Variation in (a) CCTT IM boxed volume and (b) CCTT IM power loss for 3C92, 2605SA1 and 10JNHF600 core material at 50 kHz

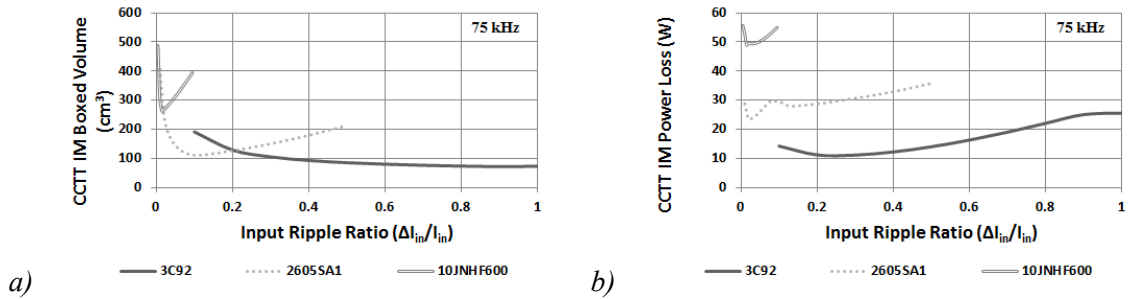


Figure 3.36. Variation in (a) CCTT IM boxed volume and (b) CCTT IM power loss for 3C92, 2605SA1 and 10JNHF600 core material at 75 kHz

Interestingly, the silicon steel material is competitive with the amorphous metal material for in the low-to-medium frequency range due to its higher thermal conductivity. As the frequency increases the silicon becomes less competitive due to its higher core loss and the

difficulty of efficiently extracting heat from the component.

Essentially, the results indicate that, unless the input ripple is very low, ferrite 3C92 material is the only logical option for this design point.

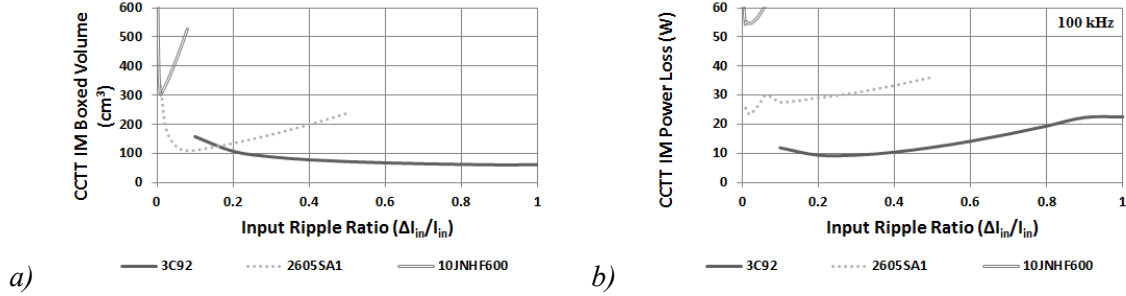


Figure 3.37. Variation in (a) CCTT IM boxed volume and (b) CCTT IM power loss for 3C92, 2605SA1 and 10JNHF600 core material at 100 kHz

3.4.2.3. Conduction-Cooled CCTT IM Boxed Volume Variation with an Efficiency Constraint

This section investigates the variation of CCTT IM boxed volume when an efficiency constraint of 99 % is imposed. The variation in CCTT IM boxed volume and power loss is presented in Fig. 3.38 and 3.39 for 16 kHz and 100 kHz operation, respectively.

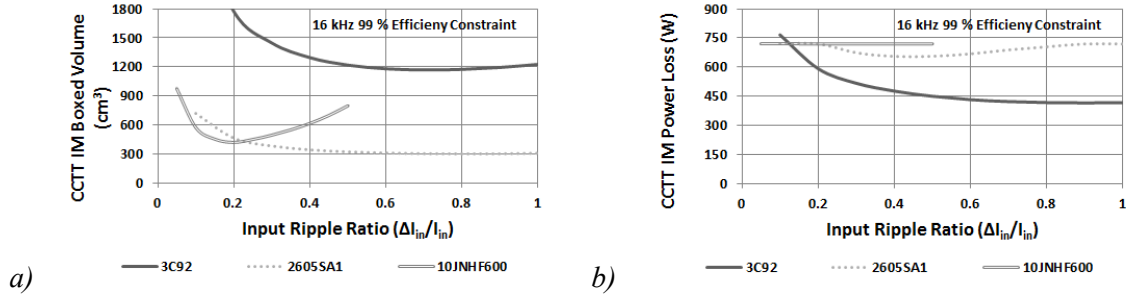


Figure 3.38. Variation in (a) CCTT IM boxed volume and (b) CCTT IM power loss for 3C92, 2605SA1 and 10JNHF600 core material at 16 kHz and 99 % efficiency constraint

Fig. 3.38 (a) indicates that the laminated materials allow for a significant reduction in boxed volume over the ferrite solution, over the entire ripple range. Fig. 3.38 (b) illustrates that the laminated materials have the maximum allowable power loss while the ferrite option has significantly lower power loss over the majority of the ripple range.

At low input ripple ratios the laminated materials are the obvious option but for ripple ratios greater than 40 % the ferrite option is competitive due to its much lower power loss. For

example, at 40 % input current ripple the amorphous metal CCTT IM is 60 % smaller and the silicon steel option is 30 % smaller than the ferrite solution. Conversely, the ferrite CCTT IM has 38 % lower power loss than the laminated options indicating that it has an efficiency of 99.4 % at this design point.

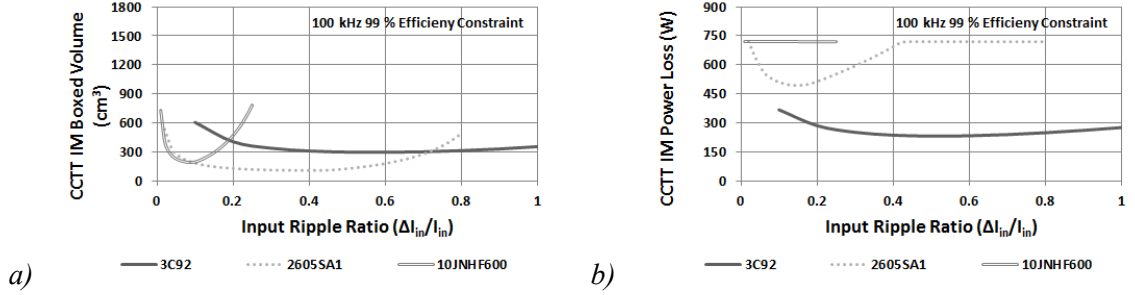


Figure 3.39. Variation in (a) CCTT IM boxed volume and (b) CCTT IM power loss for 3C92, 2605SA1 and 10JNHF600 core material at 100 kHz and 99 % efficiency constraint

Fig. 3.39 (a) indicates that the laminated materials allow for a reduction in boxed volume over the ferrite solution at low input ripple ratios. Fig. 3.39 (b) illustrates that the laminated materials have the maximum allowable power loss while the ferrite option has significantly lower power loss over all of the ripple range.

At 40 % input current ripple, the amorphous and ferrite CCTT IM's will have the same boxed volume while the ferrite option will have 48 % lower power loss.

3.5. CCTT IM Design Trade-offs

A paper design is undertaken in order to compare the CCTT IM prototype with the existing EE IM technology. The results indicate the CCTT IM is smaller in volume, due to its lower dc inductance, and also has a more controllable ac inductance. The variation of CCTT IM volume for different values of magnetizing inductance is also investigated.

3.5.1. Comparison with Traditional EE IM

In this section the CCTT IM and EE IM concepts are compared for the same input circuit conditions as in the previous section. Fig. 3.40 (a) presents the variation of CCTT IM and EE IM boxed volume as the current ripple ratio is varied. Fig. 3.40 (b) presents the variation of dc and ac leakage inductance for both designs. A similar reluctance model to that presented in Fig. 3.17, is developed for the EE IM and is used to determine its minimum boxed volume. From Fig. 3.40 (a) it is evident that the CCTT IM can achieve a size reduction over the EE IM.

At an input ripple condition of 40 %, the CCTT IM is approximately three-quarters the volume of the EE IM. As presented in Fig. 3.40 (b), both IM designs are developed to achieve the required ac leakage inductance. It is clear that the dc inductance of the CCTT IM is much closer to its ac inductance. 3D FEA is used to validate the designs and the results of the comparison are presented in Table 3.4.

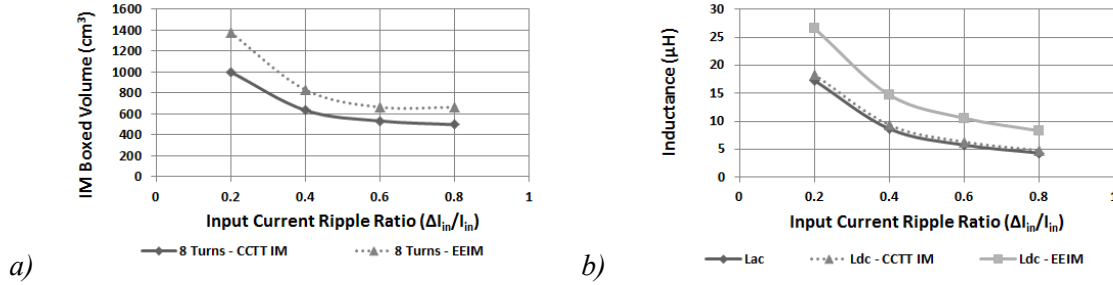


Figure 3.40. (a) Variation in CCTT IM and EE IM boxed volume with varying input current ripple and (b) highlighting the larger dc inductance of the EE IM

Table 3.4 Comparison of Dc and AC Inductance for the CCTT and EE IM Options

		CCTT IM		EE IM	
		Algorithm	3D	Algorithm	3D
$L_{lk, dc}$	μH	9.8	9.6	15.9	16.2
$L_{lk, ac}$	μH	8.5	8.4	8.5	9.2

3.5.2. Variation of CCTT IM Boxed Volume with Magnetizing Inductance

This section investigates the volume variation of the CCTT IM as the magnetizing inductance is varied. Fig. 3.41 presents the results of increasing magnetizing inductance on CCTT IM boxed volume as the input current ripple is increased. As the magnetizing inductance is increase the core cross-sectional area and number of turns will increase and so the overall boxed volume increases. On closer inspection of Fig. 2.8 in Chapter 2, it is obvious that as the magnetizing inductance is increased the magnetizing current ripple is reduced. At a duty cycle of 50 %, the phase current ripple contains only the magnetizing component. Theoretically, if the magnetizing inductance is made large enough it would be possible to have full input and phase ripple cancellation at this duty cycle point. This would result in a larger design due to the need for a larger cross-sectional area and number of turns. Conversely, the lower the magnetizing inductance the smaller the boxed volume but this comes at the expense of increased phase current ripple.

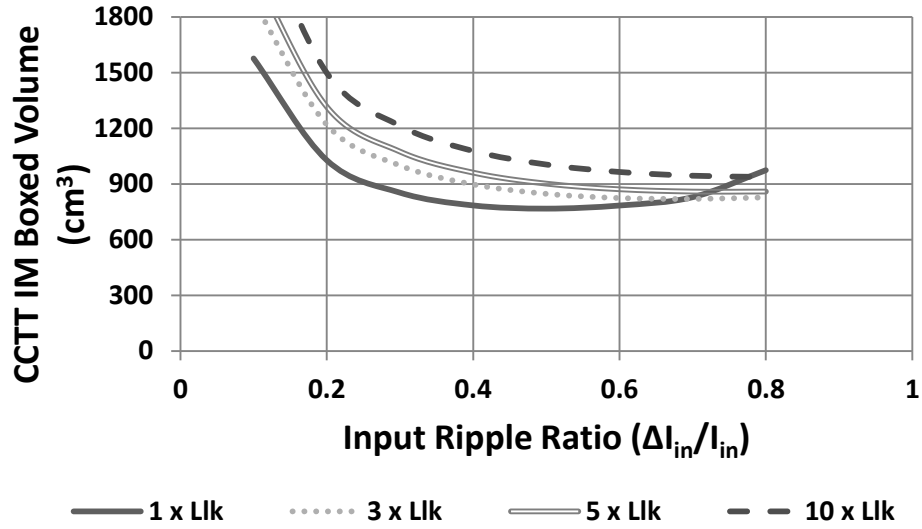


Figure 3.41. Variation in CCTT IM boxed volume for increasing values of magnetizing inductance

3.6. Conclusions

A novel CCTT IM structure is presented in this Chapter. The CCTT IM makes several improvements on existing IM and XL technologies, discussed in Chapter 1, by integrating all magnetic components into one low power loss ferrite core which is (1) easy to manufacture, (2) uses split-phase windings to minimize the amount of unwanted external dc flux, thereby reducing its volume, (3) minimizes unwanted inter-winding capacitance, (4) employs ferrite poles to help contain the leakage flux within the CCTT core window and (5) uses a low number of turns for efficient heat removal from the conductors.

Fringing flux equations accurately predict the fringing flux around the CCTT IM pole and winding regions. A dc and ac CCTT IM reluctance model and design algorithm is presented that allows engineers to quickly design and prototype the CCTT IM. 3D FEA is used to optimize and validate the reluctance models.

A design algorithm is developed in Mathematica that incorporates the fringing equations in order to develop an efficient and optimized IM design. The algorithm allows the user to compare and contrast a CCTT IM design over various frequencies, power levels and ripple ratios. The algorithm allows the user to select various core material and winding options. The algorithm also allows for the selection of different thermal options.

Design curves are presented that show the variation in CCTT IM boxed volume, for three different magnetic materials, as the input current ripple ratio is varied. The results indicate that for medium-to-high input ripple ratios ferrite 3C92 is the material of choice and while it has a

larger boxed volume its power loss is unbeatable. For low input ripple conditions the high-flux materials are competitive.

The CCTT IM is shown to have a smaller boxed volume to an equivalent EE IM along with a more controlled ac inductance. Finally, the variation in CCTT IM boxed volume as the magnetizing inductance is varied is investigated.

Chapter 4

Comparison of CCTT-Core Split-Winding Integrated Magnetic and Discrete Inductors for High-Power DC-DC Converters

This chapter presents a comparison of two magnetic component topologies for use in high-power high-current dc-dc boost converters. Firstly, a 16 kHz, 97.2 kW, three-phase (3L) dc-dc boost converter is presented and is considered as the baseline design. The magnetic components used in this converter are described in detail in [82] and are briefly covered in Section 4.2.

The integrated magnetic (CCTT IM) and two-phase discrete inductor (2L) topologies are then designed to have the same worst-phase ripple current condition, as the 3L inductors, for a 25 kHz, 72 kW, next generation prototype. The goal of the chapter is to determine whether the ferrite CCTT IM, covered in Chapter 2, is competitive with the 2L discrete inductors which are constructed using high-flux density, iron-based, amorphous metal material from Metglas [81]. An inductor design algorithm is used to design the 2L discrete inductors. The design algorithm is developed in a similar manner to the CCTT IM design algorithm presented in Chapter 3.

The magnetic components are optimized using the CCTT IM and inductor design algorithms for varying number of turns in order to achieve the minimum boxed volume. Additionally, the magnetic and semiconductor power losses are investigated over the typical operating range of an automotive fuelcell. Input and output filter capacitor sizing is undertaken and this allows for better understanding of the trade-off between magnetic component and filter capacitor sizing.

The design of a high-flux density CCTT IM design is investigated. The laminated material option allows for a smaller sized IM design in comparison with the ferrite 3C92 option,

albeit at the expense of increased power loss.

High-power experimental results are presented for the baseline 3L (97.2 kW) and CCTT IM (72 kW) converters. Low-power (3.8 kW) experimental results are presented which compare and validate the 2L and CCTT IM concepts under like-for-like operating conditions.

4.1. Introduction

High-power density magnetic components are required for military, industrial, aerospace and automotive applications. Specifically in relation to automotive applications, dc-dc converters are critical components of a fuelcell vehicle powertrain. The magnetic components in conventional single-phase boost converters, used in automotive applications, can be quite lossy, bulky and costly [23, 32-34, 49-51, 138] and innovative methods to reduce the size of these power converters are major driving forces in the design of efficient eco-friendly vehicles. The polarization curve of a PEM fuelcell [25, 39], presented in Fig. 4.1, has significant voltage reduction with load due to activation, ohmic and oxidation voltage drops from the no-load voltage. A boost converter is essential in order to stabilise the poorly-regulated output voltage of the fuelcell, and efficiently distribute this voltage to the traction motor inverters.

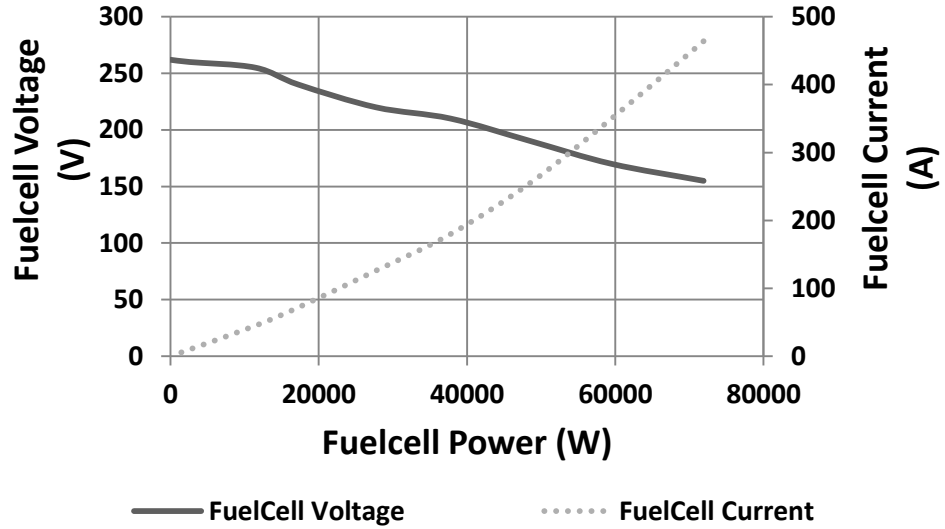


Figure 4.1. 72 kW fuelcell I-V characteristic

The two methods of implementing a two-phase interleaved boost converter, under discussion in this chapter, are presented in Fig. 4.2. Both the 2L and CCTT IM options result in input-current ripple reduction, with this ripple reduction extended to the phase-current ripple for the CCTT IM design. The 2L design has two discrete inductors typically using high B_{sat} , lossy material for automotive applications. The IM concept involves the integration of all magnetic components onto one single core. A more detailed comparison between all the methods of implementing an interleaved boost converter is covered in Chapter 1.

The goal of this chapter is to compare and contrast two interleaved boost converter topologies, namely the CCTT IM and 2L discrete inductor options. It is possible to design the magnetic components for the same worst-case input or phase current ripple.

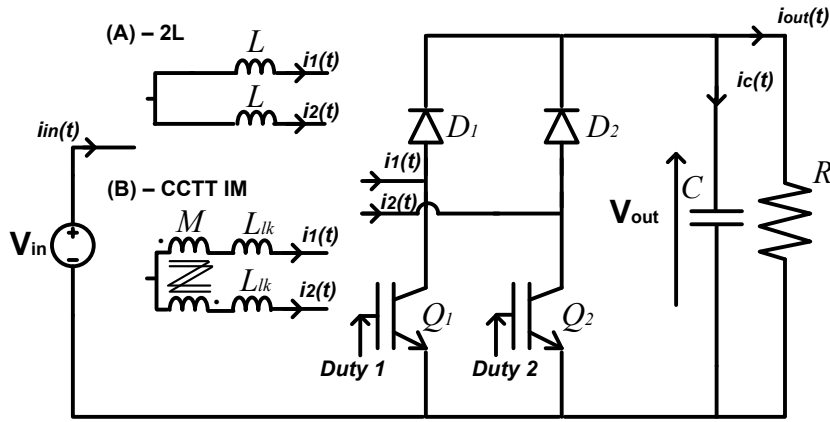


Figure 4.2. 2L and CCTT IM boost converter topologies

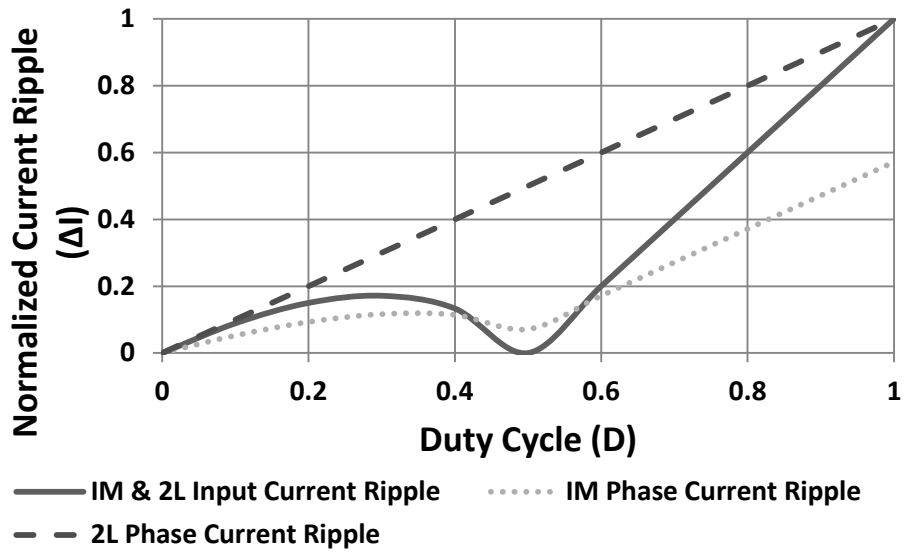


Figure 4.3. 2L and CCTT IM normalized current ripple assuming same input ripple

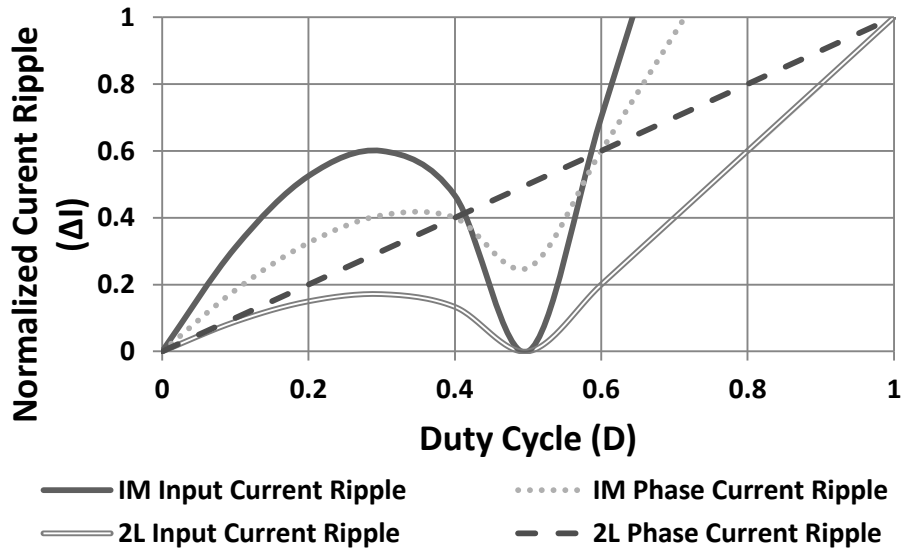


Figure 4.4. 2L and CCTT IM normalized current ripple assuming same phase ripple

Fig. 4.4 presents the normalized input and phase current ripple versus duty ratio for the 2L and CCTT IM topologies when designed to achieve the same worst-case input current ripple. Fig. 4.5 presents the normalized input and phase current ripple versus duty ratio for the 2L and CCTT IM topologies when designed to achieve the same worst-case phase current ripple. The 2L design exhibits input current ripple reduction while its phase current ripple increases linearly which increasing duty ratio. Likewise the CCTT IM exhibits input current ripple reduction but critically, due to transformer coupling, it also exhibits phase current ripple reduction.

For argument sake, if both topologies are designed for the same input current ripple, as presented in Fig. 4.4, corresponding to a duty ratio, $D = 0.6$, the 2L discrete inductors will see a significantly larger phase current ripple than the CCTT IM. In reality, this limits any comparison between the IM and 2L, for the same input current ripple, to low-input ripple ratios; typically less than 20 % as the larger phase current ripple results in unacceptable winding and core loss.

Conversely, if both topologies are designed for the same phase current ripple, as presented in Fig. 4.5, again corresponding to a duty ratio, $D = 0.6$, then the input current ripple of the CCTT IM design will be significantly greater than that of the 2L option. Fig. 4.6 illustrates that inductance saving that the CCTT IM offers in comparison to the 2L design when both options are designed to have the same worst-case phase current ripple. At worst the CCTT IM delivers an inductance saving of 47 % at $D = 0.1$ and at best it achieves an inductance saving of 85 % at $D = 0.5$. This inductance saving directly translates into a size saving.

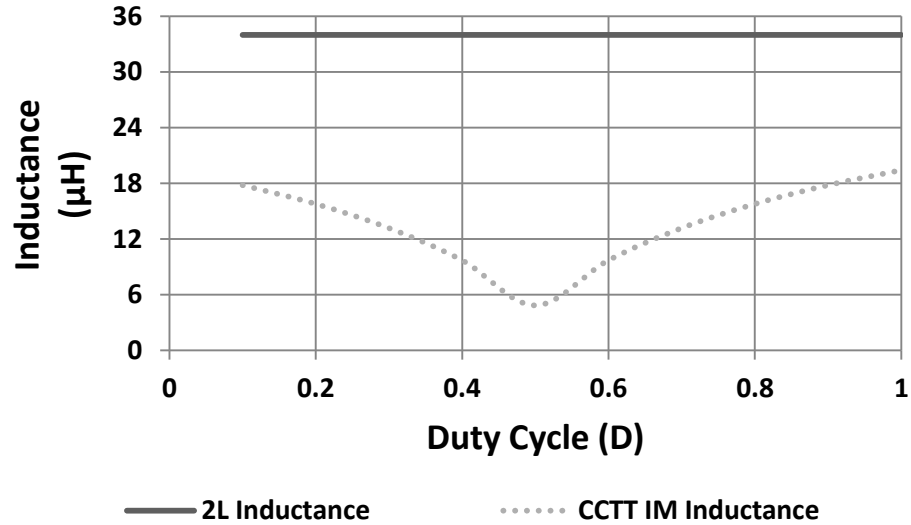


Figure 4.5. CCTT IM inductance saving when compared with 2L for same worst-case phase current ripple

Up to this point, the discussion has focused on the design of the magnetic components but it is critical to understand the effect of each topology selection on the overall performance of the

dc-dc converter. With this in mind, this chapter will look at the power loss in the semiconductor devices as well as sizing of the input and output filter capacitors.

It is also useful to understand how the power loss in the magnetic components and semiconductors vary as the fuelcell power varies. Referring back to Fig. 4.4 and Fig. 4.5, it is obvious that the CCTT IM option will see a greater reduction in phase current ripple than the 2L design as the duty cycle reduces, especially at duty ratios in the vicinity of, $D = 0.5$. This analysis will show that a low B_{sat} ferrite CCTT IM is comparable in volume with the high B_{sat} Metglas 2L discrete inductors when designed for the same worst-case phase current ripple conditions. The CCTT IM option is also more efficient over the operating range of the fuelcell as it exhibits much lower core loss and ac copper loss.

The analysis conducted in Chapter 3 illustrated how a CCTT IM constructed from a high-flux material allows for the design of a CCTT IM that has a smaller boxed volume in comparison to a CCTT IM, at the expense of increased core loss. The variation in CCTT IM boxed volume and power loss for 3C92, 2605SA1 and 10JNHF600 core materials for 25 kHz switching frequency with a 99 % efficiency constraint is presented in Fig. 4.6 (a) and (b), respectively. A paper design is undertaken to determine how the high-flux CCTT IM compares with the two other designs presented in this chapter in terms of magnetic loss, semiconductor loss and filter capacitor sizing.

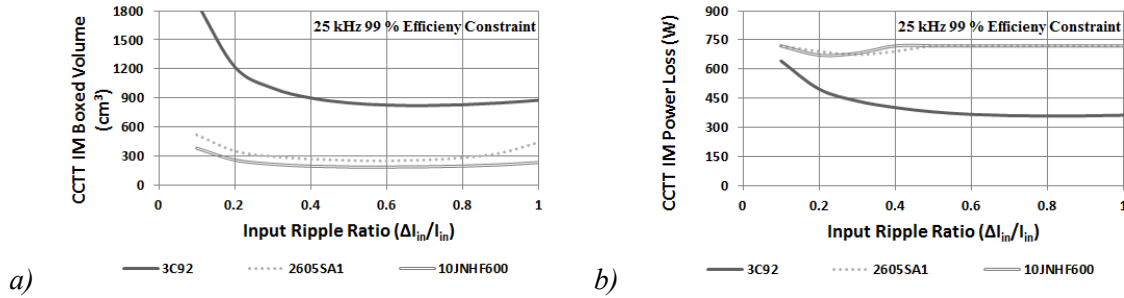


Figure 4.6. Variation in (a) CCTT IM boxed volume and (b) CCTT IM power loss for 3C92, 2605SA1 and 10JNHF600 core material at 25 kHz and 99 % efficiency constraint

4.2. Baseline Three-Phase DC-DC Boost Converter

This section describes a 3L 97.2 kW interleaved boost converter for use in automotive fuelcell applications developed by Lyons et al. [82]. The nominal operating conditions are as follows: $V_{in} = 180$ V, $V_{out} = 360$ V, $P_{in} = 97.2$ kW and $f_s = 16$ kHz. These operating conditions result in a phase inductance, L_{phase} , of $45\mu\text{H}$ with a worst case phase peak-to-peak current ripple, ΔI_{p-p} , of 125 A. Fig. 4.7 presents one of the phase inductors of the 3L topology while Fig. 4.8 presents a schematic of the 3L boost topology.

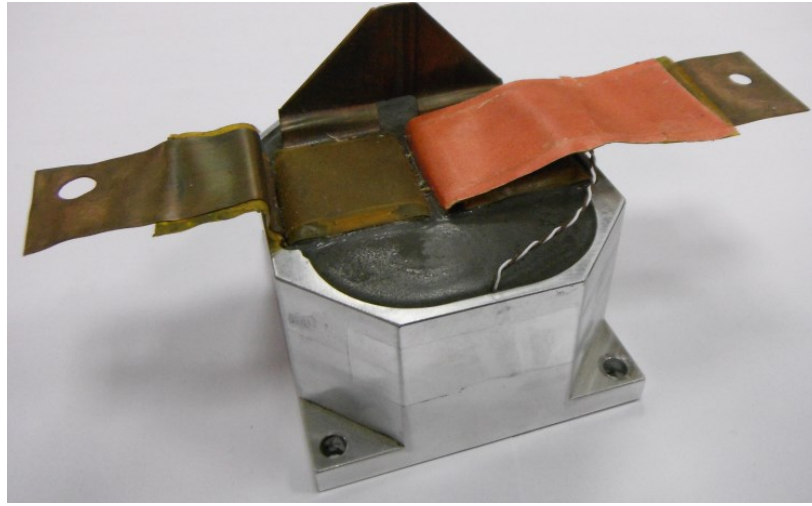


Figure 4.7. Phase inductor of 97.2 kW three-phase boost converter

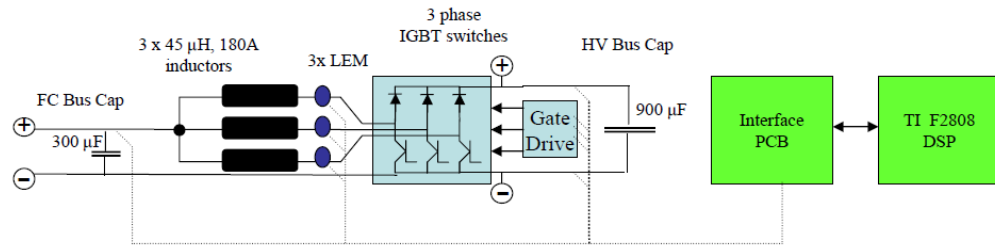


Figure 4.8. Three-phase boost converter schematic

The input and output capacitance are $300 \mu F$ and $900 \mu F$ respectively. The capacitor selected is the FFVE6K0157K from AVX and it is rated for $600 V_{dc}$, $150 \mu F$ and $100 A_{rms}$ [85]. The FFV is a film capacitor designed for dc filtering and has a maximum operating temperature of $150 ^\circ C$. It has a very low level of stray inductance and can withstand large surge voltages, high rms currents and has a long lifetime. The input capacitance consists of two FFV's in parallel while the output capacitance consists of 6 FFV's in parallel.

Three Semikron SEMiX603GB066HDs IGBT modules are used [139]. These modules are rated for $600 V$, $600 A$ operation and are chosen for their higher reliability over other Semikron IGBT modules available at the time.

A single-cut iron-based amorphous metal 2605SA1 CC core from Metglas [81] is used for the construction of the inductor. The iron-based amorphous metal material is shown to have a lower core loss than that of 6.5 % silicon steel 10JNHF600 material from JFE [80]. Although the higher thermal conductivity of the JFE material makes it competitive with the iron-based amorphous metal, the cost of the Metglas material tends to be lower than that of the JFE material. The use of a single-cut core removes the extra cost of cutting the core and it also reduces the impact of higher core loss due to the cutting of iron-based amorphous metal core material. The airgap is limited to 2 mm per leg and the winding is placed at a distance of 3 mm

for the core in order to reduce the ac winding loss due to the fringing flux [82].

The winding is constructed using copper foil due to the high peak-to-peak current ripple as a thin foil helps to reduce the ac winding loss due to fringing flux, skin and proximity effects. The main disadvantage of using a foil winding is the difficulty in removing the heat from the inner layers. If air happens to penetrate between the layers it is very difficult to efficiently remove the heat due to the low thermal conductivity of air. The foil used in the design is sourced from CMC Klebtechnik GmbH [140]. CMC provides self-bonding single-layer Kapton-insulated foil. The special Kapton is rated for 180 °C operation and is coated with thermal adhesive. When the foil is heated for the first time the thermal adhesive on the Kapton between the layers reacts to bond both layers.

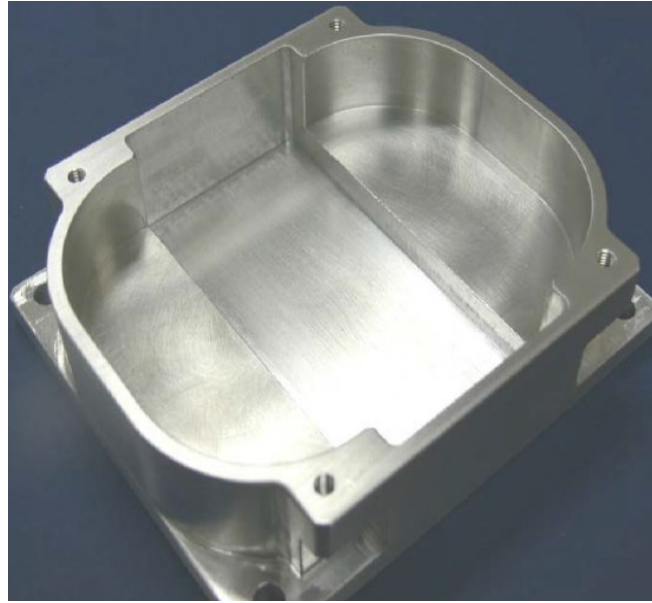


Figure 4.9. Aluminium tray for 3L boost converter

Table 4.1 Phase Inductor Parameters for 16 kHz 3L Converter

L_{phase}	P	N	$l_{\text{g/leg}}$	t_{wind}	$\Delta B_{\text{p-p}}$	P_{loss}	M_{ind}	V_{ind}
μH	kW	-	mm	mm	T	W	kg	cm^3
45	32.4	12	2	0.5	0.68	275	1.3	389

The inductor parameters are presented in Table 4.1. The inductor is potted in an aluminum tray, pictured in Fig. 4.9, in order to increase its mechanical strength. The aluminum tray also helps remove the heat from the inductor and relaxes the requirements for the thermal interface between the copper windings and cold plate. The potting material also allows for the transfer of heat between the core and copper due to its thermal conductivity. A specially developed high tension winding machine is used to construct the windings while ultrasonic welding is used to connect the both windings in series. The ultrasonic weld does not create any

extra weight in the design and there is no increase in termination heating.

4.3. Inductor Design Algorithm

This section briefly describes a CC core inductor design algorithm that is developed to validate the discrete inductor design in the 3L converter as well as to design the 2L discrete inductors.

The algorithm is based on the CCTT IM design algorithm which is modular in nature. The algorithm is developed to solve for minimum inductor boxed volume. Various electrical and magnetic parameters and constraints are input into the algorithm and the minimum inductor boxed volume is determined based on these inputs. The algorithm assumes that operation is restricted to the linear portion of the material B-H curve.

A solution is obtained by seeking the minimum total inductor boxed volume where the core basic dimensions are variables. The algorithm incorporates equations presented by Roters [105] to determine the optimum airgap length. The algorithm allows for one airgap per leg which is limited to 2 mm. The windings are kept at a distance of 3 mm from the core to minimize the effects of airgap fringing flux which is the same as the baseline design. An inductor reluctance model developed and this forms the backbone of the design algorithm.

The algorithm is implemented in Mathematica and relies on the FindMinimum function to obtain the minimized design. The inductor design algorithm allows the design and comparison of CC core inductors over a wide range of frequencies and input current ripple. The algorithm can also be used to design block core inductor designs. The algorithm is modular in structure and this allows for efficient prototyping and quick modification of an inductor design. This modular structure allows each section to be modified or replaced depending on the users design requirements and it shares many similar modules to the CCTT IM algorithm. The user is presented with the option to select which core and winding material is to be used in the inductor design. The user is limited to the choice of solid spiral copper for the windings. It is also possible to select between convection and conduction cooling. Ac copper loss estimation due to the skin effect is included in the algorithm due to the use of large solid single layer spiral conductors [135]. The proximity effects are neglected. 2D FEA is used to determine the ac copper loss due to skin, proximity and airgap fringing effects.

The algorithm consists of 9 main modules (A) – (I) with the defined constraints in (J). (J) uses the FindMinimum function to find the minimum inductor volume based on peak core and pole flux density, maximum allowable power loss, maximum allowable core and winding operating temperature, core width to thickness ratio and winding height and width. Module (E) uses the inductor reluctance model and takes all the relevant fringing regions into account in

order to determine the correct airgap length. In module (I) the inductor temperature rise is determined. The user has the option of selecting a cooling method and can choose from convection or conduction cooling. If all the design constraints in (J) are satisfied then the algorithm finishes and calculates the final inductor dimensions.

4.4. CCTT IM and 2L Magnetic Design

This section describes the design of a ferrite CCTT IM and two iron-based amorphous metal inductors. The next generation designs are for 72 kW, 25 kHz with a higher boost ratio of 155 to 420 V. The goal is to investigate whether the CCTT IM can provide any performance improvements over the high-flux Metglas discrete inductors. The previous section presented the 3L converter which has a worst-case phase current ripple of, ΔI_{p-p} , 125 A. The next generation CCTT IM and 2L options are designed to have this same worst-case phase current ripple.

In order for both designs to achieve this worst-case phase current ripple, the CCTT IM and the 2L inductors are designed for a 34 % and 10 % input current ripple ratio, respectively. This corresponds to a CCTT IM leakage inductance of 10 μ H per phase while the 2L inductors have an inductance of 33.6 μ H per phase. The magnetizing inductance of the CCTT IM is set to be three times the leakage inductance [20].

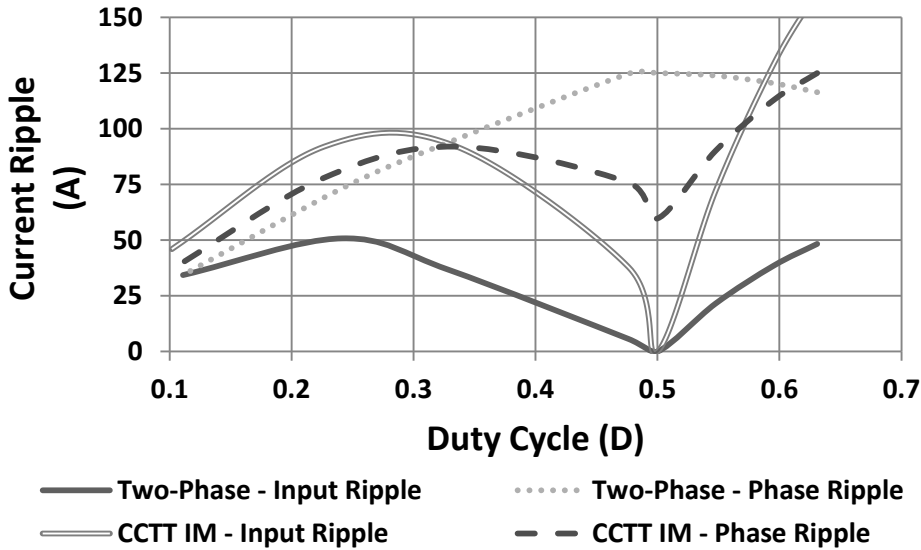


Figure 4.10. Actual 2L and CCTT IM input and phase current ripple with varying fuelcell power

Fig. 4.10 presents the variation of input and phase current ripple for both designs as the fuelcell power varies. These curves highlight the differences in both designs. For example, at a duty ratio, D , of 0.5, the phase current ripple of the 2L design is at its maximum while the CCTT IM is approximately half of that at 62.5 A and only contains the magnetizing component of the phase current ripple. The maximum phase current ripple for the CCTT IM occurs at $D = 0.63$

but interestingly the 2L has a similarly high value. Conversely, the input current ripple for the CCTT IM is at a maximum at this duty ratio while the input ripple of the 2L, while still at its maximum, is approximately three times less than that of the CCTT IM.

4.4.1. Conduction-Cooled CCTT IM and 2L Design

The CCTT IM is designed for the following input data: $V_{in} = 155$ V, $V_{out} = 420$ V, $P_{in} = 72$ kW and $f_s = 25$ kHz, as presented in Table 4.2. The design of the CCTT IM inherently considers a 2 % phase current imbalance which also increases core size in a similar manner to the magnetizing current. The cold-plate temperature is set at 70 °C. The continuous operation temperature of 3C92 material is 140 °C so the maximum allowable temperature rise for the core is 70 °C. The core profile ratio, r_c , which is the ratio of the core thickness d and the core width a , is allowed to change within the range of 1 and 2. The pole profile ratio, r_p , which is the ratio of the core thickness d and the pole height h , is allowed to change within the range of 1 and 2. The maximum allowable temperature rise for the copper windings is 70 °C. The magnetizing path air gap in the CCTT IM is limited to 3 mm in total divided into four separate air gaps. The CCTT IM design uses 5 x 5 mm single layer solid spiral copper wire to allow for the efficient removal of heat from the windings.

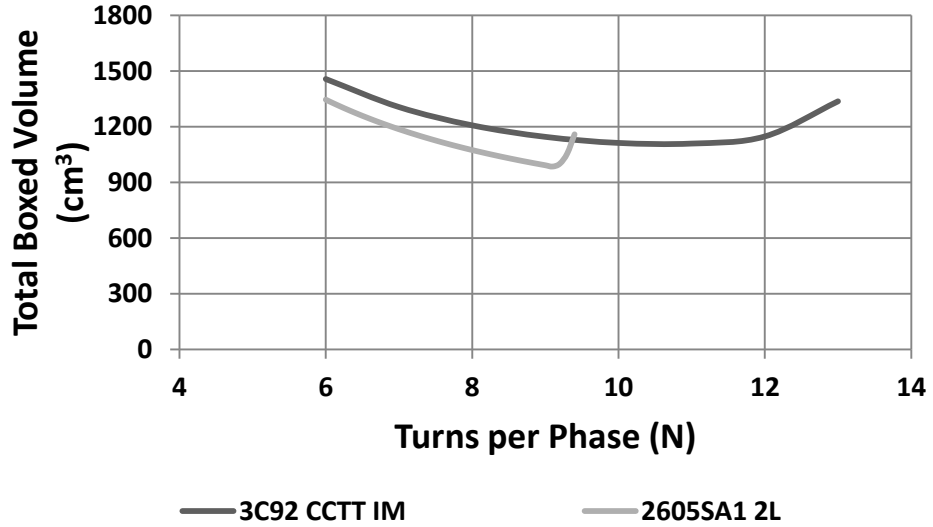


Figure 4.11. Total boxed volume vs. turns per phase

The 2L inductors are designed for the following input data: $V_{in} = 155$ V, $V_{out} = 420$ V, $P_{in} = 72$ kW and $f_s = 25$ kHz, as presented in Table 4.2. The cold-plate temperature is set at 70 °C. The continuous operation temperature of 2605SA1 material is 150 °C. In order to maintain a like-for-like comparison the maximum allowable temperature rise for the core is also set to 70 °C. The core profile ratio, r_c , which is the ratio of the core thickness d and the core width a , is

allowed to change within the range of 1 and 2. The maximum allowable temperature rise for the copper windings is 70 °C. Similar to the CCTT IM, this design assume single layer, 5 x 5 mm, square copper conductors and this ensures each design has the same current density. The air gap in the 2L discrete inductors is limited to 2 mm per leg.

A plot of total CCTT IM and 2L boxed volume as the number of turns per phase is varied is presented in Fig. 4.11. This diagram indicates that the minimum CCTT IM boxed volume occurs at 11 turns per phase while the minimum 2L boxed volume is at approximately 9 turns per phase. The total 2L boxed volume is approximately 10 % less between 6 and 9 turns per phase. After 9 turns per phase the volume of the 2L designs begins to increase.

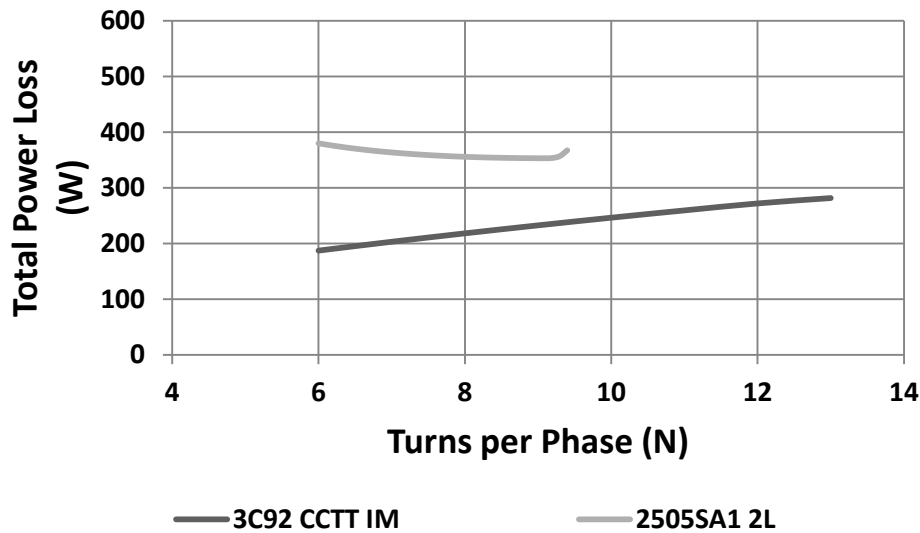


Figure 4.12. Total power loss vs. turns per phase

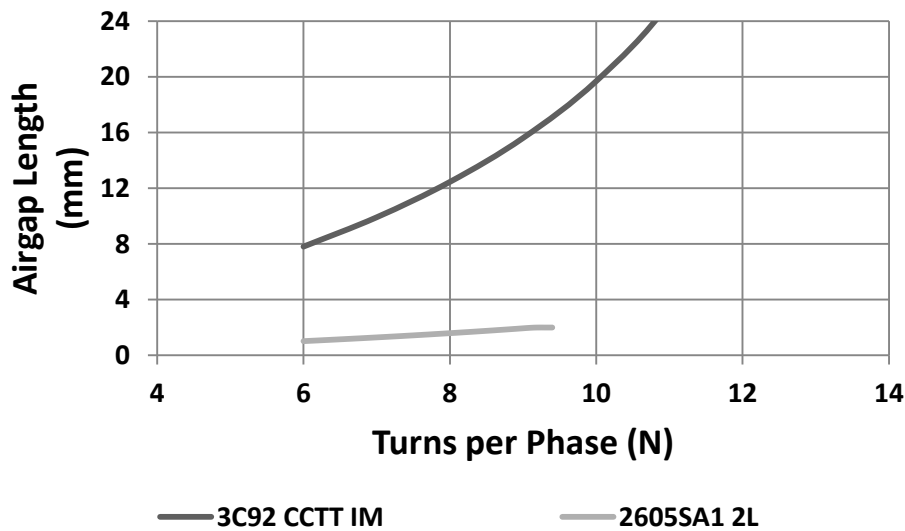


Figure 4.13. Airgap length vs. turns per phase

Table 4.2 CCTT IM and 2L Inductor Parameters

Circuit Conditions			2L	CCTT IM
Input voltage	V_{in}	V	155	155
Output voltage	V_{out}	V	420	420
Input current	I_{in}	A	464	464
Phase current	I_{phase}	A	232	232
Input power	P_{in}	kW	72	72
Frequency	f	kHz	25	25
Phase inductance	L_{phase}	μH	34	-
Leakage inductance	L_{lk}	μH	-	10
Magnetizing inductance	L_m	μH	-	30
Input ripple	ΔI_{in}	A	0	162
Phase ripple	ΔI_{phase}	A	116	125
Core and Winding Mass and Volume				
Material			2605SA1	3C92
Core mass	M_c	kg	$2 \times 1.41 = 2.82$	2.85
Copper mass	M_{cu}	kg	$2 \times 0.34 = 0.68$	0.74
Turns	N	phase	8	8
Core area	A_c	mm^2	$2 \times 1378 = 2756$	1596
Copper area	A_{cu}	mm^2	25	25
Airgap per leg	l_g	mm	1.6	-
Leakage airgap	G	mm	-	12
Total boxed volume	V_{boxed}	cm^3	$2 \times 537 = 1074$	1200
Total mass	M_{total}	kg	3.5	3.59
Total Component Power Loss at Full Rated Power				
Dc winding loss	P_{wdc}	W	176	187
Ac winding loss (FEA)	P_{wac}	W	280	81
Core loss	P_c	W	160	10
Total loss	P_t	W	616	268

Fig. 4.12 presents the total power loss of both magnetic components as the number of turns is varied. The total power loss of the CCTT IM component is in the region of 50 % less than that of the 2L option for 6 turns per phase and this reduces to approximately 30 % for 9 turns per phase. The power loss represented in this diagram is the power loss that is predicted by the design algorithm. The algorithm attempts to estimate the ac copper loss due to the skin effect but it ignores the contribution of the ac copper loss due to proximity and fringing effects.

The value for the ac winding loss presented in Table 4.2 is determined using 2D FEA.

Fig. 4.13 presents the variation in airgap length as the number of turns is varied. In the case of the CCTT IM, the main leakage airgap length begins to significantly increase as the number of turns is increased. It is desirable to keep the leakage airgap length to a reasonable length in order to minimize the amount of fringing flux. For the 2L option, the maximum airgap length is limited to 2 mm per leg and this constraint is reached for 9 turns per phase. Therefore, the overall boxed volume of the 2L inductors increases rapidly in order to accommodate the inductance requirement once the airgap constraint is achieved.

Taking all this information into account, it is decided to undertake a comparison of the 2L and CCTT IM designs for 8 turns per phase. At this condition, CCTT IM is 10 % larger than the 2L option but critically it exhibits 55 % less power loss. Also, the leakage gap length of the CCTT IM is kept at a reasonable length of 12 mm.

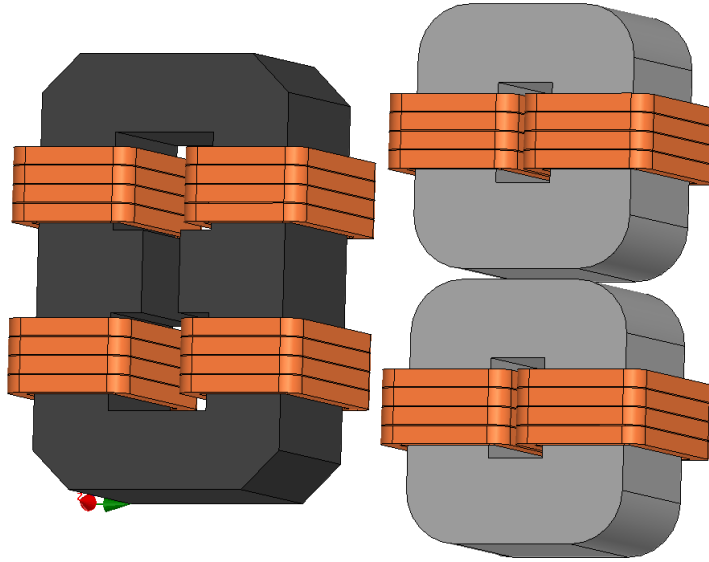


Figure 4.14. Isometric view of CCTT IM and 2L discrete inductors

Table 4.2 outlines all the relevant CCTT IM and 2L inductor parameters while Fig. 4.14 presents an isometric view of both components and this illustrates their physical size with respect to one and other.

4.4.2. Conduction-Cooled CCTT IM Prototype Development and Prototype Design

Following the analysis conducted in Section 4.4.1, a CCTT IM prototype is developed. The initial analysis resulted in a design which required an ac leakage inductance of 10 μH with a corresponding dc leakage inductance of 13 μH . The prototype is modified to have an ac leakage

inductance of 8.6 μH and a corresponding dc leakage inductance of 10 μH . This new design point corresponds to an input current ripple ratio of 40 %. The main dimensions of the CCTT IM prototype along with the circuit parameters are presented in Table 4.3. A schematic drawing of the CCTT IM prototype is presented in Appendix B.1.

Table 4.3 Initial 3C92 CCTT IM and Prototype 3C92 CCTT IM Parameters

Circuit Conditions			Initial Design	Prototype
Input voltage	V_{in}	V	155	155
Output voltage	V_{out}	V	420	420
Input current	I_{in}	A	464	464
Phase current	I_{phase}	A	232	232
Input power	P_{in}	kW	72	72
Frequency	f_s	kHz	25	25
Leakage inductance	L_{lk}	μH	10	8.6
Magnetizing inductance	L_m	μH	30	30
Input ripple	ΔI_{in}	A	162	188
Phase ripple	ΔI_{phase}	A	125	140
Core and Winding Mass and Volume				
Material			3C92	3C92
Core leg width	a	mm	28.5	28
Core window width	b	mm	30.5	28
Core window length	c	mm	92	76
Core thickness	d	mm	57	48
Pole height	h	mm	36	22
Pole length	x	mm	9	9
Leakage gap	g	mm	12	10
Magnetizing gap	l_{g_mag}	mm	4 x 0.92	4 x 0.85
Core mass	M_c	kg	2.85	2.2
Copper mass	M_{cu}	kg	0.74	0.62
Turns	N	phase	8	8
Core area	A_c	mm^2	1596	1344
Boxed volume	V_{boxed}	cm^3	1200	1040
Total Component Power Loss at Full Rated Power				
Dc winding loss	P_{wdc}	W	187	177
Ac winding loss	P_{wac}	W	81	98
Core loss	P_c	W	10	10
Total loss	P_t	W	278	285

The CCTT IM algorithm is used to develop an initial design. 3D FEA, such as dc and transient simulations, is used to determine the dc and peak flux operating conditions of the IM while 2D FEA is used to determine the ac winding power loss. 2D FEA is also used to investigate if the thermal constraints are satisfied. Although other methods of determining the core power loss are available [128, 141-146] the core loss in this analysis is determined using the modified Steinmetz equation (MSE) [136, 147]. The predicted and actual loss of the prototype CCTT IM is presented in Section 4.10.

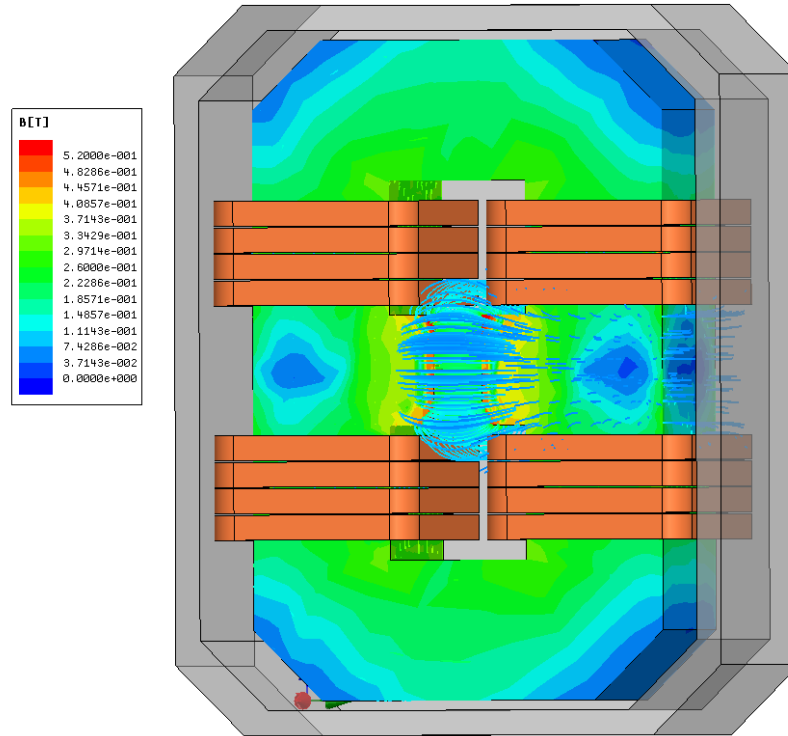


Figure 4.15. Dc flux plot of prototype CCTT IM illustrating fringing flux from the pole section

Table 4.4 CCTT IM Dc Inductance Matrix

	Phase A	Phase B
	μH	μH
Phase A	39.845	-29.91
Phase B	-29.91	39.859

3D FEA is used to validate the CCTT IM prototype and to ensure that the core does not enter into saturation when operating at its full power condition. Firstly, a dc magnetostatic simulation is carried out to determine the dc leakage and magnetizing inductance using the in-build inductance matrix. Fig. 4.15 presents a dc flux plot of the CCTT IM while Table 4.4 presents the inductance matrix result. The inductance matrix illustrates that the CCTT IM has a

self-inductance of just under 40 μH and a mutual inductance of nearly 30 μH and due to the unity turns ratio of the device, the magnetizing inductance is 30 μH . The inductance matrix indicates that the dc leakage inductance is 9.935 μH .

The second simulation employs the transient solver in order to determine the ac leakage inductance. In this simulation the leakage component of the phase current ripple is used as the input to the solver. The core is surrounded by an external aluminum shield and the inductance is determined using the in-build field calculator. Table 4.5 presents the results of the unshielded and shielded simulations. The predicted algorithm values are extremely close to the simulated values and this validates that the reluctance model works excellently in predicting the relevant inductance values.

Finally, the transient solver is used to determine the maximum flux distribution in the core when it is operating at full power. Fig. 4.17 presents the waveforms that are used as inputs to the solver. The current applied to each phase is a combination of the dc phase current, phase current imbalance, phase current ripple due to leakage and phase current ripple due to magnetizing. Fig. 4.18 presents the flux distribution at $t = 25.2 \mu\text{s}$ which corresponds to the peak phase current. The highest flux density value is in the region of greater 0.40 T, which is greater than the design point of 0.32 T, but still under the saturation flux density level of 0.52 T for 3C92.

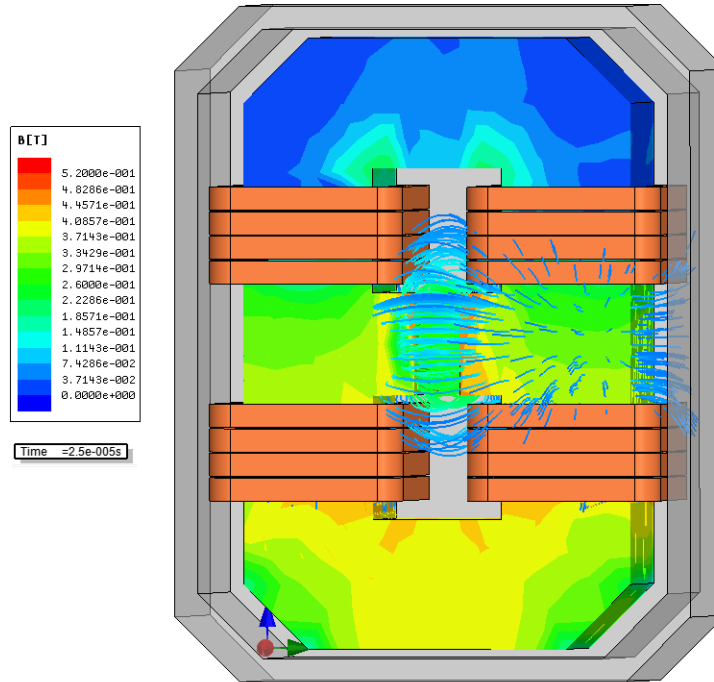


Figure 4.16. Transient simulation of prototype CCTT IM at $t = 25.2 \mu\text{s}$ corresponding to the peak of the phase current ripple

2D FEA is used to validate the thermal model of the CCTT IM design algorithm. As previously discussed in Section 3.5.1, the core and winding heat paths are assumed to be

separate. Thermal plots for the core and winding of the CCTT IM is presented in Fig. 4.18 and Fig. 4.19, respectively. The temperature rise in the core is relatively minor, at 6 °C, which is to be expected as the core is limited by its saturation flux density. The winding temperature hotspot is 38 °C which is significantly lower than its maximum allowable temperature rise of 80 °C. A further optimization point would be to reduce the size of the copper cross-sectional area. Table 4.6 presents the predicted thermal results from the algorithm and the simulated results.

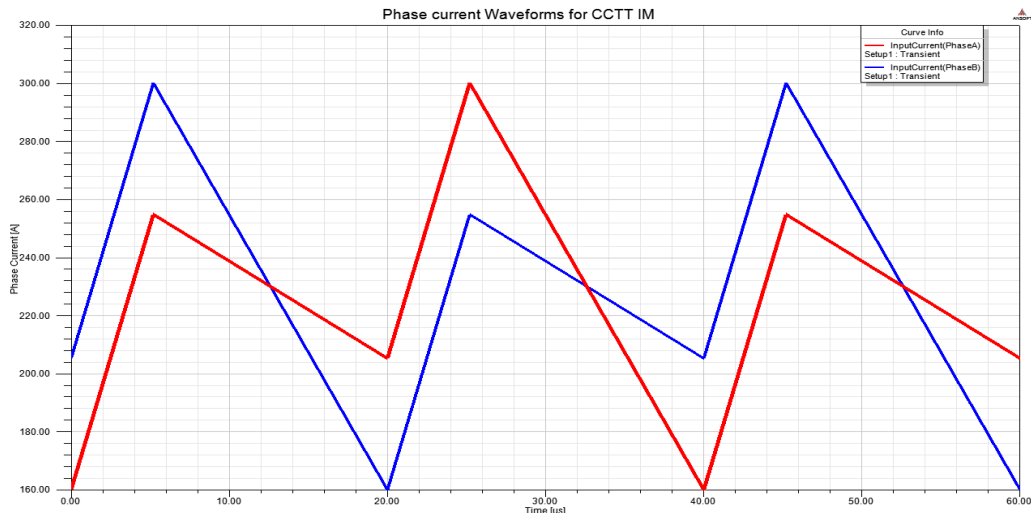


Figure 4.17. Phase current waveforms for transient simulation

Table 4.5 Comparison of Dc and Ac Inductance for 72 kW Prototype CCTT IM

		CCTT IM	
		Algorithm	3D
$L_{lk, dc}$	μH	9.8	9.9
$L_{lk, ac}$	μH	8.6	8.4

2D FEA is used to accurately determine the ac winding power loss in the CCTT IM prototype design. The phase current ripple is a combination of the magnetizing and leakage current ripple and is asymmetrical in nature. The phase current harmonics are used as inputs to the 2D solver, which is used to compute the ac winding power loss. The first five harmonics are considered. The power loss due to each harmonic is evaluated and then summed to find the total ac winding power loss. Two tests are conducted (i) to determine the ac winding loss at various winding distances from the core and pole, and (ii) to investigate the shielding effect of the pole section.

Firstly, the winding is placed at various distances from the core and pole section and the results are tabulated in Table 4.7. The results indicate very little variation in the ac winding loss.

In this analysis, it is assumed that the pole section extends a distance of 1 mm greater than the winding in order to provide some shielding effect. The pole is used to shape the flux through the leakage airgap and also to shield the windings from the flux that fringes from this airgap.

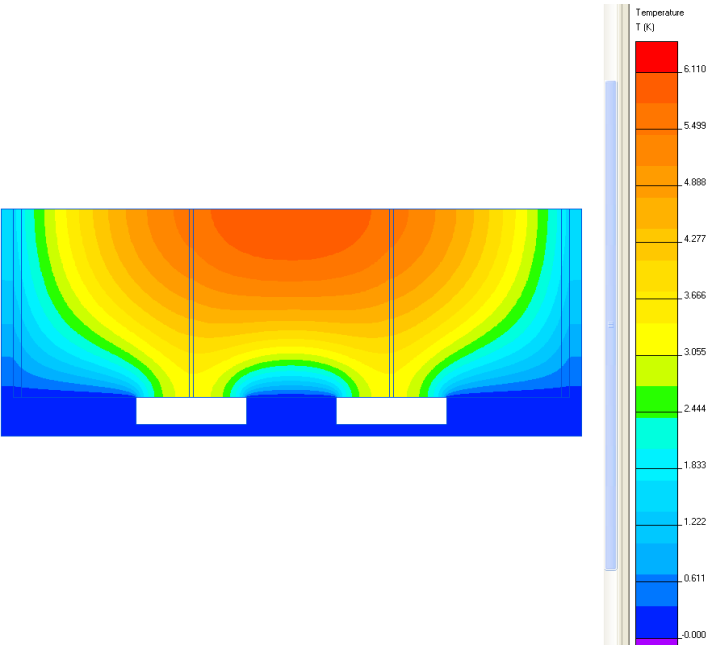


Figure 4.18. 2D thermal analysis of prototype CCTT IM core

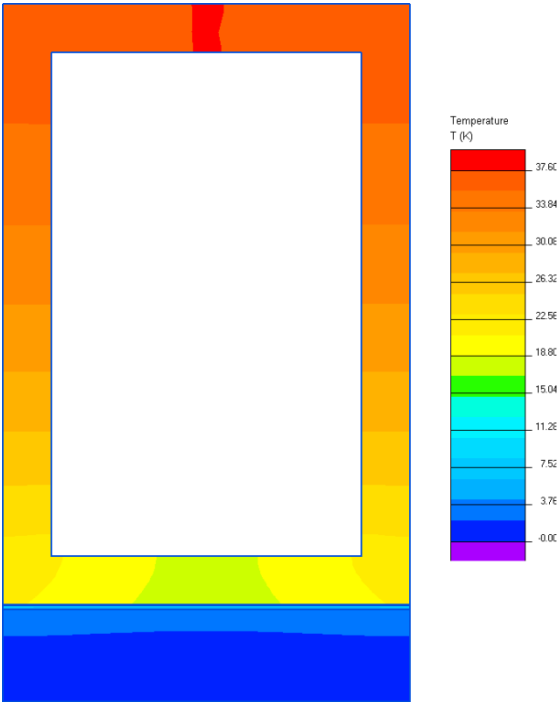


Figure 4.19. 2D thermal analysis of prototype CCTT IM winding

Table 4.6 Predicted and Simulated CCTT IM Prototype Thermal Results

		CCTT IM	
		Algorithm	2D
Core	°C	5	6
Winding	°C	44	38

Table 4.7 CCTT IM Ac Winding Power Loss in Watts

Distance from Core		Distance from Pole		
		1	2	3
	mm	mm	mm	mm
1	mm	139	142	142
2	mm	136	138	139
3	mm	134	137	138

Table 4.8 CCTT IM Ac Winding Power Loss in Watts

		Pole Shielding			
		1	2	3	4
	mm	mm	mm	mm	mm
Power Loss	W	138	105	92	84

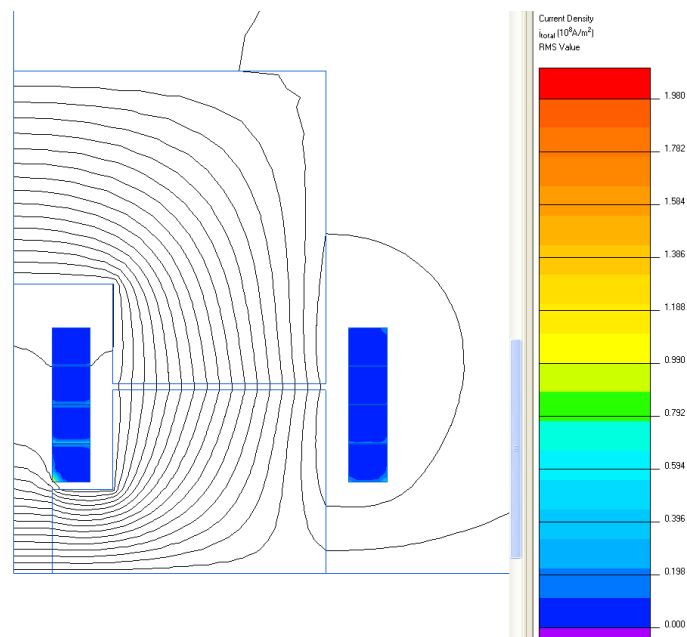


Figure 4.20. Current density plot with no pole shielding (0 mm)

In the second test, the winding is fixed at a distance of 3 mm from the core and 2 mm from the pole. With the winding fixed at this location the extension in pole length beyond the winding is allowed to vary in increments of 1mm, from 1 mm to 4 mm. Table 4.8 presents the ac power loss with the variation of pole length. It is clear that the ac winding loss is significantly reduced as the pole length is increased in order to shield the windings. In the prototype design, the pole is set to overlap the windings by 2 mm but a longer overlap should be considered to reduce the ac loss. Current density plots, Fig. 4.20 and Fig. 4.21 are included in order to illustrate the concept of how the pole sections help to shield the windings from the pole fringing flux. Fig. 4.20 is when the pole section is flush with the windings while Fig. 4.21 is when the pole sections overlap the windings by 4 mm.

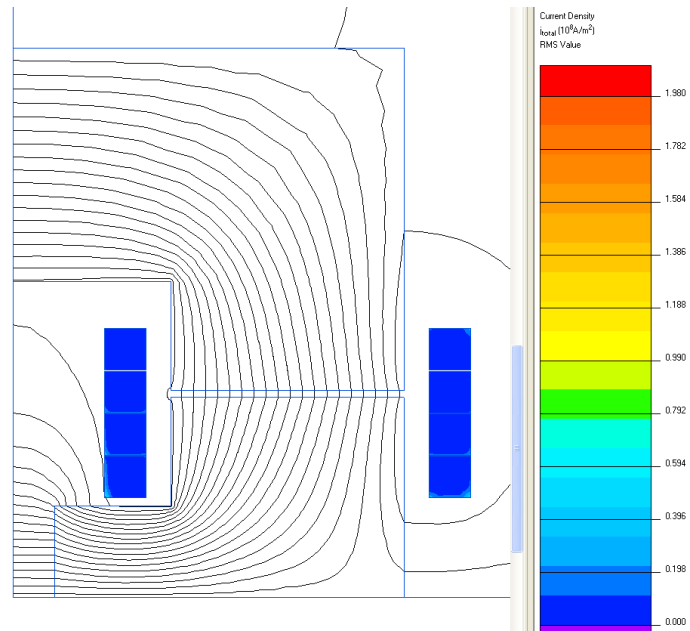


Figure 4.21. Current density plot with pole shielding (4 mm)

4.4.2.1. Distributed Leakage Gap Investigation

Using a multi-cut gap has been shown to reduce the ac power loss in inductors [22, 23]. This section investigates if a multi-cut leakage gap can help to reduce the ac power loss in the CCTT IM. Firstly, 3D FEA is used in order to confirm that the multiple-gap technique produces the required leakage inductance. Fig. 4.22 and Fig. 4.23 present 3D FEA dc flux plots for a 5 airgap and 8 airgap CCTT IM. Table 4.9 presents the dc and ac leakage inductance of a single airgap, 2 airgap, 5 airgap and 8 airgap CCTT IM. It is clear that as the number of gaps is increased the dc and ac inductance produced is reduced indicating that there is less fringing flux present.

Table 4.9 Dc and Ac Leakage Inductance for Multiple Airgap Designs

Number of Gaps	L_{dc}	L_{ac}
	μH	μH
1	11.2	8.9
2	9.3	7.6
5	8.9	7.3

Table 4.10 Ac Power Loss for Multiple Airgap Design

Number of Gaps	Power Loss
	W
2	114
5	97
8	100

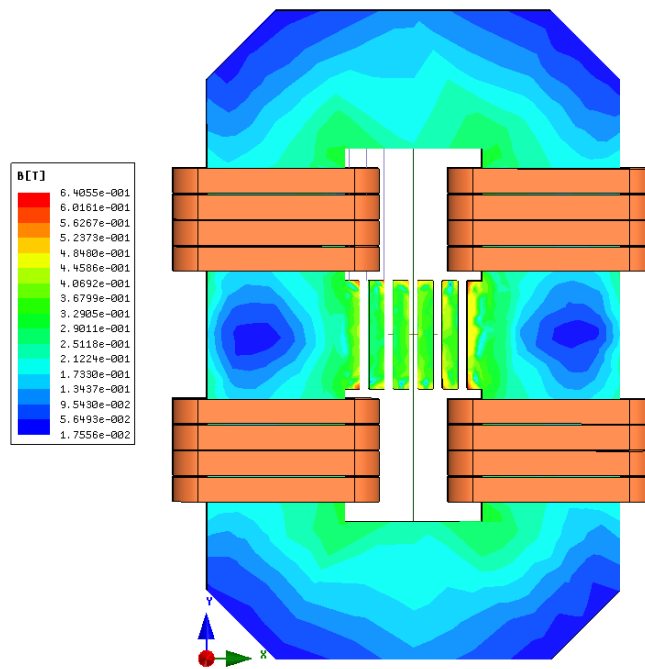


Figure 4.22. CCTT IM with 5 leakage airgap sections

2D FEA is conducted in order to determine the ac winding loss in distributed gap options. The optimal winding placement, of 3 mm from the core and 1 mm from the pole, was determined in the previous section and, in this analysis the windings are placed at this distance. The leakage current ripple for the second and fourth harmonics is used as input to the solver.

Fig. 4.24 and Fig. 4.25 present the current density plots, at the second harmonic of ± 36 A, for the 5 airgap and 8 airgap options, respectively. Table 4.10 presents the ac power loss results. The results indicate that there is little benefit in using the multi-gap in order to reduce

the ac winding loss. Although the multi-gap technique produces less fringing flux the reduced pole length means that the windings are not protected from the fringing flux.

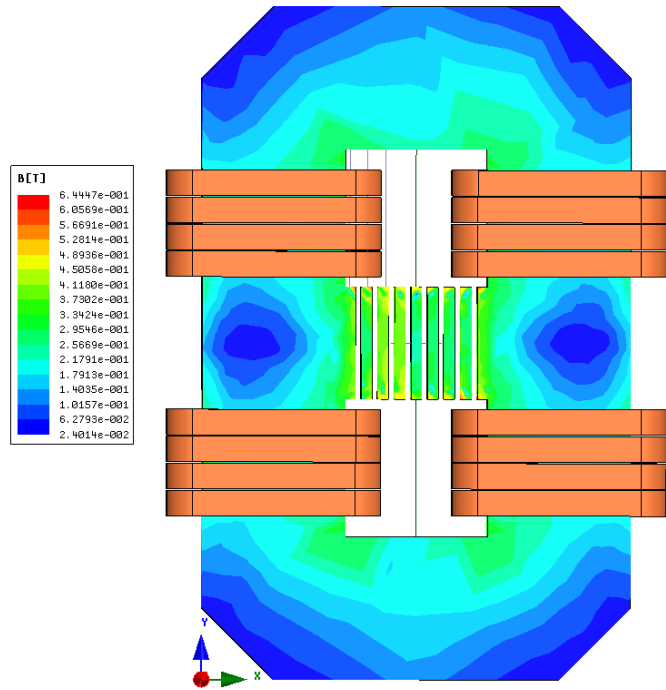


Figure 4.23. CCTT IM with 8 leakage airgap sections

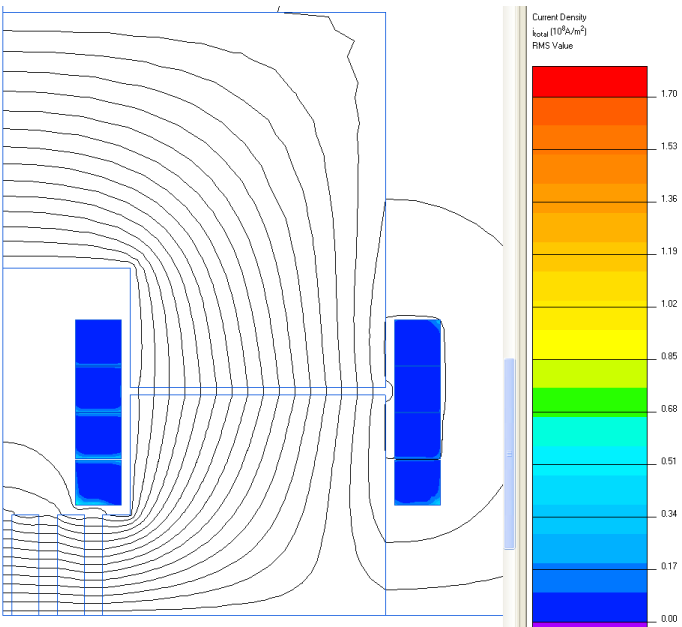


Figure 4.24. Current density plot for CCTT IM with 5 leakage airgap sections

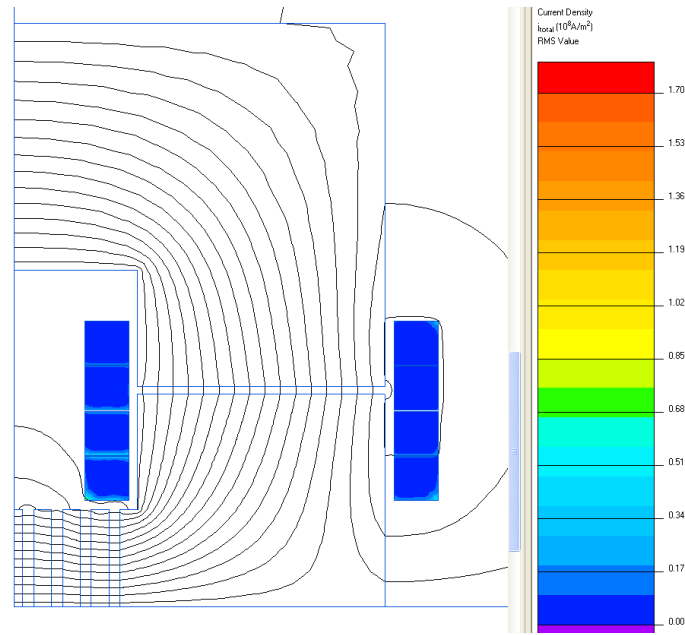


Figure 4.25. Current density plot for CCTT IM with 8 leakage airgap sections

4.4.3. Conduction-Cooled 2L Discrete Inductor Design and Validation

Following the analysis conducted in Section 4.4.1, a 2L paper design is developed. The 2L solution is still designed for the same conditions as presented in Section 4.4.1 and the main parameters are presented in Table 4.2. The 2L inductor design algorithm is used to develop an initial design. In a similar manner to the CCTT IM, 3D FEA, such as dc and transient simulations, is used to determine the dc and peak flux operating conditions of the IM while 2D FEA is used to determine the ac winding power loss. 2D FEA is also used to investigate if the thermal constraints are satisfied.

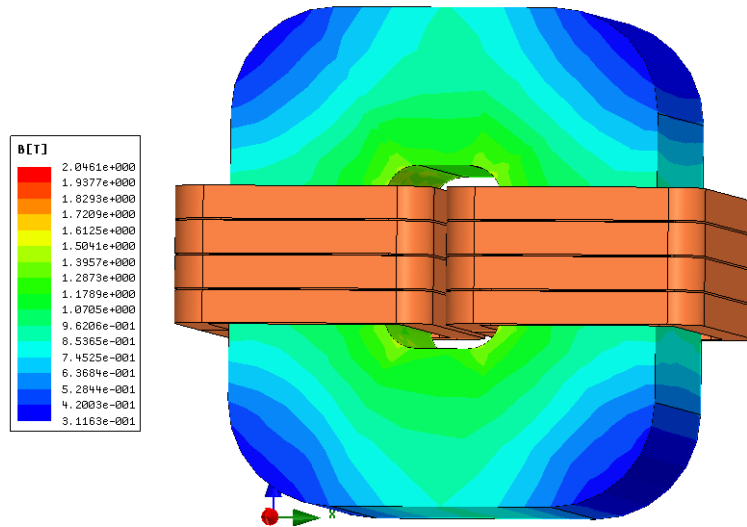


Figure 4.26. Dc flux density plot of 2L discrete inductor

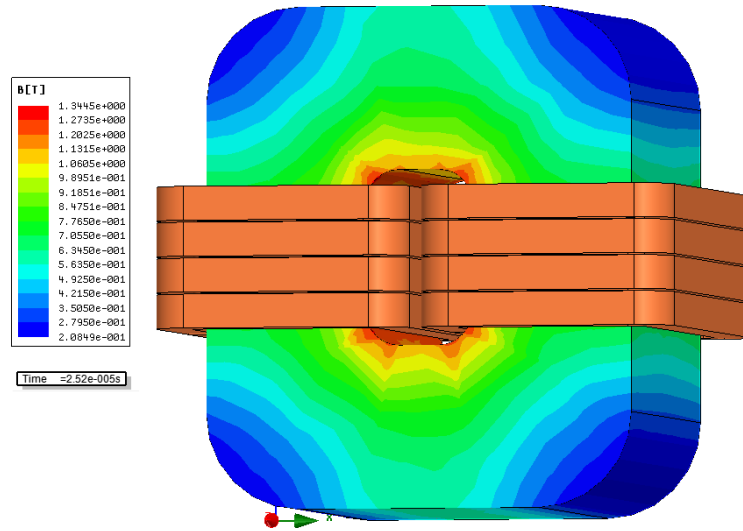


Figure 4.27. Transient flux plot of 2L discrete inductor at $t = 25.2 \mu s$

Fig. 4.26 and Fig. 4.27 present the dc and transient flux density plots for the 2L inductor respectively. Transient analysis is conducted in order to determine the flux distribution at the peak phase current ripple. Fig. 4.27 corresponds to time $t = 25.2 \mu s$ which is the peak of the phase current ripple. Both inductors are seen to operate below their saturation point.

Table 4.11 presents the inductance calculations from the FEA simulations. The algorithm appears to under predict the required inductance value as the 3D FEA indicates that the inductor will have an inductance of $38 \mu H$.

Table 4.11 Comparison of Dc and Ac Inductance for 72 kW 2L Discrete Inductor

		2L	
		Algorithm	3D
$L_{lk, dc}$	μH	35	38
$L_{lk, ac}$	μH	35	38

Fig 4.28 and Fig. 4.29 present the thermal core and winding plots of the 2L discrete inductor. The predicted and simulated temperature rise of the core and winding are presented in Table 4.12.

Table 4.12 Predicted and Simulated 2L Thermal Results

		2L	
		Algorithm	2D
Core	$^{\circ}C$	32	42
Winding	$^{\circ}C$	45	41

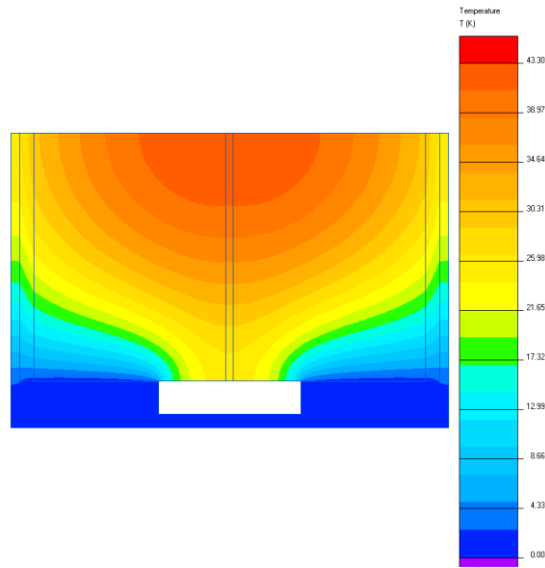


Figure 4.28. 2D thermal analysis of 2L discrete inductor core

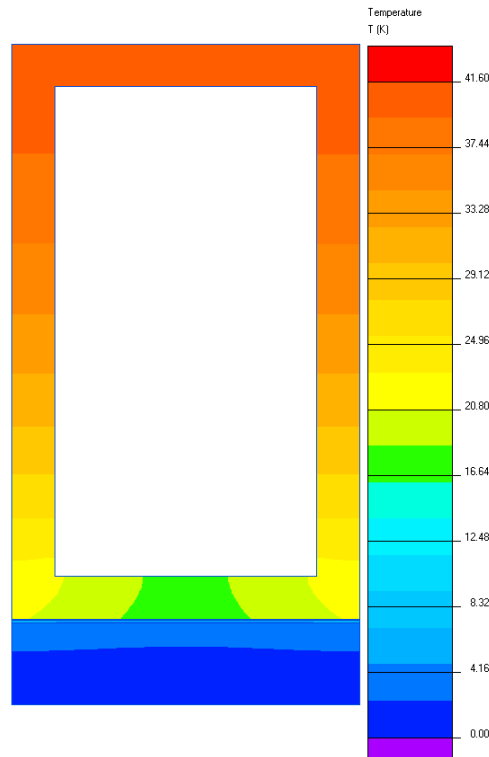


Figure 4.29. 2D thermal analysis of 2L discrete inductor winding

4.5. Semiconductor Analysis

This section outlines the methodology by which the semiconductor loss is evaluated. It is decided to use the same semiconductor modules as the 3L baseline boost converter. Therefore, two 600 V, 600 A, SEMiX603GB066HDs IGBTs with anti-parallel diodes, from Semikron are used in the analysis. The total IGBT loss is divided into the switch and diode conduction and

switching loss. Firstly, dealing with the conduction loss, the following currents are determined: inductor RMS current, $I_{l(rms)}$, switch RMS current, $I_{Q(rms)}$, switch average current, $I_{Q(avg)}$ diode RMS current, $I_{D(rms)}$, and average current, $I_{D(avg)}$. The knee voltage, V_{knee} , and on-resistance, R_{ce} , of the switch and, the forward voltage, V_f , and forward resistance, R_f , of the diode is estimated from Fig. 4.30.

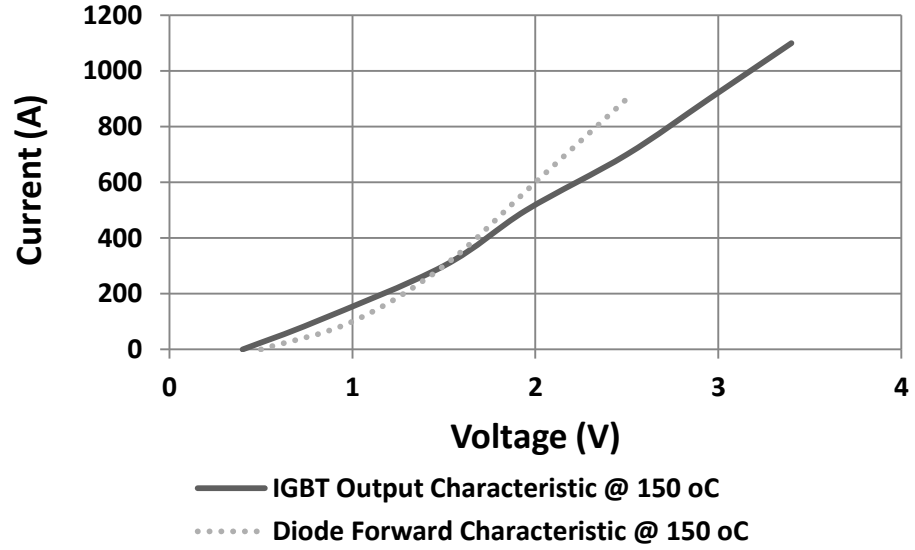


Figure 4.30. IGBT and diode characteristics

The semiconductor conduction loss is determined using the standard equation that is a function of the knee voltage, dc switch current, switch resistance and switch RMS current. The IGBT and diode conduction losses are computed using equations (4.1) and (4.2).

$$P_{Q(cond)} = V_{CE(Knee)} I_{Q(avg)} + R_{on} I_{Q(rms)}^2 \quad (4.1)$$

$$P_{D(cond)} = V_{Knee} I_{D(avg)} + R_f I_{D(rms)}^2 \quad (4.2)$$

To determine the switching loss, the turn-on and turn-off energies are estimated from Fig. 4.31. It should be noted that the diode reverse recovery energy loss is included in the IGBT turn-on loss and this helps to simplify the analysis. This information must be scaled with the actual circuit parameters as the switch turns on when the inductor current is at its minimum and the switch turns off when the inductor current is at its maximum. Equations (4.3), (4.4) and (4.5) outline how the turn-on, turn-off and total switching losses are determined.

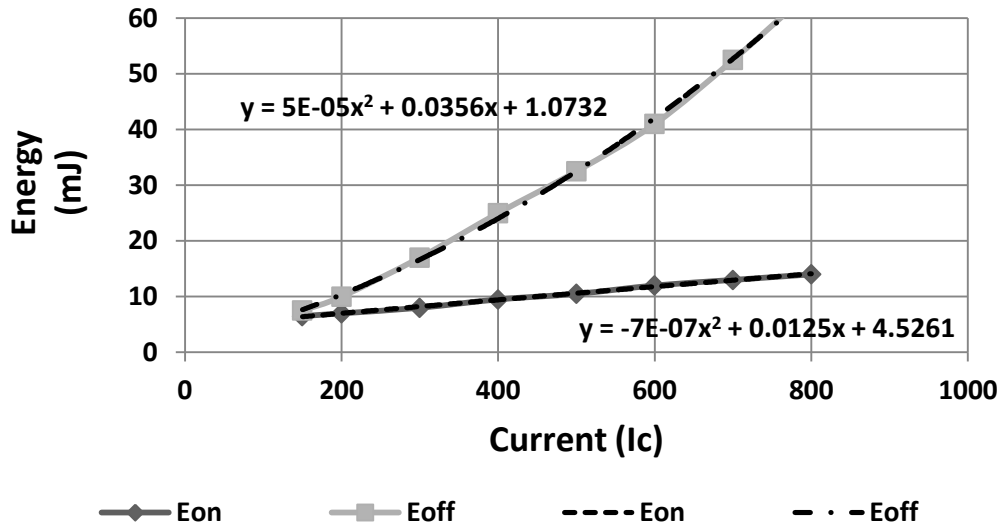


Figure 4.31. Turn-on and turn-off energy for Semikron IGBT module

$$E_{on} = (A_{on}I_{L(min)}^2 + B_{on}I_{L(min)} + C_{on}) \frac{V_o}{V_{rated}} \quad (4.3)$$

$$E_{off} = (A_{off}I_{L(max)}^2 + B_{off}I_{L(max)} + C_{off}) \frac{V_o}{V_{rated}} \quad (4.4)$$

$$P_{switching} = f_s (E_{on} + E_{off}) \quad (4.5)$$

Where V_o is the voltage on the dc-link and V_{rated} is taken from the datasheet.

If the diode reverse-recovery loss is not included with the IGBT turn-on loss then it can be determined by using (4.7). In a similar manner to the IGBT turn-on and turn-off loss, the diode reverse recovery loss is determined from the datasheet and then scaled with the actual circuit parameters.

$$E_{rr} = E_{rr_rated} \frac{I_{L(min)}}{I_{rated}} \frac{V_o}{V_{rated}} \quad (4.6)$$

$$P_{diode} = f_s (E_{rr}) \quad (4.7)$$

Table 4.13 presents a breakdown of the system currents while Table 4.14 to Table 4.18, present a breakdown of the conduction, turn-on and turn-off switching loss and diode reverse recovery loss respectively, for the following circuit parameters: $V_{in} = 155$ V, $V_{out} = 420$ V, $P_{in} = 72$ kW, $I_{in} = 464$ A and $I_{phase} = 232$ A.

Table 4.13 Breakdown of System Currents in 2L and CCTT IM Topologies

	$I_{c(rms)}$	$I_{L(rms)}$	$I_{Q(rms)}$	$I_{Q(avg)}$	$I_{D(rms)}$	$I_{D(avg)}$	$I_{L(max)}$	$I_{L(min)}$
	A	A	A	A	A	A	A	A
2L	13.9	234.4	186.2	146.4	142.4	85.6	290.2	173.8
CCTT IM	46.7	234.8	186.5	146.4	142.6	85.6	294.5	169.5

Table 4.14 Breakdown of Conduction Loss in 2L and CCTT IM Topologies

	IGBT Conduction Loss				Diode Conduction Loss				Total
	V_{ce}	R_{ce}	P_{cond_Q}	$P_{cond_Q_2Ph}$	V_f	R_f	P_{cond_D}	$P_{cond_D_2Ph}$	P_{cond_Total}
	V	mΩ	W	W	V	mΩ	W	W	W
2L	0.9	2.00	201.1	402.2	1.1	0.9	1.4	122.6	245.2
CCTT IM	0.9	2	201.3	402.6	1.1	0.9	1.4	122.6	245.2

Table 4.15 Breakdown of Turn-on Loss in 2L and CCTT IM Topologies

	V_{rated}	I_{rated}	A_{on}	B_{on}	C_{on}	E_{on}	P_{Q_on}	$P_{Q_on_2Ph}$
	V	I	-	-	-	mJ	W	W
2L	300	600	-7.00E-07	1.25E-02	4.53	9.3	233.7	467.4
CCTT IM	300	600	-7.00E-07	1.25E-02	4.53	9.2	231.8	463.7

Table 4.16 Breakdown of Turn-off Loss in 2L and CCTT IM Topologies

	V_{rated}	I_{rated}	A_{off}	B_{off}	C_{off}	E_{off}	P_{Q_off}	$P_{Q_off_2Ph}$
	V	I	-	-	-	mJ	W	W
2L	300	600	5.00E-05	3.56E-02	1.07	21.8	546.5	1093
CCTT IM	300	600	5.00E-05	3.56E-02	1.07	22.2	556.2	1112.4

Table 4.17 Breakdown of Diode Turn-on Loss in 2L and CCTT IM Topologies

	V_{rated}	I_{rated}	E_{rr_rated}	E_{rr}	P_{Q_on}	$P_{Q_on_2Ph}$
	V	I	-	-	W	W
2L	300	600	0.013	0.051	132	264
CCTT IM	300	600	0.013	0.051	129	258

Table 4.18 Total Loss in 2L and CCTT IM Topologies

	P_{cond_Total}	$P_{Switching_Total}$	P_{Total}
	W	W	W
2L	648	1828.4	2476.4
CCTT IM	648	1834.1	2482.1

4.6. Analysis of Power Loss over Variable Fuelcell Power Range

The 2L discrete inductor set presented in Table 4.2 and the CCTT IM prototype inductor presented in Table 4.3 are analysed over the operating range of a fuelcell. The voltage at the output of the fuelcell, seen in Fig. 4.1, varies from 155 V to 260 V while the dc bus is required to maintain a constant voltage of 420 V. The fuelcell current varies from 0 A at no-load to 464 A at full-load. As the fuelcell output power varies so will the losses in the magnetic and semiconductor components.

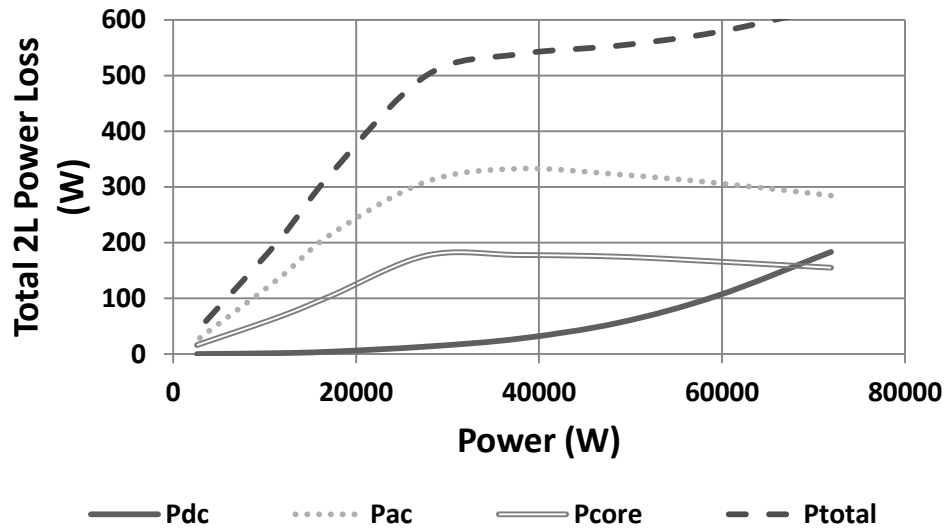


Figure 4.32. Breakdown of total 2L inductor loss with varying fuelcell power

Fig. 4.32 and Fig. 4.33 present the 2L and CCTT IM magnetic loss over fuelcell operating power respectively. This analysis indicates that the CCTT IM will have approximately half of the power loss compared to the combined 2L discrete inductors. The dc power loss in both options is essentially the same which is to be expected both designs have the same number of turns and winding cross-sectional area as well as quite a similar core cross-sectional area. It is clear that there is a significant difference in the core and ac winding loss of both designs. Interestingly, the core and ac power loss of both options follow the same curve as the phase current ripple in both converters. Therefore, the 2L discrete inductors have significant loss over

the entire fuelcell operating range while the CCTT IM sees a substantial reduction in this loss in and around the region of $D = 0.5$.

The analysis also considers the semiconductor loss in each topology, presented in Fig. 4.34 and Fig. 4.35. Interestingly, the power loss of both topologies is seen to be very similar. The conduction loss for both topologies is the same. In terms of the switching loss both designs are quite similar. Although the CCTT IM benefits from reduced phase-current ripple, especially at medium load, any reduction in turn-off current (for the IGBT) is offset by an increased turn-on current.

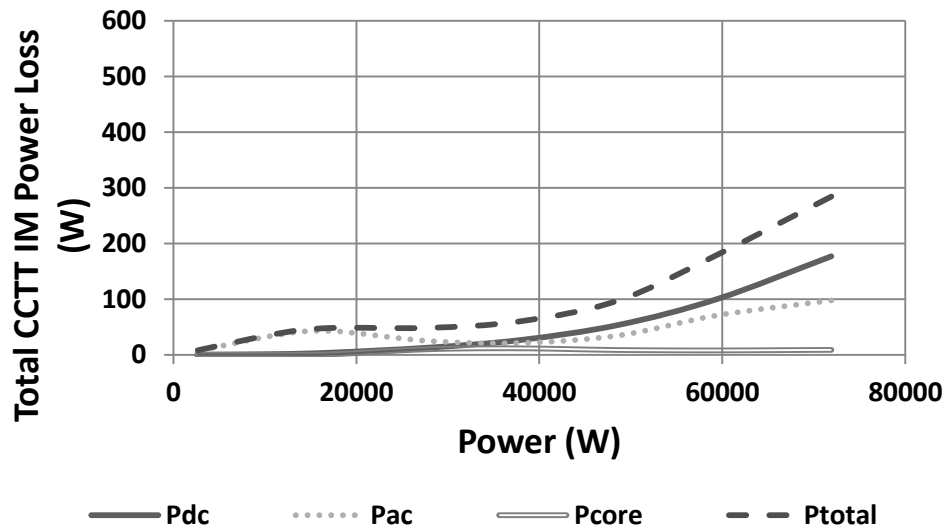


Figure 4.33. Breakdown of total CCTT IM power loss with varying fuelcell power

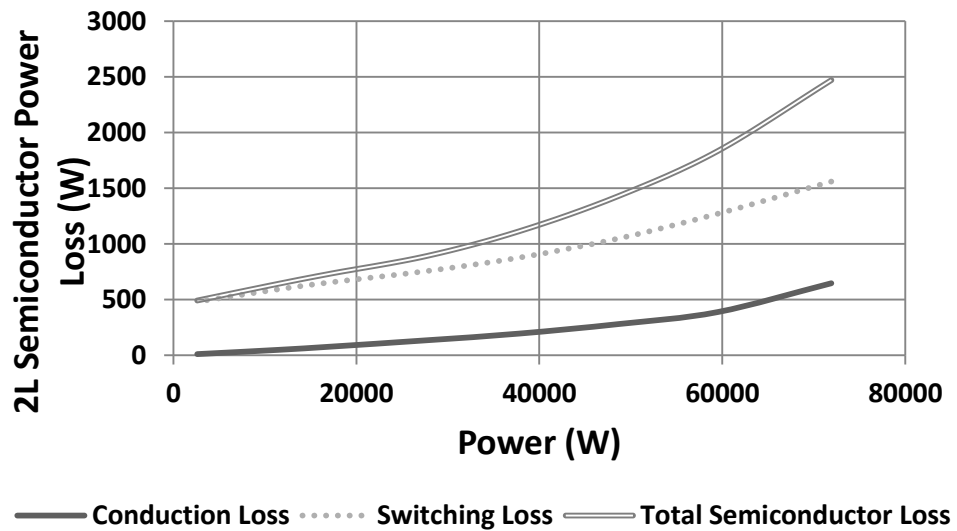


Figure 4.34. Breakdown of semiconductor loss in 2L topology

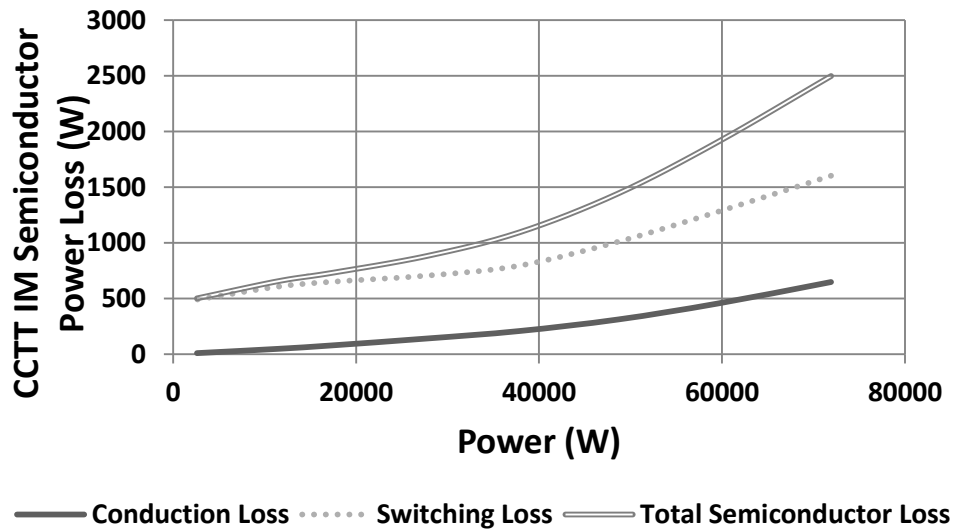


Figure 4.35. Breakdown of semiconductor loss in CCTT IM topology

Fig. 4.36 presents the total 2L and CCTT IM converter efficiencies. The CCTT IM converter efficiency is greater than that of the 2L over the entire load range and it is significantly greater at part-load conditions. The reduced 2L efficiency at part-load is explained by its greater phase current ripple which contributes to increased ac winding and core loss.

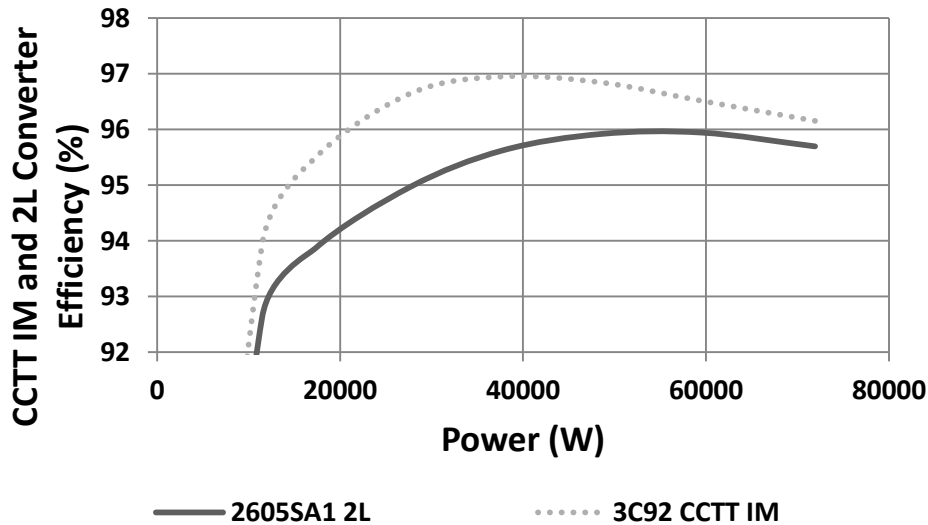


Figure 4.36. 2L and CCTT IM converter efficiency over fuelcell power range

4.7. Capacitor Sizing and Design

The CCTT IM exhibits reduced phase current ripple over the fuelcell power range with both designs having the same worst-case phase ripple current. On closer inspection of Fig. 4.10 it is clear that the CCTT IM has a much higher worst-case input current ripple. This directly

translates into the need for a larger input filter capacitance value in order to provide the filtering required by the fuelcell. This section briefly sizes the input filter capacitor of both topologies.

4.7.1. Input Filter Capacitor Sizing

Table 4.19 presents the capacitor sizing for the 2L and CCTT IM designs where both capacitors are designed to provide the same level of filtering. The input ripple of the CCTT IM is larger and this results in a larger input filter capacitor. The prototype capacitors are designed specifically for automotive applications in conjunction with a leading thin-film capacitor manufacturer.

Table 4.19 2L and CCTT IM Input Capacitor Sizing

Converter Type	C	i_{crms}	V_{cap}	T_a	T_{max}	T_{rise}
	μF	A	cm^3	$^{\circ}C$	$^{\circ}C$	$^{\circ}C$
2L	150	21	319	70	85	2
CCTT IM	372	55	742	70	85	2

4.8. 2605SA1 CCTT IM Design

This section describes the design of a high B_{sat} CCTT IM using 2605SA1 laminated material from Metglas. Fig. 4.6 (a) and (b) highlighted how an iron-based amorphous metal CCTT IM allows for a reduction in boxed volume with respect to the 3C92 CCTT IM at the expense of increased core loss. This section will outline the magnetic design of a medium-ripple amorphous metal CCTT IM and will also investigate its power loss as the fuelcell power is varied. The manufacturability of such an IM will also be discussed.

4.8.1. Conduction-Cooled 2605SA1 CCTT IM Magnetic Design

The high B_{sat} CCTT IM is designed using the same conditions as the 3C92 CCTT IM prototype as presented in Section 4.4.2, which is for 40 % input current ripple ratio. The variation in boxed volume with input current ripple for increasing number of turns is presented in Fig. 4.37. To give a complete picture, the 3C92 CCTT IM and 2L discrete inductor curves are included on the same diagram.

The boxed volume of the 2605SA1 CCTT IM is significantly smaller than that of the 3C92 CCTT IM and 2L discrete inductor set. The boxed volume varies from a maximum of $600 cm^3$ at 6 turns per phase to $300 cm^3$ at 12 turns per phase. At our design point of interest,

corresponding to 8 turns per phase, the 2605SA1 CCTT IM is 66 % smaller than the 3C92 CCTT IM and 60 % smaller than the 2L inductor set. At this point of interest the 2605SA1 CCTT IM has a similar power loss to that of the 2L inductors and this can be seen in Fig. 4.38. Designing for the same phase current ripple allows the 2605SA1 CCTT IM to have a significantly smaller size in comparison to the 2L inductor set due to its lower inductance requirement.

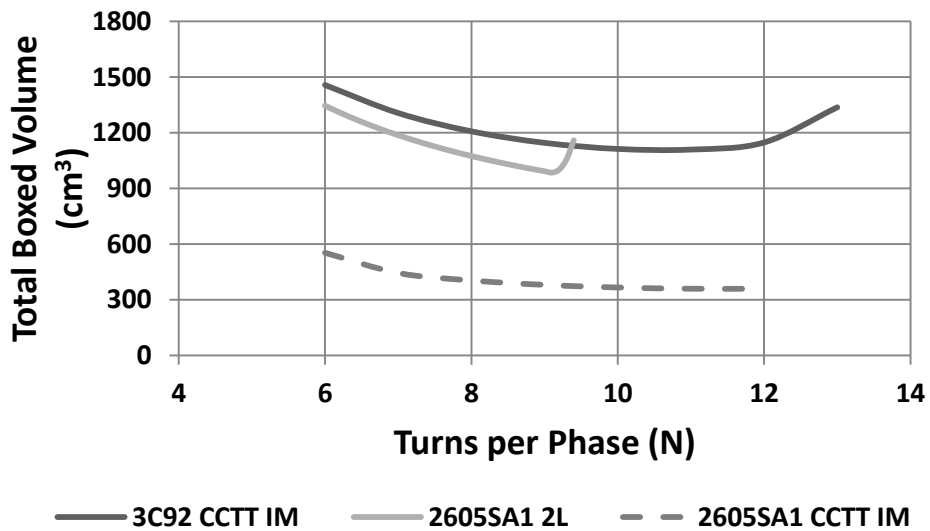


Figure 4.37. Total boxed volume vs. turns per phase

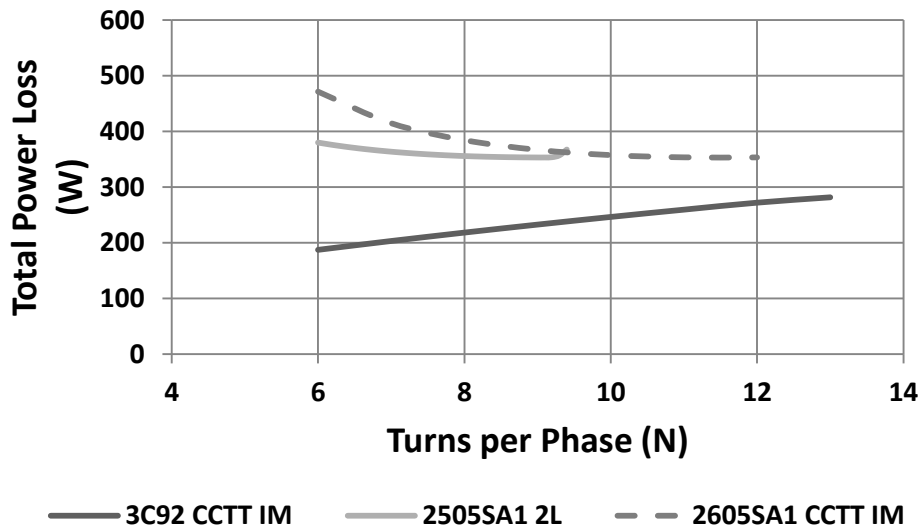


Figure 4.38. Total power loss vs. turns per phase

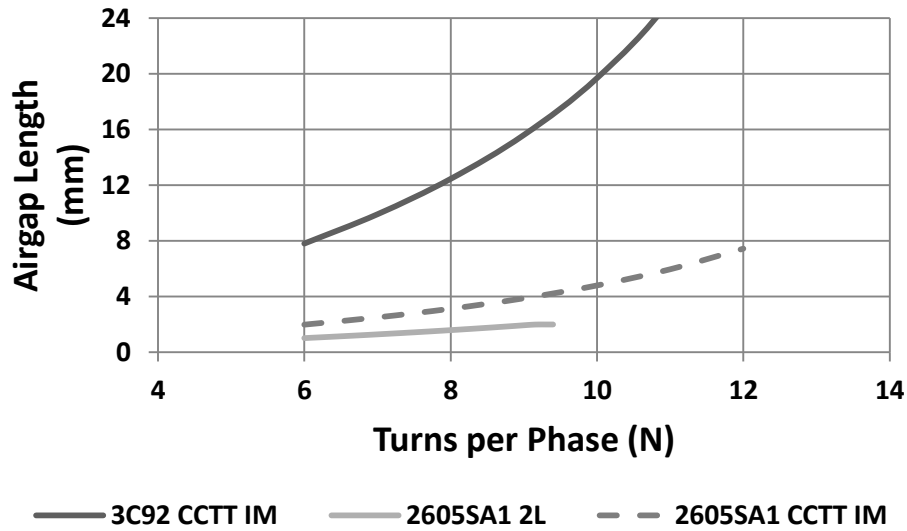


Figure 4.39. Airgap length vs. turns per phase

Fig. 4.39 presents the variation in leakage gap length with increasing ripple ratio and turns per phase. In a similar manner to the 3C92 CCTT IM, the leakage gap length increases with increasing input ripple and turns per phase. Interestingly, the leakage gap lengths are significantly smaller when compared to the same design points of the 3C92 CCTT IM.

4.8.2. Conduction-Cooled 2605SA1 CCTT IM Optimization

A comparison of the prototype 3C92 CCTT IM and the high B_{sat} CCTT IM is presented in Table 4.20. Fig. 4.40 presents an isometric view of the three inductor designs presented in this chapter. The CCTT IM designed using the laminated material is significantly smaller than the previous two designs. 2D and 3D FEA is again used to validate the CCTT IM design produced by the design algorithm. A dc and transient analysis is conducted in order to determine inductance of the IM as well as verify that it does not enter into saturation when under peak phase current conditions. Fig. 4.41 and Fig. 4.42 present the dc and transient flux plots respectively. Table 4.21 presents the results of the dc inductance matrix while Table 4.22 present the predicted and simulated dc and ac inductance of the IM component. Interestingly, on closer inspection of Fig. 4.33 (a) and (b) it is obvious that there is not as much fringing flux around the pole region as seen in the medium ripple prototype design. This is due to its relatively small leakage gap, g , which is 3 mm. The plots presented in Fig. 4.42 indicate that the CCTT IM design performs as expected under dc and full load conditions. Interestingly, it appears that the design algorithm is not as accurate in predicting the dc and ac inductance of the CCTT IM and this will be investigated in more detail.

Table 4.20 Prototype and High B_{sat} Prototype Parameters

Circuit Conditions			Prototype	High B_{sat}
Input voltage	V_{in}	V	155	155
Output voltage	V_{out}	V	420	420
Input current	I_{in}	A	464	464
Phase current	I_{phase}	A	232	232
Input power	P_{in}	kW	72	72
Frequency	f_s	kHz	25	25
Leakage inductance	L_{lk}	μH	8.5	8.5
Magnetizing inductance	L_m	μH	30	30
Input ripple	ΔI_{in}	A	188	188
Phase ripple	ΔI_{phase}	A	140	140
Core and Winding Mass and Volume				
Material			3C92	2605SA1
Core leg width	a	mm	28	19
Core window width	b	mm	28	21
Core window length	c	mm	76	77
Core thickness	d	mm	48	26
Pole height	h	mm	22	23
Pole length	x	mm	9	9
Leakage gap	g	mm	10	3.1
Magnetizing gap	I_{g_mag}	mm	4 x 0.85	4 x 0.23
Core mass	M_c	kg	2.2	0.7
Copper mass	M_{cu}	kg	0.62	0.49
Turns	N	phase	8	8
Core area	A_c	mm^2	1344	494
Boxed volume	V_{boxed}	cm^3	1040	404
Total Component Power Loss at Full Rated Power				
Dc winding loss	P_{wdc}	W	177	114
Ac winding loss	P_{wac}	W	98	100
Core loss	P_c	W	10	250
Total loss	P_t	W	285	414

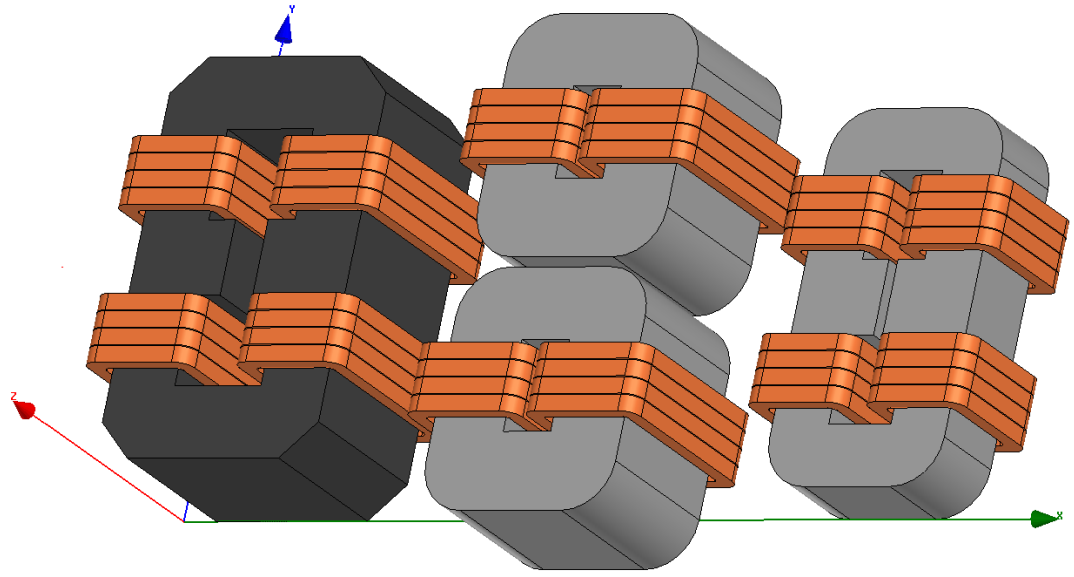


Figure 4.40. Isometric view of 3C92 CCTT IM, 2605SA1 2L and 2605SA1 CCTT IM

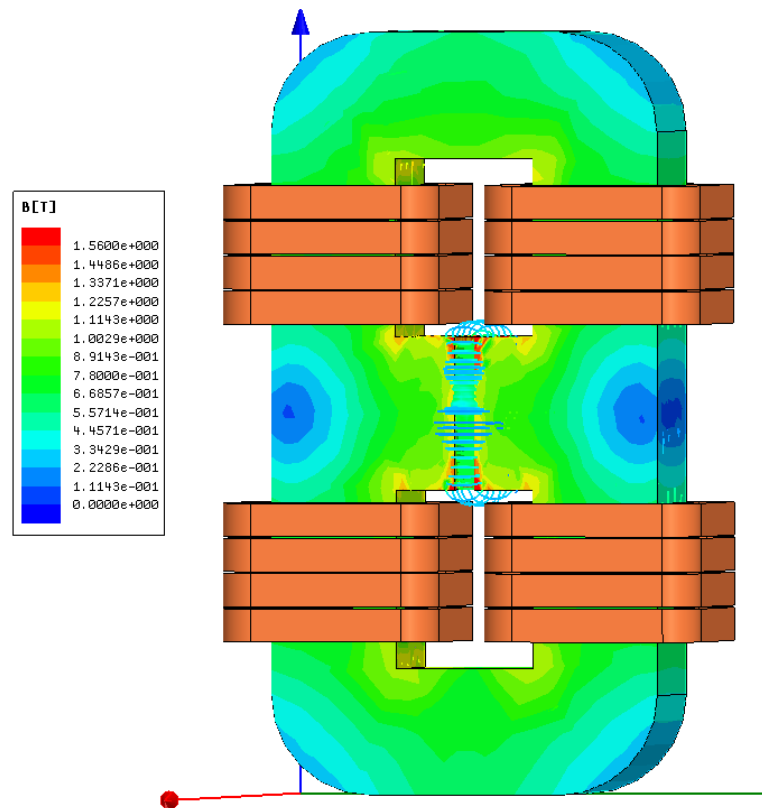


Figure 4.41. Dc flux plot of 2605SA1 CCTT IM

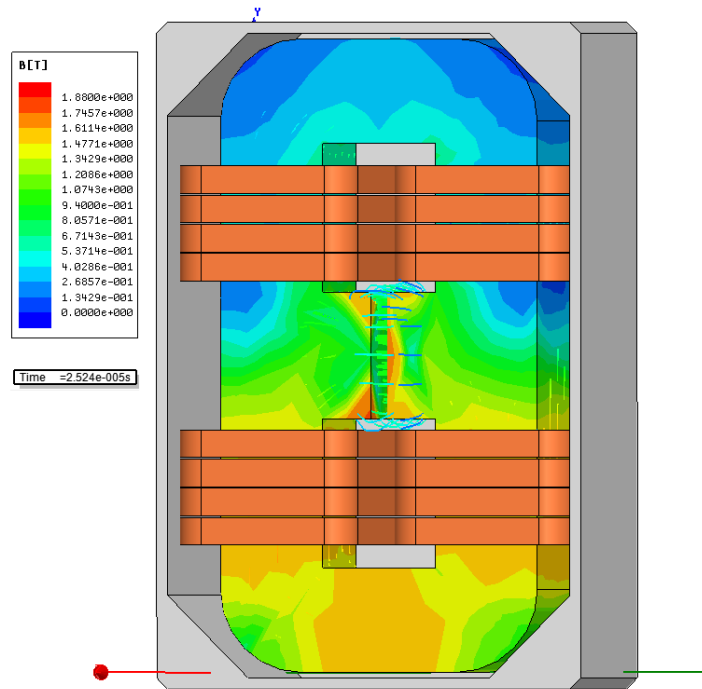


Figure 4.42. Transient flux plot of 2605SA1 CCTT IM at the peak of the phase current ripple at $t = 25.2 \mu\text{s}$

Table 4.21 Dc Inductance Matrix for 2605SA1 CCTT IM

	Phase A	Phase B
	μH	μH
Phase A	45.532	-33.239
Phase B	-33.239	45.507

Table 4.22 Comparison of Dc and Ac Inductance for the 2605SA1 CCTT IM

		2605SA1 CCTT IM	
		Algorithm	3D
$L_{lk, dc}$	μH	10.3	12.3
$L_{lk, ac}$	μH	8.6	11

4.8.3. Analysis of Power Loss over Variable Fuelcell Power Range

Similar to Section 4.6, this section investigates the power loss in the 2605SA1 CCTT IM as the fuelcell power is varied. Fig. 4.43 presents the power loss associated with the CCTT IM in question.

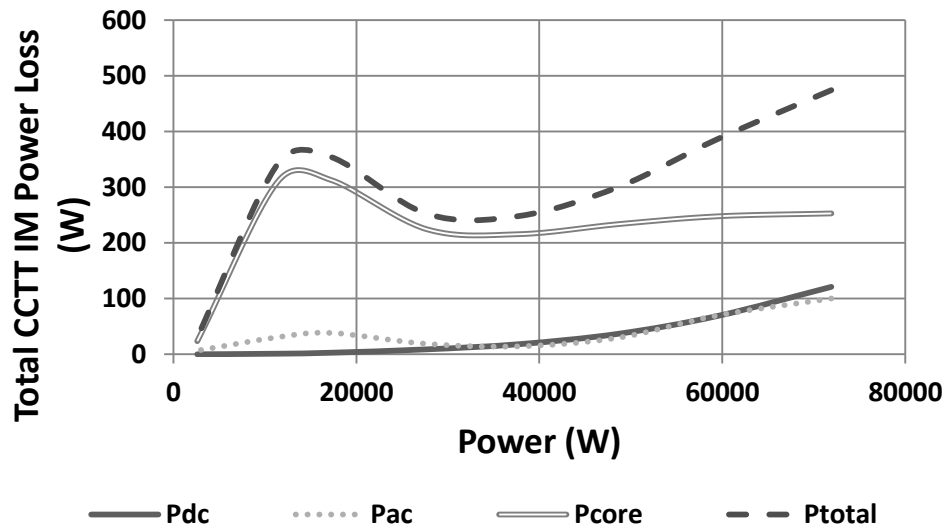


Figure 4.43. Breakdown of 2605SA1 CCTT IM power loss

In contrast to the 3C92 CCTT IM prototype, the core power loss in the 2605SA1 option is a significant contributor to the overall power loss of the device and dominates at low to medium load. The dc copper loss is similar to the medium ripple option and this is to be expected as both devices have the same number of turns, copper cross-sectional area and core cross-sectional area. The ac copper loss is also similar to the 3C92 CCTT IM design. Interestingly, the core power loss increases at low load which corresponds to low duty cycle operation. The MSE is used to determine the core power loss and at low duty cycles it predicts that there is an increase in the core power loss.

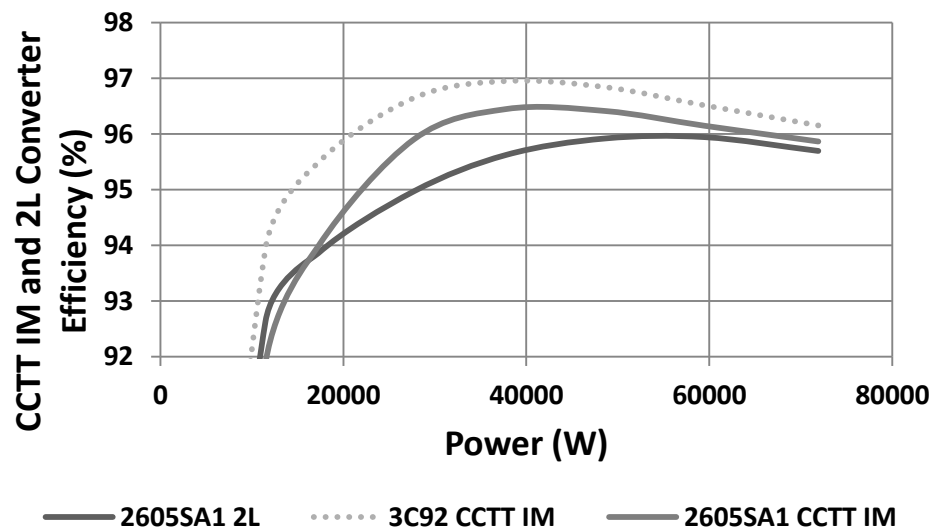


Figure 4.44. 2605SA1 CCTT IM efficiency over fuelcell power range

The overall efficiency of the 2605SA1 CCTT IM is presented in Fig. 4.44, along with the two other magnetic designs. The design is seen to be more efficient than the 2L topology over

the fuelcell power range especially at medium load conditions. The design is approximately 0.5 % less efficient than the 3C92 option.

4.8.4. Manufacturability Issues of Metglas CCTT IM

The design of a tape wound EE cores is covered in [77] and a similar method of manufacturing would be required to develop a CCTT IM from Metglas material. Different methods of implementing a CCTT IM core set using laminated materials are currently being investigated such as, a hybrid core using both Metglas and JFE material. Another possibility is the use of CC core and II blocks to develop a CCII or the use of I blocks to make an I⁸ core set. One issue to be mindful of when using laminated cores is that they are mounted correctly to ensure the correct thermal path to the heat sink, which is along the laminations. The correct orientation of laminations is also needed when using a hybrid core set consisting of Metglas and JFE material [82, 137, 148].

4.9. Experimental Results

4.9.1. 97.2 kW 3L Experimental Test Results

A 97.2 kW converter has been built and tested in order to validate the 3L inductor designs. The experimental test set-up is presented in Fig. 4.45. Experimental waveforms are presented in Fig. 4.46.

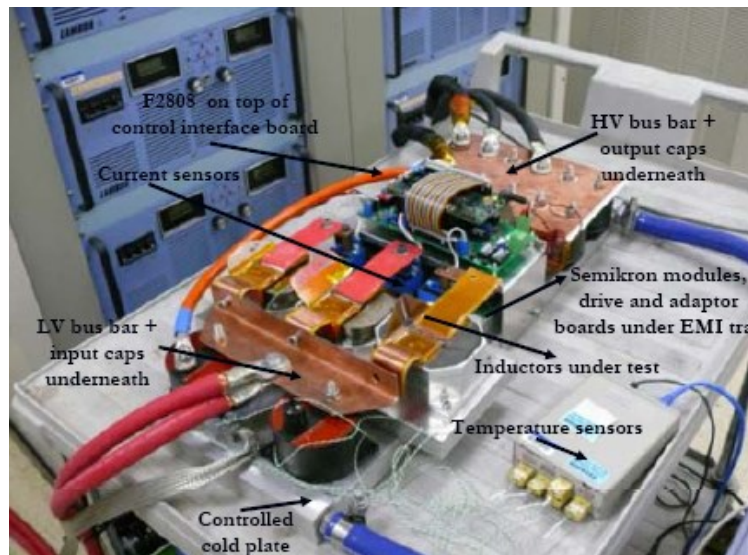


Figure 4.45. 97.2 kW three-phase experimental test set-up

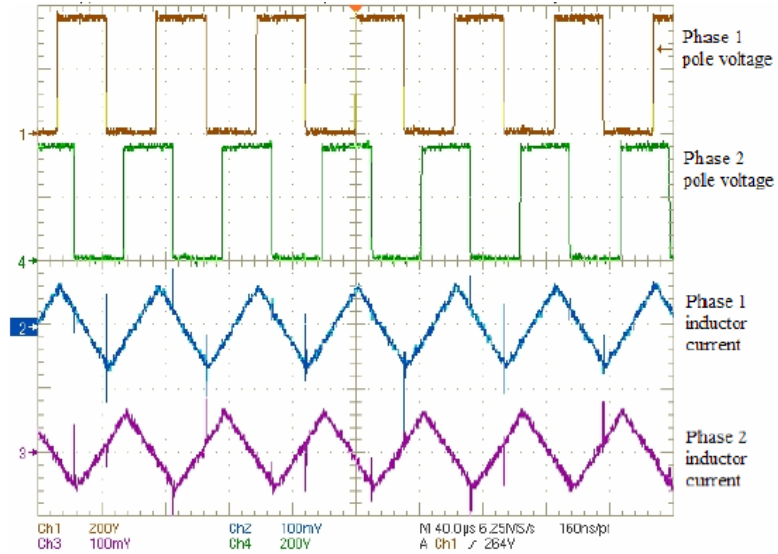


Figure 4.46. Experimental waveforms of 97.2 kW 3L converter

The prototype inductors are tested under the following conditions: $V_{in} = 180$ V, $V_{out} = 360$ V, $I_{in} = 540$ A (180 per phase), $P_{in} = 97.2$ kW and $f_s = 16$ kHz. Three Semikron SEMiX603GB066HDs IGBT modules are used in the experimental set-up. The experimental efficiency of the boost converter was measured to be 97.3 %. The temperature rise of the discrete inductors was measured to be 130 °C which translates into 230 W of loss per inductor.

4.9.2. 72 kW CCTT IM Experimental Test Results

A 72 kW converter has been built and tested to validate the CCTT IM. The prototype CCTT IM was tested under the following conditions: $V_{in} = 155$ V, $V_{out} = 420$ V, $P_{in} = 72$ kW and $f_s = 25$ kHz. Two Semikron SEMiX603GB066HDs IGBT modules are used in the experimental set-up.

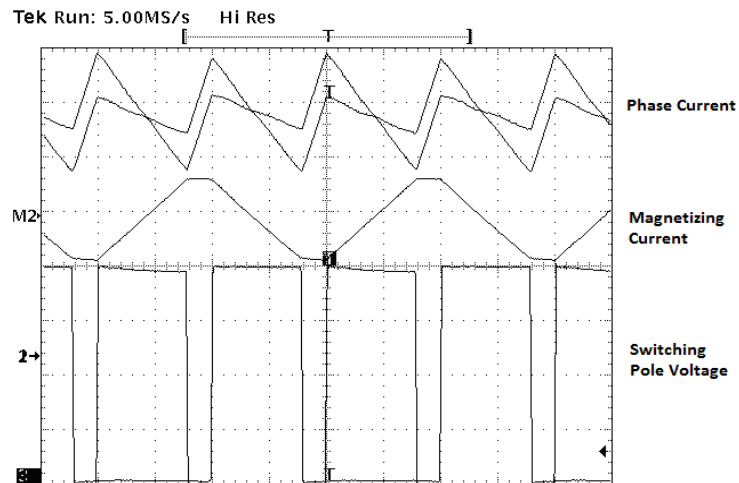


Figure 4.47. 72 kW experimental waveforms

Sample waveforms are shown in Fig. 4.47. The total measured converter efficiency versus output power is shown in Fig. 4.48 for various boost conditions corresponding to $V_{in} = 155$ V and $V_{out} = 310$ V, 360 V and 420 V. Fig. 4.49 presents the plots for converter efficiency corresponding to $V_{in} = 180$ V and $V_{out} = 310$ V, 360 V and 420 V. The converter power loss is largely due to the semiconductors. The experimental full-load efficiency is 95.5 % at $V_{out} = 420$ V and $P_{in} = 72$ kW.

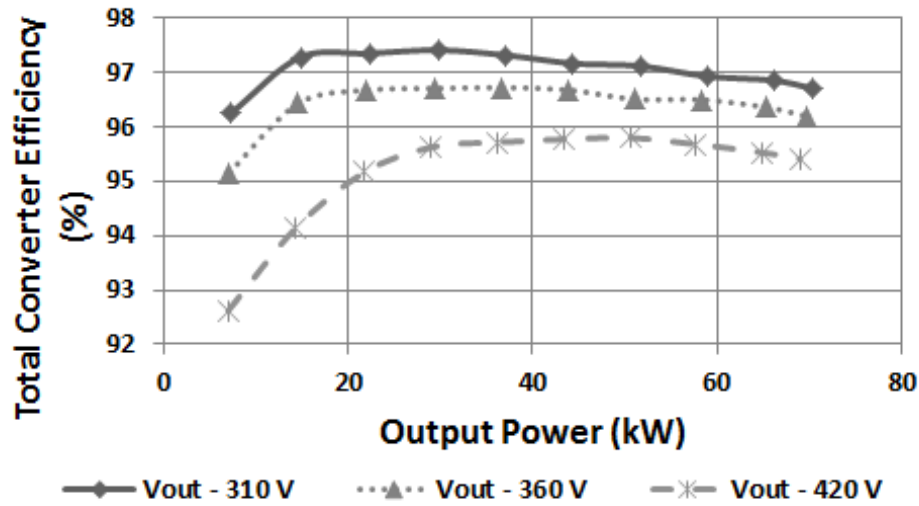


Figure 4.48. CCTT IM converter experimental efficiency at $V_{in} = 155$ V

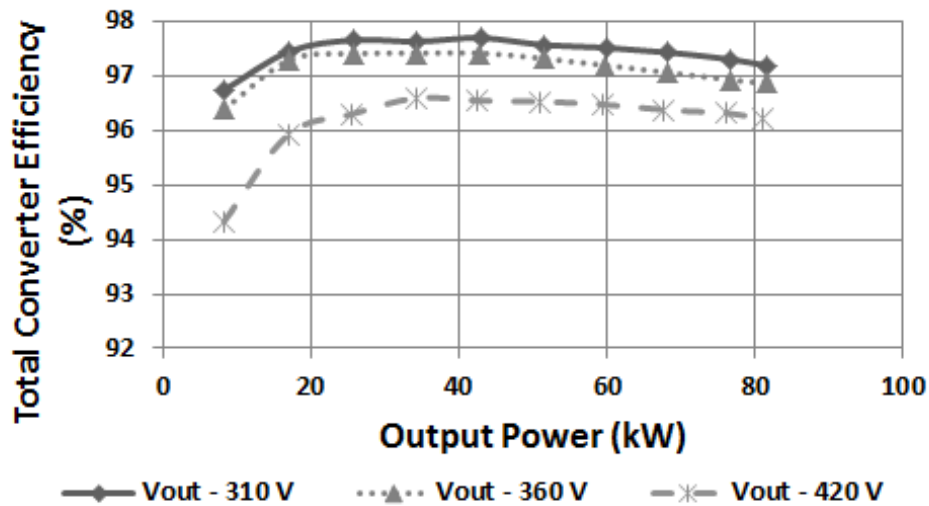


Figure 4.49. CCTT IM converter experimental efficiency at $V_{in} = 180$ V

Table 4.23 presents the predicted and measured CCTT IM prototype power loss. Calorific testing was conducted by an industrial partner to determine the CCTT IM power loss at the full load conditions of 155 V input, 420 V output at 72 kW output. The CCTT IM experimental loss is 277 W for a magnetic device efficiency of about 99.7 %.

Table 4.23 72 kW CCTT IM Power Loss

			Predicted	Experimental
Core Loss	P_{core}	W	10	-
Dc Winding	P_{dc}	W	162	-
Ac Winding	P_{ac}	W	105	-
Total	P_{total}	W	277	260

4.9.3. 3.8 kW CCTT IM and 2L Experimental Results

In order to compare the CCTT IM and 2L topologies under like-for-like operating conditions a 3.8 kW design, test and build was undertaken. The experimental set-up is presented in Fig 4.50. The prototype CCTT IM and 2L inductors were tested under the following conditions: $V_{in} = 200$ V, $V_{out} = 500$ V, $P_{in} = 3.8$ kW and $f_s = 16$ kHz. The power was varied to approximate the operation of a 3.8 kW fuelcell I-V profile.

Two CoolMos IPW60R041 Mosfet's from Infineon and two SiC schottky C3D20060D diodes from Cree are chosen as the semiconductor devices. The average current mode control scheme is implemented using an EP3C16E144C8 Cyclone III FPGA.

The prototype cores used in the testing are presented in Fig. 4.51. The CCTT IM is pictured on the left of Fig. 4.51 while the 2L inductors used in this analysis are located on the right hand side of the picture. The CCTT IM is constructed using 3C92 ferrite material.

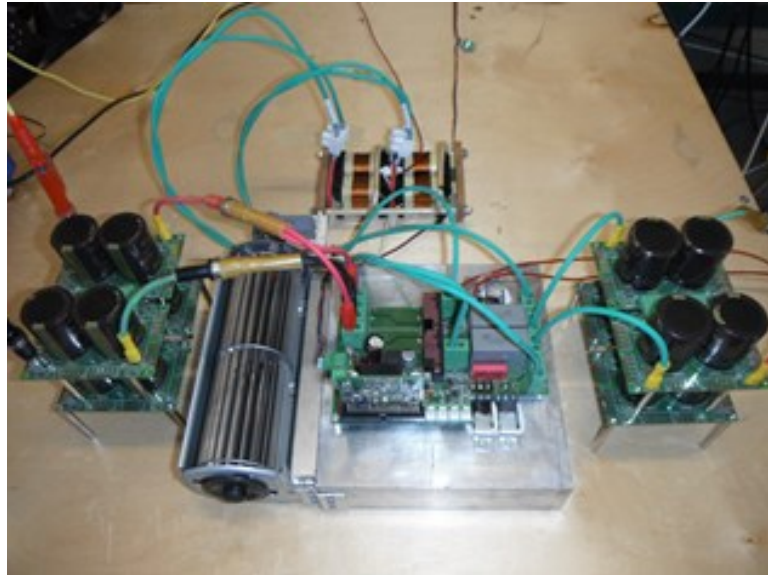


Figure 4.50. 3.8 kW experimental set-up

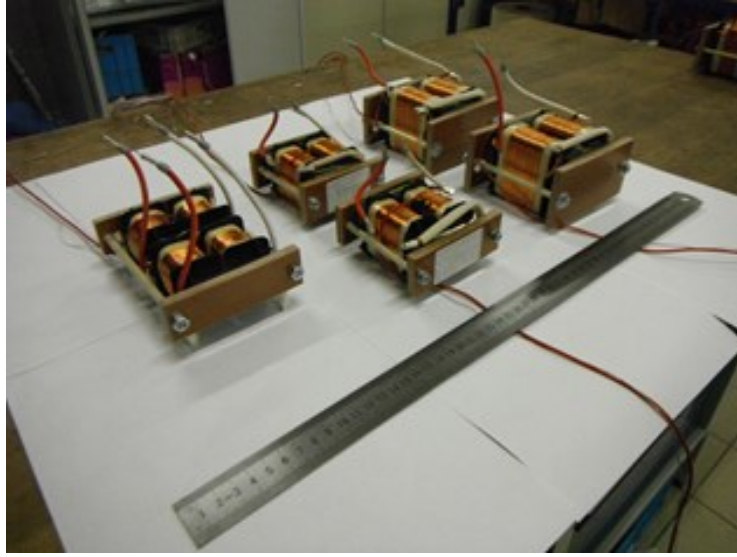


Figure 4.51. 3.8 kW CCTT IM and 2L prototype components

Ideally the 2L inductors would be constructed using the same material as used in the analysis presented in Section III. The iron-based amorphous metal 2605SA1 material was not available at the time of construction and therefore the 2L inductors are constructed using 10JNHF600 silicon steel (SiFe) from JFE, which is another high B_{sat} laminated material. This material allowed for easy construction of the prototype cores. All designs use 6 x 0.9 mm stranded copper conductors which ensures that they have the same current density. Table 4.24 presents the relevant parameters for the prototype components.

Previous work [83] indicates that the optimal design condition for inductors using 10JNHF600 is for between 10 % and 20 % phase-current ripple. As a result the 2L inductors in the experimental comparison are not designed to have the same phase current ripple as the CCTT IM as this would require a phase-current ripple of 50 %.

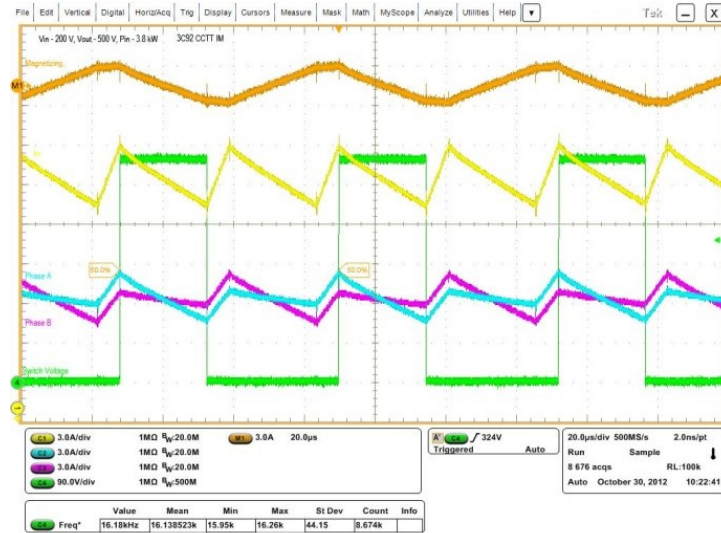


Figure 4.52. 3.8 kW 3C92 CCTT IM experimental waveforms for $D = 0.6$

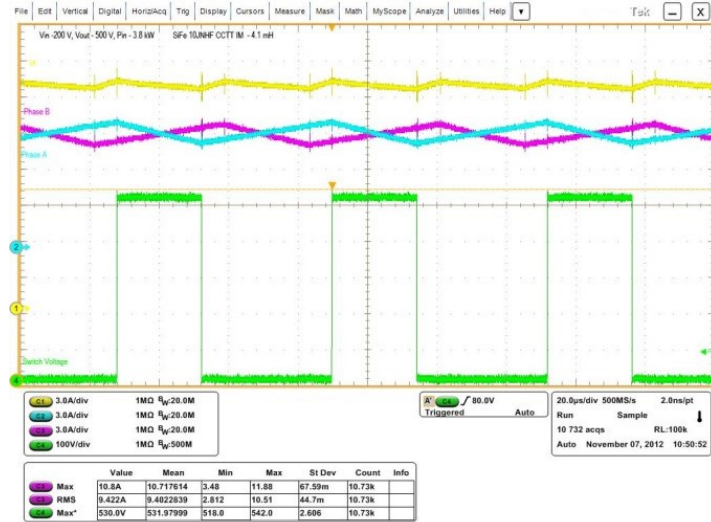


Figure 4.53. 3.8 kW 10JNHF600 2L experimental waveforms for $D = 0.6$

Experimental waveforms for the CCTT IM and discrete inductors are presented in Fig. 4.52 and Fig. 4.53, respectively. The efficiency of the two converter topologies is presented in Fig. 4.54 where the CCTT IM exhibits superior efficiency over the entire fuelcell power range.

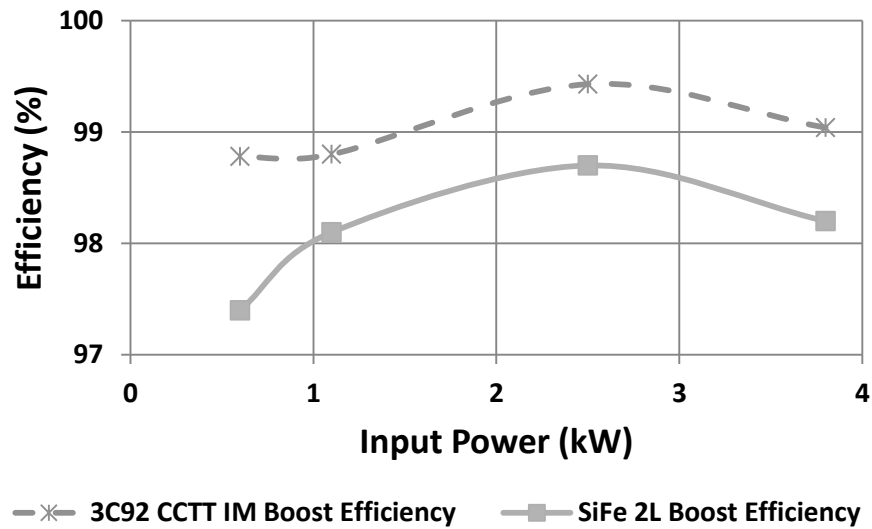


Figure 4.54. 3.8 kW experimental boost efficiency

4.10. Conclusions

This chapter compares two magnetic component topologies for use in a two-phase interleaved dc-dc converter. The CCTT IM and the 2L options, operating at 72 kW, 25 kHz, are designed to have the same worst-case phase current ripple condition as a 3L, 97.2 kW, 16 kHz baseline design. The CCTT IM is shown to have a similar boxed volume to the 2L design as the 2L option has a much higher inductance requirement. The CCTT IM is shown to have the best

efficiency while the 2L suffers from excessive core and ac winding loss at part-load due to its higher current and flux ripples at these conditions.

An amorphous metal CCTT IM design is shown to achieve a much lower boxed volume than the prototype 3C92 CCTT IM. The reduction in boxed volume comes at the expense of increased power loss. Regardless the 2605SA1 CCTT IM is shown to be more efficient than the 2L core set and it is 0.5 % less efficient than the 3C92 CCTT IM over the operating range of the fuelcell. More investigation needs to be undertaken to experimentally validate the high-flux design.

Table 4.24 3.8 kW Prototype Parameters

Inductor Design Conditions			2L	CCTT IM
Input voltage	V_{in}	V	200	200
Output voltage	V_{out}	V	500	500
Input-current	I_{in}	A	19	19
Phase-current	I_{phase}	A	9.5	9.5
Input power	P_{in}	kW	3.8	3.8
Frequency	f_s	kHz	16	16
Phase inductance	L_{phase}	μH	4111	-
Leakage inductance	L_{lk}	μH	-	535
Magnetizing inductance	L_m	μH	-	1600
Input ripple	ΔI_{in}	A	0.6	7.24
Phase ripple	ΔI_{phase}	A	1.9	4.75
Core and Winding Mass and Volume				
Material			SiFe	3C92
Core mass	M_c	kg	2 x 2.2	1.3
Turns	N	phase	100	60
Core area	A_c	mm^2	810	270
Copper area	A_{cu}	mm^2	3.8	3.8
Airgap per leg	l_g	mm	4 x 0.51	-
Leakage airgap	g	mm	-	4.1
Magnetizing airgap	l_{gm}	mm	-	4 x 0.15
Boxed Volume	V_{boxed}	cm^3	800	582
Total Component Power Loss at Full Rated Power				
Dc winding loss	P_{wdc}	W	20	18
Ac winding loss	P_{wac}	W	24	12
Core loss	P_c	W	15	2
Total loss	P_t	W	59	32

Chapter 5

8 kW Interleaved CCTT IM Boost Converter for Photovoltaic Applications

This chapter presents a comparison of two magnetic component topologies for use in a high-power high-current dc-dc boost pre-regulator for photovoltaic (PV) applications. A two-phase (2L) interleaved dc-dc boost converter consisting of two discrete toroid magnetic components is considered as the baseline design. A 3C92 CCTT-core split-winding integrated magnetic (CCTT IM) is developed and compared for similar conditions. The topologies are compared for the same worst-case phase current ripple conditions.

Firstly, the baseline industry standard 2L design is presented which consists of a toroid magnetic component along with stranded copper conductors, which are used to reduce the effects of ac copper loss. The CCTT IM component is then designed using the algorithm presented in Chapter 3. As shown in Chapter 4, the design of the CCTT IM for the same worst-case phase current ripple allows for a size saving with respect to the baseline design. The CCTT IM boxed volume is investigated as the number of turns is varied but the final CCTT IM design has the same number of turns and copper cross-sectional area as the 2L baseline design. This is in order to have a like-for-like comparison. In a similar manner to previous chapters, 3D and 2D FEA are used in order to validate the designs.

Additionally, the semiconductor loss for each topology is investigated. The variation of magnetic component and semiconductor power loss as the input power varies is also investigated.

Low-power (8 kW) experimental results are presented that indicate that the CCTT IM option allows for an approximate reduction of 50 % in both mass and boxed volume with respect to the 2L toroid inductors. Critically, this size saving does not come at the expense of reduced efficiency, and the CCTT IM is seen to be at least as efficient as the 2L baseline design.

5.1. Introduction

The I - V characteristic of a solar panel varies with environmental factors such as irradiation and temperature [27, 28]. A dc-dc converter is essential in a PV inverter power stage where it is used as a pre-regulator for MPP tracking as well as to stabilize the dc-link voltage for the dc-ac inverter, which is connected to the grid [53, 54, 57, 149-152]. The magnetic components in the conventional single-phase boost converter can be quite lossy, bulky and costly. Therefore, innovative methods to reduce magnetic component size, loss, and in turn, cost are major driving forces in the design of dc-dc converters. Interleaving, coupled and integrated magnetics are all approaches by which these goals can be met. Fig. 5.1 presents various methods of implementing a boost converter.

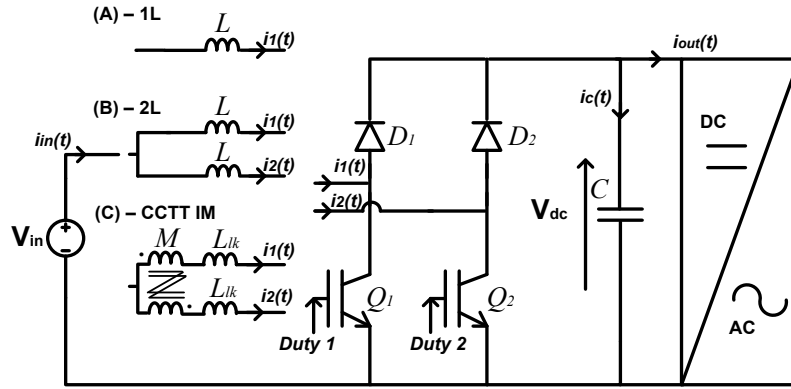


Figure 5.1. 1L, 2L and CCTT IM topologies in a boost pre-regulator

Both the 2L and CCTT IM options result in input current ripple reduction, with this ripple reduction extended to the phase current ripple for the CCTT IM design. Single-phase dc-dc converters can be used in this application but the quest for higher power density and more efficient converters have driven designers to explore multi-phase options which utilize the concept of interleaving. Magnetic components are by far the most significant contributors to the overall size of a dc-dc power converter and the two-phase interleaved dc-dc converter options presented in Fig. 5.1, and as discussed previously, allow for the reduction in the size of the magnetic component when compared with the single-phase solution. This chapter outlines the design and experimental testing of the 2L and CCTT IM topologies under like-for-like operating conditions.

The 2L, industry proven, boost converter using toroidal 3C92 discrete inductors is used as the baseline design. The goal of the analysis is to determine whether the CCTT IM can help achieve size and efficiency improvements which ultimately will result in the reduction in manufacturing cost. All of the designs have the same number of turns and copper cross sectional

area and are designed to have the same worst-case phase current ripple. All designs assume 16 kHz switching frequency and a maximum power of 8 kW.

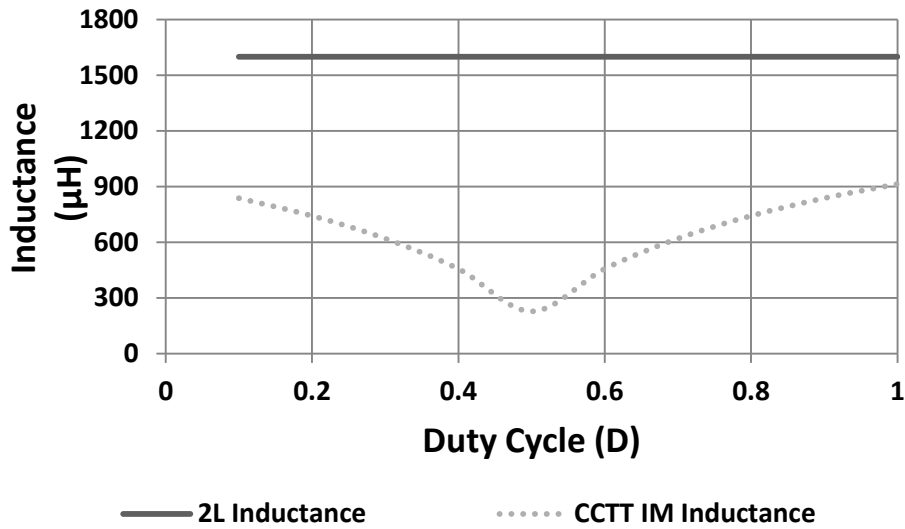


Figure 5.2. Inductance saving vs. 2L when CCTT IM is designed for the same worst-case phase current ripple

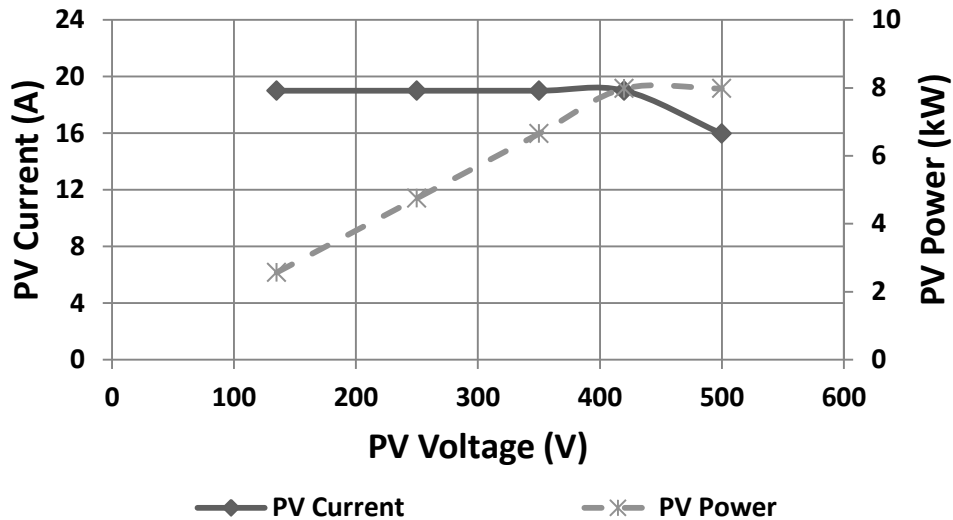


Figure 5.3. 8 kW PV test profile

Firstly, the existing 2L option is investigated and various design parameters are determined. Following this, the ferrite CCTT IM design is developed – for the same worst-case phase current ripple as the baseline design. The design algorithm, presented in Chapter 2, is used to design and optimize the CCTT IM for varying number of turns per phase. Fig. 5.2 indicates the saving in inductance that is achieved over the 2L design when the CCTT IM is designed for the same worst-case phase-current ripple conditions. This reduction in required

inductance directly translates into a size saving in comparison to the 2L design. The CCTT IM provides the largest reduction in size is in the region of 50 % duty cycle. Once the CCTT IM is designed it is evaluated over the worst-case operation of a PV string where the power loss and efficiency are determined as the input power varies. This is illustrated in Fig. 5.3. This curve assumes a constant PV current as the voltage varies and it is used to determine the worst-case operating condition for the boost inductors. In reality the boost converter is required to operate over a wide range of voltage and current conditions corresponding to the typical $I-V$ curve of a PV panel, where the system uses Maximum Power Point Tracking (MPPT) in order to extract the maximum power from the PV panel. Future work will investigate the operation of the boost converter over various MPPT conditions.

2D and 3D FEA is typically used to validate the magnetic designs with 2D FEA playing a vital part in determining the ac winding loss. In this analysis, 2D FEA is solely used to validate both designs, in terms of evaluating if they provide the correct inductance, investigating their flux density condition and evaluating their ac copper loss due to skin, proximity and airgap fringing effects. The main motivation for using 2D FEA is due to the winding configuration and required number of turns. As the designs use many parallel stranded conductors with a small cross-sectional area it would be difficult to build, as well as simulate in 3D FEA.

A paper CCTT IM design using laminated 2605SA1 material is investigated. Initially, the design indicates that a reduction in volume can be achieved over the 3C92 CCTT IM at the expense of increased core loss. Interestingly, the specific core loss of this design is relatively high which would make the efficient removal of heat difficult. When the maximum allowable specific core loss is set as a constraint the CCTT IM volume has to increase in boxed volume which results in a larger design in comparison to the 3C92 CCTT IM option. This initial analysis indicates that the use of laminated materials at this power level and cooling method is not feasible.

The semiconductors used in the experimental set-up are CoolMos MOSFETs and silicon carbide (SiC) diodes from Infineon and Cree, respectively [153, 154]. The switches have relatively low conduction and switching losses while the SiC diode has zero reverse recovery loss. The semiconductor loss is analytically determined which allows for the total converter loss and converter efficiency to be evaluated.

The paper analysis conducted in the previous sections is then compared with the 8 kW experimental results. A prototype CCTT IM is developed and constructed using ferrite 3C92 material and is compared with the baseline toroidal inductors. The experimental results look favourably on the CCTT IM design and validate the concept for use in low-power PV applications.

5.2. Baseline Two-Phase Interleaved DC-DC Boost Converter

This section describes the industry standard baseline 2L 8 kW interleaved boost converter that is used in PV applications. The 2L boost design consists of two ferrite 3C92 toroid inductors where converter is required to operate over a wide range of voltage and power conditions, which are detailed as follows: $V_{in} = 135 - 420 \text{ V}$, $V_{out} = 500 \text{ V}$, $P_{in} = 2.5 - 8 \text{ kW}$ and $f_s = 16 \text{ kHz}$

Table 5.1 2L and CCTT IM Inductor Parameters

Circuit Conditions			2L	CCTT IM
Input voltage	V_{in}	V	135	135
Output voltage	V_{out}	V	500	500
Input current	I_{in}	A	19	19
Phase current	I_{phase}	A	9.5	9.5
Input power	P_{in}	kW	8	8
Frequency	f	kHz	16	16
Phase inductance	L_{phase}	μH	1645	-
Leakage inductance	L_{lk}	μH	-	535
Magnetizing inductance	L_m	μH	-	1605
Input ripple	ΔI_{in}	A	2.35	7.3
Phase ripple	ΔI_{phase}	A	4.75	4.75
Core and Winding Mass and Volume				
Material			3C92	3C92
Core mass	M_c	kg	2 x 0.84 = 1.68	0.58
Copper mass	M_{cu}	kg	2 x 0.46 = 0.92	0.92
Turns	N	phase	60	60
Core area	A_c	mm^2	2 x 860 = 920	432
Copper area	A_{cu}	mm^2	3.82	3.82
Airgap per leg	l_g	mm	8 x 0.25	2 x 0.23
Leakage airgap	g	mm	-	3.4
Total boxed volume	V_{boxed}	cm^3	2 x 274 = 548	290
Total Component Power Loss at Full Rated Power				
Dc winding loss	P_{wdc}	W	11	11
Ac winding loss (FEA)	P_{wac}	W	10	13
Core loss	P_c	W	2	2
Total loss	P_t	W	23	26

. The nominal design point for the 2L discrete inductors is as follows: $V_{in} = 250$ V, $V_{out} = 500$ V, $P_{in} = 4.8$ kW and $f_s = 16$ kHz. This operating condition is the worst-case condition in terms of phase current ripple and result in a phase inductance, L_{phase} , of $1645 \mu H$ with a phase peak-to-peak current ripple, ΔI_{p-p} , of 4.75 A.

The input and output capacitance are $48 \mu F$ and $90 \mu F$, respectively. SiC JFET's and diodes are the semiconductor devices used in the actual converter and they result in very low power loss due to conduction and switching losses. In this analysis 600 V CoolMos MOSFETs from Infineon and SiC diodes from Cree are used. The main circuit operation conditions as well as the design variables are presented in Table 5.1.

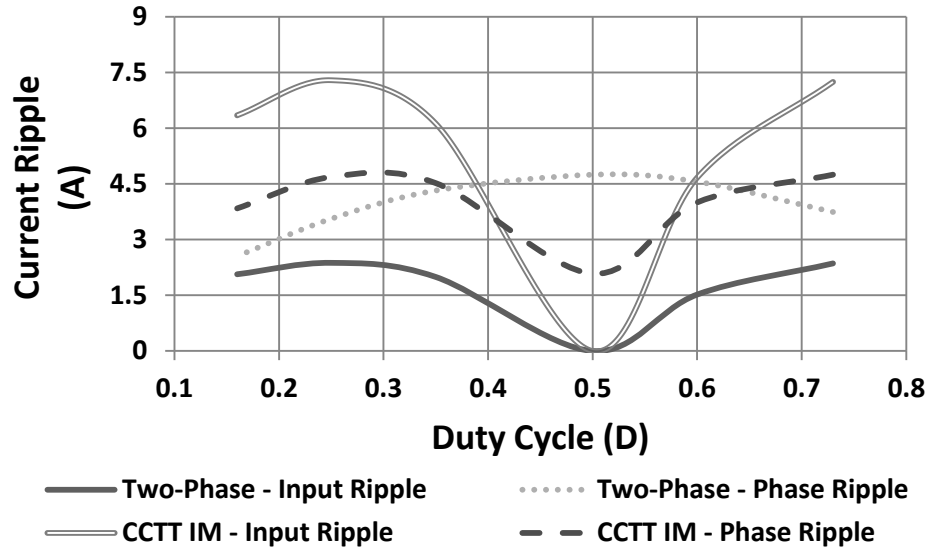


Figure 5.4. Input and phase current ripple variation for the 2L and CCTT IM converter

Fig. 5.4 presents the variation of input and phase current ripple with duty cycle for the 2L interleaved converter. The CCTT IM variation is also included and will be discussed later. These curves indicate that the worst-case input current ripple is 2 A, at $D = 0.73$, while the worst-case phase current ripple is 4.75 A occurring at $D = 0.5$. Interestingly the worst-case phase ripple condition corresponds to the condition at which complete input ripple cancellation takes place. In order to achieve this phase inductance the 2L inductors are designed for an input current ripple ratio of approximately 10 %.

The following section investigates and characterizes the existing toroidal inductor which helps gain a better understanding of its construction and operation.

5.2.1. Discrete Toroid Inductor

This section describes the 2L discrete inductors. Each toroidal inductor is constructed

from multiple ferrite 3C92 segments which are held together in a former using a stainless steel cable tie. The inductor has a total airgap of 2 mm which is distributed equally. The distributed airgap helps reduce the ac copper loss due to airgap fringing flux [82]. Each inductor has 60 turns of 6 x 0.9 mm stranded copper wire. Stranded copper wire is chosen in order to reduce the effects of ac copper loss due to skin and proximity effects and due to its ease of winding during the manufacturing process. The skin depth at 16 kHz is 0.64 mm and so the diameter of each strand is less than twice the skin depth at the first harmonic of the phase current ripple. A total of six strands are used and they are connected in parallel. The winding is placed at a distance of 3 mm from the core and this further mitigates the ac copper loss due to the fringing flux from the airgaps. Fig. 5.5 presents both 2L prototype inductors.

2D FEA was conducted on the inductor in order to validate its design. The FEA results indicate that the inductor operates in accordance to its design parameters with a dc flux density between 0.26 T and 0.3 T. The in-built inductance calculator is used to determine the inductance which is evaluated to be 1810 μH . This result is 10 % greater than the design point. The ac copper loss at the first harmonic is evaluated to be approximately 5 W.

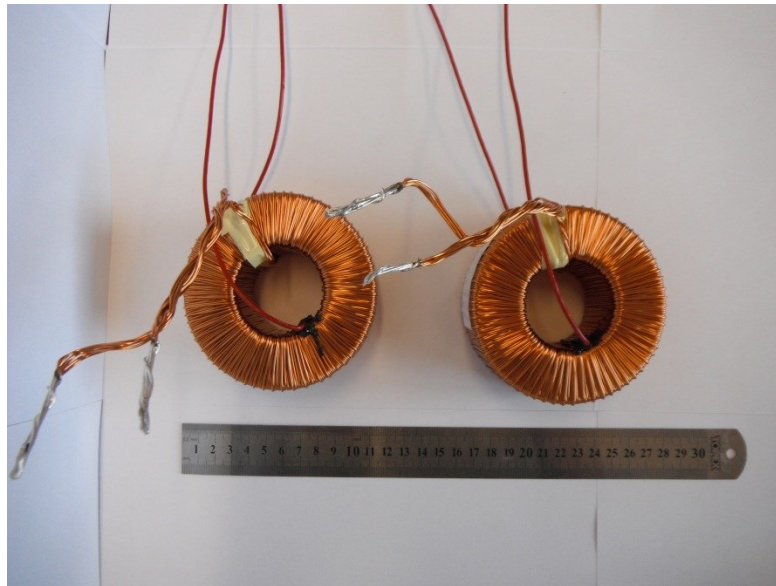


Figure 5.5. Plan view of 2L prototype inductors

The use of a toroid results in excellent core utilization where, unlike the CC core inductor, the entire core is covered by the windings. The windings are configured in a single-layer and only overlap when passing through the core window. This allows for a reduction in the proximity loss, reduced winding capacitance and easy removal of heat from the windings. The experimental results indicate the winding hotspot occurs on the inside of the core window where the stranded windings overlap. The use of a toroid also limits the amount of stray or radiated

magnetic fields.

5.3. Magnetic Design of an 8 kW CCTT IM Component

This section describes the CCTT IM 8 kW interleaved boost converter that is to be compared to the baseline design. In order to have a like-for-like comparison, the CCTT IM is designed to have the same worst-case phase current ripple as the baseline 2L design which is, $\Delta I_{p-p} = 4.75$ A. The CCTT IM is designed for an input current ripple ratio of 38 % and this corresponds to a leakage inductance, L_{lk} , of $535 \mu H$ and magnetizing inductance, L_{mag} , of $1600 \mu H$.

Fig. 5.4 presents the variation of input and phase current ripple with duty cycle for the CCTT IM interleaved converter. These curves indicate that the worst-case input current ripple is 7.3 A, at $D = 0.73$, while the worst-case phase current ripple is 4.75 A occurring also at $D = 0.73$. Interestingly it is seen that the reduction in inductance comes at the expense of increased input current ripple with respect to the 2L baseline inductors as the CCTT IM has a 70 % larger input current ripple. At $D = 0.5$, corresponding to a medium-load operating condition, the CCTT IM option has a greater than 50 % reduction in phase current ripple and the effect of this is discussed in greater detail in Section 5.5.

5.3.1. Design of an 8 kW 3C92 CCTT IM

The nominal operating condition of the interleaved boost converter is as follows: $V_{in} = 135 - 420$ V, $V_{out} = 500$ V, $P_{in} = 2.5 - 8$ kW and $f_s = 16$ kHz. The nominal design point for the CCTT IM option, at its worst operating condition, is as follows: $V_{in} = 135$ V, $V_{out} = 500$ V, $P_{in} = 2.5$ kW and $f_s = 16$ kHz. The main circuit operation conditions as well as the design variables are presented in Table 5.1. The design of the CCTT IM inherently considers a 2 % phase current imbalance which also increases core size in a similar manner to the magnetizing current. The ambient temperature is assumed to be 70 °C. The continuous operation temperature of 3C92 material is 140 °C so the maximum allowable temperature rise for the core is 70 °C. The core profile ratio, r_c , which is the ratio of the core thickness d and the core width a , is allowed to change within the range of 1 and 5. The pole profile ratio, r_p , which is the ratio of the core thickness d and the pole height h , is allowed to change within the range of 1 and 5. The maximum allowable temperature rise for the copper windings is 70 °C. The magnetizing path air gap in the CCTT IM is limited to 3 mm in total divided into four separate air gaps. The CCTT IM design uses 6 x 0.9 mm parallel stranded copper wire.

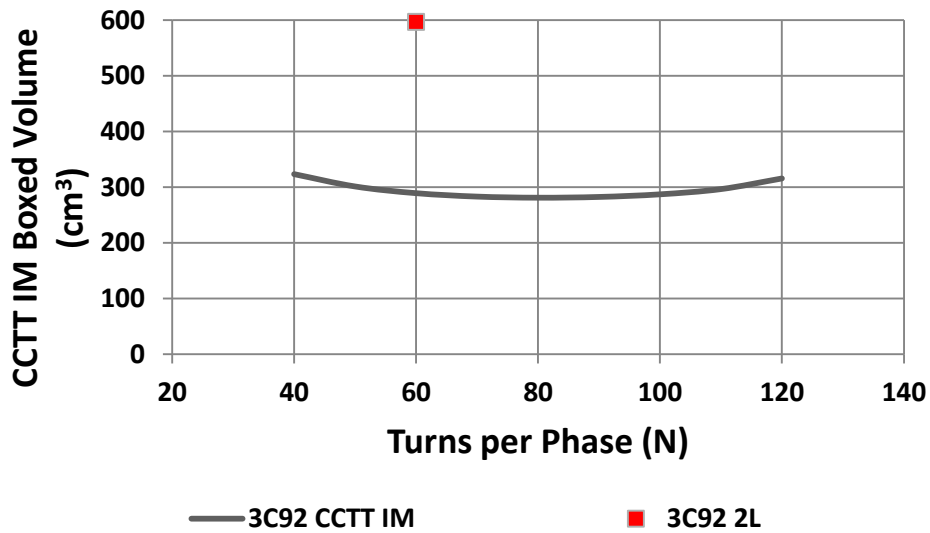


Figure 5.6. Variation in CCTT IM boxed volume with turns per phase. The total 2L boxed volume is included

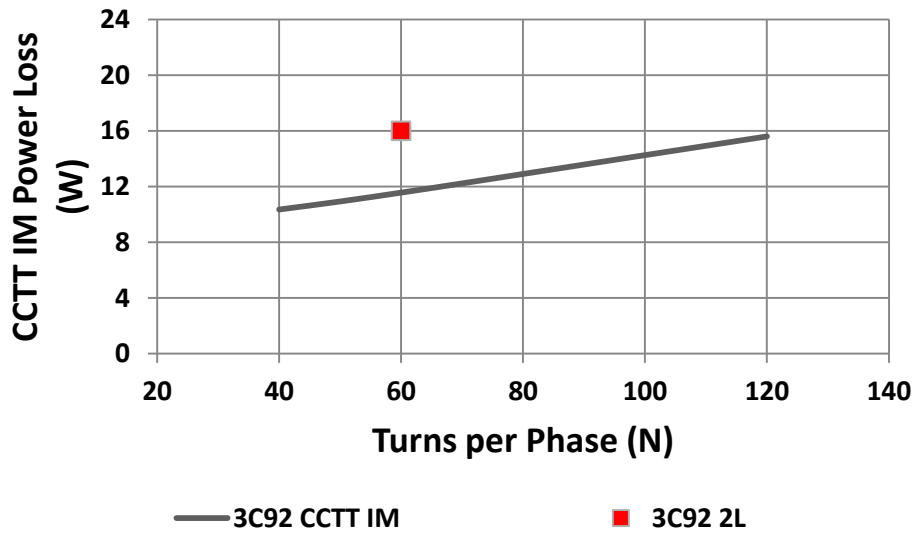


Figure 5.7. Variation in CCTT IM power loss with turns per phase

Fig. 5.6 presents the variation of CCTT IM boxed volume for varying number of turns per phase. For completeness the total boxed volume of the 2L inductors is included. The CCTT IM boxed volume varies from 320 cm³ at 40 and 120 turns per phase to 280 cm³ at 80 turns per phase, which is its minimum. At 60 turns per phase, which is our design point of interest, the CCTT IM is seen to be 50 % smaller than the 2L option.

The variation of CCTT IM power loss with varying number of turns per phase is illustrated in Fig. 5.7. This is the total power loss of the CCTT IM which is determined using the design algorithm but it does not include the ac winding loss determined from 2D FEA.

Therefore, the final power loss will be larger than depicted in this diagram. Again, in our region of interest, the CCTT IM exhibits 25 % less power loss than the combined loss of the baseline design.

Fig. 5.8 presented the variation of the main leakage airgap length as the number of turns per phase is varied. As the number to turns is increased the leakage gap length increases. At 60 turns per phase the leakage gap length is 3.4 mm.

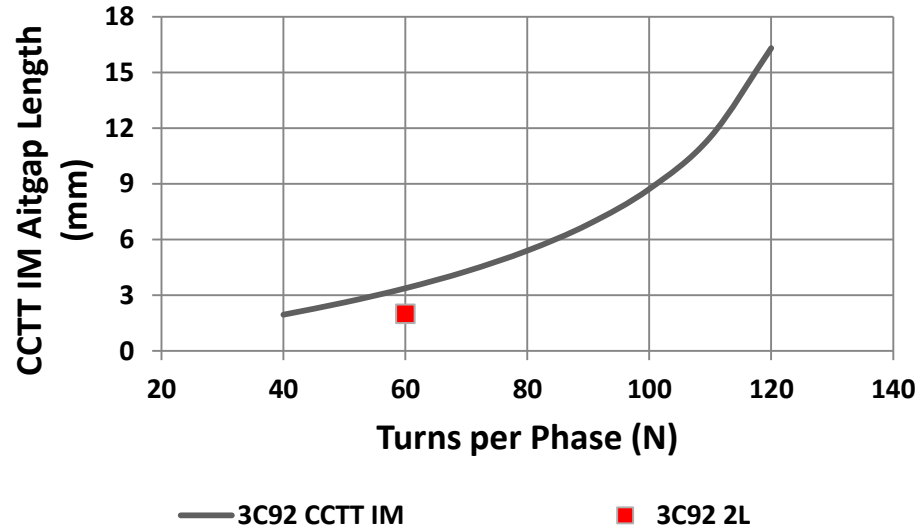


Figure 5.8. Variation in CCTT IM leakage gap length with turns per phase

5.3.2. Optimization and Validation of 8 kW CCTT IM

Following the analysis in Section 5.3.1, this section details the 2D FEA validation of the 60 turn CCTT IM. Typically, 3D FEA is employed in the CCTT IM design process in order to validate that it is operating within its specified design constraints such as, dc and ac leakage inductance, magnetizing inductance and dc and ac flux distribution. The CCTT IM design in question uses many turns of parallel stranded wire which has a relatively small diameter. The development of a 3D model for this type of design is very time consuming and the simulation time is very long due to the requirement of a fine mesh. Therefore, 2D FEA is used to validate the inductance and flux density levels of the CCTT IM. Additionally, 2D FEA is used to determine the ac copper loss of the design.

Fig. 5.9 presents the dc flux distribution in the CCTT IM. To speed up the simulation time, it is possible to reduce the full CCTT IM model to a half model due to symmetry. The dc phase current is 9.5 A. The algorithm predicted a dc bias of 0.19 T and the simulation indicates a dc bias that is below this value. The corner regions of the core and pole see a higher dc bias due to flux crowding.

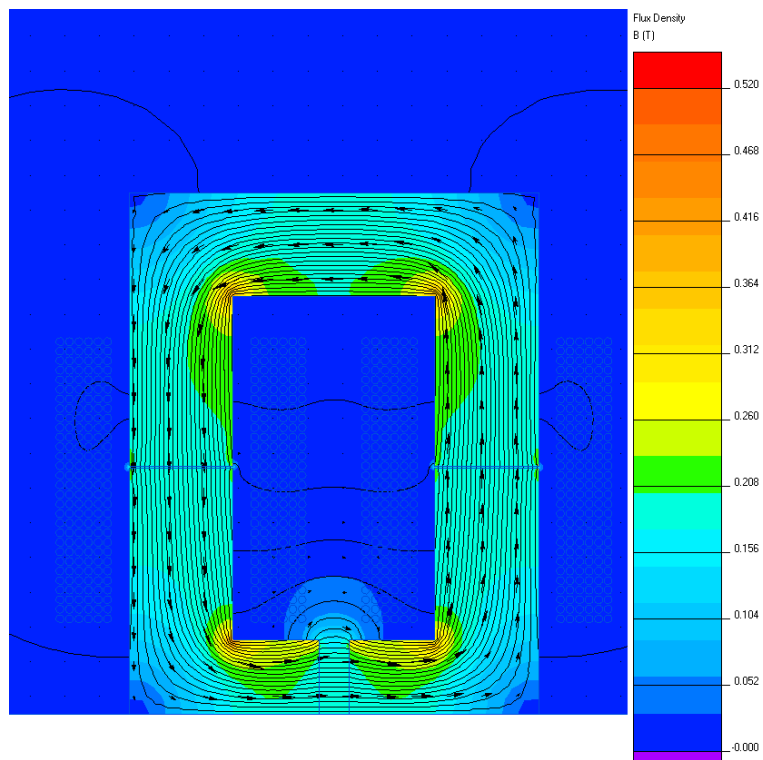


Figure 5.9. 2D dc flux plot of $\frac{1}{2}$ model CCTT IM

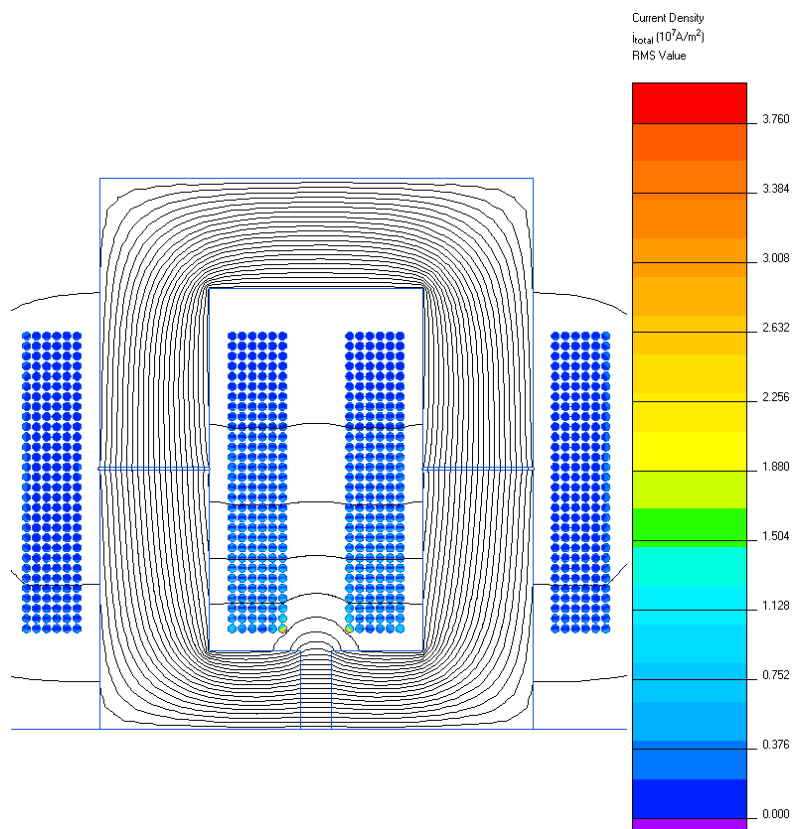


Figure 5.10. Current density plot of $\frac{1}{2}$ model CCTT IM at second harmonic of phase current ripple

The simulator's inductance calculator predicts a dc leakage inductance of $513 \mu\text{H}$ which is 15 % less than the leakage inductance predicted by the algorithm, which is $605 \mu\text{H}$. The reason for this discrepancy is the fact that the 2D simulator is not capturing all of the fringing fields from the CCTT IM. Fig. 5.10 presents a current density plot of the CCTT IM corresponding to the first harmonic of the phase current ripple at 32 kHz which is in differential mode. The ac winding loss is determined to be approximately 12 W at this condition. As in previous CCTT IM designs, the pole sections are allowed to overlap the winding by a distance of at least 2 mm in order to shape the leakage flux away from the windings.

A close up of the flux and current density distribution around the pole region is presented in Fig. 5.11. Interestingly, it appears that the outermost strand, closest to the leakage airgap exhibits the most power loss as expected. The diagram indicates that although each turn is a parallel combination of 6 strands they still exhibit the skin effect in a similar manner as if they were one solid turn.

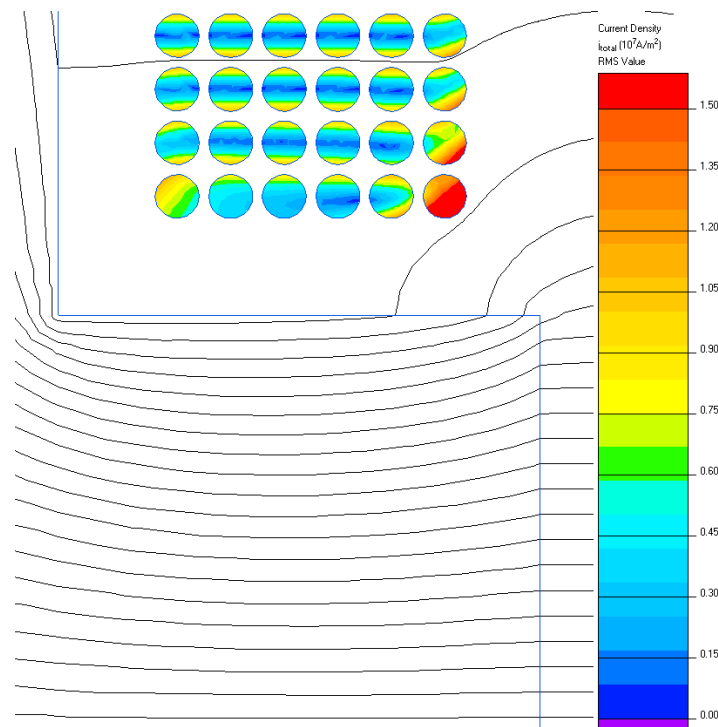


Figure 5.11. Close-up current density plot of $\frac{1}{2}$ model CCTT IM at second harmonic of phase current ripple

5.4. Semiconductor Analysis

The semiconductors used in the experimental analysis are two 600 V CoolMos MOSFETs from Infineon and two SiC diodes from Cree. The use of SiC diodes results in zero reverse

recovery loss. The semiconductor loss is evaluated with the help of [155].

5.5. CCTT IM Converter Analysis

The 2L discrete inductor set and the CCTT IM presented in Table 5.1 are analysed over the PV source profile presented in Fig. 5.3. The input voltage, V_{in} , varies from 135 - 420 V, while the input power, P_{in} , varies between 2.5 kW at low load and 8 kW at full load. The output bus voltage, V_{out} , is assumed to be constant at 500 V. The input current, I_{in} , is assumed to be constant.

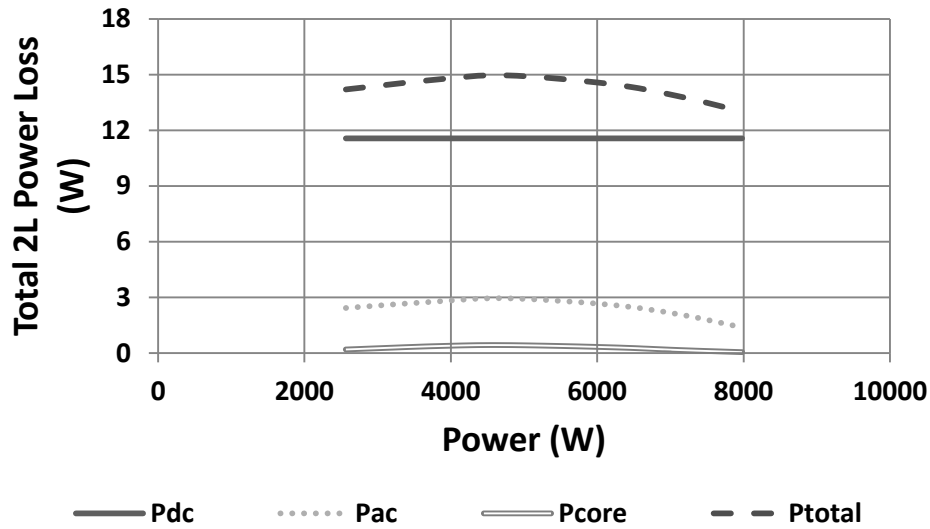


Figure 5.12. Variation in total magnetic power loss for 2L inductors

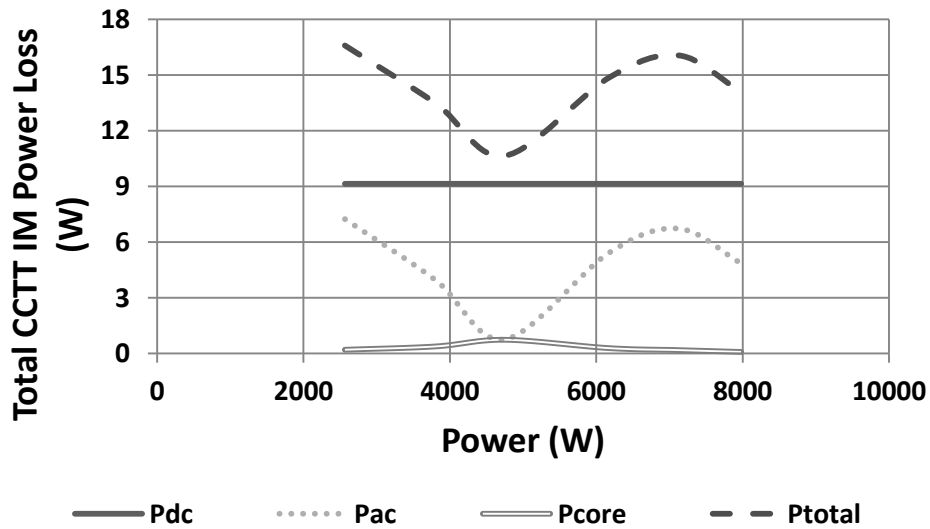


Figure 5.13. Variation in total magnetic power loss for CCTT IM

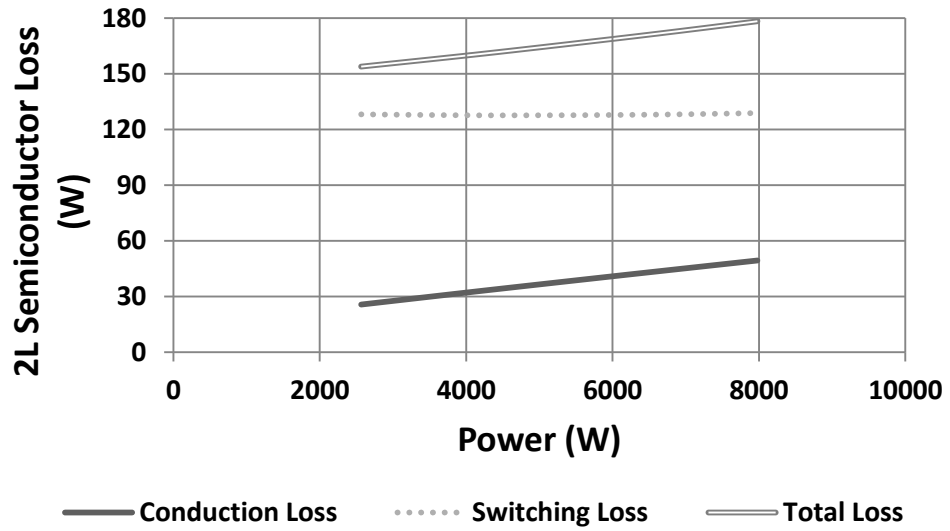


Figure 5.14. Variation in semiconductor power loss for 2L topology

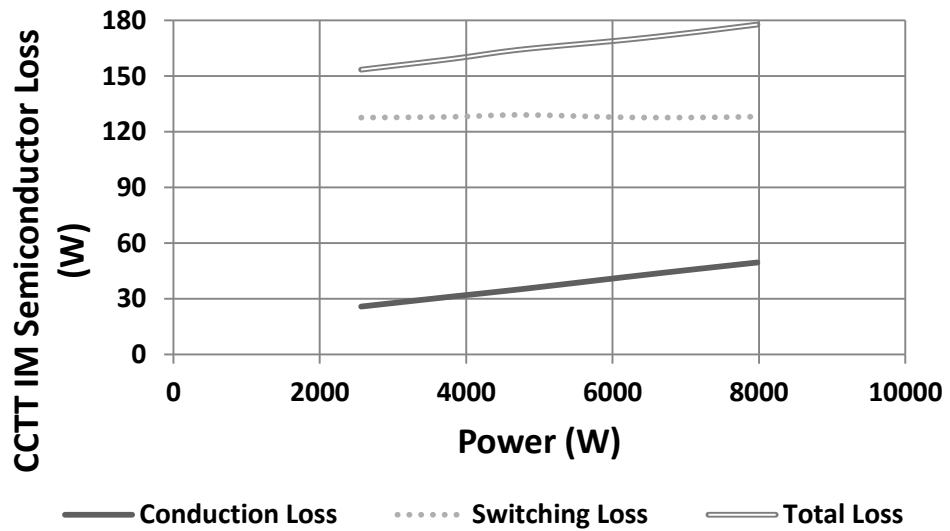


Figure 5.15. Variation in semiconductor power loss for CCTT IM topology

This section investigates how the magnetic power loss changes over different operating conditions. Additionally, the loss in the semiconductor components is also evaluated. Fig. 5.12 and Fig. 5.13 present the variation in 2L and CCTT IM magnetic component loss, respectively. The 2L loss illustrated in Fig. 5.12 is the total loss of both discrete components. The dc power loss in both designs is the dominant source of power loss. The 2L topology has its highest power loss at medium load which corresponds to a duty cycle, $D = 0.5$. Conversely the CCTT IM has its minimum power loss at this condition. This is largely due to the significant reduction in the phase current ripple at this point of operation. The ac copper loss of both designs closely

follows the current ripple graph presented in Fig. 5.4. Both designs use low-loss ferrite 3C92 for the core material which results in extremely low core power loss.

Fig. 5.14 and Fig. 5.15 present the variation in semiconductor power loss for both topologies and this illustrates that both designs have practically identical power loss. The switching loss dominates the semiconductor power loss. Fig. 5.16 presents the efficiency of the 2L and CCTT IM boost designs. Both designs have an identical efficiency which is to be expected as both designs are dominated by the semiconductor power loss, which is the same for both options.

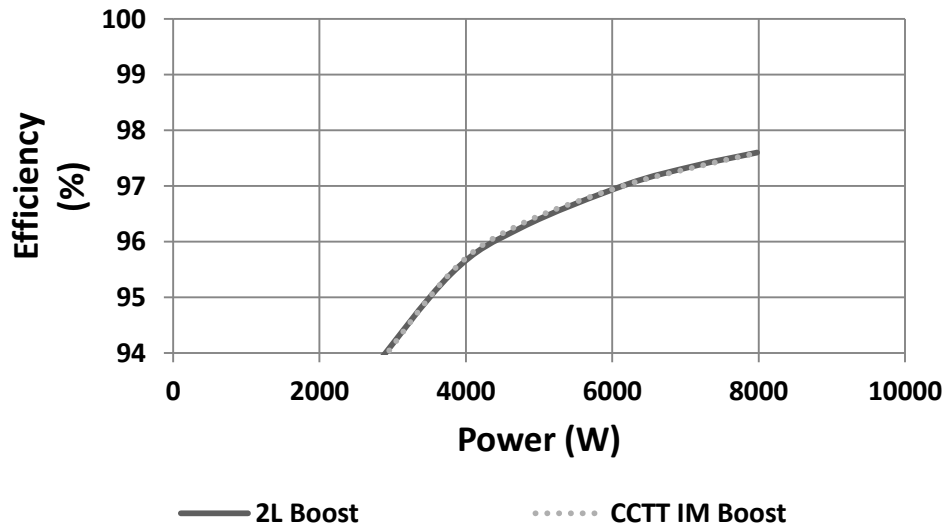


Figure 5.16. Variation in efficiency for 2L and CCTT IM boost topologies

5.6. High-Flux CCTT IM Design

This section investigates the development of a low power CCTT IM using a laminated material such as 2605SA1 from Metglas. The use of 2605SA1 material allows for a reduction in magnetic component size due to its relatively high saturation flux density in comparison to ferrite 3C92. The reduction in volume comes at the expense of increased core power loss and practical issues arise, such as the efficient removal of heat in an air cooled design, if the core power loss is too great. Therefore, it may be necessary to limit the specific core loss and temperature rise when designing a CCTT IM using a laminated material.

Fig. 5.17 presents the variation in boxed volume for two 2605SA1 CCTT IM designs. The first design has no specific core loss and a temperature rise limit of 80 °C. Conversely, the second design has a specific core loss limit of 150 kW/m³ and a temperature rise limit of 40 °C. The 2L baseline and 3C92 CCTT IM boxed volume is included to give a complete picture. The initial 2605SA1 CCTT IM design allows for a reduction in boxed volume of 40 % over the 3C92

option but interestingly, when the design is constrained by specific core loss and temperature the boxed volume of the 3C92 option is very similar to that of the 2605SA1 CCTT IM.

Fig. 5.18 presents the total power loss for all of the designs. The initial 2605SA1 CCTT IM design has a power loss that is over 100 % greater than that of the 3C93 CCTT IM. The redesigned CCTT IM has a power loss that is 26 % less than the initial 2605SA1 option but it is still 46 % greater than that of the 3C92 CCTT IM.

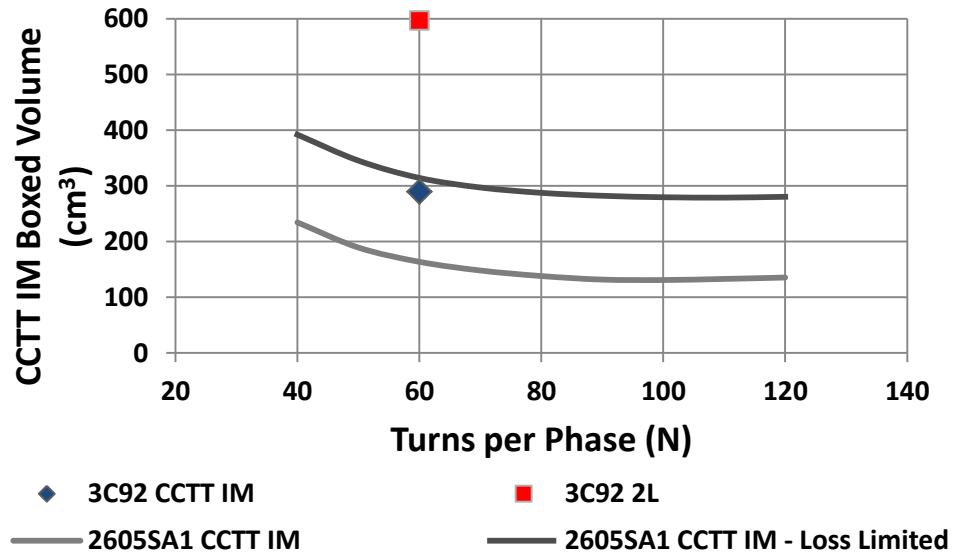


Figure 5.17. Variation in CCTT IM boxed volume with turns per phase. The total 2L boxed volume is included

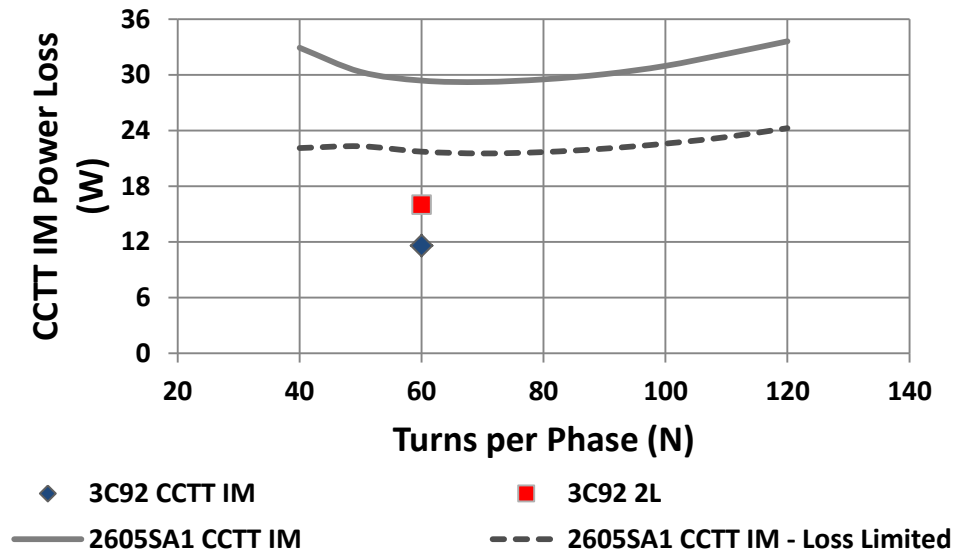


Figure 5.18. Variation in CCTT IM power loss with turns per phase

Fig. 5.19 presents the variation of leakage gap length as the number of turns is varied. The initial 2605SA1 CCTT IM has a smaller airgap than the 3C92 CCTT IM while the

redesigned 2605SA1 CCTT IM requires a larger airgap in order to produce the required leakage inductance. The above analysis indicates that the use of 2605SA1 allows for a reduction in boxed volume but this comes at the expense of excessive power loss and therefore, temperature rise. When a temperature rise limit is enforced, which would allow a practical design, the overall boxed volume significantly increases and the IM volume is greater than the 3C92 option. Thus, it is not realistic to use high flux density material at this low power level and frequency as its high saturation flux density capability is not being utilized.

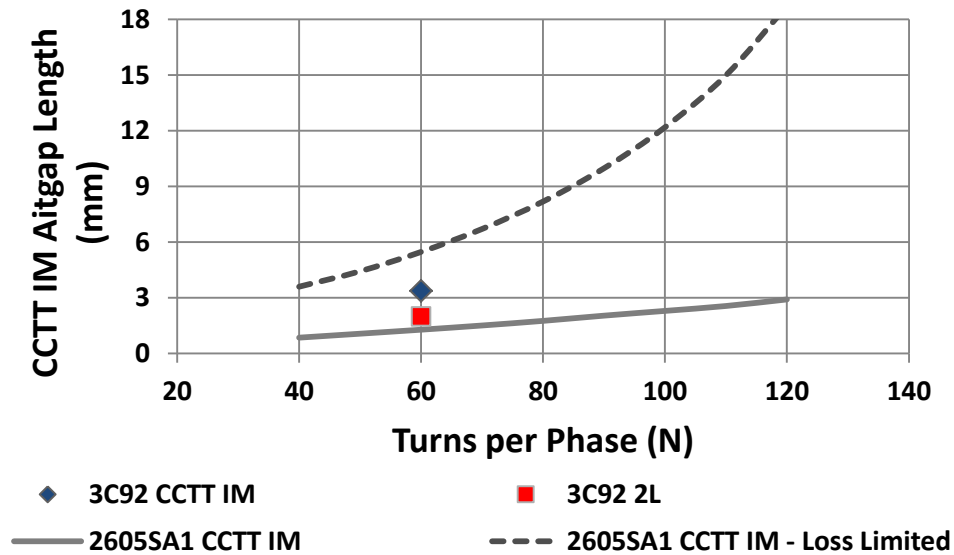


Figure 5.19. Variation in CCTT IM leakage gap length with turns per phase

5.7. Experimental Results

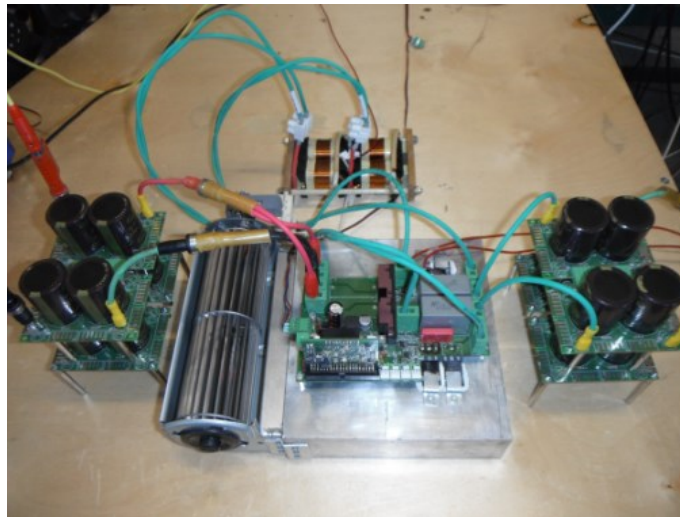


Figure 5.20. Two-phase interleaved test set-up

This section details the development and experimental testing of the prototype 3C92 2L toroid and CCTT IM inductors. The two-phase interleaved experimental test set up is presented in Fig. 5.22 and is the same test set up as presented in Section 4.9.3. The experimental test conditions are presented in Table 5.2. The magnetic components of the boost converter must meet the worst case voltage, current and power specifications as presented in Fig. 5.3.

Table 5.2 3C92 Discrete Toroid and CCTT IM Experimental Test Conditions and Information

Test #		# 1	# 2	# 3	# 4
Input Voltage (V_{in})	V	135	250	350	420
Output Voltage (V_{out})	V	500	500	500	500
Duty Cycle (D)	-	0.73	0.5	0.3	0.16
Switching Frequency (f)	kHz	16	16	16	16
Input Current (I_{in})	A	19	19	19	19
Input Power (P_{in})	kW	2.56	4.75	6.65	7.98
Load (R_{out})	Ω	97	53	38	32

5.7.1. Experimental Testing of 2L Discrete Inductors

5.7.1.1. Initial Toroid Development

The main parameters of the two toroidal inductors are presented in Table 5.3. The results are recorded using a Wayne Kerr precision magnetics analyser. The inductance vs. dc bias of each inductor is presented in Fig. 5.21 and Fig. 5.22, respectively. Both inductors are rated for 9.5 A dc and on inspection of Fig. 5.21 and Fig. 5.22, both inductors witness a reduction in inductance of approximately 7 % at this condition. Both inductors are rated for a peak current of 11.9 A where they see a reduction in inductance of approximately 22 % at this condition.

Table 5.3 2L Toroid Inductor Parameters

Inductor #		# 1	# 2
Inductance (L)	μH	1610	1670
Dc Resistance (R_{dc})	m Ω	42	42
Number of Turns (N)	phase	60	60
Conductor Type	mm	6 x 0.9 mm copper	6 x 0.9 mm copper
Airgap (g)	mm	8 x 0.25	8 x 0.25
Toroid Core Dimensions	OD/ID/H (mm)	90/50/43	90/50/43
Boxed Volume (V_{boxed})	cm ³	510	510
Total Mass (M_{total})	kg	1.28	1.28

The maximum flux density of the material used in the design was de-rated from 0.52 T (at 20 °C) to 0.36 T. The increase in dynamic permeability of the material with ac flux density will help increase its permeability and inductance at its peak operating condition.

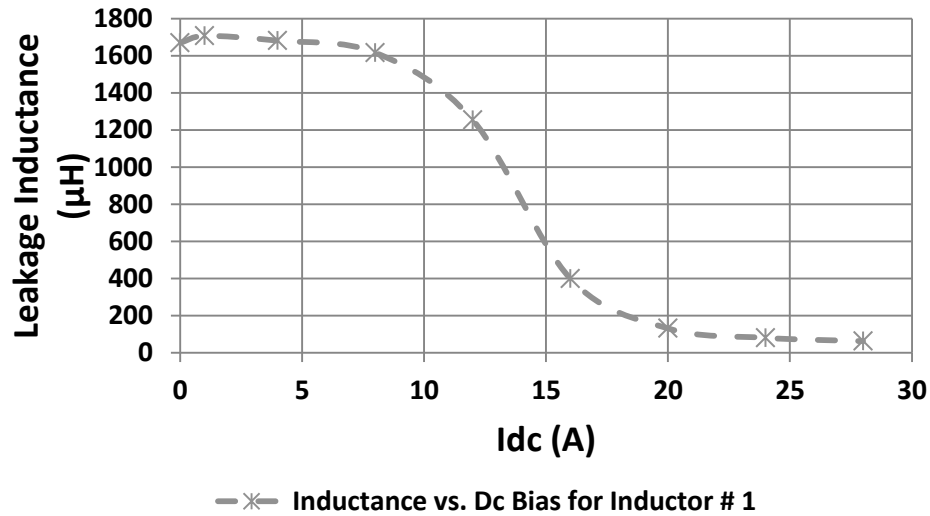


Figure 5.21. Inductance vs. dc bias for inductor #1

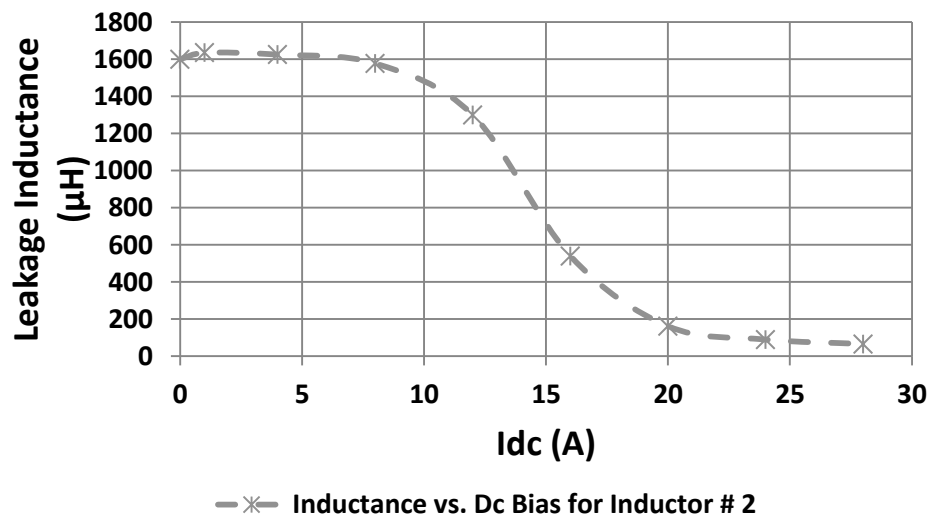


Figure 5.22. Inductance vs. dc bias for inductor #2

5.7.1.2. 3C92 Discrete Toroid Testing

The experimental testing was conducted at four different conditions which are detailed in Table 5.2. The input current and output voltage is kept constant along with the switching frequency. The input voltage is varied in order to vary the duty cycle and input power. As the

input voltage is varied the load was adjusted to achieve the same input current. Fig. 5.23 (a) and (b) present the experimental waveforms for $V_{in} = 135\text{ V}$ and 250 V , respectively. Fig. 5.24 (a) and (b) present the experimental waveforms for $V_{in} = 350\text{ V}$ and 420 V , respectively.

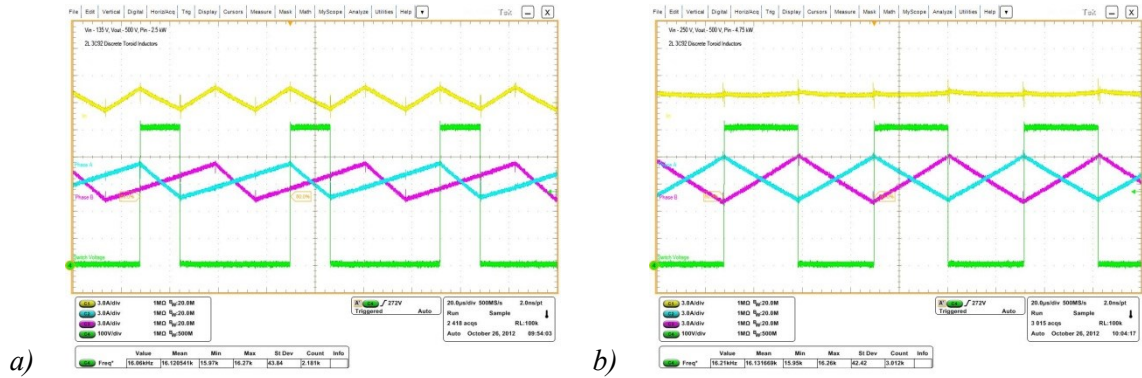


Figure 5.23. Experimental waveforms for (a) $V_{in} = 135\text{ V}$ and (b) $V_{in} = 250\text{ V}$

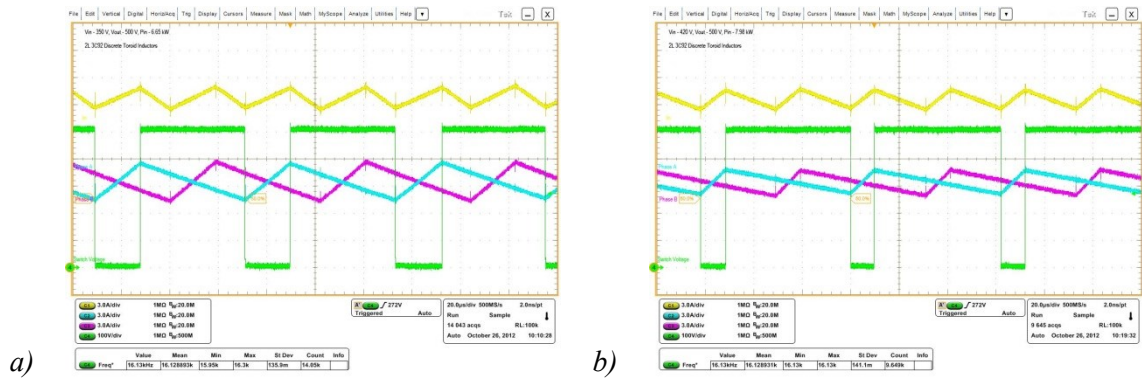


Figure 5.24. Experimental waveforms for (a) $V_{in} = 350\text{ V}$ and (b) $V_{in} = 250\text{ V}$

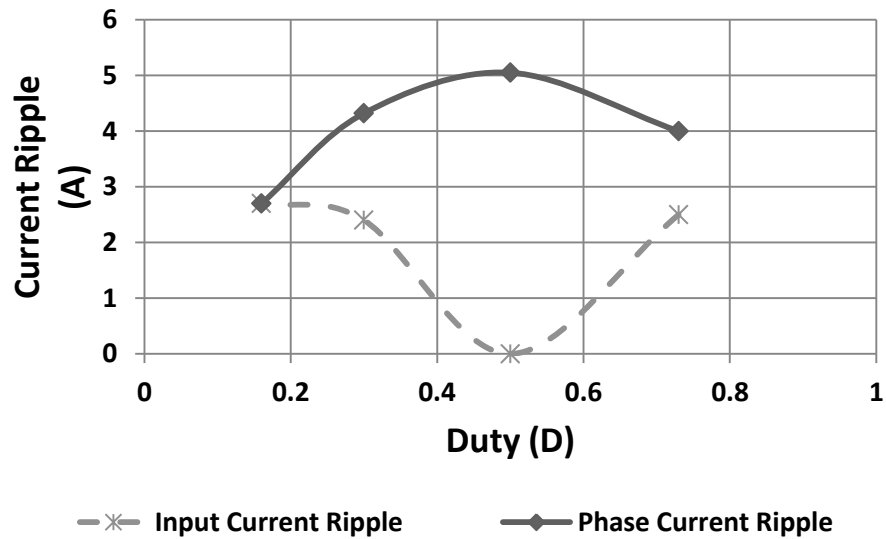


Figure 5.25. 2L experimental input and phase current ripple

Fig. 5.25 presents the 2L baseline experimental input- and phase-current ripple at each test point. The experimental ripple current readings correspond excellently with the predicted ripple current values. For example, at $D = 0.5$ the predicted phase-current ripple is 4.76 A while the experimental reading is 5 A. The experimental efficiency is presented in Fig. 5.26 is excellent over the entire input power range.

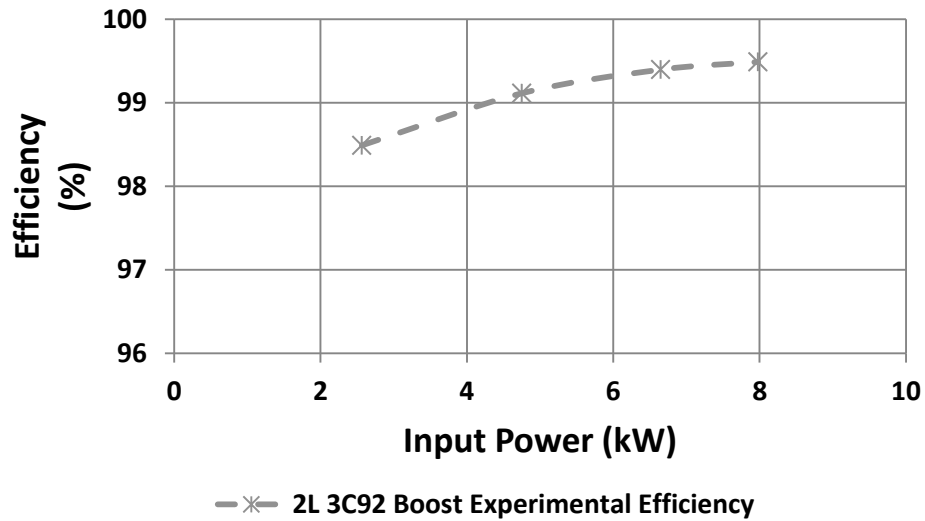


Figure 5.26. 2L experimental boost efficiency

Thermal testing was conducted for $V_{in} = 135$ V, 250 V and 420 V respectively. The worst case condition for the inductors, in terms of phase-current ripple, is at $D = 0.5$ and so it is reasonable to expect that the maximum temperature rise should be observed at this condition. Fig. 5.27 (a) and (b), Fig. 5.28 (a) and (b) and Fig. 5.29 (a) and (b) present the core and winding temperature rise of inductor # 1 and # 2 over the ambient temperature, respectively.

As expected, the worst case temperature rise over the ambient occurs at $V_{in} = 250$ V and $V_{out} = 500$ V where the temperature rise is approximately 25 °C in the core and windings for both inductors.

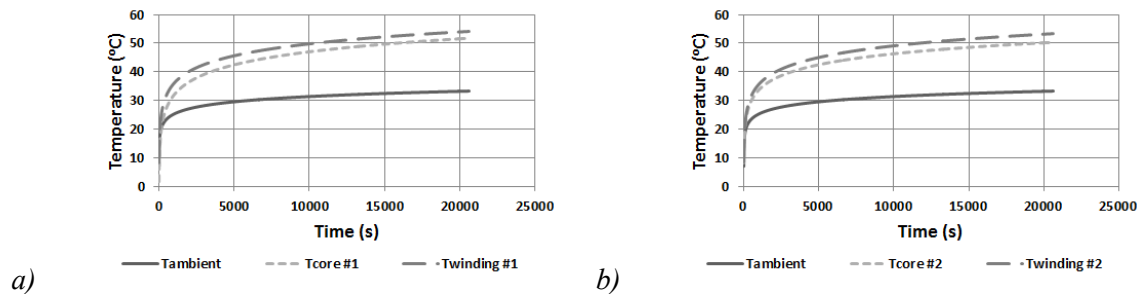


Figure 5.27. Temperature readings vs. time for $V_{in} = 135$ V, $V_{out} = 500$ V for (a) inductor #1 and (b) inductor #2

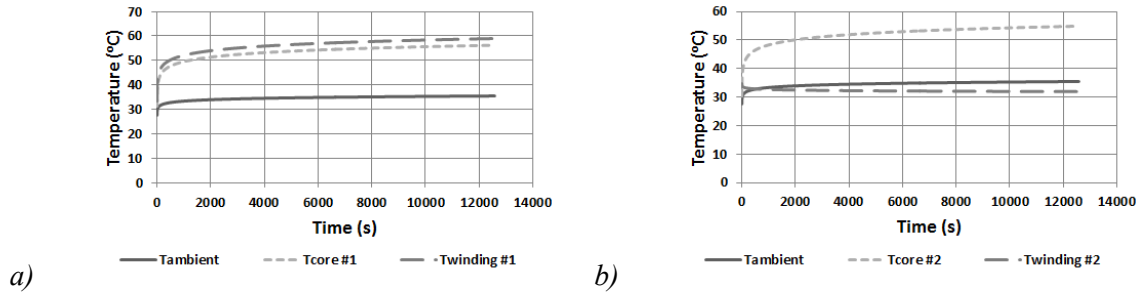


Figure 5.28. Temperature readings vs. time for $V_{in} = 250$ V, $V_{out} = 500$ V for (a) inductor #1 and (b) inductor #2

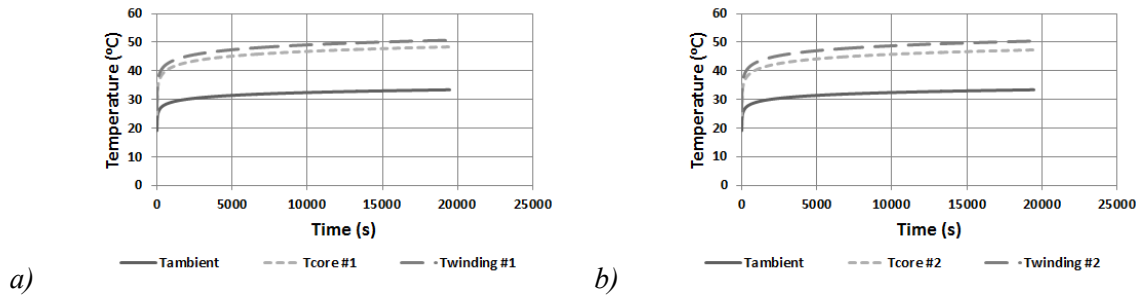


Figure 5.29. Temperature readings vs. time for $V_{in} = 420$ V, $V_{out} = 500$ V for (a) inductor #1 and (b) inductor #2

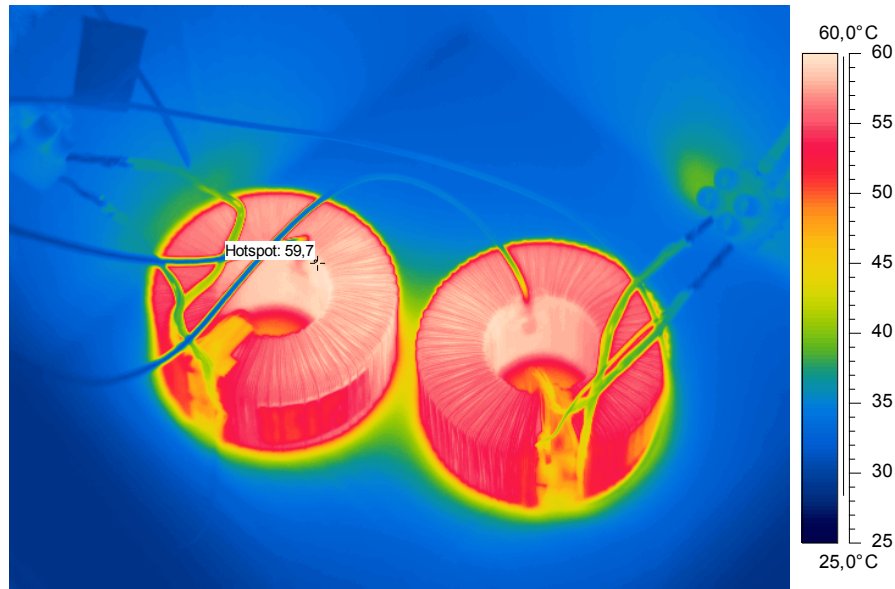


Figure 5.30. Thermal image for 2L inductors for $V_{in} = 135$ V

Thermal images were recorded at each design point and Fig. 5.30 and Fig. 5.31 present the thermal images for $V_{in} = 250$ V and 420 V for $V_{out} = 500$ V, respectively. The thermal image presented in Fig. 5.30, corresponding to $D = 0.5$, indicates a hotspot of 59.7 °C. The temperature of the MOSFET and diode at $V_{in} = 135$ V and 420 V are presented in Fig. 5.32 (a) and (b), respectively. All of the thermal images in this thesis were captured using a FLIR camera.

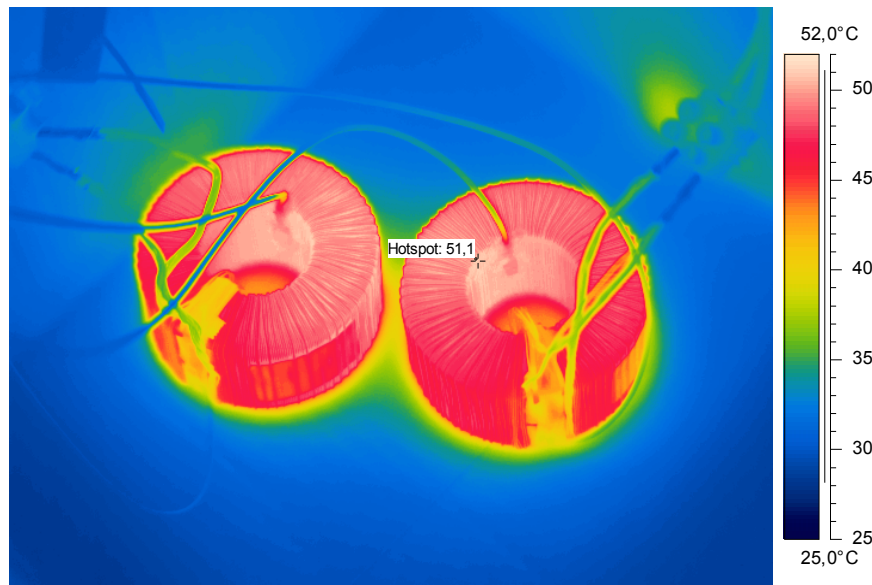


Figure 5.31. Thermal image for 2L inductors for $V_{in} = 135$ V

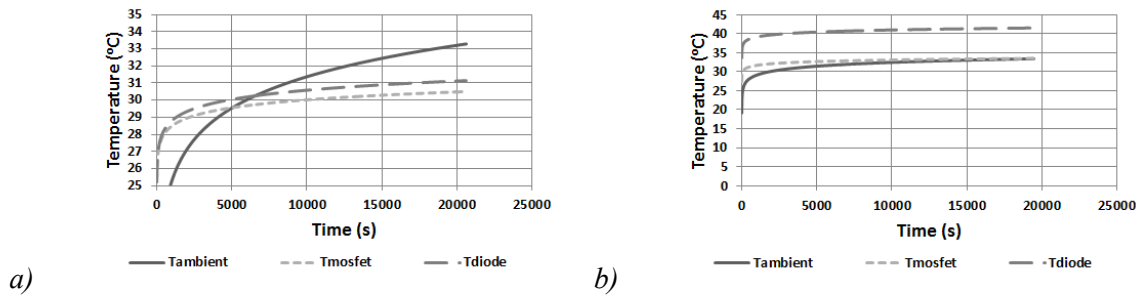


Figure 5.32. Temperature reading vs. time for (a) MOSFET and diode for $V_{in} = 135$ V and (b) MOSFET and diode for $V_{in} = 420$ V

5.7.1.3. Conclusions on 3C92 Discrete Toroid Testing

The two toroid inductors were tested under full, medium and low load conditions. A maximum temperature rise of 25 °C was observed in both inductors which occurred at a duty ratio $D = 0.5$. A thermal image of the inductors at its worst case operating point indicate a hotspot of 59.7 °C which is located on the inside wall of the toroid inductor. The efficiency of the converter is greater than 98.5 % over the entire operating range.

5.7.2. Experimental Testing of CCTT IM

5.7.2.1. Initial CCTT IM Development

A plan and isometric view of the CCTT IM is presented in Fig. 5.33 (a) and (b). A plan and isometric view of the CCTT IM and toroid inductors is presented in Fig. 5.34 (a) and (b).

The pictures indicate that there is a substantial reduction in volume in the CCTT IM. Table 5.4 presents the CCTT IM parameters.

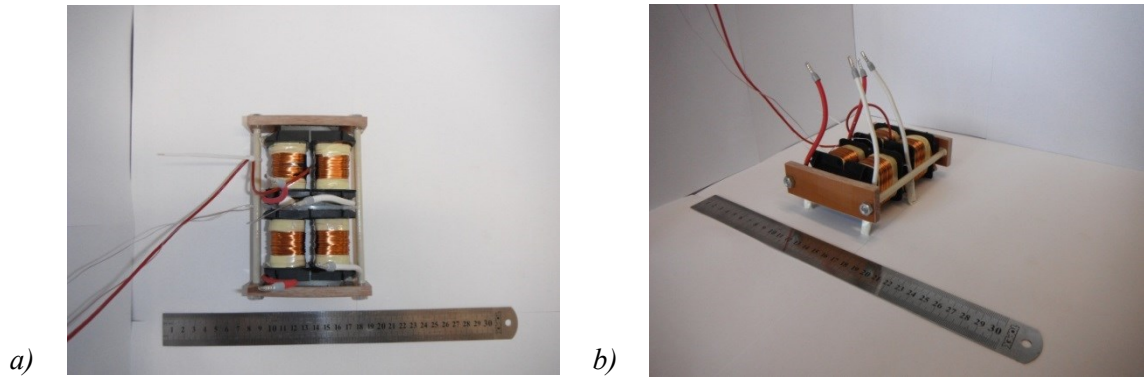


Figure 5.33. (a) Plan view and (b) isometric view of 3C92 CCTT IM

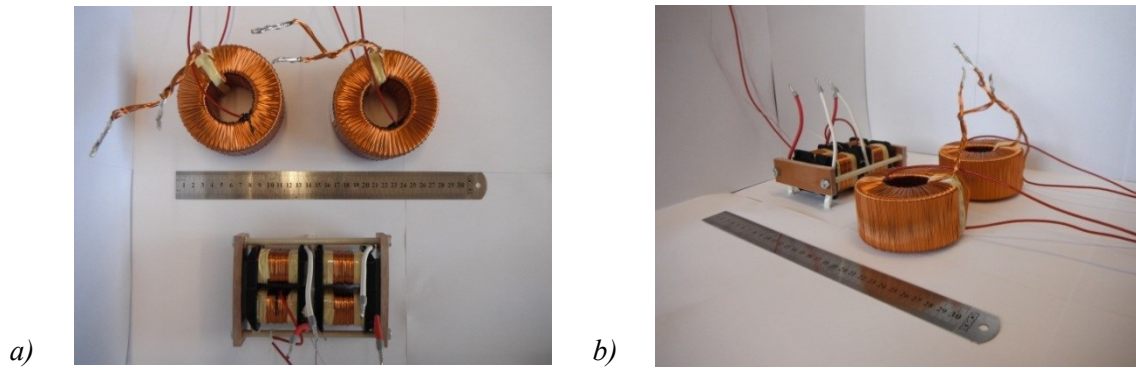


Figure 5.34. (a) Plan and (b) isometric view of 3C92 CCTT IM and 2L inductors

Table 5.4 CCTT IM Inductor Parameters

3C92 CCTT IM		
Leakage Inductance (L_{lk})	μH	578
Magnetizing Inductance (L_m)	mH	1.8
Phase A Inductance (L_a)	mH	2.40
Phase B Inductance (L_b)	mH	2.42
Dc Resistance Phase A (R_{dca})	$\text{m}\Omega$	31.5
Dc Resistance Phase A (R_{dcb})	$\text{m}\Omega$	31.5
Number of Turns (N)	phase	60
Conductor Type	mm	6 x 0.9 mm copper
Leakage Airgap (g)	mm	4.1
Magnetizing Airgap (l_{gm})	mm	4 x 0.15
Boxed Volume (V_{boxed})	cm^3	582
Total Mass (M_{total})	kg	1.28

The leakage inductance vs. dc bias is presented in Fig. 5.35. Similar to the 2L inductors, the results are recorded using a Wayne Kerr precision magnetics analyzer. The dc bias characteristic indicates that the CCTT IM will operate as designed when tested under power. The CCTT IM is rated for a peak current of 11.9 A and will see a reduction in leakage inductance of approximately 9 % when subjected to this current condition. The maximum flux density of the CCTT IM design is de-rated from 0.52 T (at 20 °C) to 0.36 T. The increase in dynamic permeability of the material with ac flux density will help increase its permeability and inductance at its peak operating condition. The leakage airgap that was predicted using the design algorithm (3.4 mm) is quite close to that used in the prototype (4.1 mm).

5.7.2.2. 3C92 CCTT IM Testing

The experimental testing was conducted at four different conditions which are detailed in Table 5.3. The test conditions are identical to what were used to test the discrete toroid inductors. The input current and output voltage is kept constant along with the switching frequency. The input voltage is varied in order to vary the duty cycle and input power. As the input voltage is varied the load was adjusted to achieve the same input current. Fig. 5.36 (a) and (b) present the experimental waveforms for $V_{in} = 135$ V and 250 V, respectively. Fig. 5.37 (a) and (b) present the experimental waveforms for $V_{in} = 350$ V and 420 V, respectively.

Fig. 5.38 presents the experimental input and phase current ripple at each test point. The CCTT IM converter efficiency as the input power is varied is presented in Fig. 5.39. The experimental ripple current readings correspond excellently with the predicted ripple current values. For example, at $D = 0.73$ the predicted phase-current ripple is 4.76 A while the experimental reading is 4.25 A. Similar to the 2L baseline design, the CCTT IM experimental efficiency is excellent over the entire input power range. The efficiency of the 2L baseline inductors is included and this shows that the CCTT IM is just as, if not more than, efficient as the 2L toroidal inductors. The plots in Fig. 5.38 and Fig. 5.39 also indicate that the reduction in input and phase current ripple at $D = 0.5$ results in increased efficiency for the CCTT IM in comparison to the 2L design. At this duty ratio the phase-current ripple of the CCTT IM is 60 % less than the phase current ripple of the 2L discrete toroid inductors.

Thermal testing is conducted for $V_{in} = 135$ V, 250 V, 350 V and 420 V respectively. The worst case condition for CCTT IM, in terms of input- and phase-current ripple, is at $D = 0.73$ and so it is reasonable to expect that the maximum temperature rise should be observed at this condition.

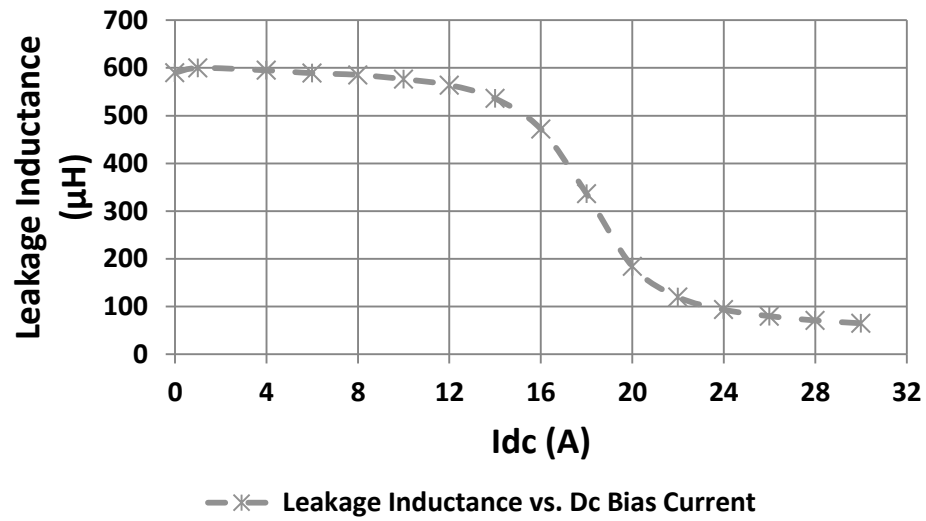


Figure 5.35. Leakage inductance vs. dc bias for 3C92 CCTT IM

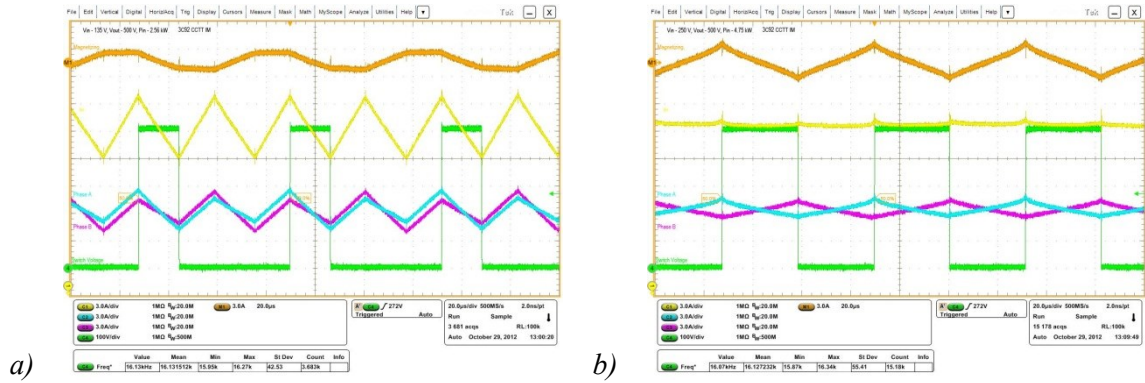


Figure 5.36. Experimental waveforms for (a) $V_{in} = 135\text{ V}$ and (b) $V_{in} = 250\text{ V}$

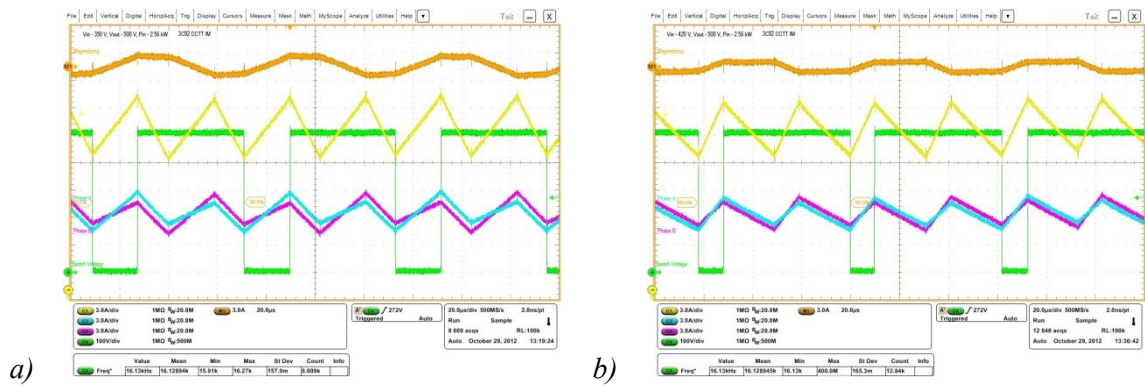


Figure 5.37. Experimental waveforms for (a) $V_{in} = 350\text{ V}$ and (b) $V_{in} = 420\text{ V}$

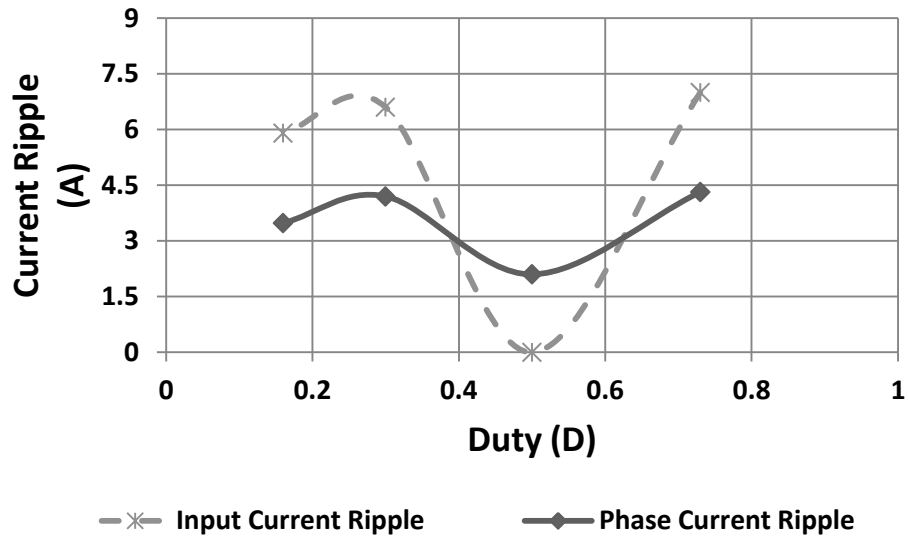


Figure 5.38. CCTT IM boost experimental input and phase current ripple

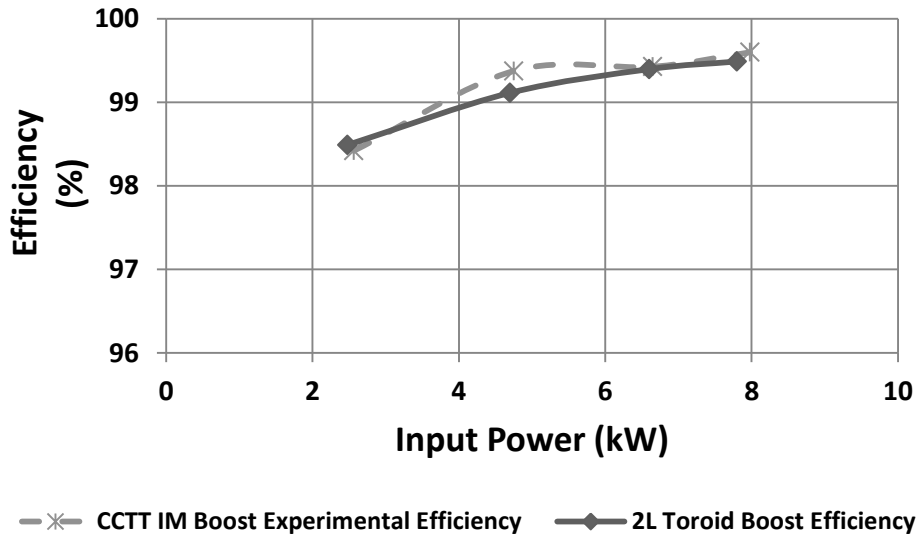


Figure 5.39. CCTT IM and 2L experimental boost efficiency

The temperature of the semiconductor switches and diodes were also recorded. Fig. 5.40 (a) and (b), Fig. 5.41 (a) and (b), Fig. 5.42 (a) and (b) and Fig. 5.43 (a) and (b) present the core and winding temperature rise of the CCTT IM and the semiconductor temperature rise over the ambient temperature, respectively. Thermal images were recorded at each design point and Fig. 5.44, Fig. 5.45, Fig. 5.46 and Fig. 5.47 present the thermal images for $V_{in} = 135$ V, 250 V, 350 V and 420 V and $V_{out} = 500$ V, respectively. The thermal images presented in Fig. 5.44 and Fig. 5.46 indicate a hotspot of nearly 85 °C.

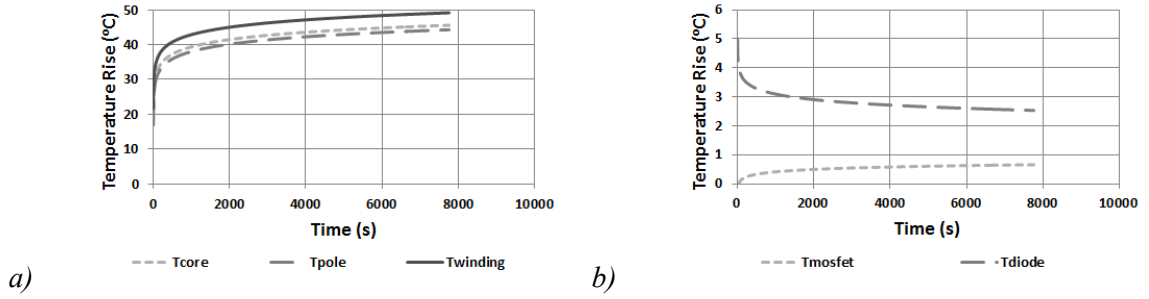


Figure 5.40. Temperature readings vs. time for $V_{in} = 135$ V, $V_{out} = 500$ V for (a) CCTT IM core, pole and winding and (b) semiconductors

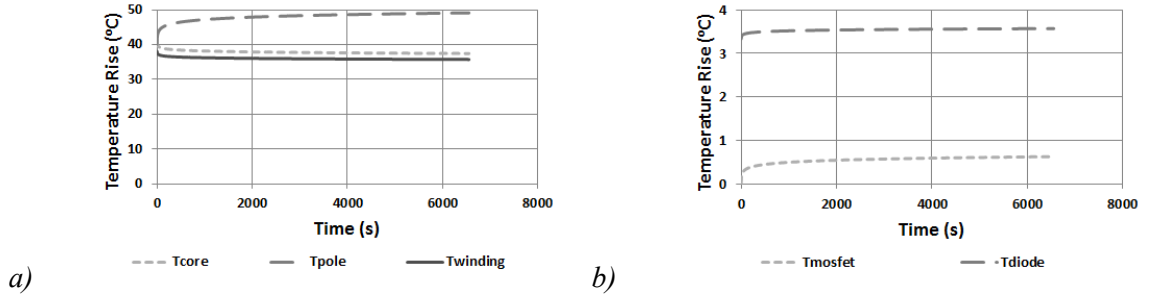


Figure 5.41. Temperature readings vs. time for $V_{in} = 250$ V, $V_{out} = 500$ V for (a) CCTT IM core, pole and winding and (b) semiconductors

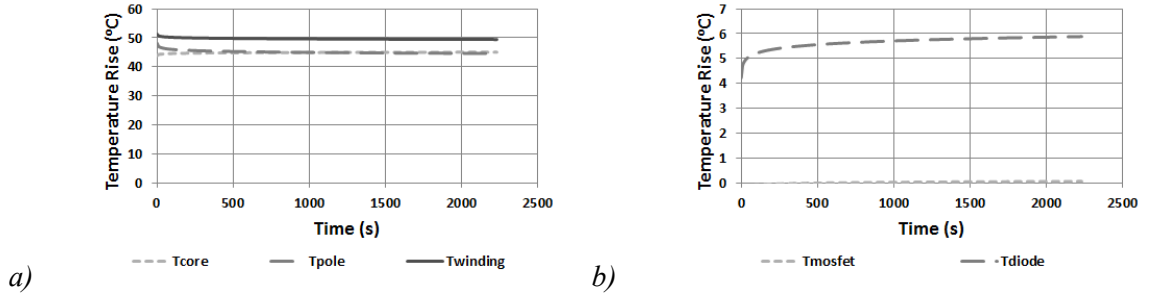


Figure 5.42. Temperature readings vs. time for $V_{in} = 350$ V, $V_{out} = 500$ V for (a) CCTT IM core, pole and winding and (b) semiconductors

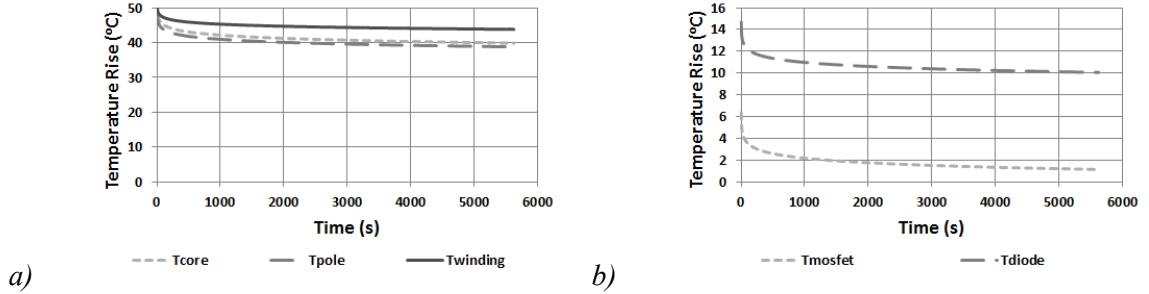


Figure 5.43. Temperature readings vs. time for $V_{in} = 420$ V, $V_{out} = 500$ V for (a) CCTT IM core, pole and winding and (b) semiconductors

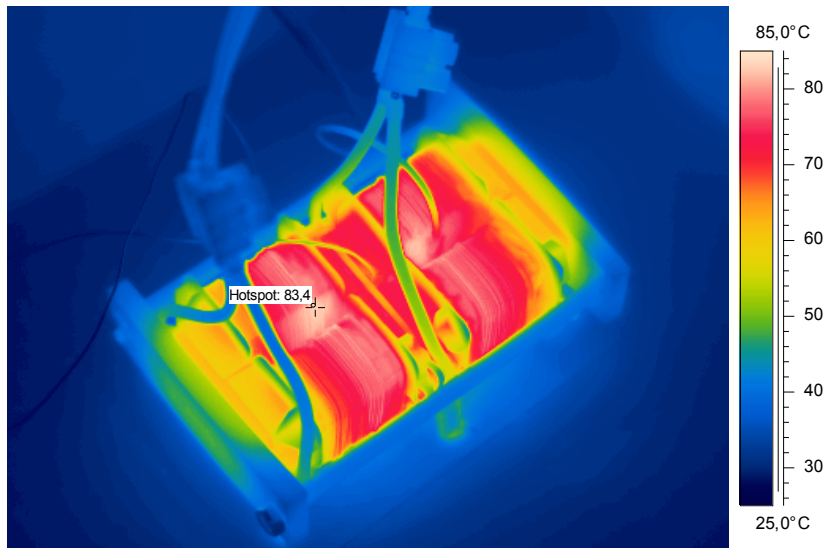


Figure 5.44. Thermal image of CCTT IM for (a) $V_{in} = 135 \text{ V}$, $V_{out} = 500 \text{ V}$

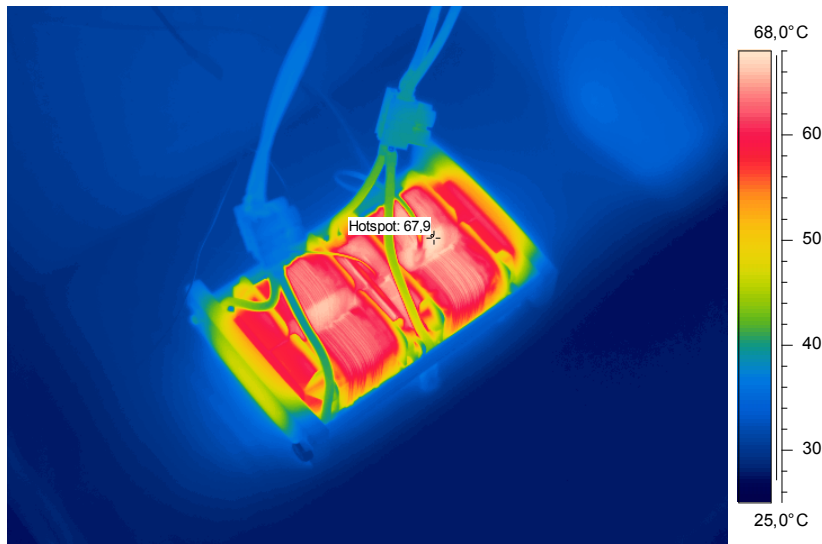


Figure 5.45. Thermal image of CCTT IM for (a) $V_{in} = 250 \text{ V}$, $V_{out} = 500 \text{ V}$

5.7.2.3. Conclusion on Feasibility of CCTT IM for use in Photovoltaic Applications

The pictures of the CCTT IM indicate that it allows for a large reduction in magnetic volume in comparison to the 2L toroid inductors. The size saving is achieved by reducing the leakage inductance, of the CCTT IM, by a factor of 3, in comparison to the toroid inductor for the same worst-case phase-current ripple. This reduction in inductance has the side-effect of increasing the input-current ripple by a factor of 3 which may result in the need for increased input capacitance in order to achieve the same level of filtering as the 2L baseline design. The CCTT IM allows for a 50 % reduction in mass and boxed volume over the 2L discrete toroid

inductors.

Experimental results showed that the CCTT IM has a marginally better efficiency in comparison to the 2L toroid inductors. This is especially true at $D = 0.5$, where the CCTT IM exhibits a 60 % reduction in phase-current ripple over the 2L design.

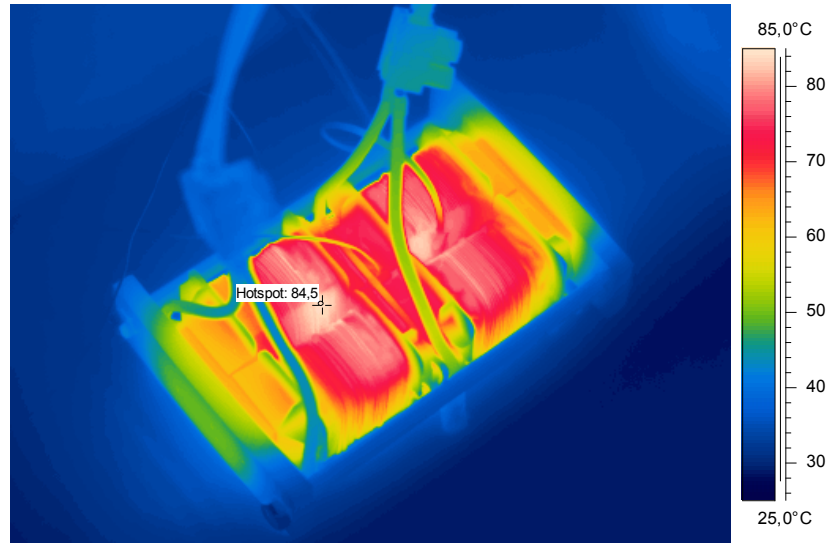


Figure 5.46. Thermal image of CCTT IM for (a) $V_{in} = 350$ V, $V_{out} = 500$ V

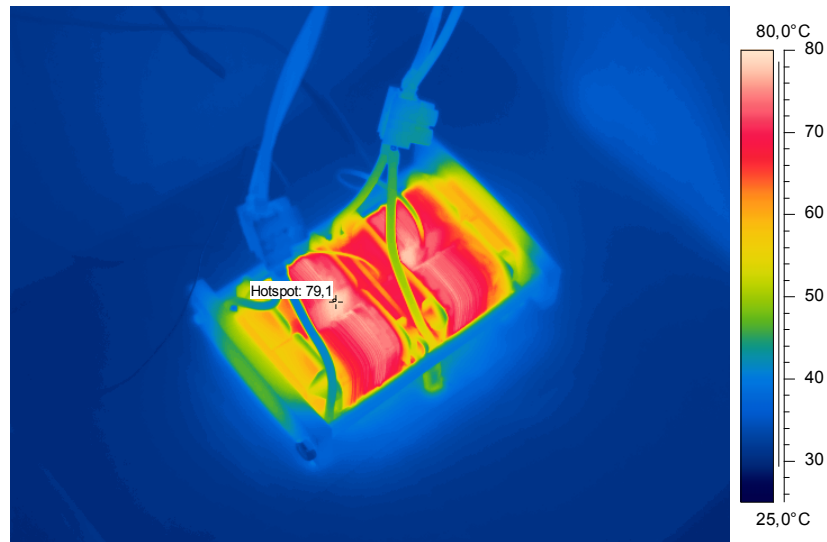


Figure 5.47. Thermal image of CCTT IM for (a) $V_{in} = 420$ V, $V_{out} = 500$ V

The maximum temperature rise of the CCTT IM occurred at $D = 0.73$ and 0.3 corresponding to maximum phase-current ripple conditions. The hotspot temperature at these test points is approximately 85 °C which corresponds to a temperature rise over the ambient of 50 °C.

In all, the 3C92 CCTT IM allows for a higher power-density magnetic solution in comparison to the baseline 2L toroidal inductors. This comes at the expense of increased input

current ripple. The effects of this on input capacitor sizing needs to be investigated as an element of future work.

5.8. Conclusions

This chapter investigated two magnetic topologies for use in a 8 kW two-phase interleaved boost converter for PV applications. The industry standard two-phase converter using two discrete 3C92 toroid inductors is considered as the baseline design. A 3C92 CCTT IM is designed to have the same worst-case phase current ripple. Designing the CCTT IM for this condition allows for a significant reduction in inductance, and therefore size in comparison to the baseline design.

The baseline 2L inductors are characterized using 2D FEA while the CCTT IM is designed using the design algorithm, presented in Chapter 2, and optimized using 2D FEA. Both designs use the same number of turn per phase and copper cross-sectional area in order to ensure the same current density. The CCTT IM allows for a reduction in boxed volume of 50 % in comparison to the baseline design. The total CCTT IM power loss is not affected by this reduction in volume but the input current ripple of the CCTT IM is seen to increase and this may have a consequential effect on the input filter capacitor sizing.

Both magnetic components are analysed over the worst-case operating range of a PV source where they are both found to have a similar power loss and efficiency. Additionally, the semiconductor loss is quantified and again, both designs have identical semiconductor power loss. As a result, the total efficiency of both designs is seen to be very similar as both are dominated by their respective semiconductor loss.

An 8 kW experimental design, test and build was undertaken to validate the CCTT IM design. The prototype CCTT IM is seen to be 50 % smaller in volume and mass in comparison to the 2L inductors. Critically, the CCTT IM is shown to be even more efficient than the 2L inductors, specifically at medium load conditions when the phase current ripple of the design is significantly smaller than that of the 2L option.

Chapter 6

Conclusions and Future Work

6.1. Thesis Summary

This thesis presents a novel CCTT-core split-winding integrated magnetic for use in high-power high-current dc-dc converter in renewable energy applications. Chapter 1 presents an introduction to the thesis and presents the background research conducted in the area of power electronic converters for use in renewable energy applications. The two main renewable energy applications that are discussed in this thesis are automotive fuelcell and PV solar inverter systems.

The circuit analysis of an integrated magnetic structure in an interleaved non-isolated dc-dc converter is presented in Chapter 2. Firstly, the converter operation in CCM for duty cycles less than and greater than 0.5 is presented. In specific applications the converter may enter into DCM, specifically, in automotive fuelcell systems the converter enters into DCM at low-load conditions. Therefore, the operation of the converter in DCM is also explored. The converter is found to have two modes of DCM operation which have been called “soft” and “hard” DCM. “Soft” DCM occurs when one phase of the converter goes to zero over a switching period while the converter enters into “hard” DCM when the input current ripple goes to zero. The circuit equations are validated using PSpice for a high-power 72 kW automotive fuelcell project.

The novel CCTT-core split-winding IM structure is presented in Chapter 3. The CCTT IM makes several improvements on existing IM technologies by integrating all magnetic components into one low power loss ferrite core which is (1) easy to manufacture, (2) uses split-phase windings to minimize the amount of unwanted external dc flux, thereby reducing its volume, (3) minimizes unwanted inter-winding capacitance, (4) employs ferrite poles to help contain the leakage flux within the CCTT core window and (5) uses a low number of turns for efficient heat removal from the conductors. Fringing flux equations accurately predict the fringing flux around the CCTT IM pole and winding regions. A dc and ac CCTT IM reluctance

model and design algorithm is presented that allows engineers to quickly design and prototype the CCTT IM. 3D FEA is used to optimize and validate the reluctance models. A design algorithm is developed in Mathematica that incorporates the fringing equations in order to develop an efficient and optimized IM design. The algorithm allows the user to compare and contrast a CCTT IM design over various frequencies, power levels and ripple ratios. The algorithm allows the user to select various core material and winding options. The algorithm also allows for the selection of different thermal options. Design curves are presented that show the variation in CCTT IM boxed volume, for three different magnetic materials, as the input current ripple ratio is varied. The results indicate that for medium-to-high input ripple ratios ferrite 3C92 is the material of choice and while it has a larger boxed volume its power loss is unbeatable. For low input ripple conditions the high-flux materials are competitive. The CCTT IM is shown to have a smaller boxed volume to an equivalent EE IM along with a more controlled ac inductance. Finally, the variation in CCTT IM boxed volume as the magnetizing inductance is varied is investigated.

Chapter 4 compares two magnetic component topologies for use in a two-phase interleaved dc-dc converter for automotive fuelcell applications. The CCTT IM and the 2L options, operating at 72 kW, 25 kHz, are designed to have the same worst-case phase-current ripple condition as a 3L, 97.2 kW, 16 kHz baseline design. The CCTT IM is shown to have a similar boxed volume to the 2L design as the 2L option has a higher inductance requirement. The CCTT IM is shown to have the best efficiency while the 2L suffers from excessive core and ac winding loss at part-load due to its higher current and flux ripples at these conditions. Experimental results are presented for the 72 kW CCTT IM converter. The predicted CCTT IM converter efficiency correlates with the experimental efficiency results. Experimental results validate the CCTT IM and 2L comparison for a set of 3.8 kW prototypes. The design and development of a high-flux material CCTT IM using amorphous metal 2605SA1 needs further investigation.

Chapter 5 compares two magnetic component topologies for use in a two-phase interleaved pre-regulator dc-dc converter for solar PV applications. The CCTT IM and the 2L options, operating at 8 kW, 16 kHz, are designed to have the same worst-case phase current ripple. The CCTT IM is shown to have a smaller boxed volume to the 2L design as the 2L option has a much higher inductance requirement. 8 kW experimental testing indicates that the CCTT IM has better efficiency than the 2L design. The prototype CCTT IM is approximately 50 % smaller in boxed volume and mass than the 2L option.

6.2. Future Work

- **CCTT IM using other Core Materials**

Investigation of the use of other magnetic materials for the construction of the CCTT IM core. The work in this thesis indicated that the use of amorphous metal material may allow for a significant reduction in magnetic volume at the expense of increased core power loss. This needs to be validated experimentally.

- **Closed Loop Control of the CCTT IM Converter**

The implementation of analogue and digital closed loop control of the CCTT IM at UCC. Further investigation of the converter operation in CCM, DCM and boundary conduction mode (BCM).

- **CCTT IM in Power Factor Correction Applications**

Analysis of the use of the CCTT IM in PFC applications. Development of an interleaved CCTT IM PFC boost converter at UCC and comparison with existing technology which uses an interleaved boost converter with two discrete inductors operating in BCM. A proposed paper investigating and comparing the CCTT IM and 2L PFC converters is currently under development and will be submitted to APEC 2014.

- **CCTT IM in High-Power Interleaved Symmetrical Boost Converter**

Investigation of the CCTT IM structure in alternative boost topologies such as symmetrical boost converters. This work is currently on-going with dtw in Poland.

- **Development of an Ac Copper Loss Model**

Investigation of the ac copper loss due to skin, proximity and skin effects, in the conductors of the CCTT IM. The development of an ac power loss model and the integration of this model into the CCTT IM design algorithm. The model should investigate various winding types such as, solid, stranded, foil and litz. The use of aluminium conductors should also be investigated.

- **CCTT IM Core Loss Investigation**

Investigation of core power loss in the CCTT IM. This is especially critical when using high-flux materials that exhibit high power loss. Investigation of core power loss due to dc bias conditions.

- **Total Converter Sizing**

Overall converter sizing including semiconductors, magnetic components, capacitors, heatsink and, other components.

Bibliography

- [1] "Renewables Global Status Report 2012," Renewable Energy Policy Network for the 21st Century, France.
- [2] E. Group, "Annual Renewable Report 2012," EirGrid2012.
- [3] G. Ailee, "Beyond the Smart-Grid," Intel, APEC2012.
- [4] C. Marnay, "Worldwide Microgrid Development: The Evolving Power Supply Paradigm," APEC 20122012.
- [5] J. McGowan, "Smart Microgrids - Powering the Electric Revolution," APEC 20112011.
- [6] N. P. Systems, "Vechile to Microgrid," 2011.
- [7] R. W. Erickson, *Fundamentals of Power Electronics*: Kluwer Academic Publishers, 2000.
- [8] F. Blaabjerg, C. Zhe, and S. B. Kjaer, "Power electronics as efficient interface in dispersed power generation systems," *Power Electronics, IEEE Transactions on*, vol. 19, pp. 1184-1194, 2004.
- [9] J. M. Carrasco, L. G. Franquelo, J. T. Bialasiewicz, E. Galvan, R. C. P. Guisado, M. A. M. Prats, *et al.*, "Power-Electronic Systems for the Grid Integration of Renewable Energy Sources: A Survey," *Industrial Electronics, IEEE Transactions on*, vol. 53, pp. 1002-1016, 2006.
- [10] M. Elbuluk and N. R. N. Idris, "The role power electronics in future energy systems and green industrialization," in *Power and Energy Conference, 2008. PECon 2008. IEEE 2nd International*, 2008, pp. 1-6.
- [11] N. C. Hingorani, "Power Electronics: Advances in the application of power electronics in generation, transmission, and distribution systems," *Power Engineering Review, IEEE*, vol. 15, p. 13, 1995.
- [12] L. Jih-Sheng, "Power conditioning systems for renewable energies," in *Electrical Machines and Systems, 2007. ICEMS. International Conference on*, 2007, pp. 209-218.
- [13] B. Kroposki, C. Pink, R. DeBlasio, H. Thomas, Simo, x, *et al.*, "Benefits of Power Electronic Interfaces for Distributed Energy Systems," *Energy Conversion, IEEE Transactions on*, vol. 25, pp. 901-908, 2010.
- [14] M. Liserre, T. Sauter, and J. Y. Hung, "Future Energy Systems: Integrating Renewable Energy Sources into the Smart Power Grid Through Industrial Electronics," *Industrial Electronics Magazine, IEEE*, vol. 4, pp. 18-37, 2010.
- [15] M. Marz, A. Schletz, B. Eckardt, S. Egelkraut, and H. Rauh, "Power electronics system integration for electric and hybrid vehicles," in *Integrated Power Electronics Systems (CIPS), 2010 6th International Conference on*, 2010, pp. 1-10.
- [16] C. C. Chan, "The State of the Art of Electric, Hybrid, and Fuel Cell Vehicles," *Proceedings of the IEEE*, vol. 95, pp. 704-718, 2007.
- [17] C. C. Chan and Y. S. Wong, "Electric vehicles charge forward," *Power and Energy Magazine, IEEE*, vol. 2, pp. 24-33, 2004.
- [18] M. C. Wehrey, "What's new with hybrid electric vehicles," *Power and Energy Magazine, IEEE*, vol. 2, pp. 34-39, 2004.
- [19] www.toyota.com.
- [20] www.gm.com.
- [21] www.ford.com.
- [22] www.nissian.com.
- [23] S. Nozawa, T. Maekawa, E. Yagi, Y. Terao, and H. Kohno, "Development of new power control unit for compact-class vehicle," in *Power Semiconductor Devices & IC's (ISPSD), 2010 22nd International Symposium on*, 2010, pp. 43-45.
- [24] D. U. Sauer, "Propulsion systems for hybrid and fuel cell electric vehicles," presented at

- the EPE, 2007.
- [25] A. Kirubakaran, S. Jain, and R. K. Nema, "A review on fuel cell technologies and power electronic interface," *Renewable and Sustainable Energy Reviews*, vol. 13, pp. 2430-2440, 12// 2009.
 - [26] J. Van Mierlo, Y. Cheng, J.-M. Timmermans, and P. Van den Bossche, "Comparison of Fuel Cell Hybrid Propulsion Topologies with Super-Capacitor," in *Power Electronics and Motion Control Conference, 2006. EPE-PEMC 2006. 12th International*, 2006, pp. 501-505.
 - [27] S. AG, "Inverter and PV System Technology," *Renewables Insight - Energy Industry Guides* 2012.
 - [28] Solmetric, "Guide To Interpreting I-V Curve Measurements of PV Arrays," 2011.
 - [29] A. Sharma, "The Future Development of the Solar Inverter, Power Optimizer and Microinverter Market," presented at the APEC, 2012.
 - [30] R. Simpson, "Evolution of microinverter," *Power One*, APEC 2012 2012.
 - [31] E. Energy, "Reliability of Enphase Micro-Inverters," 2009.
 - [32] Y. Bong-Gi, K. Jong-Soo, L. Byoung-Kuk, C. Gwang-Bo, and Y. Dong-Wook, "Optimization of powder core inductors of buck-boost converters for Hybrid Electric Vehicles," in *Vehicle Power and Propulsion Conference, 2009. VPPC '09. IEEE*, 2009, pp. 730-735.
 - [33] Y. Bong-Gi, L. Sang-Won, C. Gwang-Bo, Y. Dong-Wook, and L. Byoung-Kuk, "Comparison of simulation and experimental results for Mega Flux inductors in Hybrid Electric Vehicles," in *Power Electronics and ECCE Asia (ICPE & ECCE), 2011 IEEE 8th International Conference on*, 2011, pp. 1950-1957.
 - [34] M. Gerber, J. A. Ferreira, I. W. Hofsjager, and N. Seliger, "A high-density heat-sink-mounted inductor for automotive applications," *Industry Applications, IEEE Transactions on*, vol. 40, pp. 1031-1038, 2004.
 - [35] R. M. Schupbach and J. C. Balda, "Comparing DC-DC converters for power management in hybrid electric vehicles," in *Electric Machines and Drives Conference, 2003. IEMDC'03. IEEE International*, 2003, pp. 1369-1374 vol.3.
 - [36] D. P. Urciuoli and C. W. Tipton, "Development of a 90 kW bi-directional DC-DC converter for power dense applications," in *Applied Power Electronics Conference and Exposition, 2006. APEC '06. Twenty-First Annual IEEE*, 2006, p. 4 pp.
 - [37] G. Calderon-Lopez and A. J. Forsyth, "High-Power Dual-Interleaved ZVS Boost Converter with Interphase Transformer for Electric Vehicles," in *Applied Power Electronics Conference and Exposition, 2009. APEC 2009. Twenty-Fourth Annual IEEE*, 2009, pp. 1078-1083.
 - [38] G. Calderon-Lopez, A. J. Forsyth, and D. R. Nuttall, "Design and Performance Evaluation of a 10-kW Interleaved Boost Converter for a Fuel Cell Electric Vehicle," in *Power Electronics and Motion Control Conference, 2006. IPEMC 2006. CES/IEEE 5th International*, 2006, pp. 1-5.
 - [39] S. Chandrasekaran and L. U. Gokdere, "Integrated magnetics for interleaved DC-DC boost converter for fuel cell powered vehicles," in *Power Electronics Specialists Conference, 2004. PESC 04. 2004 IEEE 35th Annual*, 2004, pp. 356-361 Vol.1.
 - [40] J. Czogalla, L. Jeli, and C. R. Sullivan, "Automotive application of multi-phase coupled-inductor DC-DC converter," in *Industry Applications Conference, 2003. 38th IAS Annual Meeting. Conference Record of the*, 2003, pp. 1524-1529 vol.3.
 - [41] S. Dwari and L. Parsa, "A Novel High Efficiency High Power Interleaved Coupled-Inductor Boost DC-DC Converter for Hybrid and Fuel Cell Electric Vehicle," in *Vehicle Power and Propulsion Conference, 2007. VPPC 2007. IEEE*, 2007, pp. 399-404.
 - [42] J. Elmes, R. Kersten, I. Batarseh, M. Pepper, and K. Mansfield, "Modular bidirectional DC-DC converter for hybrid/electric vehicles with variable-frequency interleaved soft-switching," in *Vehicle Power and Propulsion Conference, 2009. VPPC '09. IEEE*, 2009,

- pp. 448-454.
- [43] A. Fratta, P. Casasso, G. Griffero, P. Guglielmi, S. Nieddu, and G. M. Pellegrino, "New design concepts and realisation of hybrid DC/DC coupling reactors for light EVs," in *Industrial Electronics Society, 2003. IECON '03. The 29th Annual Conference of the IEEE*, 2003, pp. 2877-2882 Vol.3.
 - [44] A. Fratta, G. Griffero, S. Nieddu, G. Pellegrino, and F. Villata, "Inductive three-level V.-supplied conversion cell by new hybrid coupling reactor family," in *Industry Applications Conference, 2002. 37th IAS Annual Meeting. Conference Record of the*, 2002, pp. 2378-2385 vol.4.
 - [45] A. Fratta, G. Griffero, S. Nieddu, G. M. Pellegrino, and F. Villata, "New hybrid iron-ferrite-core coupling reactors upgrade effectiveness of H-bridge-based power conversion structures," in *Industrial Electronics, 2002. ISIE 2002. Proceedings of the 2002 IEEE International Symposium on*, 2002, pp. 884-889 vol.3.
 - [46] A. Fratta, P. Guglielmi, F. Villata, and A. Vagati, "Efficiency and cost-effectiveness of AC drives for electric vehicles improved by a novel, boost DC-DC conversion structure," in *Power Electronics in Transportation, 1998*, 1998, pp. 11-19.
 - [47] S. Gui-Jia and T. Lixin, "A Three-Phase Bidirectional DC-DC Converter for Automotive Applications," in *Industry Applications Society Annual Meeting, 2008. IAS '08. IEEE*, 2008, pp. 1-7.
 - [48] X. Haiping, W. Xuhui, E. Qiao, G. Xin, and K. Li, "High Power Interleaved Boost Converter in Fuel Cell Hybrid Electric Vehicle," in *Electric Machines and Drives, 2005 IEEE International Conference on*, 2005, pp. 1814-1819.
 - [49] M. Hirakawa, M. Nagano, Y. Watanabe, K. Ando, S. Nakatomi, S. Hashino, *et al.*, "High power density interleaved DC/DC converter using a 3-phase integrated close-coupled inductor set aimed for electric vehicles," in *Energy Conversion Congress and Exposition (ECCE), 2010 IEEE*, 2010, pp. 2451-2457.
 - [50] M. Hirakawa, M. Nagano, Y. Watanabe, K. Andoh, S. Nakatomi, and S. Hashino, "High power density DC/DC converter using the close-coupled inductors," in *Energy Conversion Congress and Exposition, 2009. ECCE 2009. IEEE*, 2009, pp. 1760-1767.
 - [51] M. Hirakawa, Y. Watanabe, M. Nagano, K. Andoh, S. Nakatomi, S. Hashino, *et al.*, "High power DC/DC converter using extreme close-coupled inductors aimed for electric vehicles," in *Power Electronics Conference (IPEC), 2010 International*, 2010, pp. 2941-2948.
 - [52] M. Nakahama, M. Yamamoto, and Y. Satake, "Trans-linked multi-phase boost converter for electric vehicle," in *Energy Conversion Congress and Exposition (ECCE), 2010 IEEE*, 2010, pp. 2458-2463.
 - [53] C. N. M. Ho, H. Breuninger, S. Pettersson, G. Escobar, L. Serpa, and A. Coccia, "Practical implementation of an interleaved boost converter using SiC diodes for PV applications," in *Power Electronics and ECCE Asia (ICPE & ECCE), 2011 IEEE 8th International Conference on*, 2011, pp. 372-379.
 - [54] J. Doo-Yong, J. Young-Hyok, P. Sang-Hoon, J. Yong-Chae, and W. Chung-Yuen, "Interleaved Soft-Switching Boost Converter for Photovoltaic Power-Generation System," *Power Electronics, IEEE Transactions on*, vol. 26, pp. 1137-1145, 2011.
 - [55] H. Yao-Ching, H. Te-Chin, and Y. Hau-Chen, "An Interleaved Boost Converter With Zero-Voltage Transition," *Power Electronics, IEEE Transactions on*, vol. 24, pp. 973-978, 2009.
 - [56] Y. Bo, L. Wuhua, Z. Yi, and H. Xiangning, "Design and Analysis of a Grid-Connected Photovoltaic Power System," *Power Electronics, IEEE Transactions on*, vol. 25, pp. 992-1000, 2010.
 - [57] M. Technology, "Grid-Connected Solar Microinverter Reference Design using a dsPIC® Digital Signal Controller," 2011.
 - [58] J. Shen, "Advances and Trends in Power Semiconductors," 2010.

- [59] K. Shenai, "High Efficiency Power Electronics Switching in Renewable Energy Applications," presented at the APEC, 2011.
- [60] A. Elasser, M. H. Kheraluwala, M. Ghezzi, R. L. Steigerwald, N. A. Evers, J. Kretschmer, *et al.*, "A comparative evaluation of new silicon carbide diodes and state-of-the-art silicon diodes for power electronic applications," *Industry Applications, IEEE Transactions on*, vol. 39, pp. 915-921, 2003.
- [61] F. Chimento, S. Musumeci, A. Raciti, M. Melito, and G. Sorrentino, "Super-Junction MOSFET and SiC Diode Application for the Efficiency Improvement in a Boost PFC Converter," in *IEEE Industrial Electronics, IECON 2006 - 32nd Annual Conference on*, 2006, pp. 2067-2072.
- [62] M. Janicki, D. Makowski, P. Kedziora, L. Starzak, G. Jablonski, and S. Bek, "Improvement Of PFC Boost Converter Energy Performance Using Silicon Carbide Diode," in *Mixed Design of Integrated Circuits and System, 2006. MIXDES 2006. Proceedings of the International Conference*, 2006, pp. 615-618.
- [63] B. Eckardt, A. Hofmann, S. Zeltner, and M. Maerz, "Automotive Powertrain DC/DC Converter with 25kW/dm(exp3) by using SiC Diodes," *Integrated Power Systems (CIPS), 2006 4th International Conference on*, pp. 1-6, 2006.
- [64] V. R. Garuda, M. K. Kazimierczuk, M. L. Ramalingam, L. Tolkkinen, and M. D. Roth, "High temperature testing of a buck converter using silicon and silicon carbide diodes," in *Energy Conversion Engineering Conference, 1997. IECEC-97., Proceedings of the 32nd Intersociety*, 1997, pp. 317-322 vol.1.
- [65] K. Shenai, "Silicon carbide power converters for next generation aerospace electronics applications," in *National Aerospace and Electronics Conference, 2000. NAECON 2000. Proceedings of the IEEE 2000*, 2000, pp. 516-523.
- [66] L. D. Stevanovic, K. S. Matocha, P. A. Losee, J. S. Glaser, J. J. Nasadoski, and S. D. Arthur, "Recent advances in silicon carbide MOSFET power devices," in *Applied Power Electronics Conference and Exposition (APEC), 2010 Twenty-Fifth Annual IEEE*, 2010, pp. 401-407.
- [67] K. S. Boutros, C. Rongming, and B. Hughes, "GaN power electronics for automotive application," in *Energytech, 2012 IEEE*, 2012, pp. 1-4.
- [68] S. Dargahi and S. S. Williamson, "On the suitability of Gallium-Nitride (GaN) based automotive power electronics," in *Vehicle Power and Propulsion Conference (VPPC), 2010 IEEE*, 2010, pp. 1-6.
- [69] M. A. Khan, G. Simin, S. G. Pytel, A. Monti, E. Santi, and J. L. Hudgins, "New Developments in Gallium Nitride and the Impact on Power Electronics," in *Power Electronics Specialists Conference, 2005. PESC '05. IEEE 36th*, 2005, pp. 15-26.
- [70] V. C. V. Alex Van Den Bossche, *Inductors and Transformers for Power Electronics*: CRC Press, 2005.
- [71] M. Bartoli, N. Noferi, A. Reatti, and M. K. Kazimierczuk, "Modeling Litz-wire winding losses in high-frequency power inductors," in *Power Electronics Specialists Conference, 1996. PESC '96 Record., 27th Annual IEEE*, 1996, pp. 1690-1696 vol.2.
- [72] M. Bartoli, A. Reatti, and M. K. Kazimierczuk, "Minimum copper and core losses power inductor design," in *Industry Applications Conference, 1996. Thirty-First IAS Annual Meeting, IAS '96., Conference Record of the 1996 IEEE*, 1996, pp. 1369-1376 vol.3.
- [73] B. Carston, "Magnetics Design Seminar," PEI Technologies, 1996.
- [74] K. J. Hartnett, J. G. Hayes, M. G. Egan, and M. S. Rylko, "CCTT-Core Split-Winding Integrated Magnetic for High-Power DC-DC Converters," *Power Electronics, IEEE Transactions on*, vol. PP, pp. 1-1, 2013.
- [75] B. J. Lyons, J. G. Hayes, and M. G. Egan, "Design Algorithm for High-Current Gapped Foil-Wound Inductors in Low-to-Medium Frequency DC-DC Converters," in *Power Electronics Specialists Conference, 2007. PESC 2007. IEEE*, 2007, pp. 1760-1766.

- [76] S. Maniktala, *Switching Power Supply Design & Optimization*: McGraw-Hill, 2004.
- [77] C. W. T. McLyman, *Transformer and Inductor Design Handbook*, 2nd ed.: Marcel Dekker, Inc, 1998.
- [78] H. N. S. Michael J. Moran, *Fundamentals of Engineering Thermodynamics*: VCH Wiley, 1998.
- [79] www.ferroxcube.com.
- [80] www.jfesteel.com.
- [81] www.metglas.com.
- [82] B. Lyons, "High-Current Inductors for High-Power Automotive DC-DC Converters," Ph.D., Electrical and Electronic Engineering, University College Cork, Cork, 2008.
- [83] M. Rylko, "Magnetic Materials and Soft-Switching Topologies for High-Current DC-DC Converters," Ph.D., Electrical and Electronic Engineering, University College Cork, Cork, 2011.
- [84] www.epcos.com.
- [85] www.avx.com.
- [86] www.kemet.com.
- [87] www.vishay.com.
- [88] K. S. Davide Montanari, Fabio Scagliarini, and M. N. Dietmar Zeidler, Claes Nender. (2009, Film Capacitors for Automotive and Industrial Applications.
- [89] Epcos. (2009, Film Capacitors for Solar Inverter Systems.
- [90] Epcos, "Power Capacitors for Industrial Applications and Renewable Energy," 2012.
- [91] T. M. U. a. W. P. R. Ned Mohan, *Power Electronics - Converters, Applications, and Design*: John Wiley & Sons, Inc, 1995.
- [92] L. Balogh and R. Redl, "Power-factor correction with interleaved boost converters in continuous-inductor-current mode," in *Applied Power Electronics Conference and Exposition, 1993. APEC '93. Conference Proceedings 1993., Eighth Annual*, 1993, pp. 168-174.
- [93] C. Bridge and L. Balogh, "Understanding Interleaved Boundary Conduction Mode PFC Converters," in *Fairchild Power Seminars, 2008-2009*, 2008.
- [94] J. Imaoka, Y. Ishikura, T. Kawashima, and M. Yamamoto, "Optimal design method for interleaved single-phase PFC converter with coupled inductor," in *Energy Conversion Congress and Exposition (ECCE), 2011 IEEE*, 2011, pp. 1807-1812.
- [95] L. Jeli, C. R. Sullivan, and A. Schultz, "Coupled-inductor design optimization for fast-response low-voltage," in *Applied Power Electronics Conference and Exposition, 2002. APEC 2002. Seventeenth Annual IEEE*, 2002, pp. 817-823 vol.2.
- [96] W. Jun, T. Jin, and K. Smedley, "A new interleaved isolated boost converter for high power applications," in *Applied Power Electronics Conference and Exposition, 2006. APEC '06. Twenty-First Annual IEEE*, 2006, p. 6 pp.
- [97] T. J. Liang and K. C. Tseng, "Analysis of integrated boost-flyback step-up converter," *Electric Power Applications, IEE Proceedings -*, vol. 152, pp. 217-225, 2005.
- [98] X. Liu, B. Zhang, J. Yu, J. Gallagher, and J. Feng, "A Non-isolated Voltage Regulator Module with Integrating Coupled-Inductor," in *Power Electronics Specialists Conference, 2005. PESC '05. IEEE 36th*, 2005, pp. 438-442.
- [99] C. Liu Xue, B. Zhang, L. Zhao, and J. Hu, "A new voltage regulator module with integrating coupled magnetic," in *Industrial Electronics Society, 2005. IECON 2005. 31st Annual Conference of IEEE*, 2005, p. 6 pp.
- [100] H. N. Nagaraja, D. Kastha, and A. Petra, "Design Principles of a Symmetrically Coupled Inductor Structure for Multiphase Synchronous Buck Converters," *Industrial Electronics, IEEE Transactions on*, vol. 58, pp. 988-997, 2011.
- [101] X. Peng, Y. Mao, W. Pit-Leong, and F. C. Lee, "Design of 48 V Voltage regulator modules with a novel integrated magnetics," *Power Electronics, IEEE Transactions on*, vol. 17, pp. 990-998, 2002.

- [102] W. Pit-Leong, X. Peng, P. Yang, and F. C. Lee, "Performance improvements of interleaving VRMs with coupling inductors," *Power Electronics, IEEE Transactions on*, vol. 16, pp. 499-507, 2001.
- [103] P. Xu and F. C. Lee, "Design of high-input voltage regulator modules with a novel integrated magnetics," in *Applied Power Electronics Conference and Exposition, 2001. APEC 2001. Sixteenth Annual IEEE*, 2001, pp. 262-267 vol.1.
- [104] A. M. S. a. C. R. Sullivan, "Voltage Converter with Coupled Inductive Windings, and Associated Methods," 2002.
- [105] H. C. Roters, *Electromagnetic Devices*: J. Wiley & Sons, 1941.
- [106] P. Zumel, O. Garcia, J. A. Cobos, and J. Uceda, "Magnetic integration for interleaved converters," in *Applied Power Electronics Conference and Exposition, 2003. APEC '03. Eighteenth Annual IEEE*, 2003, pp. 1143-1149 vol.2.
- [107] K. J. Hartnett, M. S. Rylko, J. G. Hayes, and M. G. Egan, "A comparison of classical two phase (2L) and transformer coupled (XL) interleaved boost converters for fuel cell applications," in *Applied Power Electronics Conference and Exposition (APEC), 2010 Twenty-Fifth Annual IEEE*, 2010, pp. 787-793.
- [108] K. J. Hartnett, J. G. Hayes, M. G. Egan, and M. S. Rylko, "Novel CCTT-core split-winding integrated magnetic for High-Power DC-DC converters," in *Energy Conversion Congress and Exposition (ECCE), 2011 IEEE*, 2011, pp. 598-605.
- [109] K. H. John Hayes, Marek Rylko, "CCTT-Core Split-Winding Integrated Magnetic," 2011.
- [110] K. J. Hartnett, J. G. Hayes, M. G. Egan, and M. S. Rylko, "Comparison of CCTT split-winding and EE integrated magnetics for high-power dc-dc converters," in *Vehicle Power and Propulsion Conference (VPPC), 2011 IEEE*, 2011, pp. 1-6.
- [111] A. Balakrishnan, W. T. Joines, and T. G. Wilson, "Air-gap reluctance and inductance calculations for magnetic circuits using a Schwarz-Christoffel transformation," *Power Electronics, IEEE Transactions on*, vol. 12, pp. 654-663, 1997.
- [112] A. F. Hoke and C. R. Sullivan, "An improved two-dimensional numerical modeling method for E-core transformers," in *Applied Power Electronics Conference and Exposition, 2002. APEC 2002. Seventeenth Annual IEEE*, 2002, pp. 151-157 vol.1.
- [113] E. Santi and S. Cuk, "Accurate leakage models of gapped magnetic circuits," in *Applied Power Electronics Conference and Exposition, 1993. APEC '93. Conference Proceedings 1993., Eighth Annual*, 1993, pp. 596-603.
- [114] A. Van den Bossche, V. Valchev, and T. Filchev, "Improved approximation for fringing permeances in gapped inductors," in *Industry Applications Conference, 2002. 37th IAS Annual Meeting. Conference Record of the*, 2002, pp. 932-938 vol.2.
- [115] Y. Yang, D. Yan, and F. C. Lee, "A new coupled inductors design in 2-phase interleaving VRM," in *Power Electronics and Motion Control Conference, 2009. IPEMC '09. IEEE 6th International*, 2009, pp. 344-350.
- [116] M. S. Rylko, B. J. Lyons, K. J. Hartnett, J. G. Hayes, and M. G. Egan, "Magnetic material comparisons for high-current gapped and gapless foil wound inductors in high frequency dc-dc converters," in *Power Electronics and Motion Control Conference, 2008. EPE-PEMC 2008. 13th*, 2008, pp. 1249-1256.
- [117] K. W. E. Cheng and P. D. Evans, "Calculation of winding losses in high frequency toroidal inductors using multistrand conductors," *Electric Power Applications, IEE Proceedings -*, vol. 142, pp. 313-322, 1995.
- [118] M. E. Dale and C. R. Sullivan, "General Comparison of Power Loss in Single-Layer and Multi-Layer Windings," in *Power Electronics Specialists Conference, 2005. PESC '05. IEEE 36th*, 2005, pp. 582-589.
- [119] M. E. Dale and C. R. Sullivan, "Comparison of Loss in Single-Layer and Multi-Layer Windings with a DC Current Component," in *Industry Applications Conference, 2006. 41st IAS Annual Meeting. Conference Record of the 2006 IEEE*, 2006, pp. 1870-1875.

- [120] P. L. Dowell, "Effects of eddy currents in transformer windings," *Electrical Engineers, Proceedings of the Institution of*, vol. 113, pp. 1387-1394, 1966.
- [121] P. D. Evans and W. M. Chew, "Reduction of proximity losses in coupled inductors," *Electric Power Applications, IEE Proceedings B*, vol. 138, pp. 51-58, 1991.
- [122] J. A. Ferreira, "Improved analytical modeling of conductive losses in magnetic components," *Power Electronics, IEEE Transactions on*, vol. 9, pp. 127-131, 1994.
- [123] W. G. Hurley, E. Gath, and J. G. Breslin, "Optimizing the AC resistance of multilayer transformer windings with arbitrary current waveforms," in *Power Electronics Specialists Conference, 1999. PESC 99. 30th Annual IEEE*, 1999, pp. 580-585 vol.1.
- [124] W. G. Hurley, E. Gath, and J. G. Breslin, "Optimizing the AC resistance of multilayer transformer windings with arbitrary current waveforms," *Power Electronics, IEEE Transactions on*, vol. 15, pp. 369-376, 2000.
- [125] R. A. Jensen and C. R. Sullivan, "Optimal core dimensional ratios for minimizing winding loss in high-frequency gapped-inductor windings," in *Applied Power Electronics Conference and Exposition, 2003. APEC '03. Eighteenth Annual IEEE*, 2003, pp. 1164-1169 vol.2.
- [126] P. N. Murgatroyd, "Calculation of proximity losses in multistranded conductor bunches," *Physical Science, Measurement and Instrumentation, Management and Education, IEE Proceedings A*, vol. 136, pp. 115-120, 1989.
- [127] C. Schaef and C. R. Sullivan, "Inductor design for low loss with complex waveforms," in *Applied Power Electronics Conference and Exposition (APEC), 2012 Twenty-Seventh Annual IEEE*, 2012, pp. 1010-1016.
- [128] C. R. Sullivan, "Aluminum Windings and Other Strategies for High-Frequency Magnetics Design in an Era of High Copper and Energy Costs," in *Applied Power Electronics Conference, APEC 2007 - Twenty Second Annual IEEE*, 2007, pp. 78-84.
- [129] P. Wallmeier, "Improved analytical modeling of conductive losses in gapped high-frequency inductors," *Industry Applications, IEEE Transactions on*, vol. 37, pp. 1045-1054, 2001.
- [130] N. Wang, x, T. Donnell, x, and C. Mathuna, "An Improved Calculation of Copper Losses in Integrated Power Inductors on Silicon," *Power Electronics, IEEE Transactions on*, vol. 28, pp. 3641-3647, 2013.
- [131] R. P. Wojda and M. K. Kazimierczuk, "Winding resistance of litz-wire and multi-strand inductors," *Power Electronics, IET*, vol. 5, pp. 257-268, 2012.
- [132] N. Xi and C. R. Sullivan, "An improved calculation of proximity-effect loss in high-frequency windings of round conductors," in *Power Electronics Specialist Conference, 2003. PESC '03. 2003 IEEE 34th Annual*, 2003, pp. 853-860 vol.2.
- [133] N. Xi and C. R. Sullivan, "Simplified high-accuracy calculation of eddy-current loss in round-wire windings," in *Power Electronics Specialists Conference, 2004. PESC 04. 2004 IEEE 35th Annual*, 2004, pp. 873-879 Vol.2.
- [134] T. Xu and C. R. Sullivan, "Stranded wire with uninsulated strands as a low-cost alternative to litz wire," in *Power Electronics Specialist Conference, 2003. PESC '03. 2003 IEEE 34th Annual*, 2003, pp. 289-295 vol.1.
- [135] C. R. Sullivan, "Power Magnetics Design and Measurement of Power Magnetics," presented at the APEC, 2012.
- [136] J. Reinert, A. Brockmeyer, and R. W. A. A. De Doncker, "Calculation of losses in ferro- and ferrimagnetic materials based on the modified Steinmetz equation," *Industry Applications, IEEE Transactions on*, vol. 37, pp. 1055-1061, 2001.
- [137] M. S. Rylko, B. J. Lyons, J. G. Hayes, and M. G. Egan, "Revised Magnetics Performance Factors and Experimental Comparison of High-Flux Materials for High-Current DC–DC Inductors," *Power Electronics, IEEE Transactions on*, vol. 26, pp. 2112-2126, 2011.
- [138] Y. Bong-Gi, L. Byoung-Kuk, L. Sang-Won, C. Gwang-Bo, and Y. Dong-Wook,

- "Experimental comparison of Mega Flux and JNEX inductors in high power dc-dc converter of Hybrid Electric Vehicles," in *Vehicle Power and Propulsion Conference (VPPC), 2011 IEEE*, 2011, pp. 1-7.
- [139] www.semikron.com. SEMiX 603GB066HDs.
 - [140] d. B. CMC klebetechnik Gmbh, Robert-Bosch-Strae 8, D-67227, Frankenthal, Germany.
 - [141] J. Muhlethaler, J. Biela, J. W. Kolar, and A. Ecklebe, "Core losses under DC bias condition based on Steinmetz parameters," in *Power Electronics Conference (IPEC), 2010 International*, 2010, pp. 2430-2437.
 - [142] J. Muhlethaler, J. Biela, J. W. Kolar, and A. Ecklebe, "Core Losses Under the DC Bias Condition Based on Steinmetz Parameters," *Power Electronics, IEEE Transactions on*, vol. 27, pp. 953-963, 2012.
 - [143] J. Muhlethaler, J. W. Kolar, and A. Ecklebe, "Loss modeling of inductive components employed in power electronic systems," in *Power Electronics and ECCE Asia (ICPE & ECCE), 2011 IEEE 8th International Conference on*, 2011, pp. 945-952.
 - [144] J. D. Pollock, W. Lundquist, and C. R. Sullivan, "Predicting inductance roll-off with dc excitations," in *Energy Conversion Congress and Exposition (ECCE), 2011 IEEE*, 2011, pp. 2139-2145.
 - [145] C. R. Sullivan, J. H. Harris, and E. Herbert, "Core loss predictions for general PWM waveforms from a simplified set of measured data," in *Applied Power Electronics Conference and Exposition (APEC), 2010 Twenty-Fifth Annual IEEE*, 2010, pp. 1048-1055.
 - [146] K. Venkatachalam, C. R. Sullivan, T. Abdallah, and H. Tacca, "Accurate prediction of ferrite core loss with nonsinusoidal waveforms using only Steinmetz parameters," in *Computers in Power Electronics, 2002. Proceedings. 2002 IEEE Workshop on*, 2002, pp. 36-41.
 - [147] J. Reinert, A. Brockmeyer, and R. W. De Doncker, "Calculation of losses in ferro- and ferrimagnetic materials based on the modified Steinmetz equation," in *Industry Applications Conference, 1999. Thirty-Fourth IAS Annual Meeting. Conference Record of the 1999 IEEE*, 1999, pp. 2087-2092 vol.3.
 - [148] M. S. Rylko, K. J. Hartnett, J. G. Hayes, and M. G. Egan, "Magnetic Material Selection for High Power High Frequency Inductors in DC-DC Converters," in *Applied Power Electronics Conference and Exposition, 2009. APEC 2009. Twenty-Fourth Annual IEEE*, 2009, pp. 2043-2049.
 - [149] M. Acanski, J. Popovic-Gerber, and B. Ferreira, "Design of a flexible very low profile high step-up PV module integrated converter," in *Energy Conversion Congress and Exposition (ECCE), 2012 IEEE*, 2012, pp. 2942-2948.
 - [150] L. Quan and P. Wolfs, "A Review of the Single Phase Photovoltaic Module Integrated Converter Topologies With Three Different DC Link Configurations," *Power Electronics, IEEE Transactions on*, vol. 23, pp. 1320-1333, 2008.
 - [151] F. Yu and M. Xudong, "A Novel PV Microinverter With Coupled Inductors and Double-Boost Topology," *Power Electronics, IEEE Transactions on*, vol. 25, pp. 3139-3147, 2010.
 - [152] F. Yu, M. Xudong, and X. Yan, "Study on PV micro-inverter with coupled inductors and double boost topology," in *Industrial Electronics and Applications (ICIEA), 2012 7th IEEE Conference on*, 2012, pp. 2054-2058.
 - [153] www.cree.com. C3D20060D–Silicon Carbide Schottky Diode.
 - [154] www.infineon.com, 600 V CoolMOS C6 Power Transistor IPW60R041C6.
 - [155] M. P. Dr. Dusan Graovac, Andreas Kiep, "MOSFET Power Losses Calculation Using the Datasheet Parameters," Infineon Application Note July 2006.

Appendix A

Modified Steinmetz Equation

A.1. Application of the Modified Steinmetz Equation (MSE) to the CCTT IM Waveforms

In this Appendix the Modified Steinmetz Equation is applied to the waveforms of the CCTT IM. It attempts to improve the empirical Steinmetz equation (A.1.1) in order to make a more accurate calculation of the core loss in applications with non-sinusoidal flux-waveforms. The MSE is presented in (A.1.2) where the average remagnetization, f_{eq} , is presented in (A.1.3).

$$P_{scp} = kf^m B_{ac}^n \quad (\text{A.1.1})$$

$$P_{csp,MSE} = (kf_{eq}^{m-1} B_{ac}^n) f \quad (\text{A.1.3})$$

$$f_{eq} = \frac{2}{\pi^2 \Delta B^2} \int_0^T \left(\frac{dB}{dt} \right)^2 dt \quad (\text{A.1.3})$$

Firstly, before applying it MSE to the CCTT IM waveforms, the MSE is applied to the waveforms of a single-phase boost converter. This will help build up an understanding of how to apply the equation. The normalized switching and equivalent frequency for a single-phase boost converter is presented in Fig. A.1. This graph illustrates that, as the duty cycle approaches $D = 0.1$, the equivalent switching frequency is nearly 2.4 times the switching frequency.

To demonstrate the calculation of the MSE equivalent switching frequency a sample calculation is performed. The familiar switching waveforms for a single-phase boost converter are presented in Fig. A.2. Assuming that the remanence in the core material is zero, the current and flux density is proportional as illustrated in Fig. A.2. The equivalent switching frequency is determined in a piece-wise linear fashion as presented in (A.1.4) – (A.1.7):

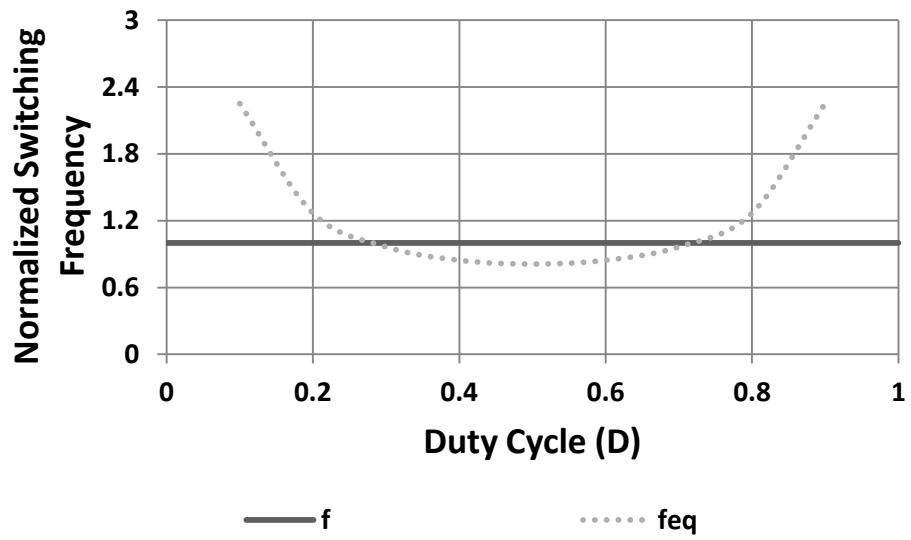


Figure A.1. Normalized switching frequency for a single-phase boost converter

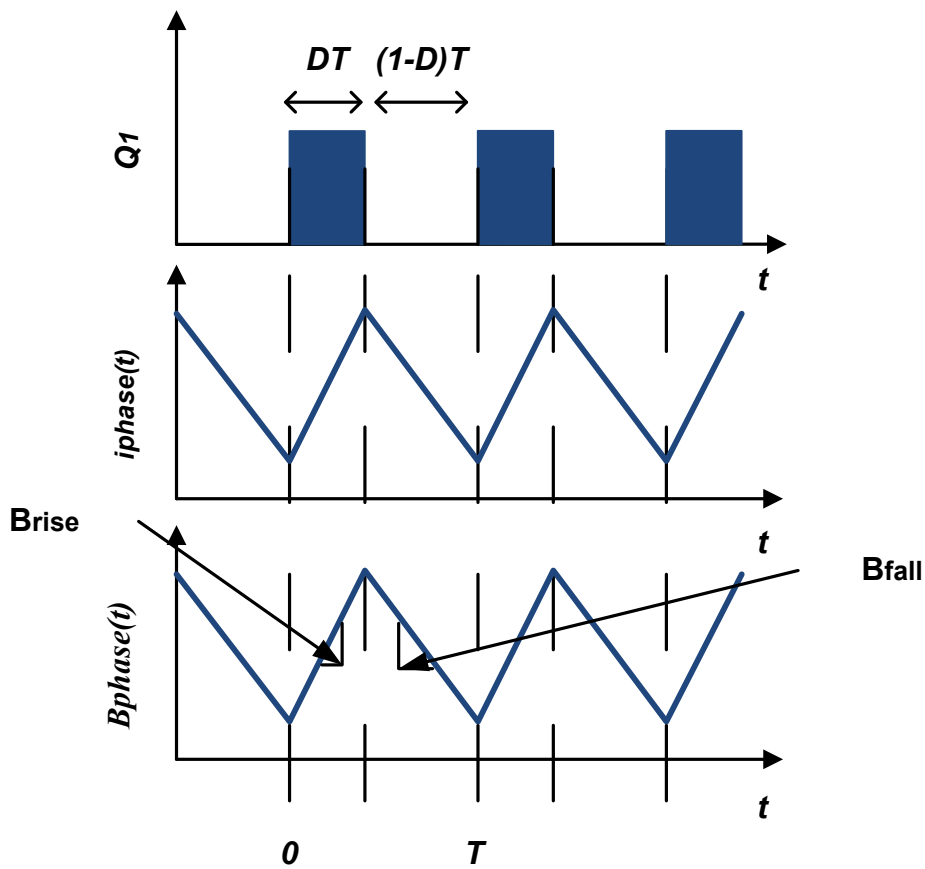


Figure A.2. Single-phase boost converter inductor current and flux density waveforms

$$f_{eq} = \frac{2}{\pi^2 \Delta B^2} \int_0^T \left(\frac{\Delta B}{dt} \right)^2 dt \quad (A.1.4)$$

$$f_{eq} = \frac{2}{\pi^2 \Delta B^2} \left(\left(\frac{\Delta B_{rise}}{DT} \right)^2 DT + \left(\frac{\Delta B_{fall}}{(1-D)T} \right)^2 (1-D)T \right) \quad (A.1.5)$$

$$f_{eq} = \frac{2}{\pi^2} \left(\frac{1}{\Delta B_{rise}^2} \left(\frac{\Delta B_{rise}}{DT} \right)^2 DT + \frac{1}{\Delta B_{fall}^2} \left(\frac{\Delta B_{fall}}{(1-D)T} \right)^2 (1-D)T \right) \quad (A.1.6)$$

$$f_{eq} = f \frac{2}{\pi^2} \left(\frac{1}{D(1-D)} \right) \quad (A.1.7)$$

The result in (A.1.7) means that the equivalent switching frequency is a function of the switching frequency and duty cycle. The Steinmetz parameter, k , m and n are extracted from the material core loss curves at this equivalent frequency in order to calculate the specific core power loss as presented in (A.1.2). The variation of Steinmetz parameters for ferrite 3C92, Metglas 2605SA1 and JFE 10JNHF600 is presented in Table A.1.

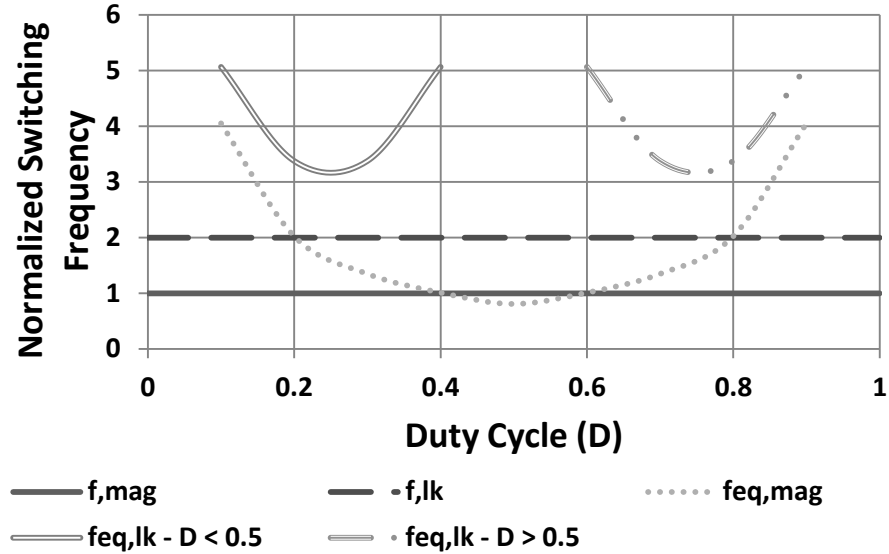


Figure A.3. Normalized switching frequency for a CCTT IM boost converter

The normalized switching and equivalent frequency for a CCTT IM boost converter is presented in Fig. A.3. This graph illustrates that when using the traditional Steinmetz equation the frequency of the leakage component is twice that of the magnetizing component, which is operating at the switching frequency of the converter. When using the MSE the equivalent frequency of the magnetizing and leakage component is 4 and 5 times greater than the converter

switching frequency, respectively, as the duty cycle, $D = 0.1$. To illustrate the MSE a sample calculation is performed which considers a duty cycle of greater than 0.5. The familiar switching waveforms for duty cycles greater than 0.5 is presented in Fig. A.4. The phase current ripple is decomposed into its magnetizing and leakage components which then are considered individually. Due to symmetry the decomposed current composed components are considered over half of the switching interval or $0.5 T$. Firstly, considering the leakage component of the phase current ripple, the following method is used to determine the equivalent switching frequency.

$$f_{eq, lk} = \frac{2}{\Delta B_{lk}^2 \pi^2} \cdot \left[\left(\frac{\Delta B_{lk}}{(D-0.5)T} \right)^2 (D-0.5)T + \left(\frac{\Delta B_{lk}}{(1-D)T} \right)^2 (1-D)T \right] \cdot 2 \quad (A.1.8)$$

The first component of (A.1.8) corresponds to the rise time of the leakage current ripple during interval 1. The second component corresponds to the fall time of the leakage current ripple during interval 2. (A.1.8) is multiplied by two in order to account for the full switching period. Simplification of (A.1.8) results in the following:

$$f_{eq, lk} = f_s \frac{4}{\pi^2} \cdot \left(\frac{0.5}{(D-0.5) \cdot (1-D)} \right) \quad (A.1.9)$$

Now considering the magnetizing component of the phase current ripple, the following method is used to determine the equivalent switching frequency.

$$f_{eq, mag} = \frac{2}{\Delta B_{mag}^2 \pi^2} \cdot \left[\left(\frac{\Delta B_{mag}}{(D-0.5)T} \right)^2 (D-0.5)T + \left(\frac{\Delta B_{mag}}{(1-D)T} \right)^2 (1-D)T \right] \cdot 2 \quad (A.1.10)$$

The first component of (A.1.10) corresponds to the magnetizing current ripple during interval 1. From inspection of Fig. A.4 it is obvious that the magnetizing current ripple during this interval is zero. The second component corresponds to the rise time of the magnetizing current ripple during interval 2. (A.1.10) is multiplied by two in order to account for the full switching period. Simplification of (A.1.10) results in the following:

$$f_{eq, mag} = f_s \frac{4}{\pi^2} \cdot \left(\frac{1}{(1-D)} \right) \quad (A.1.11)$$

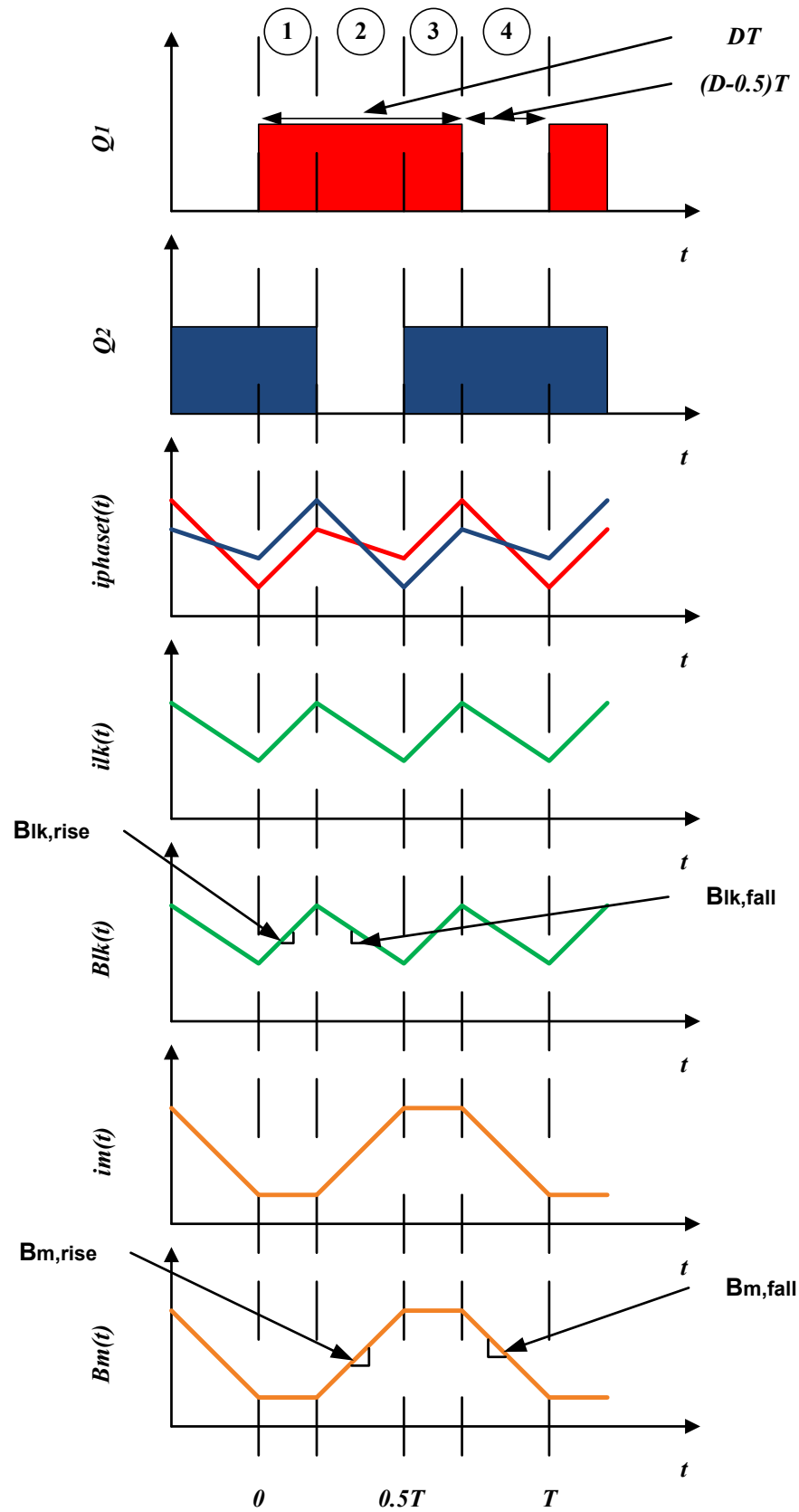


Figure A.4. IM circuit switching waveforms for duty cycle, $D > 0.5$

Table A.1 highlights the variation in the equivalent leakage and magnetizing frequencies for various switching frequencies at a duty cycle of 0.63, which is the design point for the high-power CCTT IM prototype.

Table A.1 Equivalent Leakage and Magnetizing Frequencies at $D = 0.63$.

Switching Frequency (f_s)	Equivalent Leakage ($f_{eq,lk}$)	Equivalent Magnetizing ($f_{eq,mag}$)
kHz	kHz	kHz
16	67	17
25	104	27
50	209	54
75	314	82
100	419	109

Table A.2 Steinmetz Parameters for Ferrite 3C92, Metglas 2605SA1 and JFE 10JNHF600

Material	Steinmetz Parameters for P_{cspMSE} , P_{cspmag} and $P_{csp lk}$ in W/m^3					
Ferroxcube 3C92	f_s	100 kHz	200 kHz	500 kHz	-	-
	k	16.18	1.8×10^{-6}	0.000624	-	-
	m	1.32	2.73	2.19	-	-
	n	3.27	3.45	3.15	-	-
Metglas 2605SA1	f_s	20 kHz	50 kHz	100 kHz	100+ kHz	-
	k	13.7	0.204	1.03	0.162	-
	m	1.32	1.71	1.54	1.71	-
	n	1.97	1.85	1.79	1.81	-
JFE 10JNHF600	f_s	20 kHz	30 kHz	50 kHz	100 kHz	100+ kHz
	k	95.8	1.04×10^{-5}	0.0054	1.86	2.09×10^{-7}
	m	1.32	2.7	2.15	1.58	3
	n	2.11	2	2	1.92	2

The relevant Steinmetz parameters, at the equivalent magnetizing and leakage frequencies, are extracted from the core material data sheet and applied to the following equations:

$$P_{cspmag} = \left(k_{mag} (f_{eq,mag})^{n_{mag}-1} (B_{acmag})^{n_{mag}} \right) f_s \quad (\text{A.1.12})$$

$$P_{csplk} = \left(k_{lk} (f_{eq,lk})^{n_{lk}-1} (B_{aclk})^{n_{lk}} \right) f_s \quad (\text{A.1.13})$$

Table A.2 presents the variation in the value of the Steinmetz parameters for ferrite 3C92, Metglas 205SA1 and JFE 10JNHF600 material.

Appendix B

CCTT IM Schematic

B.1. High-Power 72 kW CCTT IM Schematic

